ornl

NUREG/CR-4219
Volume 1
ORNL/TM-9593/V1

OAK RIDGE
NATIONAL
LABORATORY

MARTIN MARIETTA

Heavy-Section Steel Technology Program Semiannual Progress Report for October 1984–March 1985

C. E. Pugh

Prepared for the U.S. Nuclear Regulatory Commission
Office of Nuclear Regulatory Research
Under Interagency Agreements DOE 40-551-75 and 40-552-75

OPERATED BY
MARTIN MARIETTA ENERGY SYSTEMS, INC.
FOR THE UNITED STATES
DEPARTMENT OF ENERGY

Available from

Superintendent of Documents
U.S. Government Printing Office
Post Office Box 37082
Washington, D.C. 20013-7982

and

National Technical Information Service
Springfield, VA 22161

NUREG/CR-4219
Volume 1
ORNL/TM-9593/V1
Dist. Category RF

Engineering Technology Division

HEAVY-SECTION STEEL TECHNOLOGY PROGRAM SEMIANNUAL PROGRESS REPORT FOR OCTOBER 1984–MARCH 1985

C. E. Pugh

Manuscript Completed – May 15, 1985
Date Published – June 1985

Prepared for the
U.S. Nuclear Regulatory Commission
Office of Nuclear Regulatory Research
under Interagency Agreements DOE 40-551-75 and 40-552-75

NRC FIN No. B0119

Prepared by the
OAK RIDGE NATIONAL LABORATORY
Oak Ridge, Tennessee 37831
operated by
MARTIN MARIETTA ENERGY SYSTEMS, INC.
for the
U.S. DEPARTMENT OF ENERGY
under Contract No. DE-AC05-840R21400

CONTENTS

LIST OF FIGURES

LIST OF TABLES

PREFACE

The Heavy-Section Steel Technology (HSST) Program, which is sponsored by the Nuclear Regulatory Commission, is an engineering research activity devoted to extending and developing the technology for assessing the margin of safety against fracture of the thick-walled steel pressure vessels used in light-water-cooled nuclear power reactors. The program is being carried out in close cooperation with the nuclear power industry. This report covers HSST work performed in October 1984–March 1985. The work performed by Oak Ridge National Laboratory (ORNL) and by subcontractors is managed by the Engineering Technology Division. Major tasks at ORNL are carried out by the Engineering Technology Division and the Metals and Ceramics Division. Prior progress reports on this program are ORNL-4176, ORNL-4315, ORNL-4377, ORNL 4463, ORNL-4512, ORNL-4590, ORNL-4653, ORNL-4681, ORNL-4764, ORNL-4816, ORNL-4855, ORNL-4918, ORNL-4971, ORNL/TM-4655 (Vol. II), ORNL/TM-4729 (Vol. II), ORNL/TM-4805 (Vol. II), ORNL/TM-4914 (Vol. II), ORNL/TM-5021 (Vol. II), ORNL/TM-5170, ORNL/NUREG/TM-3, ORNL/NUREG/TM-28, ORNL/NUREG/TM-49, ORNL/NUREG/TM-64, ORNL/NUREG/TM-94, ORNL/NUREG/TM-120, ORNL/NUREG/TM-147, ORNL/NUREG/TM-166, ORNL/NUREG/TM-194, ORNL/NUREG/TM-209, ORNL/NUREG/TM-239, NUREG/CR-0476 (ORNL/NUREG/TM-275), NUREG/CR-0656 (ORNL/NUREG/TM-298), NUREG/CR-0818 (ORNL/NUREG/TM-324), NUREG/CR-0980 (ORNL/NUREG/TM-347), NUREG/CR-1197 (ORNL/NUREG/TM-370), NUREG/CR-1305 (ORNL/NUREG/TM-380), NUREG/CR-1477 (ORNL/NUREG/TM-393), NUREG/CR-1627 (ORNL/NUREG/TM-401), NUREG/CR-1806 (ORNL/NUREG/TM-419), NUREG/CR-1941 (ORNL/NUREG/TM-437), NUREG/CR-2141, Vol. 1 (ORNL/TM-7822), NUREG/CR-2141, Vol. 2 (ORNL/TM-7955), NUREG/CR-2141, Vol. 3 (ORNL/TM-8145), NUREG/CR-2141, Vol. 4 (ORNL/TM-8252), NUREG/CR-2751, Vol. 1 (ORNL/TM-8369/V1), NUREG/CR-2751, Vol. 2 (ORNL/TM-8369/V2), NUREG/CR-2751, Vol. 3 (ORNL/TM-8369/V3), NUREG/CR-2751, Vol. 4 (ORNL/TM-8369/V4), NUREG/CR-3334, Vol. 1 (ORNL/TM-8787/V1), NUREG/CR-3334, Vol. 2 (ORNL/TM-8787/V2), NUREG/CR-3334, Vol. 3 (ORNL/TM-8787/V3), NUREG/CR-3744, Vol. 1 (ORNL/TM-9154/V1), and NUREG/CR-3744, Vol. 2 (ORNL/TM-9154/V2).

SUMMARY

1. PROGRAM MANAGEMENT

The total program is arranged into ten tasks: (1) program management, (2) fracture methodology and analysis, (3) material characterization and properties, (4) environmentally assisted crack-growth studies, (5) crack-arrest technology, (6) irradiation effects studies, (7) stainless steel cladding evaluations, (8) intermediate vessel tests and analyses, (9) thermal-shock technology, and (10) pressurized-thermal-shock technology. Progress reports are issued on a semiannual basis, and the chapters of those reports correspond to the ten tasks.

The work performed at Oak Ridge National Laboratory (ORNL) and under existing research and development subcontracts is included in this report. During the report period, 43 program briefings, reviews, or presentations were made, and 9 technical documents were published. Program subcontracts were monitored and coordinated.

2. FRACTURE METHODOLOGY AND ANALYSIS

Developments were made to the ORNL fracture codes to permit improved finite-element modeling of nozzle-corner crack regions. The resulting mesh generation code was labeled ORNOZL. The ORNL codes ORMGEN and ORVIRT were distributed to two organizations. Further dynamic-fracture analyses were performed on a laboratory-sized panel specimen that shows promise for being useful in providing high K_{Ia} data in the presence of a rising K field.

A preliminary investigation of existing precracked Charpy V-notch data revealed a possible relation between dynamic-initiation toughness and time to fracture, which might be useful as an aid in estimating the crack-arrest toughness.

Integrated fracture-mechanics experimentation and finite-element analyses are being conducted at the Southwest Research Institute (SwRI) to develop improved predictions for crack arrest in high-upper-shelf toughness conditions. Viscoplastic material characterization experiments were performed to enable use of the Bodner-Partom model in the finite-element fracture analyses. A 2-D finite-element computer code was developed for performing viscoplastic analyses. Cleavage-fibrous transition studies continued at the University of Maryland (UM) with emphasis on local variations of carbon content and size effects in fracture morphology.

3. MATERIAL CHARACTERIZATION

Mechanical and fracture properties characterization of the wide-plate crack-arrest material was performed. A subcontract was let for the purchase of stainless steel clad plate A 533 grade B class 1 steel with properties in each region conducive to allowing brittle crack propagation in the base plate while the cladding remains tough.

4. ENVIRONMENTALLY ASSISTED CRACK-GROWTH TECHNOLOGY

Both fatigue crack-growth rate and fractography results are presented for the recently begun matrix of tests on a high-sulfur steel. Effects of frequency, R ratio, temperature, and environment are being studied; results are consistent with existing data and show increasing growth rates with higher R ratio and temperature. Static-load cracking tests are under way for base, weld, and heat-affected zone materials, and no further cracking was observed during this period. Study was undertaken of the manganese sulfide inclusion distribution within the test steel being used in this task.

5. CRACK-ARREST TECHNOLOGY

The task to perform wide-plate crack-arrest tests at the National Bureau of Standards (NBS) continued. Heavy-Section Steel Technology (HSST) plate 13A was the test material, and ORNL designed, machined, and shipped four additional specimens to NBS. The first test, WP-1.1, was performed at the end of last report period. ORNL, SwRI, and UM performed posttest dynamic-fracture analyses using the computer codes SWIDAC and SAMCR. The NBS made preparations for the second test, WP-1.2, which was performed on January 17. Detailed pretest and posttest (static and dynamic) analyses were performed for WP-1.2.

In other areas, UM continued to administer the ASTM E24.01.06 round robin on crack-arrest testing. In addition, Battelle Columbus Laboratories (BCL) drafted a report on their compilation of a crack-arrest data base that contains 478 data points at temperatures from $RT_{NDT} - 114°C$ to $RT_{NDT} + 102°C$. BCL also instrumented the wide-plate specimens to monitor crack speeds in tests WP-1.1 and WP-1.2.

6. IRRADIATION EFFECTS STUDIES

The Fifth Irradiation Series addresses irradiation effects on the initiation toughness of two high-copper welds. Irradiation of 6 of the 12 planned capsules has been completed. These capsules included Charpy V-notch, tensile, drop-weight, 1T compact, and 4T compact specimens. Irradiation of capsules 7 and 8 was started in early March and will be completed early next report period. The target fluence for this series of irradiations was raised from 1.5 to 1.75×10^{23} neutrons/m^2. The Sixth Series will examine the shift in the crack-arrest toughness of these same two weldments. Preliminary specimen complement and capsule design was completed. The Seventh Series is evaluating irradiation effects on stainless steel cladding. Phase 1 study was completed on an irradiated one-wire submerged-arc clad material. Fracture characteristics were examined in terms of microstructure and irradiation effects. Plans were made for the phase 2 study of a commercially produced three-wire cladding representative of that used in the fabrication of early reactor vessels.

7. CLADDING EVALUATIONS

Preparation of a topical report on the ORNL clad-beam tests that were performed in earlier report periods was completed, and the report was sent to reproduction. Two segments of a BWR pressure vessel were obtained for flaw and properties characterization. This material has been clad, and segments of both longitudinal and circumferential welds were included. A nondestructive examination plan was developed for the study of this material.

8. INTERMEDIATE VESSEL TESTS AND ANALYSIS

Work continued on preparation of a topical report on the intermediate vessel test ITV-8A, which involved a low-upper-shelf weld.

9. THERMAL-SHOCK TECHNOLOGY

As a part of the Integrated Pressurized Thermal-Shock Program, probabilistic fracture-mechanics calculations were made for the H.B. Robinson-2 (HBR-2) reactor pressure vessel to obtain a best estimate of the conditional probability of vessel failure [$P(F|E)$] associated with numerous postulated transients. Those studies indicated that $P(F|E)$ for HBR-2 was very small because of low concentrations of nickel and low values of RT_{NDT_o}.

Studies pertaining to an evaluation of the behavior of subclad flaws under thermal-shock loading conditions were continued. Calculations were made for three test facilities to determine which one would be most suitable for thermal-shock experiments with clad cylinders having subclad flaws. The results indicate that the existing thermal-shock test facility would be appropriate for the first experiment.

10. PRESSURIZED-THERMAL-SHOCK TECHNOLOGY

Extensive static and dynamic posttest fracture analyses were performed for PTSE-1, the first pressurized-thermal-shock test. A topical report covering PTSE-1 was completed and is in reproduction. PTSE-2 will be a study of warm prestressing and upper-shelf instability. For this test, the vessel (V-8) used in PTSE-1 will be repaired with a low-upper-shelf insert in the region to be flawed. Parametric fracture analyses were performed to confirm the test feasibility and to determine the ranges of material properties required for an optimum test. Efforts to procure suitable test material and appropriate thermocouple systems for PTSE-2 were pursued with contracts being let in each case.

HEAVY-SECTION STEEL TECHNOLOGY PROGRAM SEMIANNUAL PROGRESS REPORT FOR OCTOBER 1984–MARCH 1985*

C. E. Pugh

ABSTRACT

The Heavy-Section Steel Technology (HSST) Program is conducted for the Nuclear Regulatory Commission. The studies are related to all areas of the technology of materials fabricated into thick-section primary-coolant containment systems of light-water-cooled nuclear power reactors. The focus is on the behavior and structural integrity of steel pressure vessels containing cracklike flaws. Starting with FY 1984, the program is organized into ten tasks: (1) program management, (2) fracture methodology and analysis, (3) material characterization and properties, (4) environmentally assisted crack-growth studies, (5) crack-arrest technology, (6) irradiation effects studies, (7) cladding evaluations, (8) intermediate vessel tests and analysis, (9) thermal-shock technology, and (10) pressurized-thermal-shock technology. During this period, extensions were made to the fracture analysis codes by developing an improved nozzle-corner crack model. Copies of the ADINA-ORMGEN-ORVIRT analysis codes were distributed to numerous organizations outside Oak Ridge National Laboratory (ORNL). Elastodynamic analyses were performed by ORNL and Southwest Research Institute in support of the wide-plate crack-arrest tests that the National Bureau of Standards are performing for the HSST Program. Characterization studies included deformation and fracture properties tests of wide-plate material and crack-growth rate tests of high-sulfur vessel steels. Analytical assessments were made of laboratory specimens with potential for use in obtaining high crack-arrest toughness data. Further results from K_{Ia} tests were received for the ASTM round robin. Four series of irradiations were continued for the study of K_{Ic} shifts for welds with different copper contents, and test plans proceeded for the Sixth and Seventh Irradiation Series. Work was completed on the report covering ORNL clad-beam tests. Work on the report on ITV-8A that contained a low-upper-shelf weldment was continued. Exploratory analytical fracture studies were carried out for clad cylinders undergoing thermal-shock loadings, and fracture assessments continued for the Integrated Pressurized Thermal-Shock Program. Posttest analyses were completed for the first pressurized thermal-shock test (PTSE-1), and preparation of

*This report is written in terms of metric units. Conversion from SI to English units for all SI quantities are listed on a foldout page at the end of this report.

the topical report on PTSE-1 was completed. Contracts were let for procurement of low-upper-shelf energy test material and thermocouple thimbles for use in PTSE-2.

---

1. PROGRAM MANAGEMENT

C. E. Pugh

The Heavy-Section Steel Technology (HSST) Program, a major safety program sponsored by the Nuclear Regulatory Commission (NRC) at the Oak Ridge National Laboratory (ORNL), is concerned with the structural integrity of the primary systems [particularly the reactor pressure vessels (RPVs)] of light-water-cooled nuclear power reactors. The structural integrity of these vessels is ensured by (1) designing and fabricating RPVs according to standards set by the code for nuclear pressure vessels, (2) detecting flaws of significant size that occur during fabrication and in service, and (3) developing methods of producing quantitative estimates of conditions under which fracture could occur. The program is concerned mainly with developing pertinent fracture technology, including knowledge of (1) the material used in these thick-walled vessels, (2) the flaw-growth rate, and (3) the combination of flaw size and load that would cause fracture and thus limit the life and/or operating conditions of this type of reactor plant.

The program is coordinated with other government agencies and with the manufacturing and utility sectors of the nuclear power industry in the United States and abroad. The overall objective is a quantification of safety assessments for regulatory agencies, professional code-writing bodies, and the nuclear power industry. Several activities are conducted under subcontract by research facilities in the United States and through an informal cooperative effort on an international basis. Five research and development subcontracts are currently in force.

The program tasks are arranged according to the work breakdown structure shown in Fig. 1.1. Accordingly, the chapters of this progress report correspond to these ten tasks. During this report period, the 5-year program plan[1] was updated to be applicable to FY 1984–1988 and was distributed to the NRC for comment. It will be issued as a NUREG report early next period.

Two foreign technical specialists were at ORNL on temporary assignments to the HSST Program during this period. Dr. Hermann Stamm of the Institute für Reaktorbauelemente, Kernforschungszentrum Karlsruhe, Federal Republic of Germany, completed a 9-month assignment at the end of January 1985. Mr. Robert Wanner of the Swiss Federal Institute for Reactor Research is at ORNL for 1 year, through June 1985. Mr. Stefan Brosi, of the same institute, reported to ORNL on March 18 for an assignment through June to work on nozzle-cracking analyses for Project Heiss Damph Reaktor experimental/analytical studies.

During this period, 43 program briefings, reviews, or presentations were made by the HSST staff at technical meetings and at program reviews for NRC staff or visitors. There were nine publications that include one

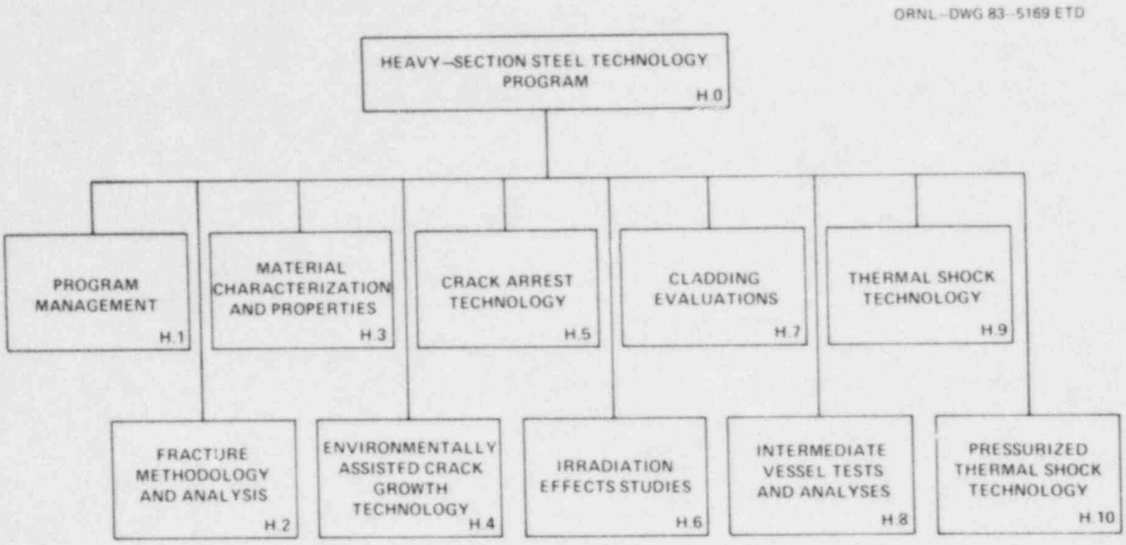

Fig. 1.1. Level-2 work breakdown structures for HSST Program.

technical progress report,[2] six topical reports,[3-8] and two technical papers.[9-10]

In addition, the following eight papers were presented at the NRC Twelfth Water Reactor Safety Research Information Meeting, October 23–25, 1984, Gaithersburg, Maryland; a summary of each is given in Ref. 11.

W. H. Bamford, "Environmentally Assisted Crack-Growth Studies."

R. G. Berggren, J. J. McGowan, B. H. Menke, R. K. Nanstad, and K. R. Thoms, "Irradiation Effects in Low-Alloy Reactor Pressure Vessel Steels."

R. H. Bryan, "Results and Conclusions from the First Pressurized-Thermal-Shock Experiment."

R. D. Cheverton, "PTS Fracture Mechanics Methodology and Conclusions."

W. R. Corwin, R. G. B[illegible] and R. K. Nanstad, "Fracture Properties of a Neutron-Irr[illegible]ainless Steel Submerged-Arc Weld Cladding Overlay."

R. J. Fields, "Wide-Plate Crack-Arrest Tests."

M. F. Kanninen, J. Ahmed, B. R. Bass, and V. Papaspyropoulos, "Wide-Plate Crack-Arrest Analysis."

M. F. Kanninen and J. Strosnider, "EPFM Analysis and Blind Test of Cracked Pipe to Validate IWB-3640 Rules."

References

1. *Heavy-Section Steel Technology Program — Five-Year Plan FY 1983–1987*, NUREG/CR-3595 (ORNL/TM-9008), Martin Marietta Energy Systems, Inc., Oak Ridge Natl. Lab., April 1984.

2. C. E. Pugh, *Heavy-Section Steel Technology Program Semiannual Prog. Rep. October 1983–March 1984*, NUREG/CR-3744, Vol. 2 (ORNL/TM-9154/V2), Martin Marietta Energy Systems, Inc., Oak Ridge Natl. Lab.

3. W. R. Corwin, *Assessment of Radiation Effects Relating to Reactor Pressure Vessel Cladding*, NUREG/CR-3671 (ORNL-6047), Martin Marietta Energy Systems, Inc., Oak Ridge Natl. Lab., July 1984.

4. W. R. Corwin, R. G. Berggren, and R. K. Nanstad, *Charpy Toughness and Tensile Properties of a Neutron-Irradiated Stainless Steel Submerged-Arc Weld Clad Overlay*, NUREG/CR-3927 (ORNL/TM-9309), Martin Marietta Energy Systems, Inc., Oak Ridge Natl. Lab., September 1984.

5. C. W. Schwartz et al., *SAMCR: A Two-Dimensional Dynamic Finite Element Code for the Stress Analysis of Moving CRacks*, NUREG/CR-3891 (ORNL/Sub/79-7778/3), Martin Marietta Energy Systems, Inc., Oak Ridge Natl. Lab., November 1984.

6. J. J. McGowan, *Tensile Properties of Irradiated Nuclear Grade Pressure Vessel Plate and Welds for the Fourth HSST Irradiation Series*, NUREG/CR-3978 (ORNL/TM-9516), Martin Marietta Energy Systems, Inc., Oak Ridge Natl. Lab., January 1985.

7. R. W. Wanner, B. R. Bass, and J. G. Merkle, *Results of the 3rd European Group on Fracture Round Robin on Elastic-Plastic Fracture Mechanics*, Letter Report from the Oak Ridge Natl. Lab. to L. H. Larsson, Joint Research Center, Ispra, Italy (January 1985).

8. D. G. Ball et al., *Stress-Intensity-Factor Influence Coefficients for Surface Flaws in Pressure Vessels*, NUREG/CR-3723 (ORNL/CSD/TM-216), Martin Marietta Energy Systems, Inc., Oak Ridge Natl. Lab, February 1985.

9. J. J. McGowan and R. K. Nanstad, "A Direct Comparison of Unloading Compliance and Potential Drop Techniques in J-Integral Testing," *Proceedings of the 1984 Society for Experimental Mechanics Fall Conference, November 4–7, 1984, Milwaukee, Wis.*, Society for Experimental Mechanics.

10. R. H. Bryan et al., "The Heavy-Section Steel Technology Pressurized-Thermal-Shock Experiment PTSE-1," submitted for publication in *Journal of Engineering Fracture Mechanics*.

11. Stanley A. Szawlewicz, comp., *Twelfth Water Reactor Safety Research Information Meeting, Volume 4 — Material Engineering Research*, NUREG-CP-0058, Vol. 4, U.S. Nuclear Regulatory Commission, January 1985.

2. FRACTURE METHODOLOGY AND ANALYSIS

2.1 Development of the ORNOZL Finite-Element Mesh Generating Code for Nozzle Corner Cracks

B. R. Bass J. K. Walker

During this report period, a prototype version of the ORNOZL finite-element mesh generating code was developed for nozzle-corner crack analysis. Program ORNOZL automatically generates a fully three-dimensional (3-D) finite-element model of a nozzle-cylinder intersection containing a mathematically or user-defined corner crack. As few as five input cards are required to execute the program. Output from ORNOZL consists of files containing nodal point coordinates and element connectivities that completely define the 3-D finite-element model. These files are written in formats that are compatible with the ADINA structural analysis finite-element program.[1] Fracture-mechanics parameters for the finite-element model are determined from the ORVIRT[2] program, which functions as a postprocessor of the conventional solution obtained from ADINA. In applications, the energy release rate is evaluated pointwise by ORVIRT from solution data written to the nodal point and element portholes of ADINA and from a virtual extension of the crack front produced by ORNOZL.

Features of the ORNOZL code include a crack-tip modeling scheme identical to that used in the ORMGEN-3D code[3] for cylinder and plate geometries. Special wedge or collapsed-prism crack-tip elements are employed along the crack front to model the appropriate singularity in the stress field. One-eighth, one-quarter, or one-half of the complete structure is modeled, depending on the number of symmetry planes in the nozzle-crack configuration. The program contains a clad option that allows for either an embedded or a penetrating corner crack in the clad material. Future development of the ORNOZL code will include user-selected options for two different types of nozzle reinforcement and for expanded flexibility of admissible crack configurations.

Figure 2.1 depicts an ORNOZL-generated, 3-D, finite-element model of an Oak Ridge National Laboratory–intermediate test vessel (ORNL-ITV) nozzle-vessel configuration containing two corner cracks. One-quarter of the geometry is modeled, implying the presence of two symmetric corner cracks in the longitudinal plane of the vessel. The finite-element model consists of 2616 nodes, 456 20-node isoparametric brick elements, 48 crack-tip wedge elements, and 218 3-D internal pressure elements. Five input cards were required to generate the model. The corresponding single-corner crack model (one plane of symmetry) (Fig. 2.2) is defined by 3306 nodes, 591 20-node isoparametric elements, 48 crack-tip wedge elements, and 284 3-D internal pressure elements.

ORNL-DWG 85-4337 ETD

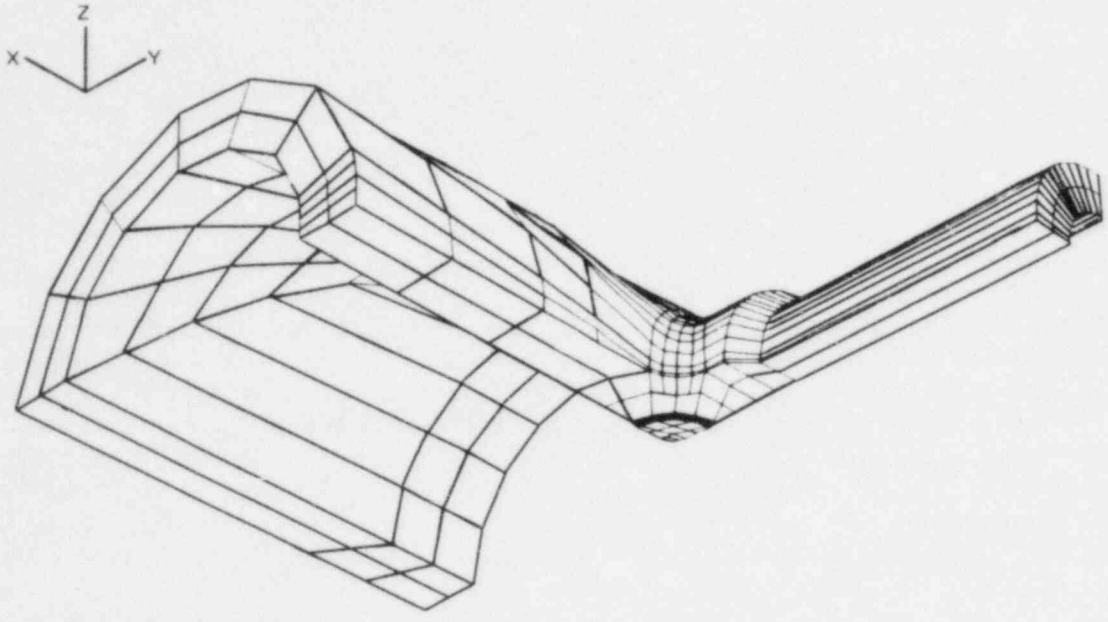

Fig. 2.1. Finite-element model of ITV with two symmetric corner cracks in longitudinal plane of vessel.

ORNL-DWG 85-4338 ETD

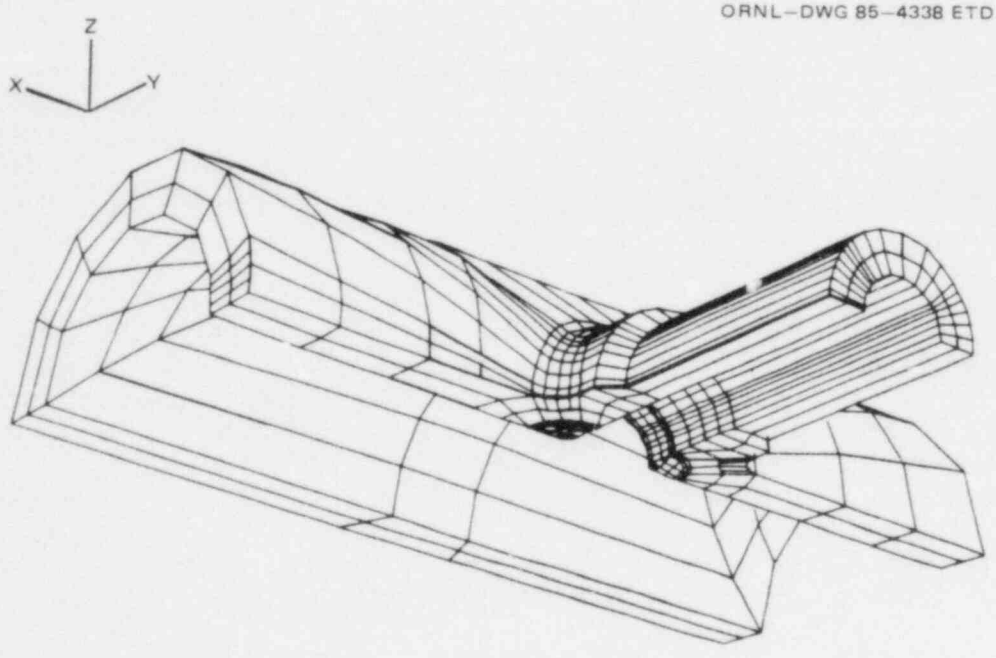

Fig. 2.2 Finite-element model of ITV with single-corner crack in longitudinal plane of vessel.

2.2 Effects of Loading Rate on Dynamic-Fracture-Toughness Values Measured with Instrumented PCCV Specimens

J. G. Merkle

In reviewing the background for the dynamic-toughness data obtained by several laboratories using instrumented precracked Charpy V-notch (PCCV) specimens of TSE-5A material furnished by ORNL, an apparent effect of time to maximum load on dynamic-fracture toughness at temperatures above RT_{NDT} was noticed. The data for which this observation was made are not the TSE-5A data, but earlier data contained in reports published by a joint Pressure Vessel Research Committee (PVRC)/Metal Properties Council (MPC) task group and the Electric Power Research Institute (EPRI).

Following an evaluation test series organized by the joint PVRC/MPC task group,[4] which used specimens of A 533 grade B class 1 steel (HSST Plate 02), EPRI sponsored the development of improved test procedures[5,6] and subsequently sponsored a round-robin test program using several heats of pressure vessel steel.[7] The test procedures that were specified included limits on the minimum time to maximum load to avoid early inertial load peaks and excessive amplifier attenuation. These limits were applied in terms of upper limits on initial hammer energy, thus on the velocity at the beginning of impact. A lower limit on initial hammer energy was also established, in this case for the purpose of preserving an approximately linear decrease in hammer velocity with time during the impact event and also of preventing the hammer velocity from decreasing more than 20% during impact. Although no experimental data were published to show the basis for the lower limit on initial hammer energy, an inquiry to Server[8] revealed that unpublished data did show toughness increases apparently caused by velocity decreases exceeding 20% of the velocity at the beginning of impact. In other words, observed loading rate effects were the basis for the lower limit on initial hammer energy specified in the EPRI-instrumented impact testing procedures.

If loading rate effects had been observed at the beginning of the EPRI program, they might be expected to be apparent in data preceding the EPRI program, especially at temperatures above the RT_{NDT} at which strain-rate effects are especially significant. Such data are available in the PVRC/MPC report,[4] which contains instrumented PCCV data, including time to maximum load obtained by seven different laboratories for HSST Plate 02 at 48.89°C (120°F). These data, listed in Table 2.1, are expressed in terms of K_{Id}, having been converted from elastic-plastic J_{Id} values by using the expression

$$K_{Id} = \sqrt{EJ_{Id}} , \qquad (2.1)$$

where J_{Id} is calculated from the impact energy, according to analytical procedures for estimating specimen displacement from hammer velocity. The data in Table 2.1 are plotted in Fig. 2.3 and show a definite tendency to decrease with decreasing time to maximum load t_M, thus with increasing loading rate. Fitting a straight line to the data by eye and

Table 2.1. Dynamic-initiation fracture-toughness values for HSST Plate 02 at 48.89°C (120°F) measured with instrumented PCCV specimens (Ref. 4)

Laboratory	Specimen No.	t_M (μs)	K_{Id} (MPa•$\sqrt{m}$)
1	95	390	181
	73	144	153
	65	168	162
	76	168	164
2	90	355	193
	102	300	190
	112	460	233
3	36	360	173
	140	390	185
	157	390	188
	168	212	175
4	58	398	211
	45	272	194
	30	505	248
5	160	500	259
	119	400	176
	138	400	209
6	80	340	195
	78	469	246
	91	328	215
7	114	364	207
	89	286	213
	83	428	222
	94	396	225

extrapolating to $t_M = 0$ gives a limiting high rate value of $K_{Id} = 108$ MPa•$\sqrt{m}$. Comparing this value with the Materials Research Laboratory (MRL) crack-arrest data[9] for HSST Plate 02 shown in Fig. 2.4 indicates excellent agreement, implying at least a connection between high-rate initiation toughness and crack-arrest toughness values.

To determine whether the same trend is evident in the later EPRI round-robin data, additional PCCV dynamic-toughness values for HSST Plate 02 at 37.78 and 48.89°C were obtained from the summary of the EPRI data.[10] These values are listed in Table 2.2 along with values of t_M calculated from the relation

$$t_M = \frac{K_{Id}}{\dot{K}} , \qquad (2.2)$$

using the data given in Ref. 10. The two values for 48.89°C (120°F) have been plotted in Fig. 2.3 and appear to be consistent with the PVRC/MPC data. The data for 37.78°C (100°F) are plotted in Fig. 2.5, from which it can be seen that the values of t_M for the EPRI data lie in a higher

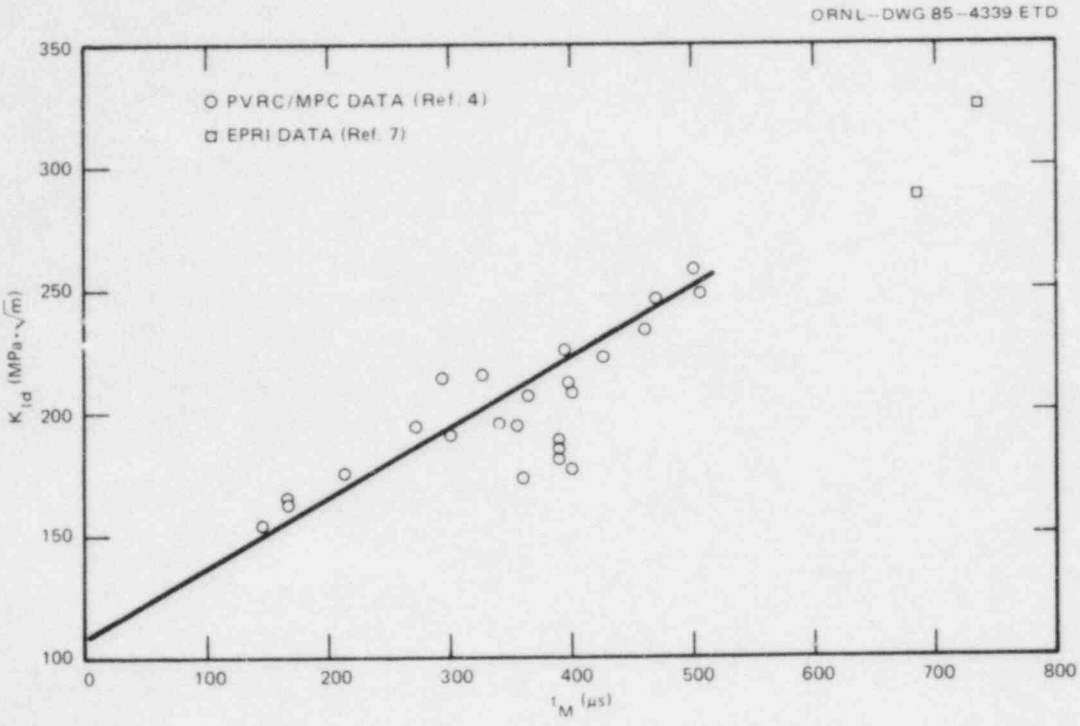

Fig. 2.3. Dynamic-initiation fracture-toughness values for HSST Plate 02 at 48.89°C measured with instrumented PCCV specimens.

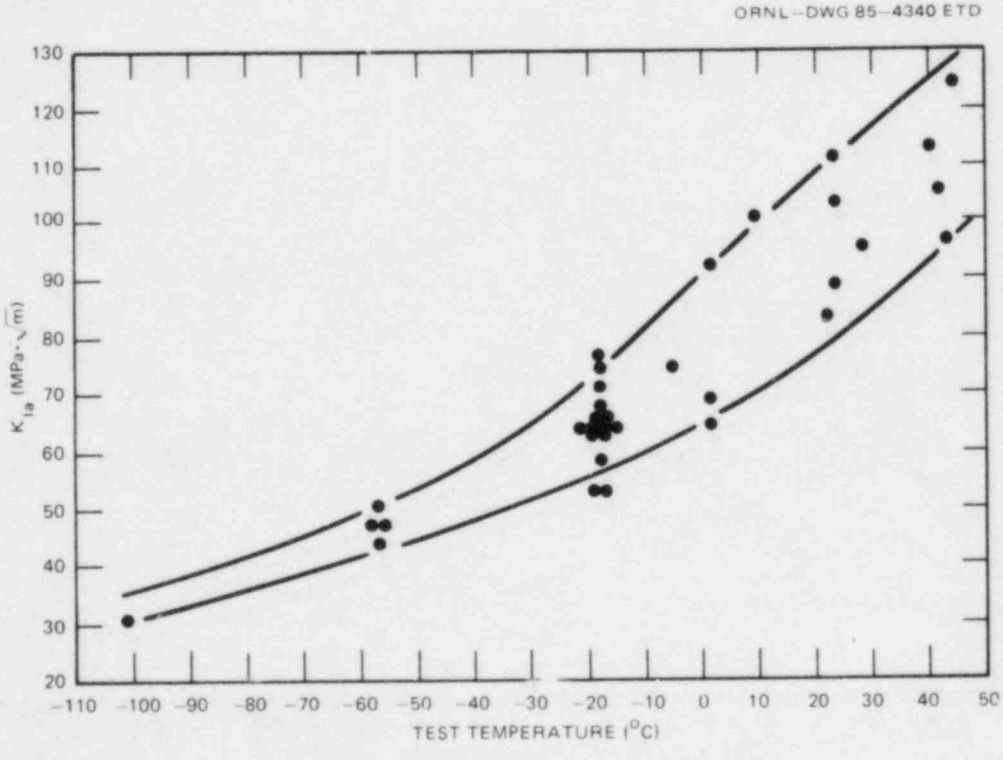

Fig. 2.4. Crack-arrest toughness of HSST Plate 02 as a function of temperature; data from tests where crack front was within 2.54 mm of minimum section (Ref. 9).

Table 2.2. Dynamic-initiation fracture-toughness values for HSST Plate 02 measured with instrumented PCCV specimens (Ref. 10)

Specimen No.	Test temperature (°C)	K_{Id} (Mpa•$\sqrt{m}$)	$\dot{K} \times 10^{-6}$ $\left(\frac{Mpa \cdot \sqrt{m}}{s}\right)$	t_M (μs)
9	48.89	286.81	0.42	683
65	48.89	323.08	0.44	734
10	37.78	297.80	0.34	876
11	37.78	301.10	0.34	886
10	37.78	295.60	0.34	869
11	37.78	270.33	0.40	676
22	37.78	302.20	0.54	560
26	37.78	270.33	0.35	772
23	37.78	314.29	0.38	827
24	37.78	289.01	0.46	628
48	37.78	229.67	0.46	499
5	37.78	237.36	0.42	565
38	37.78	246.15	0.44	559
1	37.78	256.04	0.45	569

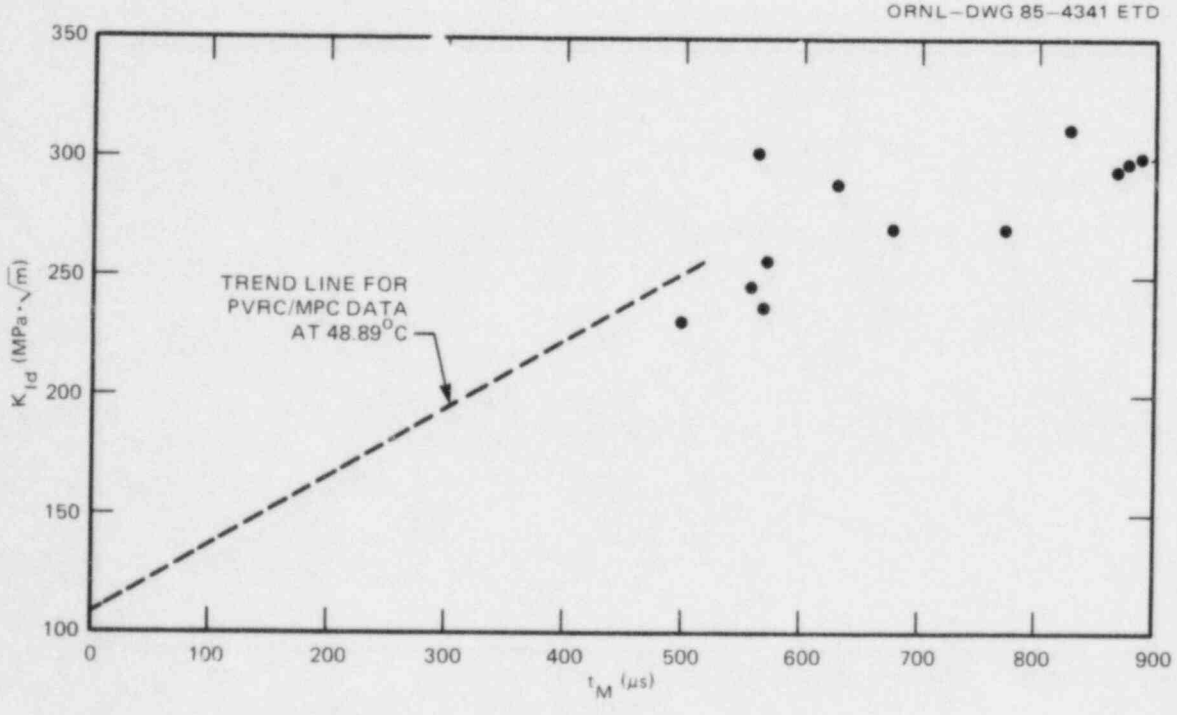

Fig. 2.5. Dynamic-initiation fracture-toughness values for HSST Plate 02 at 37.78°C measured with instrumented PCCV specimens (Ref. 10).

range than those of the PVRC/MPC data. Establishing a trend with t_M for the data in Fig. 2.5 is not as easy as for the data in Fig. 2.3 partly because, at the large values of t_M (slower loading rates), cleavage may have occurred after maximum load or not at all in some cases, thus causing the toughness values (calculated at maximum load) to level off. However, it is reasonable to assume that the data in Fig. 2.3 should form an upper bound to the data in Fig. 2.5 because of the difference in test temperatures. The implication of these observations is that consideration should be given to testing over a broad range of t_M values, say 150 to 800 μs, and then extrapolating to $t_M = 0$ to estimate K_{Ia}.

2.3 Fracture Analysis of a Small Panel Crack-Arrest Specimen

B. R. Bass H. K. Stamm
C. E. Pugh

Early laboratory studies of crack arrest have led to test specimens that reduce the dynamic effects of the running crack. The appropriateness of current specimen recommendations is being examined through a round-robin test program.[11] However, these specimens provide limited constraint of deformation in the crack-plane region and a driving force that decreases with crack extension. These factors have limited the generation of valid data to low temperatures that are below those where arrest is most likely to occur in a pressurized-thermal-shock (PTS) scenario. The Heavy-Section Steel Technology (HSST) Program is providing crack-arrest data over a greatly expanded temperature range through tests of wide-plate specimens,[12] thermally shocked cylinders,[13] and PTS tests.[14] The wide-plate test series provides the opportunity to obtain significant numbers of data points at affordable costs. The thermal-shock and PTS tests provide validation data under multiaxial transient conditions.

Recent studies[15] have been conducted by the HSST Program to evaluate the usefulness of a relatively small panel specimen (45.7 × 76.2 × 2.54 cm) for crack-arrest experiments. The goal is for the panel to be designed for measurement of K_{Ia} values at temperatures approaching the upper shelf of the material. Additional conditions are that crack arrest should take place in a rising K_I field and that the resultant load should not exceed 2447 kN (the capacity of the available testing machine). It is proposed that crack arrest in a rising K_I field be achieved by applying a temperature gradient across the specimen. Crack propagation must initiate at lower-shelf temperatures and run into a region at high temperature with high K_{Ia} levels. In Ref. 15, a panel specimen with a stub (Fig. 2.6) was proposed to meet the above requirements. The stub is cooled to serve as a crack-starter region and is mechanically loaded to provide K_I levels that are high enough for initiation. An eccentric load is applied to the panel to produce a rising K_I field. Static analyses[15] were carried out for the specimen of Fig. 2.6 to determine the maximum attainable stress-intensity factor. For a resultant tensile load on the stub of $F_s = 66.7$ kN and panel load of $F_p = 2447$ kN, which were uniformly applied over $0 < Y_s < 10.2$ cm and 30.5 cm $< Y_p < 40.6$ cm (Y measured from left edge), respectively, the K_I field has a value of 60.4 MPa$\cdot\sqrt{m}$ with the crack tip at Y = 20.3 cm and rises to a peak value of 220 MPa$\cdot\sqrt{m}$ at Y = 20.3 cm.

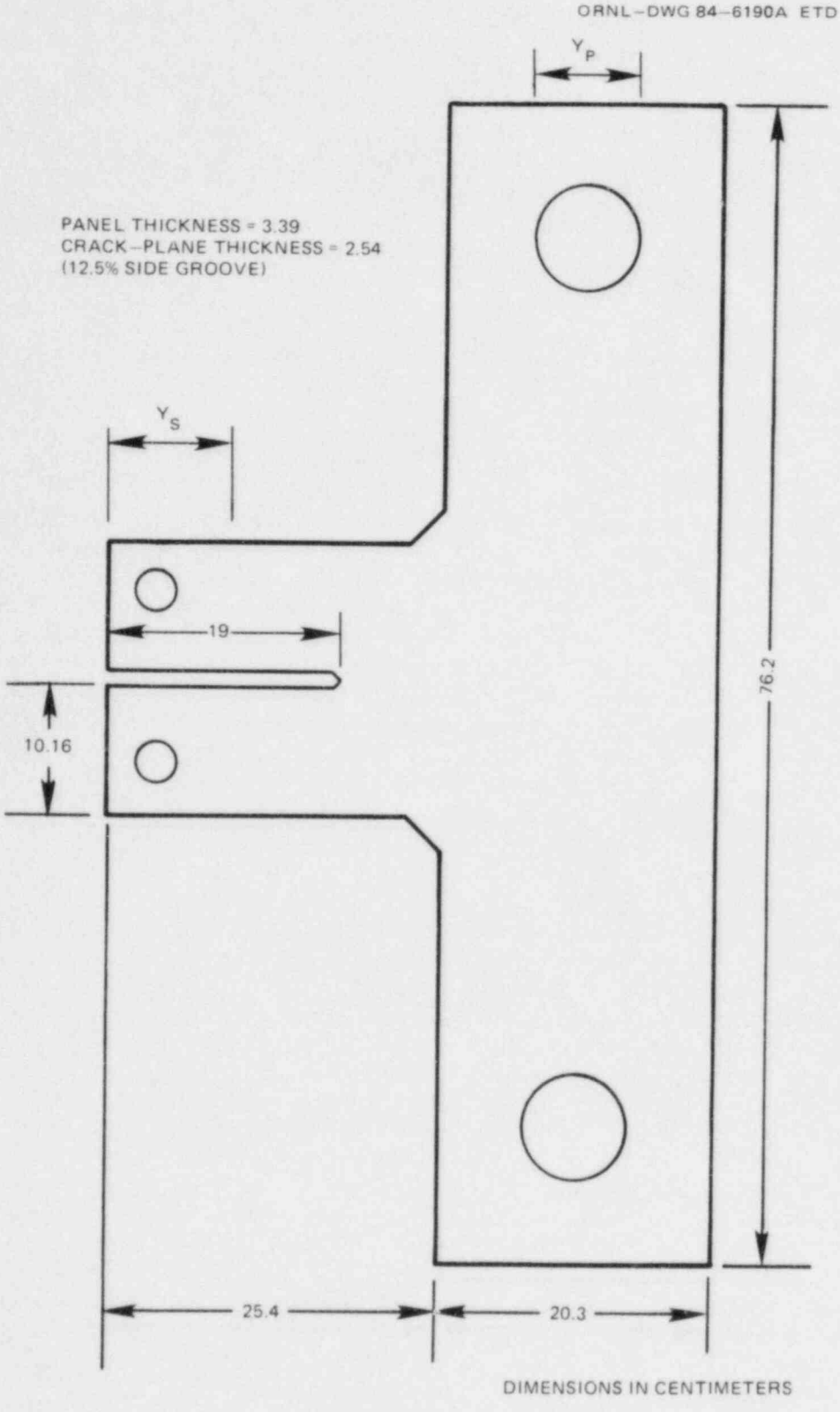

Fig. 2.6. Recommended crack-arrest panel configuration.

During this report period, the panel specimen of Fig. 2.6 was subjected to further static and dynamic analyses to assess its usefulness for producing K_{Ia} data in the temperature regime of upper-shelf material behavior. These analyses were carried out using the finite-element codes ADINAT for temperature analysis[16] and SWIDAC for static and dynamic-elastic analyses.[17] All finite-element calculations were based on a two-dimensional (2-D) plane-stress model. The plate had a thickness of 3.39 cm and was assumed side-grooved to a depth of 12.5% of the thickness, resulting in a net thickness of 2.54 cm in the crack plane. The computations were based on a plate thickness of 3.39 cm, with the side grooves taken into account by adjustment of the resulting stress-intensity factor. Material properties for the panel were the same as those adopted for the wide-plate study described in Sects. 5.1 and 5.3.

The thermal boundary conditions for the panel are illustrated in Fig. 2.7. The two surfaces of the stub, denoted C_1 and C_2, are cooled to the temperature T_{min}, while the back surface (surface H) of the panel specimen is heated to a temperature T_{max}. All other surfaces of the plate are assumed to be insulated. The finite-element results from ADINAT for the steady state (dimensionless) temperature distribution in the crack plane under these boundary conditions are also shown in the figure. The values of the heating and cooling temperatures T_{max} and T_{min}, respectively, are used in the analyses to adjust the length of the crack jump in postulated run-arrest events.

The panel crack-arrest specimen was subjected to static and dynamic analyses to determine the effects of loading and thermal gradient on the predicted run-arrest event. To keep the stub force low and to produce a driving force high enough to propagate the crack into the panel, a crack-tip temperature of $T_{CT} = -55°C$, corresponding to $K_{Ic} = 67.8$ MPa$\cdot\sqrt{m}$ from Eq. (5.2), was selected for these analyses. Initiation is assumed to occur ~25% above K_{Ic}, based on a probable elevation in apparent toughness from prevailing plane-stress conditions. Two of the analyses utilized a mechanical load combination denoted as the reference load case, with stub load $F_s = 0.111$ MN (25 kips) and panel load $F_p = 1.75$ MN (393 kips). The loads are applied as point loads (at the top of the pin holes) at the locations indicated in Fig. 2.8. Results of the stability analyses for the reference load case are shown in Figs. 2.8 and 2.9 and in Table 2.3 for the two temperature gradients defined by the following boundary conditions: case A – $T_{min} = -119°C$, $T_{max} = 190°C$ and case B – $T_{min} = -99.6°C$, $T_{max} = 116°C$. The location X_{US} where the temperature equals the onset of Charpy upper shelf is shown in Table 2.3. Stability conditions of the arrested crack are expressed in terms of the limit crack lengths for reinitiation a_{rein}, for tensile instability a_{I1}, and for tearing instability a_{I2}. (These limit crack lengths are discussed in more detail in Sect. 5.2.) For cases A and B, the limit crack length beyond which tensile instability of the arrested crack should be expected is $a_{I1} = 32.4$ cm. Tearing instability occurs if the arrested crack length exceeds $a_{I2} = 31.7$ cm. Therefore, the instability range is determined primarily by fracture caused by tensile instability. The limit crack length for reinitiation in cleavage a_{rein} is temperature dependent through the K_{Ic} function. If the crack-tip temperature remains fixed and the temperature of the back surface T_{max} is reduced, the limit length a_{rein} is increased as shown in Figs. 2.8 and 2.9. Thus, the interval in which the arrested

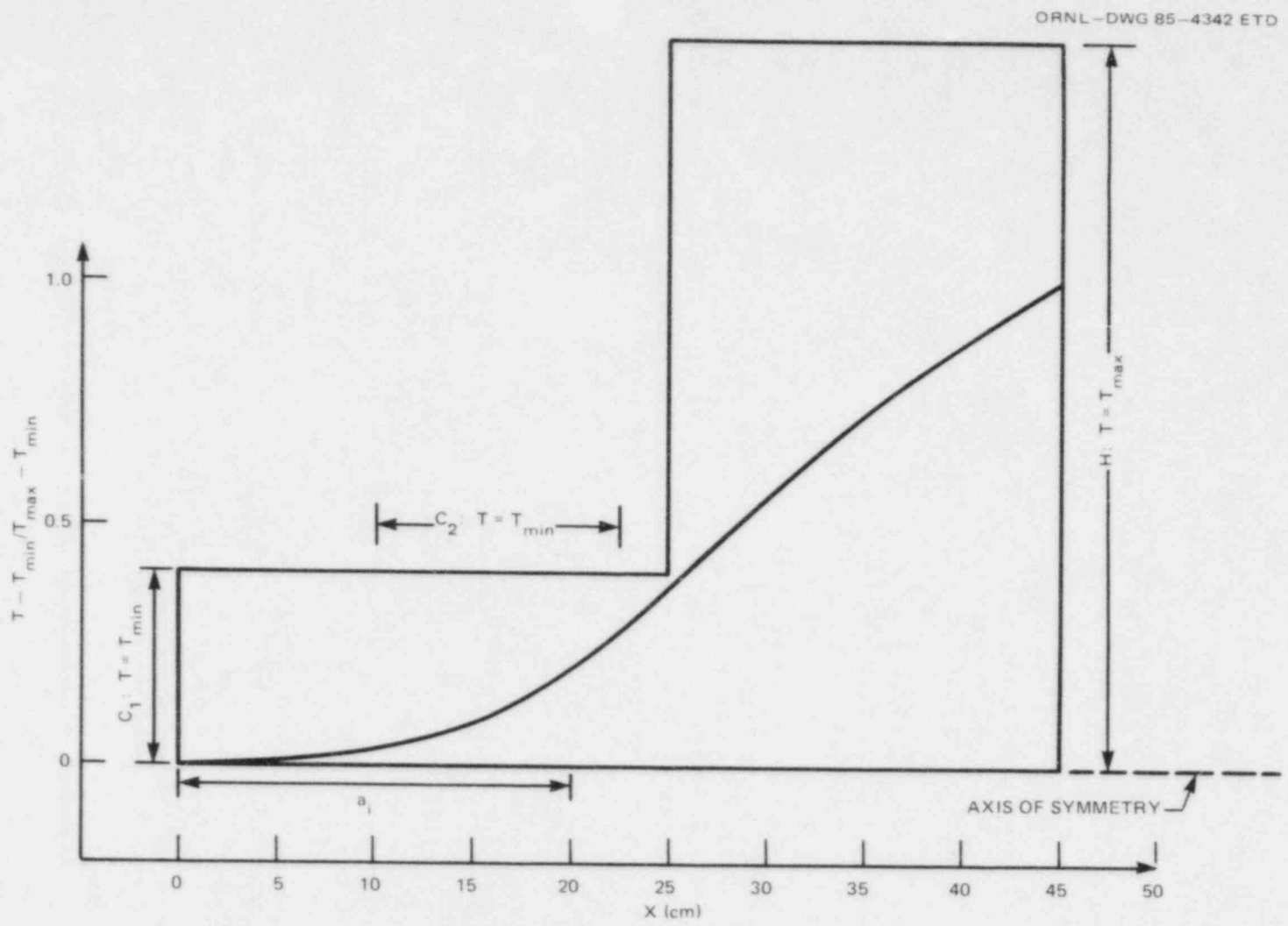

Fig. 2.7. Steady state temperature distribution in the crack plane of the panel specimen.

Table 2.3. Results of two analyses performed for stubbed-panel crack-arrest specimen under a linear transverse temperature gradient

Analysis No.[a]	Loads[b] FS (MN)	Loads[b] FP (MN)	T_{min} (°C)	T_{max} (°C)	T_{CT} (°C)	X_{US} (cm)	K_{Ii}[c] (MPa·√m)	K_{Ic} (MPa·√m)	Δa (cm)	a_f (cm)	a_f/w	T_{arr} (°C)	K_{Ia}[d] (MPa·√m)	Δt[e] (μs)	a_{rein}	a_{I1}	a_{I2}
A	0.111	1.75	−119.0	190.0	−55	30.5	84.5	67.8	10.2	30.5	0.67	55.0	181/210	3	25.7	32.4	31.7
B	0.111	1.75	−99.6	116.0	−55	35.2	84.5	67.8	17.8	38.1	0.83	73.1	293/320	3	30.5	32.4	31.7

[a] All analyses assumed the y components of displacements at load points are fixed during propagation.

[b] 1.0 MN = 225 kips.

[c] K_{Ii} is the assumed initial K_I under load control and crack length a_i.

[d] The first K_{Ia} value is the dynamic factor computed by SWIDAC in the time step immediately preceding arrest; the second value is the toughness computed at the arrest-point temperature from Eq. (3) in Sect. 5.1.

[e] Time step used in dynamic analysis.

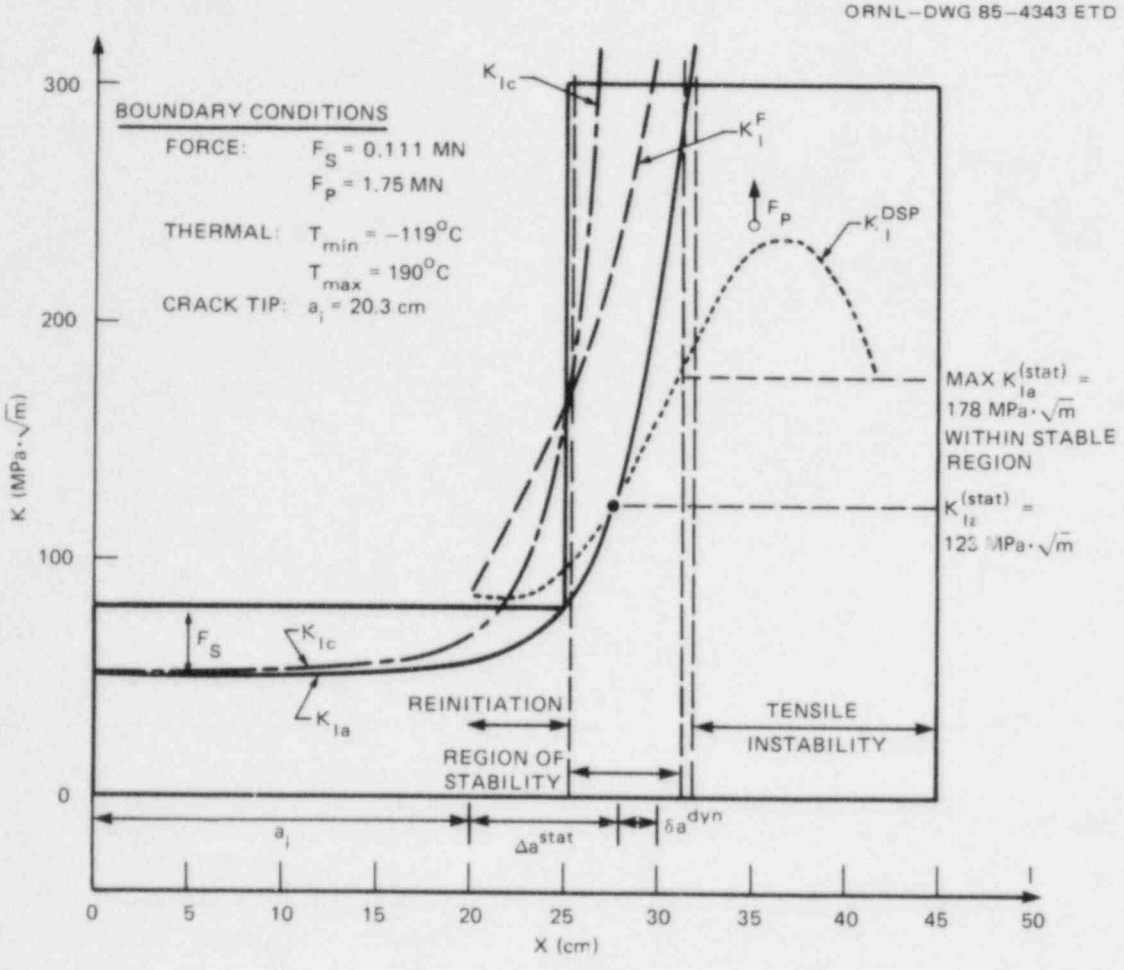

Fig. 2.8. Results from static analysis of reference load case A.

crack is stable, after full load is applied, can become small or even disappear as T_{max} is reduced. Also included in Figs. 2.8 and 2.9 are the initiation toughness K_{Ic}, arrest toughness K_{Ia}, static stress-intensity factor assuming force-controlled boundary conditions K_I^F, and factor assuming fixed load-pin displacement K_I^{DSP}. The intersection of the K_I^{DSP}-curve with the K_{Ia} curve yields the static prediction of the arrested crack length and corresponding arrest toughness, the values of which are indicated in Figs. 2.8 and 2.9.

The elastodynamic analyses of cases A and B were carried out with the load points fixed (in the axial direction) at the displacements computed for these points at the initiation load. As indicated in Fig. 2.10 and Table 2.3, the dynamic prediction of crack-arrest length exceeds the static prediction by ~2 cm for both cases A and B. Because of the steep K_{Ia} gradient in the arrest region, these differences in arrested crack length lead to large differences in the predicted crack-arrest toughness K_{Ia}. In Fig. 2.10, the dynamic stress-intensity-factor curves $K_I^{DYN}(a)$

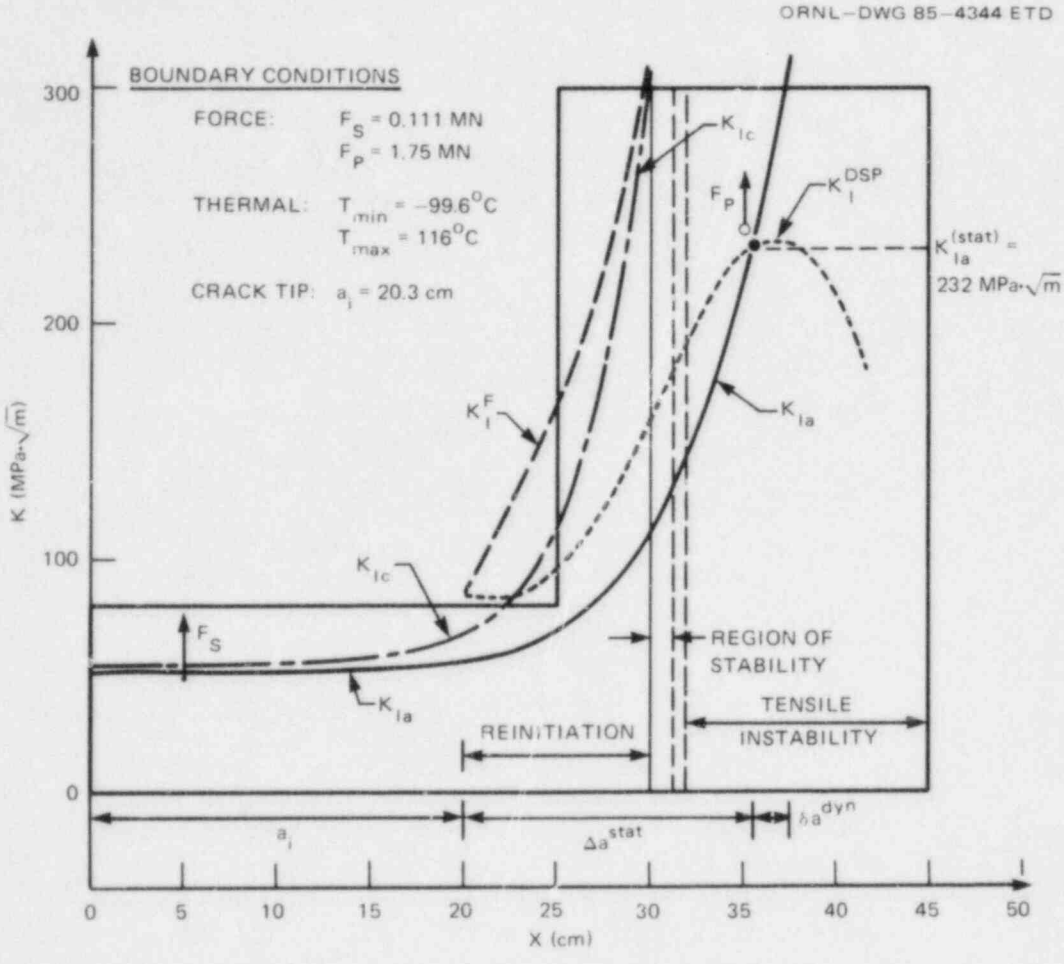

Fig. 2.9. Results from static analysis of reference load case B.

for cases A and B are significantly different from the curve for the static factor $K_I^{DSP}(a)$, which is calculated on the basis of fixed load-pin displacements. In particular, $K_I^{DYN}(a)$ for case B does not show a maximum similar to $K_I^{DSP}(a)$ but rises to much higher values and results in a longer predicted crack jump. These results indicate that a static calculation with the boundary conditions of this model is not sufficient to predict either the length of the crack jump or the correct values of the arrest toughness.

The two cases presented here demonstrate that in a crack-arrest experiment, it should be possible to control the length of a crack jump and, consequently, the stability behavior by an appropriate choice of boundary conditions T_{min} and T_{max}. From analysis of case A, K_{Ia} values higher than 200 MPa·√m should be attainable if the arrested crack is required to remain stable. If crack arrest in the instability region is acceptable, analysis of case B suggests that K_{Ia} values >300 MPa·√m could be measured in the test.

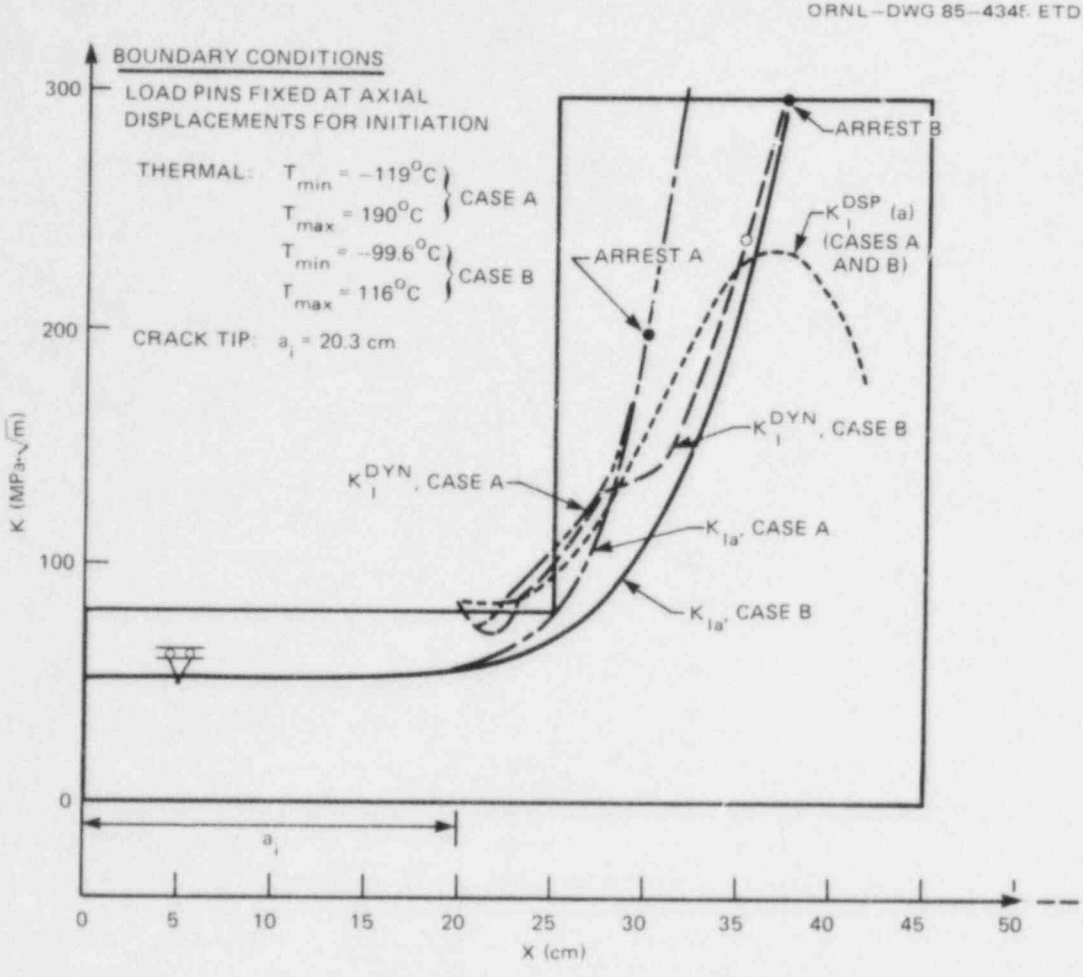

Fig. 2.10. Comparison of static and dynamic analyses of reference load cases A and B.

2.4 Elastodynamic and Viscoplastic-Dynamic Fracture-Mechanics Analyses

M. F. Kanninen* R. J. Dexter*
S. J. Hudak, Jr.* J. H. Fitzgerald*
K. W. Reed* K. S. Chan*
J. D. Achenbach†

2.4.1 Objectives and approach

The principal objective of this research subcontract is to assist the HSST Program in obtaining reliable material fracture-toughness data

*Engineering and Materials Sciences Division, Southwest Research Institute, San Antonio, Texas.

†Department of Civil Engineering, Northwestern University, Evanston, Illinois.

and analysis procedures for the prediction of crack arrest at high-toughness (upper-shelf) conditions. The research combines finite-element analyses with small-scale fracture experimentation and the wide-plate testing being performed at the National Bureau of Standards (NBS) (see Chap. 5). The focal point is a dynamic-viscoplastic finite-element analysis model because (1) unless the crack jump length is small, dynamic effects can significantly influence a run-arrest event in a laboratory test and (2) rapid crack propagation will induce rate-sensitive inelastic deformation that will require strain-rate effects to be taken into account. The basic research issue centers on the quantification of a kinetic crack-growth criterion for these conditions. The research falls into four categories: (1) the application of existing elastodynamic analyses to wide-plate tests, (2) the development of test methods to obtain dynamic-crack-propagation/arrest data on high-toughness materials using small-scale laboratory specimens, (3) the development of a viscoplastic-dynamic analysis procedure, and (4) asymptotic crack-tip analyses for viscoplastic-dynamic crack propagation.

2.4.2 Dynamic-crack-propagation/arrest testing

To properly analyze the Southwest Research Institute (SwRI) dynamic-crack-propagation experiments, it is necessary to simultaneously measure both crack length and specimen deflection as functions of time. As discussed previously, an eddy-current technique was selected to dynamically measure the specimen boundary conditions. This is one of the few techniques having the potential to accurately track displacements in the microsecond regime. Because the initial experiments in this program, as well as in another recently completed SwRI program, indicated an apparent incompatibility between the experimental and analytical results, it was deemed necessary to conduct a dynamic calibration of the eddy-current transducer. In particular, it was necessary to verify that the transducer was capable of responding to the high displacement rates that occur during dynamic-crack-propagation experiments in small-scale laboratory specimens. To illustrate, it has been found in other work that the specimen arms in a compact specimen experience a displacement rate of about 3 to 10 m/s while achieving a total displacement of 1 to 3 mm. This means that the total event occurs in a time interval on the order of 100 μs.

To simulate the above conditions, an experiment was designed using the Split Hopkinson Bar (SHB) system shown schematically in Fig. 2.11. In this experiment the eddy-current transducer was mounted on the stationary transmitter bar while the moving incident bar was used as the target for the transducer signal. Employed in this configuration, the SHB system required no modification, although the experiment destroyed the transducer. Nevertheless, this approach was cost-effective because the replacement cost of the transducer was significantly less than the total cost of modifying the SHB system.

In this experiment the initial gap between the transducer and target was 1.52 mm. The incident bar was then impacted with a 38.7-cm-long projectile having the same diameter and material properties as the bars in the system. The longitudinal strain in the incident bar was measured by the strain-gage bridge at the midlength of the bar. The impact velocity

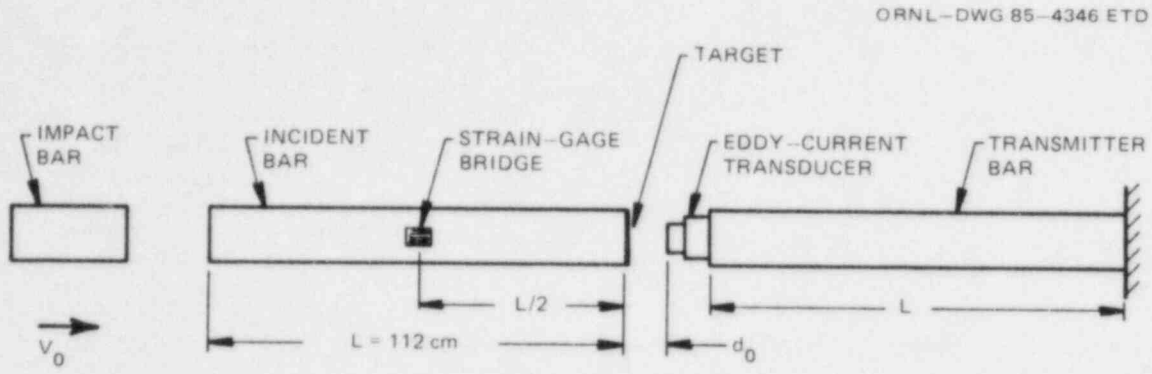

Fig. 2.11. Schematic of the SHB system used to dynamically calibrate the eddy-current displacement transducer.

V_0 was determined from

$$V_0 = 2C_0\varepsilon_1 , \qquad (2.3)$$

where C_0 is the wave velocity (≈5080 m/s) and ε_1 is the longitudinal strain in the incident bar.

Figure 2.12 shows the time-coincident signals from both the strain-gage bridge and the eddy-current transducer. The measured amplitude of the strain-pulse corresponds to an impact velocity of 23.4 m/s from Eq. (2.3). This is close to the estimated velocity of the arm separation in a dynamically fracturing compact-type specimen. Also indicated in Fig. 2.12 are several relevant time intervals. Specifically, at Δt_1 is the time required for the pulse to travel between the strain-measurement location and the far end of the bar that is serving as the target, while Δt_2 is the time required for the target to reach the transducer. Theoretically, these time intervals are given by the relations $\Delta t_1 = (L/2)/C_0$ and $\Delta t_2 = d_0/V_0$. Table 2.4 provides a comparison between the measured and theoretical time intervals and between the initial set gap d_0 and the dynamically measured gap. The latter was obtained from the eddy-current

Table 2.4. Summary of the dynamic calibration of the eddy-current transducer

Calibration term	Experiment	Theory
Δt_1, μs	118	110
Δt_2, μs	68	65
Initial static d_0, mm	1.52	
Dynamically measured d_0, mm	1.51	

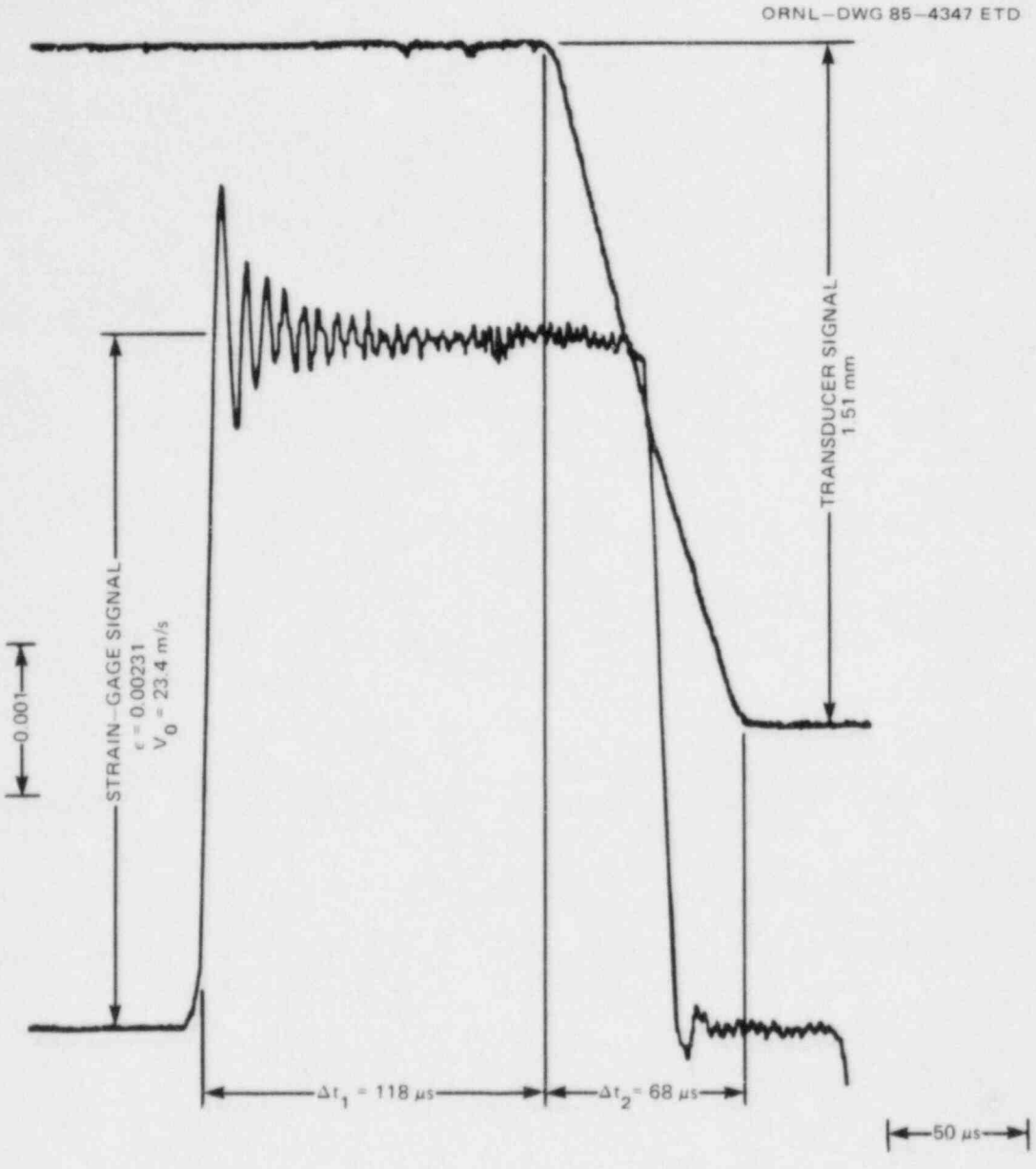

Fig. 2.12. Time-coincident response of the strain-gage bridge and eddy-current transducer.

transducer (Fig. 2.12), assuming the static calibration given in Fig. 2.13 to be applicable.

The excellent agreement between the dynamically measured and theoretical time intervals, as well as the agreement between the dynamically measured and initially set d_0 values, attests to the adequacy of the frequency response of the eddy-current transducer for the displacement rates used in the test. Furthermore, considering the linearity of the transducer output (Fig. 2.11) over most of the measurement range and the small amount of rounding at the ends of this response curve, it is estimated that the eddy-current transducer will perform satisfactorily to

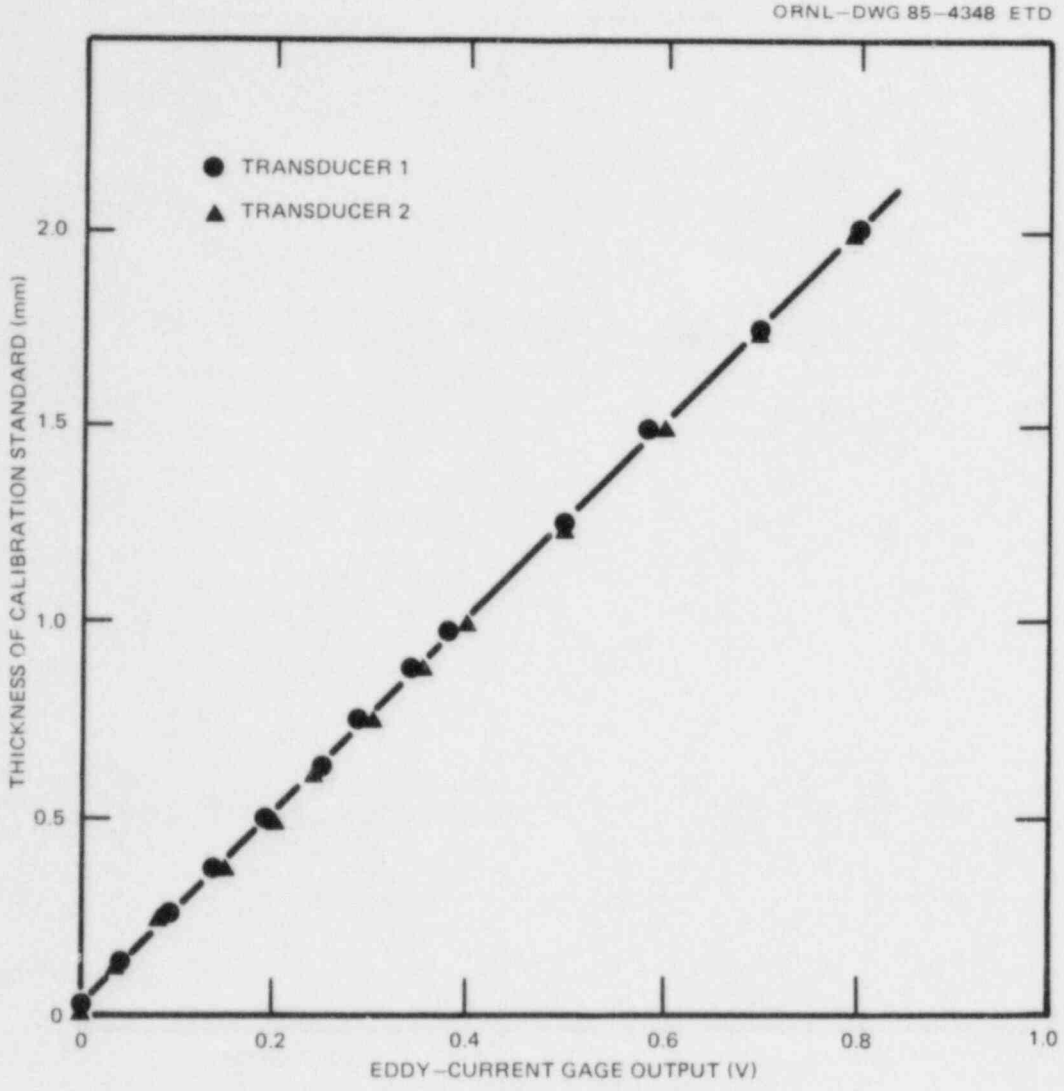

Fig. 2.13. Static calibration curve for eddy-current transducers.

displacement rates of about 50 m/s, which is about twice the ratio used in the dynamic calibration and at least five times the ratios believed to occur in the specimen tests. Therefore, it is concluded that the eddy-current transducer is capable of making the displacement measurements needed in the dynamic-crack-propagation testing portion of this research.

A dynamic-fracture experiment was conducted at −50°C using a wedge-loaded compact specimen with W = 100 mm and B = 25 mm and a notch root diameter of 0.38 mm. Crack initiation was achieved at an applied load-line displacement of 0.66 mm, which corresponds to K_o = 157 MPa•$\sqrt{m}$. The crack grew and subsequently arrested at a/w = 0.92. Unfortunately, because of a triggering problem, dynamic measurements of crack length and load-line displacement were not obtained. But if it is assumed that the load-line displacement remained constant throughout the crack propagation and arrest event, the statically computed K_{Ia} value is 34 MPa•$\sqrt{m}$. Because previous experience indicates that the load-line displacement can

increase significantly during crack propagation with the current loading system, this value is undoubtedly considerably lower than the actual K_{Ia}. The specimen also exhibited some macroscopic branching, particularly at a/w = 0.5, although one crack eventually became dominant during the final stages of crack growth and arrest. This behavior indicates the need to use side-grooved specimens for future tests.

2.4.3 Preliminary development of a viscoplastic-dynamic finite-element crack propagation model

The development of a new finite-element program for dyn: crack-propagation analysis was initiated. The new program is need or several reasons. First, it has become apparent that the exist WIDAC code is basically only a linear-elastic fracture-mechanics tion that cannot be conveniently modified to treat inelastic material avior. Second, because SWIDAC was prepared to run in a Control Data Corporation computer environment, execution costs placed a severe constraint on the use of this program in the nonlinear regime. Finally, the implementation of inelastic behavior into SWIDAC (e.g., the Bodner-Partom viscoplastic)[18,19] would involve substantial unwieldy and costly reprogramming that would not be cost-effective.

The new program is being developed specifically to treat materially nonlinear fracture problems. In contrast to the approach originally proposed, which was to append an inelastic material description to a linear-elastic code, the new code starts from a general treatment of inelasticity that will incorporate fracture mechanics. The difficulties encountered in the original approach are thereby avoided from the outset. Furthermore, the new program is being written specifically to run on SwRI's VAX 11/780 minicomputer. The analysis costs, which had begun to constrain application of SWIDAC, will thereby be avoided. The following describes the basis for the new code.

Nomenclature

$\underline{X}$	position vector in natural or material coordinates
$\underline{x}$	position vector in spatial coordinates
∇_x	gradient operator in material coordinates
∇	gradient operator in spatial coordinates
$\dot{a}$	substantial or material derivative of "a"
$(\nabla_{\underline{x}}\underline{x})$	deformation gradient
$J_x \equiv$	$\det(\nabla_{\underline{x}}\underline{x})$
$\underline{v}$	$\dot{\underline{x}}$ • velocity $\underline{a} = \dot{\underline{v}}$ = acceleration
$\nabla\underline{v}$	$(\nabla_{\underline{x}}\underline{x})^{-1}$ $(\nabla_{\underline{x}}\underline{v})$ velocity gradient

$\underline{\varepsilon}$ $\quad \frac{1}{2}(\nabla \underline{v}^T + \nabla \underline{v})$: stretching

$\underset{\sim}{\omega}$ $\quad \frac{1}{2}(\nabla \underline{v}^T - \nabla \underline{v})$: spin

$\dot{J}$ $\quad \dot{J}_x / J_x = \nabla \cdot \underline{v}$ = dilatation

$\underset{\sim}{\sigma}$, $\overset{\circ}{\underset{\sim}{\sigma}}$ Cauchy "true" stress and rate

$\overset{\circ}{\underset{\sim}{\tau}}$ $\quad \dot{J}\underset{\sim}{\sigma} + \overset{\circ}{\underset{\sim}{\sigma}}$: Kirchoff stress rate

$\overset{\circ}{\underset{\sim}{t}}$ $\quad -(\underset{\sim}{\varepsilon} + \underset{\sim}{\omega})\underset{\sim}{\sigma} + \dot{J}\underset{\sim}{\sigma} + \overset{\circ}{\underset{\sim}{\sigma}}$: nominal stress rate

$\overset{\circ}{\underset{\sim}{\tau}}^*$ $\quad \dot{J}\underset{\sim}{\sigma} + \overset{\circ}{\underset{\sim}{\sigma}} - \underset{\sim}{\omega}\underset{\sim}{\sigma} + \underset{\sim}{\sigma}\underset{\sim}{\omega}$: "corotational rate" of Kirchoff stress

The following exact expression for the linear momentum balance is the basis for the finite-element equations:

$$\nabla \cdot \overset{\circ}{\underset{\sim}{t}} + \rho \underline{\dot{b}} = \rho \underline{\dot{a}} \ . \tag{2.4}$$

The constitutive equations admitted by the finite-element algorithm are of the form

$$\overset{\circ}{\underset{\sim}{\tau}}^* = \underset{\approx}{C} : \underset{\sim}{\varepsilon} - \underset{\sim}{\varepsilon}^{vp} - \underset{\sim}{\varepsilon}^{th} \ , \tag{2.5}$$

where $\underset{\approx}{C}$ is the elastic matrix given by

$$C_{ijkl} = 2\mu \left\{ \left(\delta_{ik}\delta_{lj} \right) + \frac{\nu}{(1 - 2\nu)} \left(\delta_{ij}\delta_{kl} \right) \right\} . \tag{2.6}$$

In Eq. (2.5), $\underset{\sim}{\varepsilon}^{vp}$ is the viscoplastic strain rate, and $\underset{\sim}{\varepsilon}^{th}$ is the thermal strain rate. In Eq. (2.6), δ_{ij} is the Kronecker delta, μ the shear modulus, and ν the Poisson ratio. In addition, the viscoplastic strain rate may depend on any number of scalar or tensorial internal variables. This facilitates the introduction of different viscoplastic models to the finite-element analysis.

In developing a finite-element formulation of the linear momentum balance, first, a weighted residual expression is formed using Eq. (2.4) and the traction boundary condition

$$- \int_V \left\{ \left(\nabla \cdot \overset{\circ}{\underset{\sim}{t}} + \rho \underline{\dot{b}} - \rho \underline{\dot{a}} \right) \cdot \delta \underline{v} \right\} dV$$

$$+ \int_{S_\sigma} \left(\underline{n} \cdot \overset{\circ}{\underset{\sim}{t}} - \overset{\circ}{\underline{T}} \right) \cdot \underset{\sim}{\sigma} \cdot \delta \underline{v} \, dS = 0 \ . \tag{2.7}$$

Integration by parts in Eq. (2.7) yields

$$\int_V \left\{ \dot{\underset{\sim}{t}} : \nabla \delta \underline{v} - \rho \dot{\underline{b}} \cdot \delta \underline{v} + \rho \dot{\underline{b}} \cdot \delta \underline{v} \right\} dV - \int_{S_\sigma} \dot{\overline{\underline{T}}} \cdot \delta \underline{v} \, dS = 0 \, . \tag{2.8}$$

Equation (2.7) is analogous to the well-known "virtual work" principle. Equation (2.8) is valid for any size deformation and any material of the class described by Eq. (2.5).

Introduction of the constitution equation in Eq. (2.8) is accomplished by means of a change of variables:

$$\dot{\underset{\sim}{t}} = \dot{\underset{\sim}{\tau}}^* - \underset{\sim\sim}{\varepsilon\sigma} - \underset{\sim\sim}{\sigma\omega} \tag{2.9}$$

(see $\dot{\underset{\sim}{t}}$ and $\dot{\underset{\sim}{\tau}}^*$ in nomenclature). Use of Eq. (2.5) in Eq. (2.9) gives

$$\dot{\underset{\sim}{t}} = \underset{\approx}{C} : \left(\underset{\sim}{\varepsilon} - \underset{\sim}{\varepsilon}^{vp} - \underset{\sim}{\varepsilon}^{th} \right) - \underset{\sim\sim}{\varepsilon\sigma} - \underset{\sim\sim}{\sigma\omega} \, . \tag{2.10}$$

Substitution of Eq. (2.10) into Eq. (2.8) gives

$$\int_V \underbrace{\{\underline{v}\delta\underline{v} : C : \nabla v}_{(a)} \quad \underbrace{- \nabla \delta v : C : \varepsilon^{vp}}_{(b)} \quad \underbrace{- \nabla \delta v : C : \varepsilon^{th}}_{(c)}$$

$$\underbrace{- (\nabla \delta v) : (\varepsilon\sigma + \sigma\omega)}_{(d)} \quad \underbrace{- \rho \dot{b} \cdot \delta v}_{(e)}$$

$$\underbrace{- \rho \dot{a} \cdot \delta v\} \, dv}_{(f)} \quad \underbrace{- \int_{S_\sigma} \dot{\overline{T}} \cdot \delta v \, dS = 0}_{(g)} \, . \tag{2.11}$$

Standard finite-elements methodology then provides, corresponding to underscored terms above (a) stiffness matrix [K], (b) viscoplastic pseudo-load Pvp, (c) thermal pseudo-load $\{\dot{P}_{th}\}$, (d) initial stress matrix [S], (e) body force load $\{\dot{P}_b\}$, (f) mass matrix [M], and (g) traction load $\{\dot{P}_T\}$.

In finite-element notation, Eq. (2.11) becomes

$$[M] \{\ddot{v}\} + [[K] - [S]] \{v\} = \{\dot{P}\}$$

$$\{\dot{P}\} \equiv \{\dot{P}_T\} + \{\dot{P}_{vp}\} + \{\dot{P}_{th}\} + \{\dot{P}_b\} \, . \tag{2.12}$$

The initial stress matrix (d) is discarded for linear-elastic and infinitesimal strain viscoplastic analyses. However, in elastoplastic and

stability analyses [S] *must* be retained. (This is a major shortcoming of many finite-element programs designed for elastoplastic analysis.) Equation (2.12) may be written as an initial value problem

$$\begin{aligned} \{\dot{x}\} &= \{v\}, \\ \{\dot{v}\} &= \{a\}, \\ \{\dot{a}\} &= [M]^{-1} \{\dot{P} - [K] \{v\}\}, \\ \{x(o) &= x_o\}, \{v(o) = v_o\}, \{a(o) = a_o\}. \end{aligned} \tag{2.13}$$

Because of the presence of viscoplasticity, integration schemes such as the popular Newmark are relatively inaccurate even when stable. Inasmuch as the current program will be applied to research problems and is not intended for "production" engineering, the fourth order accurate Runge-Kutta scheme is used for integration of Eq. (2.13). Stability bounds must be observed in the time-step selection. In dynamic-fracture analysis, however, where time-steps are on the order of microseconds, this seldom imposes any hardship.

2.4.4 Temperature effects for fracture in viscoplastic materials

The dissipation of mechanical energy in a viscoplastic body produces increases in temperature. This effect can be pronounced near the tip of a propagating crack where substantial amounts of energy are dissipated as plastic work. In addition, when a crack propagates, the flux of energy into the crack tip also produces an additional heat source. This is important because the viscoplastic constitutive relations are temperature dependent. Thus, the rise of temperature in a cracked body (particularly near the crack tip) may not be negligible. For a 2-D geometry, the temperature distribution is governed by

$$k\nabla^2 T - \rho c \frac{\partial T}{\partial t} = \dot{W}_p + (F - 2\gamma\dot{a})[x_1 - a(t)] \ , \tag{2.14}$$

where t is time, T is temperature, k is thermal conductivity, ρ is density, c is specific heat, $\dot{W}_p$ is the rate of dissipation of mechanical energy per unit volume, F is the flux of energy into the crack tip, γ is the specific surface energy, and a is the position of crack tip. Note that $\dot{W}_p\ (x_1, x_2, t)$ is a distributed quantity, while the difference between the flux of energy into the crack tip and the rate of increase of surface energy ($2\gamma\dot{a}$) acts as a propagating concentrated heat source.

The heat production terms in Eq. (2.14) can be considered in more detail. First, consider the dissipation rate of mechanical energy, which

is the rate of plastic work and can be expressed as

$$\dot{W}_p = \sigma_{ij}\dot{\varepsilon}^{(p)}_{ij} \ , \tag{2.15}$$

where σ_{ij} and $\dot{\varepsilon}^{(p)}_{ij}$ are the components of stress and plastic strain rate, respectively. Next, consider the flux of energy into the crack tip when the singular behavior at the crack tip is of the square-root type (as it is for the Bodner-Partom model[18,19]). The Mode-I case gives

$$F = -\frac{\dot{a}^3(1-\alpha^2)^{1/2}\ [K_I(t,\dot{a})]^2}{2\mu c_T^2\ D(\alpha,\beta)} \ , \tag{2.16}$$

where

$$\alpha = \dot{a}/c_L,$$

$$c_L = [(\gamma - 2\mu)/\rho]^{1/2},$$

$$\beta = \dot{a}/c_T,$$

$$c_T = (\mu/\rho)^{1/2},$$

$$D(\alpha,\beta) = (\beta^2 - 2)^2 - 4(1-\alpha^2)^{1/2}\ (1-\beta)^{1/2},$$

and $K_I(t,\dot{a})$ is the dynamic stress-intensity factor. Equation (2.16) simplifies at small values of $\dot{a}$ when the material inertia may be neglected.

The modified version of the Bodner-Partom theory[18,19] accounts for temperature dependence of the mechanical behavior. Essentially, the "constants" Z_1 and n in the Bodner-Partom model depend on temperature in the general way

$$Z_1 = (A_1 + B_1 T)/T \ ,$$

$$n = -CT + D \ . \tag{2.17}$$

Some simplifying assumptions will make it possible to solve Eq. (2.14) with appropriate conditions on the crack faces. For example, consider

$$x_2 = 0, \quad x_1 < a(t): \quad \frac{\partial T}{\partial x_2}(x_1, 0^{\pm}, t) = 0 \ . \tag{2.18}$$

A simplifying assumption is that only the singular parts of the stresses and plastic-strain rates are taken into account in the computation of $\dot{W}_p$; that is, only heat production near the crack tip is considered. Then

$$W_p = \frac{W(t)}{r^p} \psi(\theta) , \tag{2.19}$$

where p is a constant to be determined, and

$$r^2 = [x_1 - a(t)]^2 + x_2^2 , \tag{2.20}$$

while $\psi(a)$ gives the angular dependence, which can be computed. A steady state solution to Eq. (2.14) can probably be obtained. The temperature rise caused by $\dot{W}_p$ is still to be investigated. Note that the term $(F - 2\psi\dot{a})\delta[x_1 - a(t)]$ gives rise to a logarithmic temperature singularity. Thus, for a numerical calculation, the additional features in each time step are the computation of the rate of energy dissipation, the corresponding temperature increase from Eq. (2.14), and the subsequent adjustment of the constitutive model parameters according to Eq. (2.17).

2.5 Cleavage-Fibrous Transition Studies*

G. R. Irwin† X-J. Zhang†
R. Chona† W. L. Fourney†
R. J. Sanford† D. B. Barker†
C. W. Schwartz†

Collection and study of information on this topic have been the main activities during this report period. Supplementary research investigations were also performed with regard to local variations of carbon content and size effects in fracture morphology. A limited extension of the investigation to include a low-upper-shelf weldment is also in progress. A topical report on the investigation is being prepared and should be completed during the next report period.

Using the association of hardness with carbon content, estimates can be made of the average percent carbon in local regions. Figure 2.14(*a*) shows hardness indents along three lines on a quenched specimen of A 508 steel. A total of 99 Vickers hardness measurements were made. The results are shown in Fig. 2.14(*b*), in which each data point represents the average of three adjacent hardness readings. Figure 2.15 shows the approximate hardness of carbon steels in a quenched condition.[20]

An indication of the variation in carbon content was obtained from the average of the highest five and lowest ten hardness measurements along each of the three lines. The high values averaged out to 647 HV, while the low values averaged out to 524 HV or 0.29 and 0.20% carbon, respectively. The overall average is 575 HV or 0.23% carbon, which

*Work sponsored by the HSST Program under Subcontract No. 7778 between Martin Marietta Energy Systems, Inc., and the University of Maryland.

†Department of Mechanical Engineering, University of Maryland, College Park.

ORNL PHOTO 1765–85

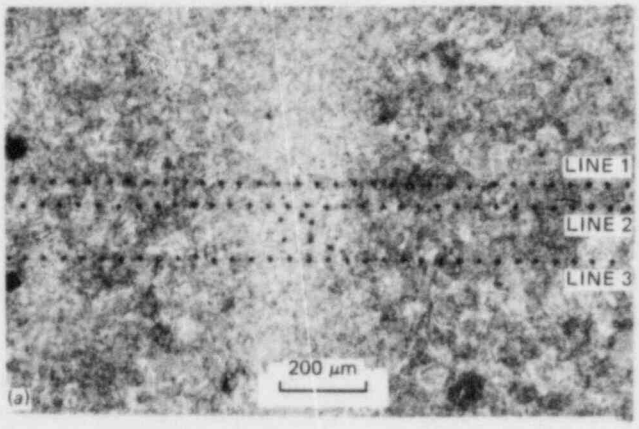

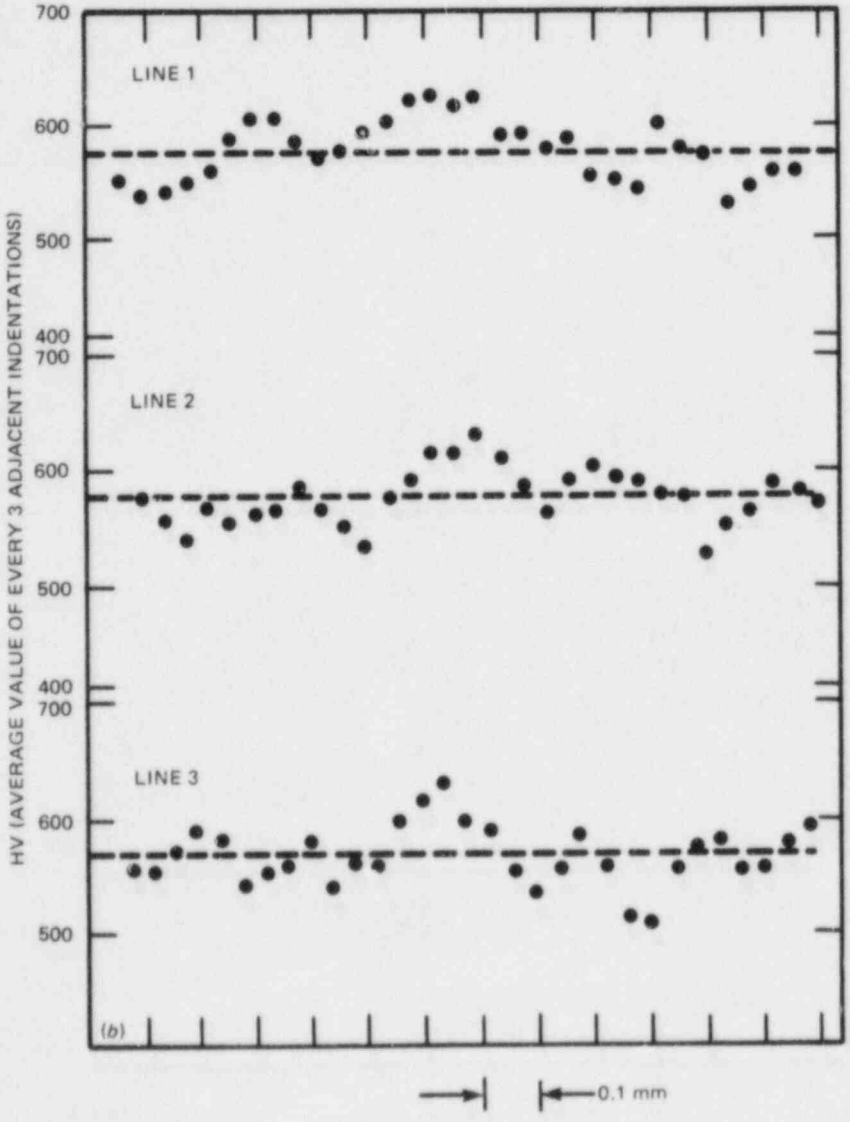

Fig. 2.14. Vickers microhardness (*a*) indents along three parallel lines on a quenched A 508 steel sample; (*b*) values as a function of indentation location. Each data point represents the average of three adjacent hardness readings.

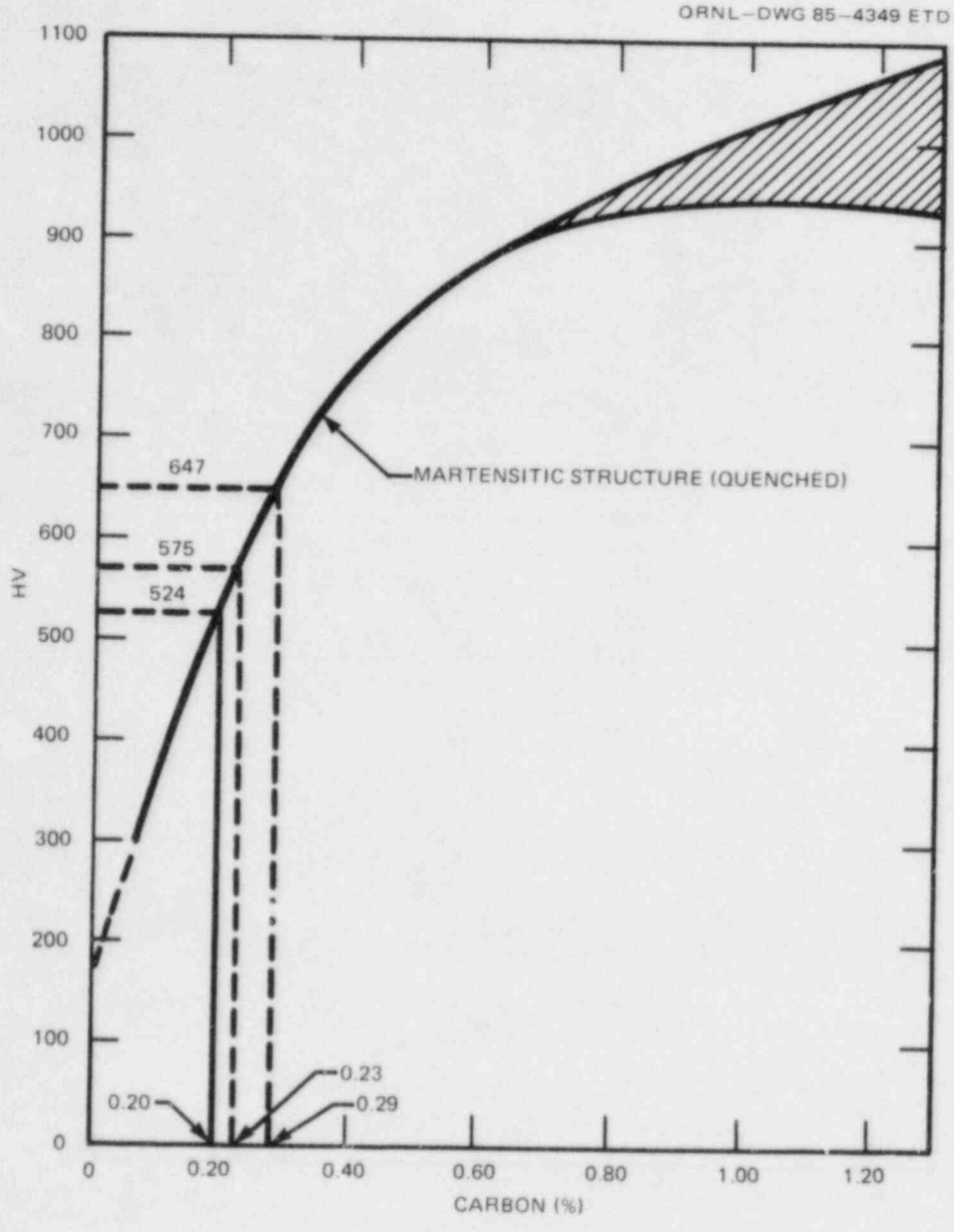

Fig. 2.15. The relation between hardness and carbon content for quenched steels (Ref. 20).

agrees well with the chemical analysis supplied with the A 508 steel. Evidently, regions about the size of prior austenite grains (about 200 μm) possess substantial differences in deformation resistance, which correlate with differences of percent carbon.

Examinations of large fracture surfaces produced in the ORNL thermal-shock-experiment tests have consistently shown variations in height of fracture surface irregularities that are larger than those found in small specimen tests of the same steel. Figure 2.16 shows a comparison between the surface irregularities for a 6-cm-thick specimen of A 508 steel and

ORNL PHOTO 1766-85

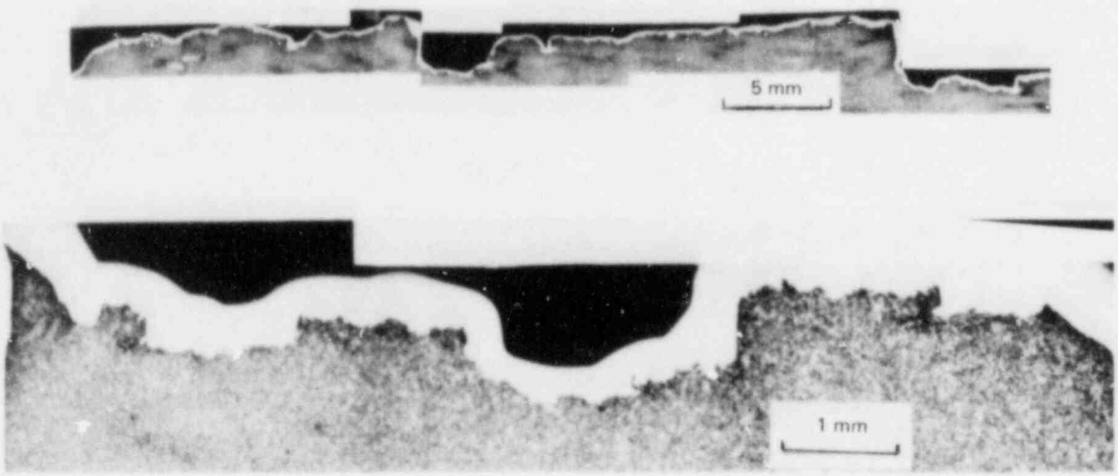

Fig. 2.16. Fracture surface profiles comparing fracture surface irregularities in the cleavage-dominated region for a 6-cm-thick specimen (upper profile) and a CVN specimen (lower profile) of A 508 steel.

those on a Charpy V-notch (CVN) specimen of the same material. The magnifications of the two profile views shown have been adjusted so that the lengths in each view were proportional to the specimen thickness. It can be seen that the largest fracture surface irregularities have magnitudes that are proportional to the size (thickness) of the specimen.

A preliminary examination of a low-upper-shelf weldment indicated a more uniform microstructure with regard to carbide banding than was found in our specimens of A 533 grade B and A 508 steels. Measurements of the loss-of-cleavage temperature with CVN specimens are in progress.

References

1. K. J. Bathe, *ADINA — A Finite Element Program for Automatic Dynamic Incremental Nonlinear Analysis*, Report 82448-1, Massachusetts Institute of Technology, Cambridge, Mass., 1975 (revised 1978).

2. B. R. Bass and J. W. Bryson, *Applications of Energy Release Rate Techniques to Part-Through Cracks in Plates and Cylinders; Volume 2. ORVIRT: A Finite Element Program for Energy Release Rate Calculations for 2-Dimensional and 3-Dimensional Crack Models*, ORNL/TM-8527/V2, Union Carbide Corp. Nuclear Div., Oak Ridge Natl. Lab., February 1983.

3. B. R. Bass and J. W. Bryson, *Applications of Energy Release Rate Techniques to Part-Through Cracks in Plates and Cylinders; Volume 1. ORMGEN-3D: A Finite Element Mesh Generator for 3-Dimensional Crack Geometries*, ORNL/TM-8527/V1, Union Carbide Corp. Nuclear Div., Oak Ridge Natl. Lab., December 1982.

4. *PVRC/MPC Task Group on Fracture Toughness Properties for Nuclear Components: Final Report*, Pressure Vessel Research Committee, Welding Research Council, New York, October 1977.

5. W. L. Server, "Impact Three-Point Bend Testing for Notched and Precracked Specimens," *J. Test. Eval.* 6(1), 29–34 (January 1978).

6. P. McConnell and W. Server, "EPRI Instrumented Impact Test Procedures," in *Proceedings of CSNI Meeting on Instrumented PCCV Testing*, Paper No. I.1, held at EPRI, Palo Alto, Calif., December 1–3, 1980.

7. W. L. Server, J. W. Sheckherd, and R. A. Wullaert, *Fracture Toughness Data for Ferritic Nuclear Pressure Vessel Materials*, EPRI NP-119, Effects Technology, Inc., Santa Barbara, Calif., April 1976.

8. W. L. Server, Idaho National Engineering Laboratory personal communication to J. G. Merkle, Oak Ridge Natl. Lab., Dec. 7, 1984.

9. P. B. Crosley and E. J. Ripling, *Crack Arrest in an Increasing K-Field*, HSSTP-TR-27, Materials Research Laboratory, Glenwood, Ill., January 1978.

10. W. L. Server and W. Oldfield, *Nuclear Pressure Vessel Steel Data Base*, EPRI NP-933, Fracture Control Corporation, Goleta, Calif., December 1978.

11. W. L. Fourney, G. R. Irwin, and R. Chona, "ASTM Round Robin on K_{Ia} Testing," p. 110 in *Heavy-Section Steel Technology Program Semiannual Prog. Rep. April–September 1984*, NUREG/CR-3744, Vol. 2 (ORNL/TM-9154/V2), Martin Marietta Energy Systems, Inc., Oak Ridge Natl. Lab.

12. C. E. Pugh, "Crack Arrest Technology," pp. 83–137 in *Heavy-Section Steel Technology Program Semiannual Prog. Rep. April–September 1984*, NUREG/CR-3744, Vol. 2 (ORNL/TM-9154/V2), Martin Marietta Energy Systems, Inc., Oak Ridge Natl. Lab.

13. R. D. Cheverton et al., "Fracture Mechanics Data Deduced from Thermal-Shock and Related Experiments with LWR Pressure Vessel Material," *Journal of Pressure Vessel Technology* 105, 102–10 (May 1983).

14. R. H. Bryan, "Pressurized-Thermal-Shock Technology," pp. 142–74 in *Heavy-Section Steel Technology Program Semiannual Prog. Rep. October 1983–March 1984*, NUREG/CR-3744, Vol. 1 (ORNL/TM-9154/V1), Martin Marietta Energy Systems, Inc., Oak Ridge Natl. Lab.

15. H. K. Stamm, "Analysis of a Panel Crack-Arrest Specimen," pp. 9–17 in *Heavy-Section Steel Technology Program Semiannual Prog. Rep. April–September 1984*, NUREG/CR-3744, Vol. 2 (ORNL/TM-9154/V2), Martin Marietta Energy Systems, Inc., Oak Ridge Natl. Lab.

16. K. J. Bathe, *ADINAT — A Finite Element Program for Automatic Dynamic Incremental Nonlinear Analysis of Temperatures*, Report 82448-5, Massachusetts Institute of Technology, Cambridge, Mass., May 1977.

17. J. Jung et al., *Finite Element Analysis of Dynamic Crack Propagation*, presented at the 1981 ASME Failure Prevention and Reliability Conference, Sept. 23–26, 1981, Hartford, Conn.

18. S. R. Bodner and Y. Partom, "Constitutive Equations for Elastic-Viscoplastic Strain-Hardening Materials," *J. Appl. Mech.* 42, 385–89 (1975).

19. M. F. Kanninen et al., "Elastodynamics and Viscoplastic-Dynamic Fracture-Mechanics Analysis," pp. 36–46 in *Heavy-Section Steel Technology Program Semiannual Prog. Rep. April–September 1984*, NUREG/CR-3744, Vol. 2 (ORNL/TM-9154/V2), Martin Marietta Energy Systems, Inc., Oak Ridge Natl. Lab.

20. E. C. Bain, *Function of the Alloying Elements in Steels*, American Society of Metals, Cleveland, 1939.

3. MATERIAL CHARACTERIZATION AND PROPERTIES

R. K. Nanstad

3.1 Directory to Other Material Properties Reporting

Primarily for internal management and budgetary control purposes, the Heavy-Section Steel Technology (HSST) Program has made a separate task (Task H.3) of the work on material characterization and properties determinations. However, for the readers' convenience some contributions are placed within other chapters of this report according to the larger tasks that correspond to the particular material studies. Therefore, in addition to the work reported in this chapter, please refer to Sect. 5.3 for properties studies in support of wide-plate crack-arrest tests and Subsect. 6.4.2 for further cladding properties information.

3.2 Stainless Steel Cladding Investigations

W. R. Corwin

It had been determined that the combination of materials properties required in phase 2 of the stainless steel cladding investigation should include a relatively tough cladding at the same temperature at which the base plate is frangible.* If this combination of materials properties could be achieved, then meaningful experiments could be conducted on the ameliorating effect of tough cladding in limiting surface crack extension in a brittle substrate, hypothesized to occur in a thermal shock or pressurized-thermal-shock transient in a light-water reactor (LWR). A subcontract was let to Combustion Engineering (CE) to provide clad-beam test specimens similar to those utilized in phase 1 of these investigations,[1] but with the required material properties. Detailed, extensive specifications were incorporated to ensure that the required material properties would be obtained. The crux of these specifications was that stainless steel cladding be supplied with a minimum Charpy toughness of 54 J at the temperature at which the A 533 grade B base plate upon which it was applied was brittle, in this case either the temperature corresponding to a 27-J Charpy energy or 11°C below its drop-weight nil-ductility temperature (NDT), whichever was lower. Further requirements were that the cladding be applied using commercial equipment and procedures utilized in LWR vessel fabrication and that it be chemically and mechanically uniform within the limits of the specifications.

---

*Details of phase 1 of the stainless steel cladding investigations on which this statement are founded are described in the phase 1 summary report (Ref 1); the draft of this report was completed this report period.

To meet these requirements, a three-wire series submerged-arc welding process* was used to apply the cladding in conjunction with a special heat treatment schedule of the base plate and completed weldments. The base plate (HSST Plate 012B) was first given a normalizing treatment at 1032°C for 2 h, followed by air cooling instead of a standard quench and temper. The base plate was machined into large specimen blanks, and the cladding was then applied to the blanks.

The completed weldments were given a postweld heat treatment (PWHT) of 593°C for 10 h and then were furnace cooled. Although the PWHT was milder than that typically given a clad LWR vessel, the combined normalizing and PWHT produced cladding with Charpy properties similar to those obtained with a typical LWR PWHT (607°C for 40 h) (Fig. 3.1). At the same time, they maintained the Charpy impact ductile-to-brittle transition temperature (DBTT) of the base plate high enough that the combination of material properties required by the program could be obtained.

Base metal and cladding qualification blocks were examined by CE as a part of their subcontract. The DBTT of the normalized plate was only slightly lowered by the PWHT chosen (Fig. 3.2). An interpolation of the

*A discussion of the welding process and the resulting uniformity of chemical, mechanical, and metallurgical properties is included in Subsect. 6.4.2, Seventh HSST Irradiation Series: Stainless Steel Cladding Investigations — Phase 2.

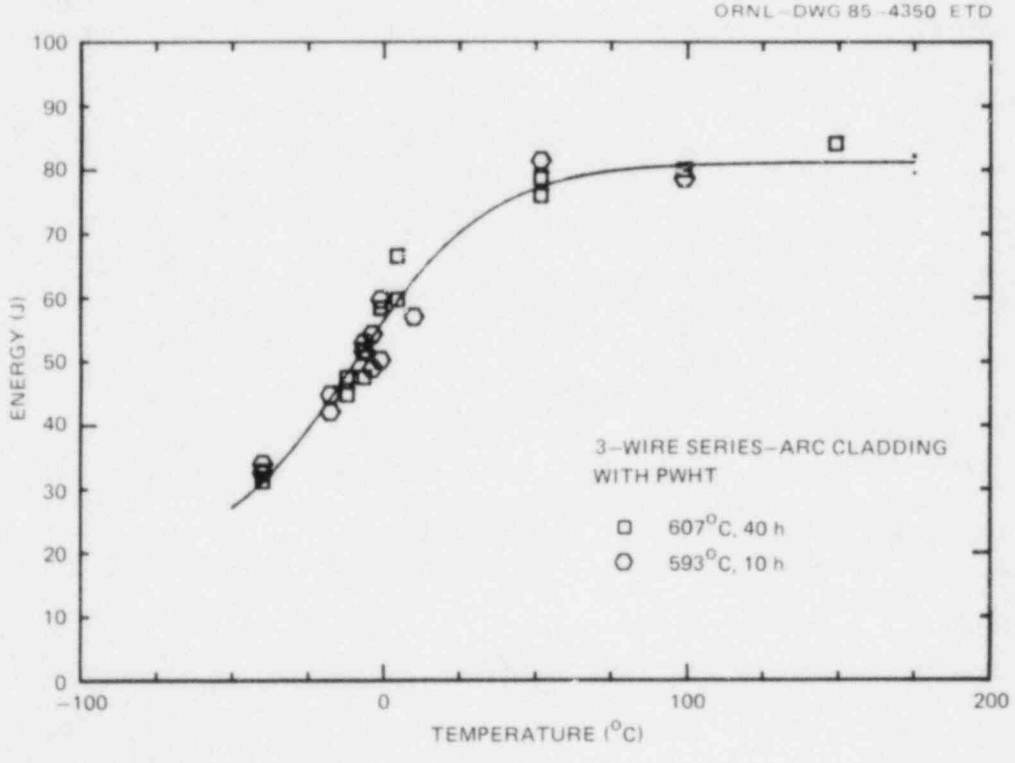

Fig. 3.1. The Charpy energies of cladding postweld heat treated at 607°C for 40 h and 593°C for 10 h form a single population.

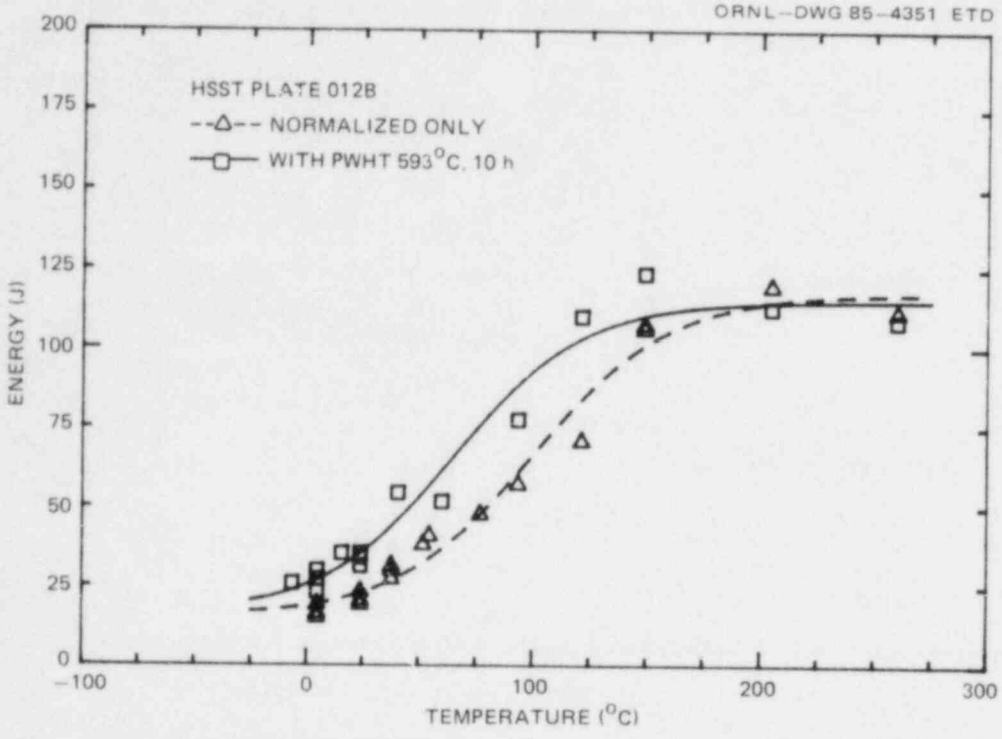

Fig. 3.2. A PWHT at 593°C for 10 h only slightly lowered the DBTT of the normalized A 533 grade B material, evidenced by its Charpy impact behavior.

lower-bound data, which would be expected to control failure in a large structural test such as a clad beam, yields a temperature of ~15°C at 27-J Charpy energy. In comparison, the NDT of the plate is 49°C. Examining the Charpy behavior of the cladding (Fig. 3.1) and again interpolating between minimum values give Charpy energies in the cladding of 58 J at 15°C and 71 J at 38°C (NDT − 11°C). While the temperatures of the Phase 2 clad-beam tests have not yet been decided, any temperature between ~38 and 0°C apparently will provide a brittle base plate and a cladding that is appreciably tougher (Fig. 3.3).

The atypical heat treatment of the base plate also produced tensile properties stronger than normal for A 533 grade B class 1 material. The yield and ultimate strengths in the base plate after PWHT were 597 and 735 MPa, respectively. These values are actually more typical of the strength of irradiated base plate and may provide a better simulation of material properties of a vessel in the field.

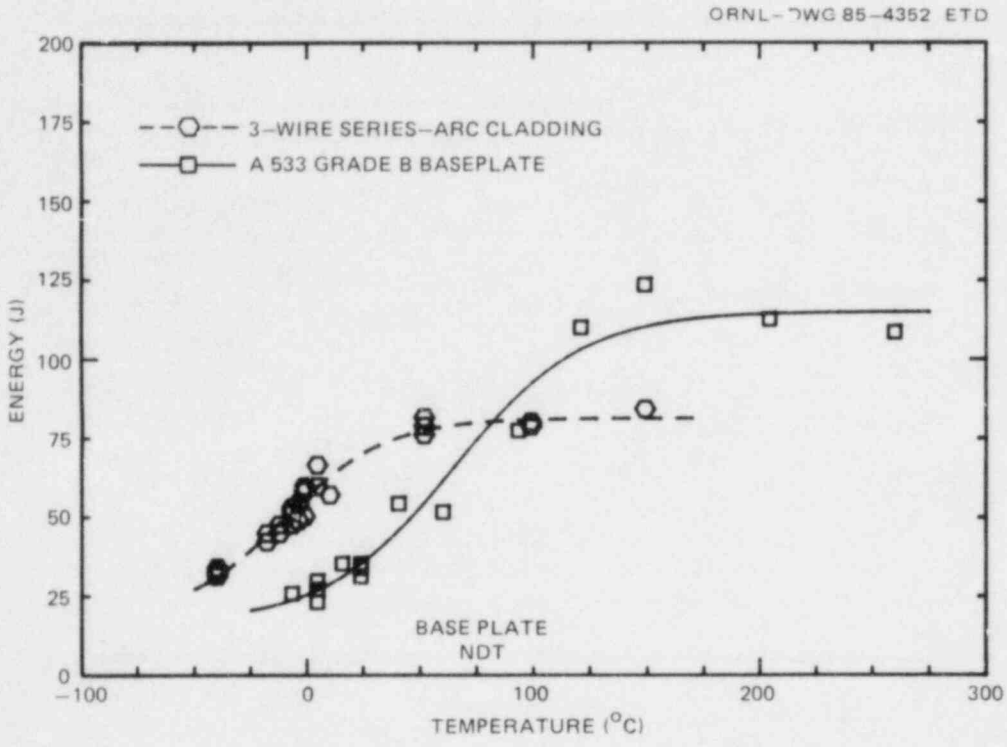

Fig. 3.3. Carefully selected fabrication practice heat treatment resulted in a temperature window where the Charpy toughness of the cladding is appreciably greater than that of the base plate.

Reference

1. W. R. Corwin et al., *Effect of Stainless Steel Weld Overlay Cladding on the Structural Integrity of Flawed Steel Plates in Bending*, NUREG/CR-4015 (ORNL/TM-9390), Martin Marietta Energy Systems, Inc., Oak Ridge Natl. Lab., April 1985.

4. ENVIRONMENTALLY ASSISTED CRACK-GROWTH TECHNOLOGY*

W. H. Bamford† R. J. Jacko‡
I. W. Wilson‡ L. J. Ceschini‡

4.1 Introduction

The objective of this task is to characterize the crack-growth rate properties of light-water reactor (LWR) materials exposed to primary-coolant environments. The work now being conducted falls into five major areas:

1. corrosion fatigue crack-growth tests in simulated pressurized-water reactor (PWR) environment,
2. static-load K_{ISCC} tests in simulated PWR environment,
3. fractographic examination of specimen fracture surfaces,
4. characterization of environment by measurement of electrochemical potential, and
5. participation in the international cyclic crack-growth review group (ICCGR).

The fatigue crack-growth-rate tests are carried out on 2T-CT specimens in autoclaves installed in recirculating water systems. Crack length is monitored by an external LVDT through a compliance relationship with the face opening of the specimen. Data acquisition is computer based. The water system is purged of oxygen at the beginning of each test, and the open circuit corrosion potential is monitored by hydrogen and silver-silver chloride electrodes. The water chemistry maintained in the system is given in Table 4.1. The system has a relatively low flow rate. Also, the static-load K_{ISCC} specimens are precracked in accordance with American Society for Testing and Materials (ASTM) recommendations, bolt-loaded with bolts of the identical material, and inserted into the fatigue crack-growth test chambers that are set on the bottom. These specimens are removed periodically at the conclusion of crack-growth tests for crack-length measurements.

4.2 Fatigue Crack Growth

Two aspects of crack growth are being studied: the impact of sulfur content and the relationship between the static and dynamic crack-growth

*Work sponsored by the Heavy-Section Steel Technology Program under Subcontract 11X-21598C between Martin Marietta Energy Systems, Inc., and Westinghouse Electric Corporation, Plant Engineering Division.

†Westinghouse Electric Corporation, Plant Engineering Division, Pittsburgh, PA 15230.

‡Westinghouse Research and Development Laboratories, Pittsburgh, PA 15235.

Table 4.1. Water chemistry specifications

Component	Quantity
Boron (as boric acid)	0 (pH = 9) or 1000 ppm (pH = 5)
Lithium (as lithium hydroxide)	0.68 ppm
Chloride ions	<0.15 ppm
Flouride ions	<0.10 ppm
Dissolved oxygen	<1 ppb
Dissolved hydrogen	25–35 cm^3/kg
Particulates	Filtered to <25 μm
Total solids	<0.5 ppm

rates observed in heat-affected zone (HAZ) specimens. Earlier tests in this program have shown that the material chemistry has an important influence on the level of crack-growth enhancement in a water environment.[1,2] This finding has now been confirmed by a number of other investigators,[3-5] and now more detailed study of a high-sulfur steel plate is being carried out.

The relationship between constant-load cracking and fatigue cracking of HAZ materials has been under study for several years, and findings thus far have shown no discernible relationship. This work is discussed in some detail in Sect. 4.3.

4.2.1 High-sulfur material characterization

Now that it is widely understood that high-sulfur materials are more susceptible to environmental enhancement, the goal is to obtain detailed knowledge of the behavior of a typical high-sulfur steel. To accomplish this goal, a commercially produced reactor pressure vessel steel was chosen, and a matrix of tests was devised to study the effects of R ratio, temperature, frequency, and boron content of the water. Testing on this matrix, under way for over a year, is nearing completion. The results have important applications because the steels involved represent those used in early construction and, also, are likely to exhibit the most enhanced crack growth.

The test matrix is shown in Table 4.2, and testing is nearly complete at 204 and 288°C. Test results at 93°C should be available in the next report period.

The results from the most recent tests (at 204°C) are shown in Fig. 4.1. Two specimens were tested at 1 cycle per minute (0.017 Hz) in borated vs unborated environments, and the crack-growth behavior was essentially the same. The observed growth rates were much lower than those obtained at 288°C (see Fig. 4.2) and reported in the previous progress

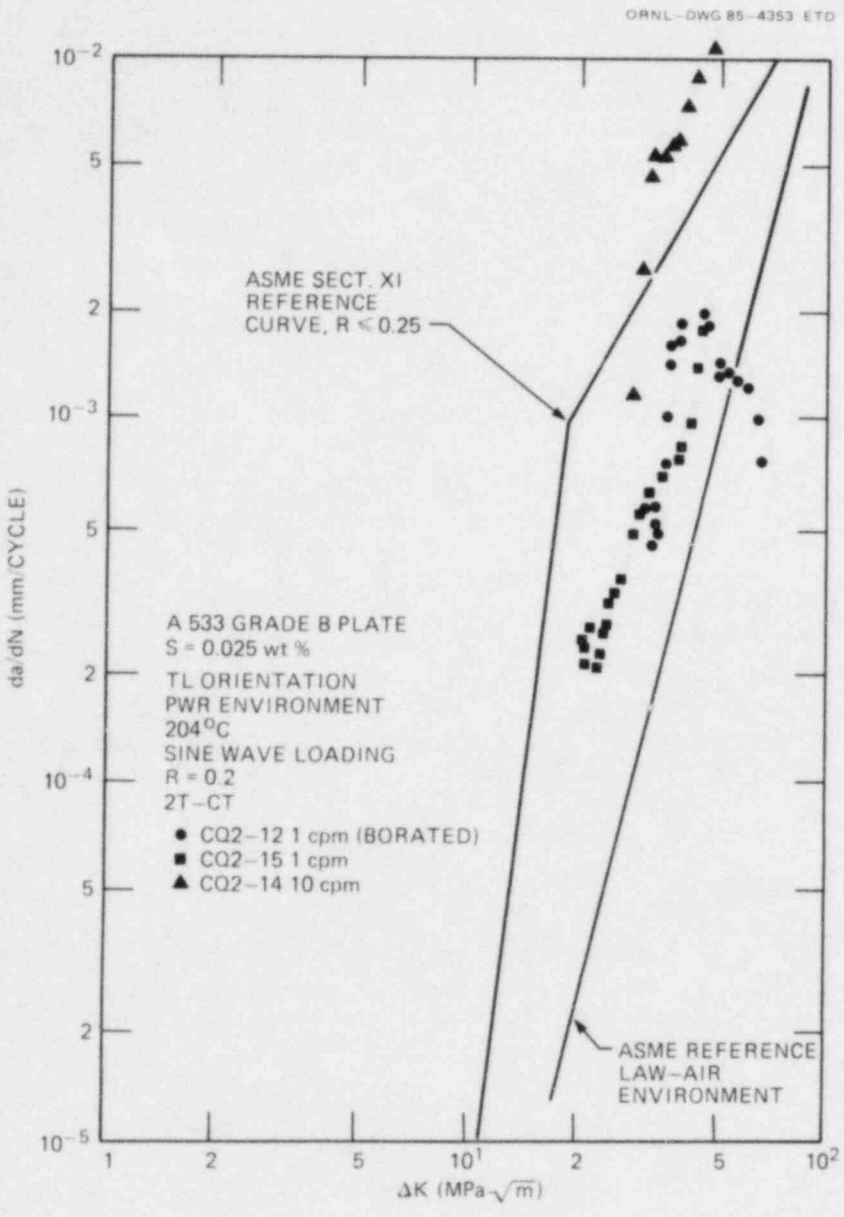

Fig. 4.1. Comparison of crack-growth-rate results for high-sulfur steel tested at 204°C and R = 0.2 for borated and unborated environments. Note the enhanced growth rate at 10 cycles per minute.

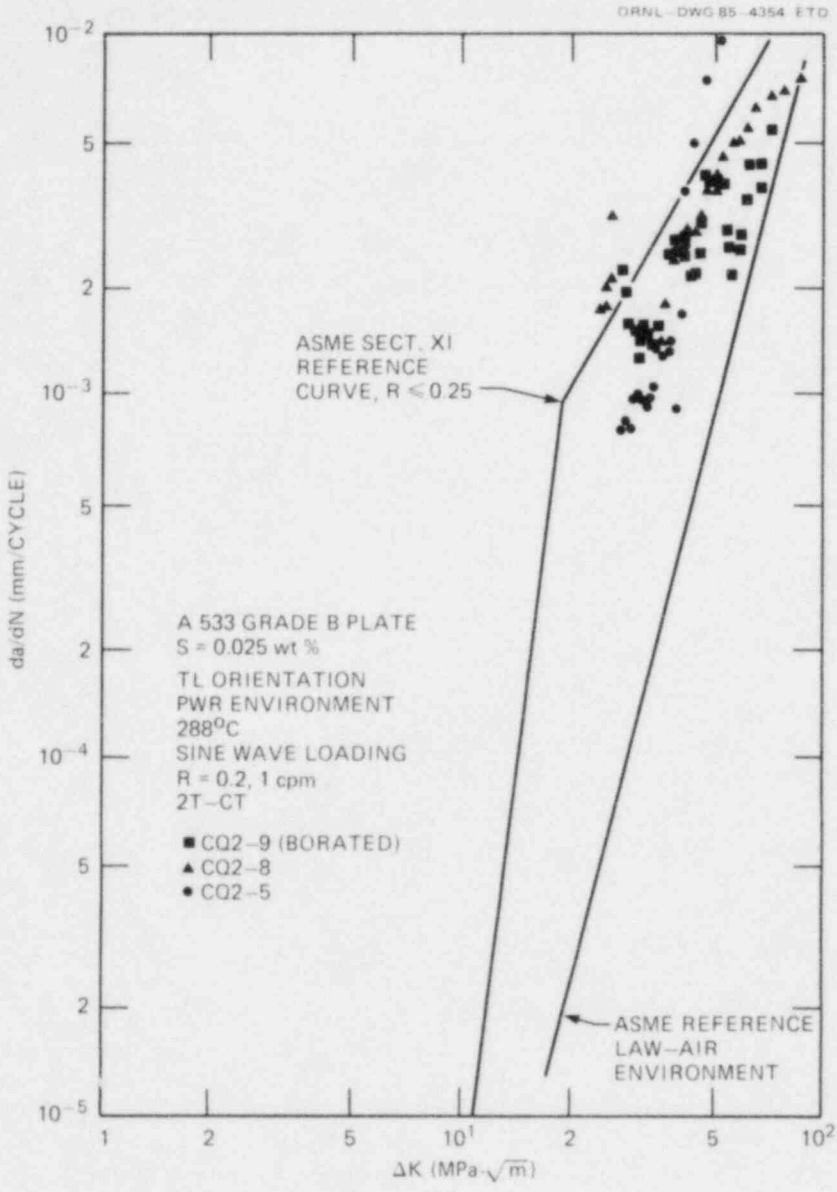

Fig. 4.2. Comparison of crack-growth-rate results for high-sulfur steel tested at 288°C and R = 0.2 results for borated and unborated environments.

Table 4.2. Test matrix for study of frequency and temperature effects for high-sulfur A 533 grade B steel

Test temperature (°C)	R ratio = 0.2		R ratio = 0.7	
	Frequency (cycles per minute)	Specimen	Frequency (cycles per minute)	Specimen
288	1	CQ2-5	1	CQ2-6
	1	CQ2-8	10	CQ2-11
	1 (borated)	CQ2-9		
204	1 (borated)	CQ2-12	1	CQ2-7
	1[a]	CQ2-15	10	CQ2-10
	10[a]	CQ2-14		
93				

[a]Tests completed during this report period.

report.[6] At 288°C the boron level did not influence the growth rates either, but the observed rates were near the *ASME Code* Sect. XI reference lines.[7]

Note that the 10-cycles-per-minute test shown in Fig. 4.1 showed higher growth rates than the 1-cycle-per-minute test. This phenomenon is very clearly shown in this set of tests and is the opposite of the effect of frequency at the higher temperature of 288°C (Ref. 8), where 1-cycle-per-minute data are generally the most accelerated. This behavior has also been observed by Vander Sluys in constant ΔK fatigue crack-growth-rate tests of the same class of materials.[4] Note that no observable trend of crack-growth rate as a function of frequency was found at R = 0.7 at 204°C, as reported in the previous period.[6]

As part of a specimen exchange arranged with Materials Engineering Associates (MEA), several specimens of heat CQ2 were tested at MEA.[5] Figure 4.3 shows that the crack-growth rates obtained by MEA were essentially the same as those obtained in this program (Fig. 4.2) for R = 0.2 and a 1-cycle-per-minute sinusoidal loading at 288°C. Another interesting finding was that the growth rate did not appear to be affected by the flow rate in the MEA tests, with the flow rates varying from 50 to 1000 L/h. (The systems used in the Westinghouse program have flow rates of ~50 L/h.)

The level and distribution of manganese sulfide inclusions in this steel have been studied through the use of sulfur prints, and a discussion of this work is included in Sect. 4.4 of this report.

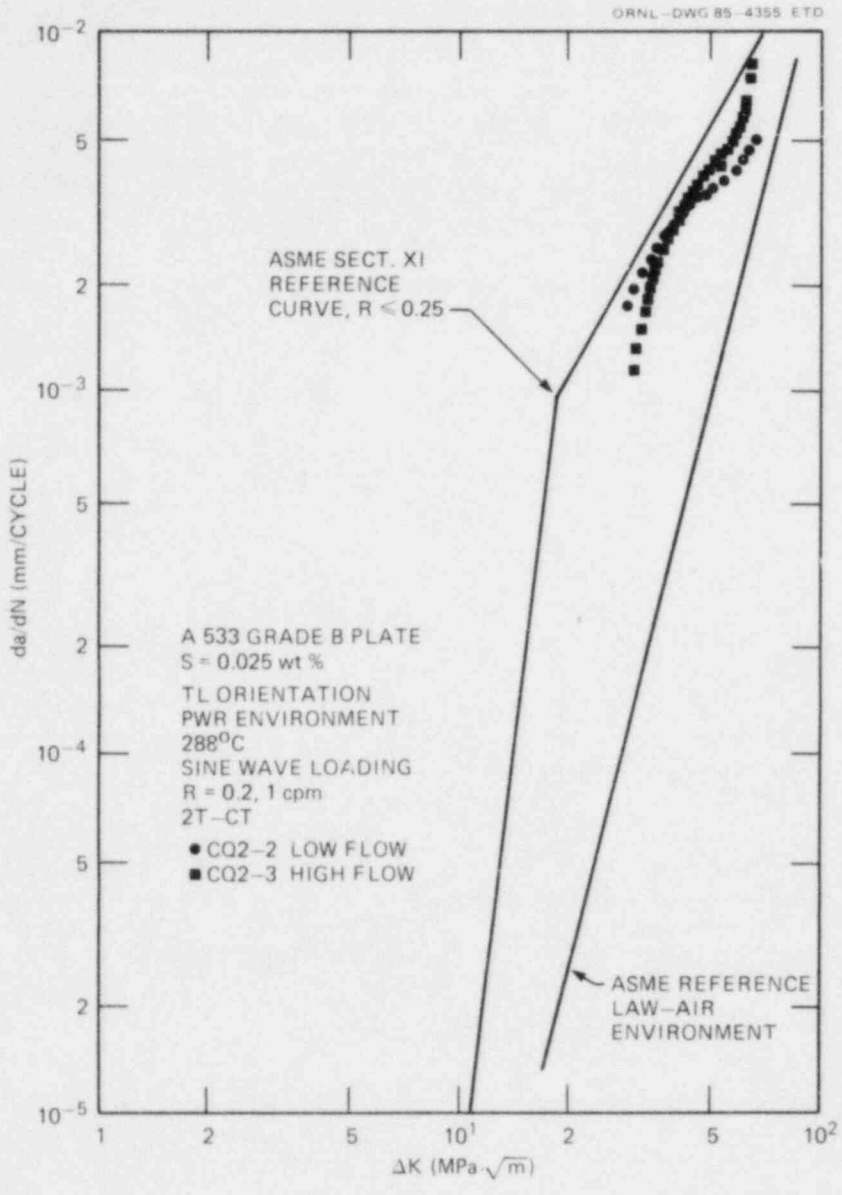

Fig. 4.3. Crack-growth-rate results obtained by MEA[5] on heat CQ2 at 288°C and R = 0.2. Low- and high-flow rate tests produced similar results.

4.2.2 Crack-growth testing of HAZ specimens

Because static-load cracking has been observed in several specimens, the crack-growth-rate behavior of these same materials was investigated to determine if any relationships existed. The materials for which both static and fatigue crack-growth results are available are found in Table 4.3.

Crack-growth-rate test results (Fig. 4.4) were obtained on material KH for the first time during this report period. The observed rates were somewhat lower than obtained on other HAZ materials, as shown in an earlier paper dealing with this subject.[9] However, the growth rates obtained were very similar to another previously tested[6] HAZ material, DD. This growth-rate behavior is typical of a steel with lower sulfur content and is confirmed by the reported sulfur content of the adjacent base metal, as shown in Table 4.4 for the HAZ materials tested to date. Because both of these materials showed static-load cracking, as the earlier HAZ materials had, it is not clear that there is any relationship between crack growth under static and fatigue loadings.

Sulfur prints for both materials, KH and DD, are presented in Sect. 4.4 of this report.

Table 4.3. Fatigue crack-growth-rate testing to complement static-load tests

Test material	R ratio = 0.2		R ratio = 0.7	
	Frequency (cycles per minute)	Specimen	Frequency (cycles per minute)	Specimen
Linde 124 weld HAZ				
Material C	1	C-24-HAZ-1	1	C-23-HAZ-1
Material CQ	1	CQ-1 HAZ	1	CQ-2 HAZ
			5	CQ-3 HAZ
Linde 80 weld HAZ				
Material C	1	C-3 HAZ	1	C-4 HAZ
A 533 grade B	1	2D 3Q-6	1	02GB-2
plate 04	1	2D 3Q-5	1	2D1Q-2
Linde 0091 weld				
Material D	1	D-1 HAZ	1	D-2 HAZ
			1	D-4 HAZ
			1	D-6 HAZ
Material DD	1	DD-1 HAZ	1	DD-2 HAZ
Linde 124 weld				
Material KH	1	KH-1 HAZ		

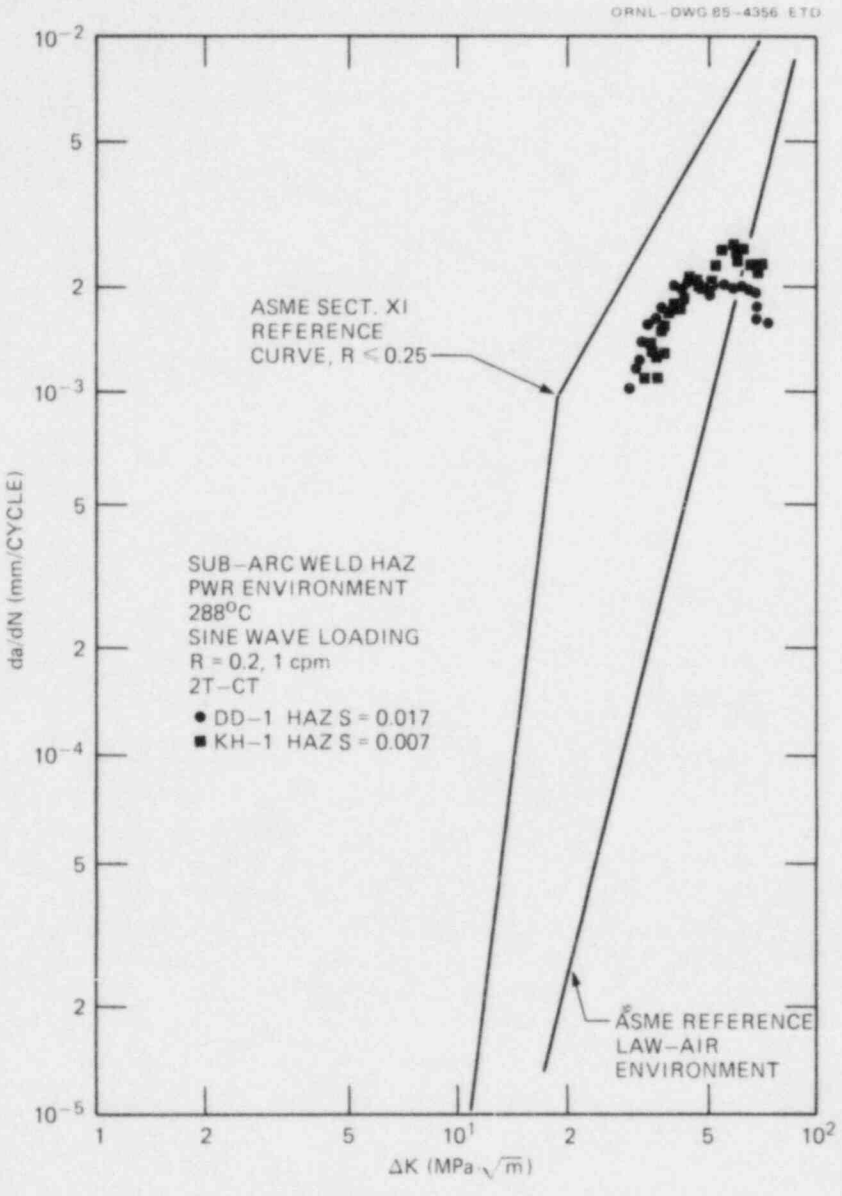

Fig. 4.4. Crack-growth-rate results for HAZ materials tested at 288°C and R = 0.2.

Table 4.4. Sulfur content of materials tested

Test material	Heat designation	Sulfur content (wt %)
A 533 grade B class 1 plate	IN	0.025
	PN	0.016
	TW	0.004
	04A	0.018
Linde 124 weld HAZ (adjacent base metal)	C	0.019
	CQ	0.019
	KH	0.007
Linde 0091 weld HAZ (adjacent base metal)	D	0.020
	DD	0.017

4.3 Static-Load Testing

Static-load crack-growth rates (if any) are characterized by using 2.54-cm-thick, bolt-loaded WOL specimens, which sit in the bottom of the fatigue chambers. The specimens are precracked in fatigue and then loaded to different values of stress-intensity factor K_I. If the crack extends, the load decreases, and eventually an equilibrium point, the threshold for static load cracking identified as K_{ISCC}, is reached. This work has been under way since 1974, and more than 25 specimens have been tested. No cracking has occurred in welds or forging materials in over 10 years of testing. On the other hand, cracking did occur in plate specimens and in all of the HAZ materials tested thus far. The time to crack initiation for the HAZ materials has averaged ~2,000 h, but for the plate material >37,000 h was required.

During this report period no additional cracking has occurred on any of the specimens. An update of the exposure times is provided in Table 4.5.

4.4 Examination of Specimens — Sulfur Prints

4.4.1 High-sulfur material matrix

As part of the sulfur-effects study, the distribution of manganese sulfide inclusions in a plate is being examined. It is well known that these inclusions migrate to the top center region of the ingot, and the largest concentrations are eliminated by topping the ingot. Those inclusions that remain are rolled into the plate and would, therefore, be

Table 4.5. Status of bolt-loaded specimens in simulated PWR environment (February 1, 1985)

Material	Specimen	Applied stress-intensity factor (Mpa·$\sqrt{m}$)	Total time loaded to date (h)	Time in environment (h)
A 533 grade B class 1 plate (HSST plate 4)	04A-114[a]	90	74,098	48,994
	04A-116[a]	88	74,098	48,994
A 508 class 2 forging	F-13	110	80,014	55,446
	F-14	99	80,014	56,654
	F-15	88	80,014	56,654
Linde 124 weld	C-13	110	80,014	55,783
	C-14	99	80,014	55,783
Linde 124 weld HAZ	CQ-1-HAZ[a]	110	28,708 (1,816)[b]	14,394 (1,262)[b]
	CQ-2-HAZ	99	33,604	18,410
	CQ-3HAZ[a]	88	29,136 (3,360)[b]	12,274 (2,616)[b]
Linde 0091 weld HAZ	D-7HAZ	99	32,876	27,136
	D-8HAZ[c]	88	32,876 (7,196)[b]	14,384 (4,160)[b]
	D-9HAZ	77	32,876	27,136
Linde 124 weld HAZ	K-3HAZ	66	9,216 (4,320)[b]	7,283 (4,138)[b]
	K-4HAZ	77	9,216 (4,320)[b]	7,283 (4,138)[b]
	K-5HAZ	88	9,216 (4,320)[b]	7,283 (4,138)[b]
Linde 0091 weld HAZ	DD-3HAZ	66	10,656 (5,760)[b]	9,296 (5,280)[b]
	DD-4HAZ[a]	77	10,656 (5,760)[b]	9,296 (5,280)[b]
	DD-5HAZ	88	10,656 (5,760)[b]	9,296 (5,280)[b]

[a]Removed from testing.

[b]Hours at first observed crack extension.

[c]Extension since last report.

likely to remain in the center portion after rolling. Sulfur prints were used to determine whether this was indeed true for the steel CQ2 used in this study.

Earlier work in this program, which studied the crack-growth behavior of steels with radically different sulfur contents, showed definitively that crack growth was affected by sulfur content.[2] The materials had sulfur contents ranging from 0.004 (heat TW) to 0.026 wt % (heat IN). Heat PN had an intermediate level of sulfur, 0.016 wt %. Sulfur prints of these three materials are shown in Fig. 4.5, and the differences in sulfur level are clearly visible, with the darker prints indicating the higher level of sulfur.

The specimen cutting diagram for heat CQ2 is shown in Fig. 4.6. Two rows of specimens were removed, with each row having four specimens through the thickness (shown in the side view). Sulfur prints were made of a plane just below the fracture surface of several of the specimens, and a clear change in the level of sulfur is visible as a function of distance through the thickness, with the darkest region near the center as expected.

To further verify this finding, a through-thickness slice was made of the plate (diagram of Fig. 4.6). A sulfur print was made of the entire slice, and Fig. 4.7 shows that there is also a clear concentration of manganese sulfide inclusions indicated near the center of the plate.

4.4.2 Sulfur characterization of HAZ specimens

To study the sulfide-inclusion variations in the two recently tested HAZ materials, sulfur prints were made both before and after testing of the specimens. The manner in which the HAZ specimens are removed from a typical weldment is shown in Fig. 4.8. This figure is typical of all the HAZ specimens tested in this program because they are positioned on the weldment only after the cross section has been etched lightly to reveal the HAZ. Also in this figure are sulfur prints from specimen DD-1 HAZ, showing both the side and top views, as indicated on the specimen sketch. Note that the portion of the print where the weld is located is almost devoid of indications because the manganese sulfide inclusions in this weld are very small and do not show up well in a sulfur print; also, the weld itself is low in sulfur. This is shown more clearly in Figs. 4.9 and 4.10, which are whole-specimen prints of the two HAZ materials, heat DD and heat KH, most recently tested.

4.5 International Cyclic Crack-Growth-Rate Group

Membership is maintained in the International Cyclic Crack-Growth-Rate review group, an interdisciplinary group began in 1977 to share information on corrosion fatigue. A detailed summary of the background and work of this group has been given in a previous progress report,[10] and a complete report of the group's status was given recently.[11] The status of the continuing activities of the group is reviewed periodically in these reports; this section reviews the discussions of technical interest.

ORNL–PHOTO 1767–85

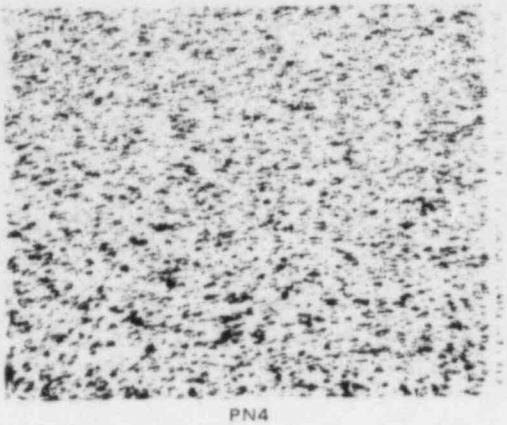

PN4

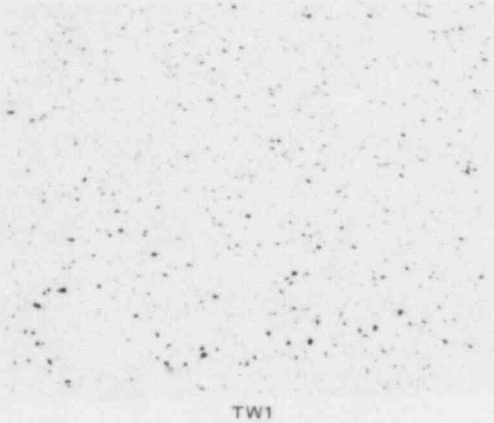

TW1

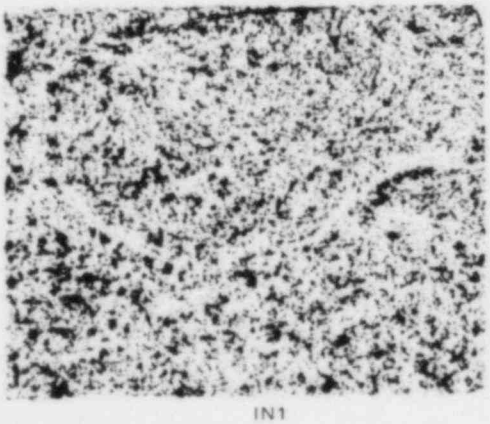

IN1

Fig. 4.5. Sulfur prints for low-, medium-, and high-sulfur steels tested previously.

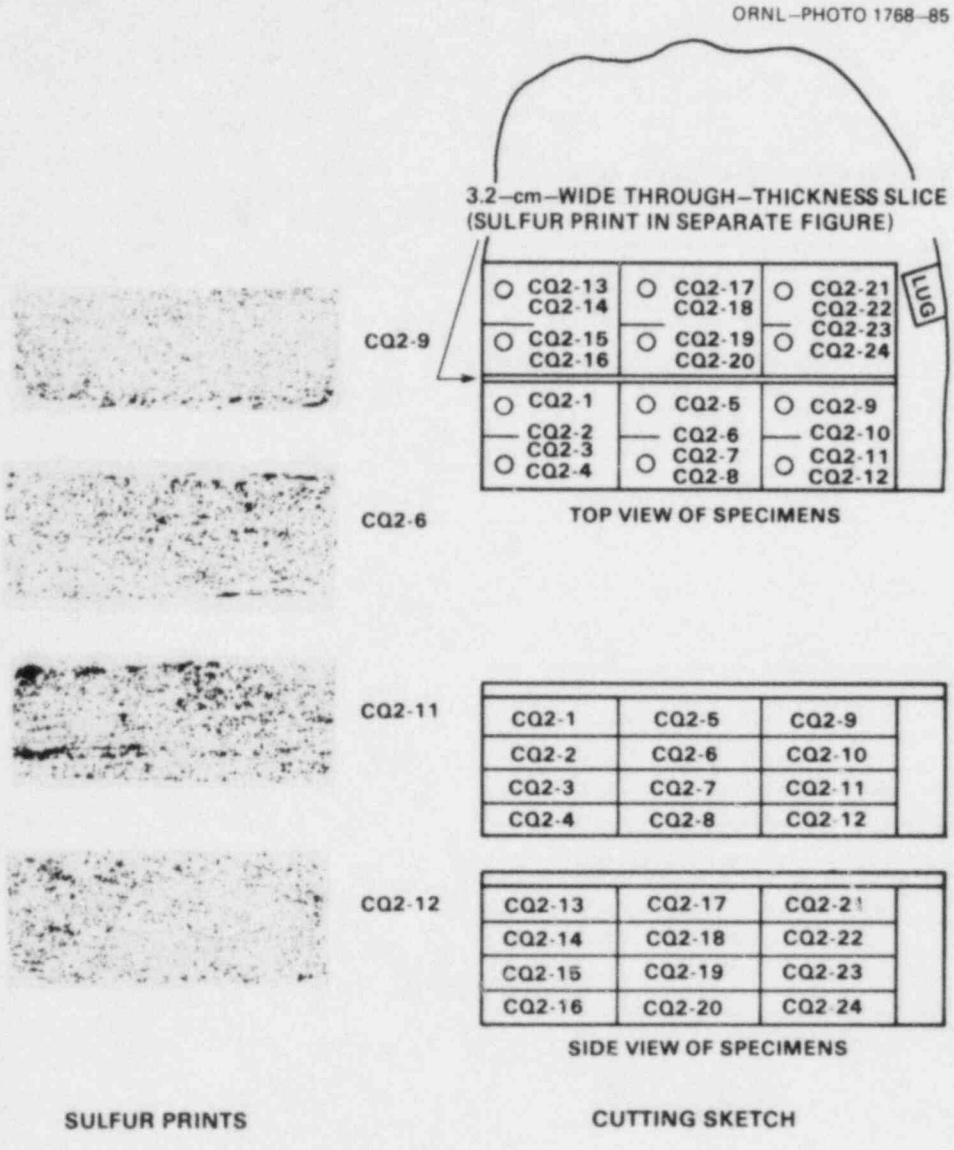

Fig. 4.6. Cutting sketch for heat CQ2 with examples of sulfur prints for different locations in the plate thickness.

ORNL–PHOTO 1769–85

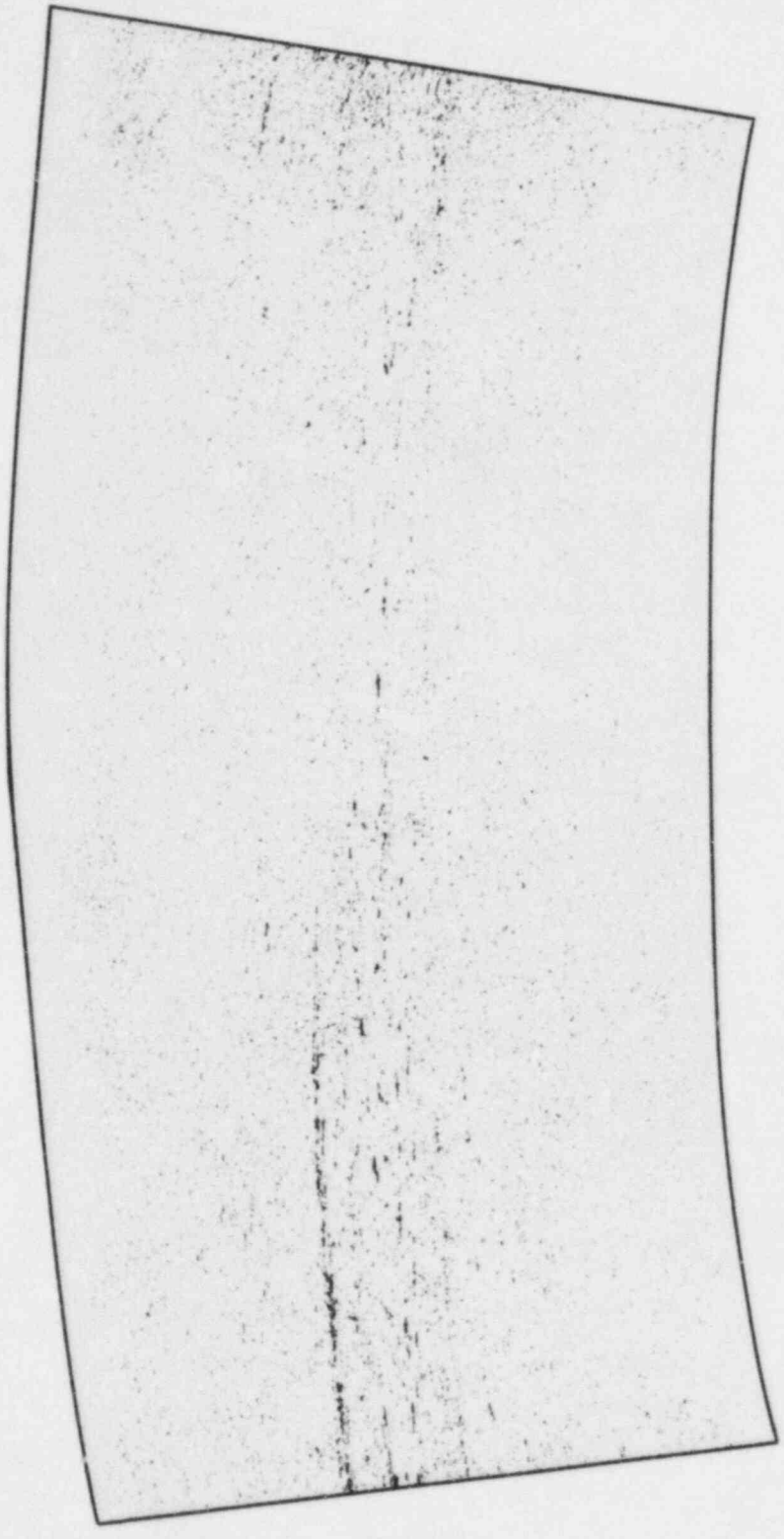

Fig. 4.7. A full-thickness sulfur print of heat CQ2, showing concentration of the manganese-sulfide inclusions near the plate center.

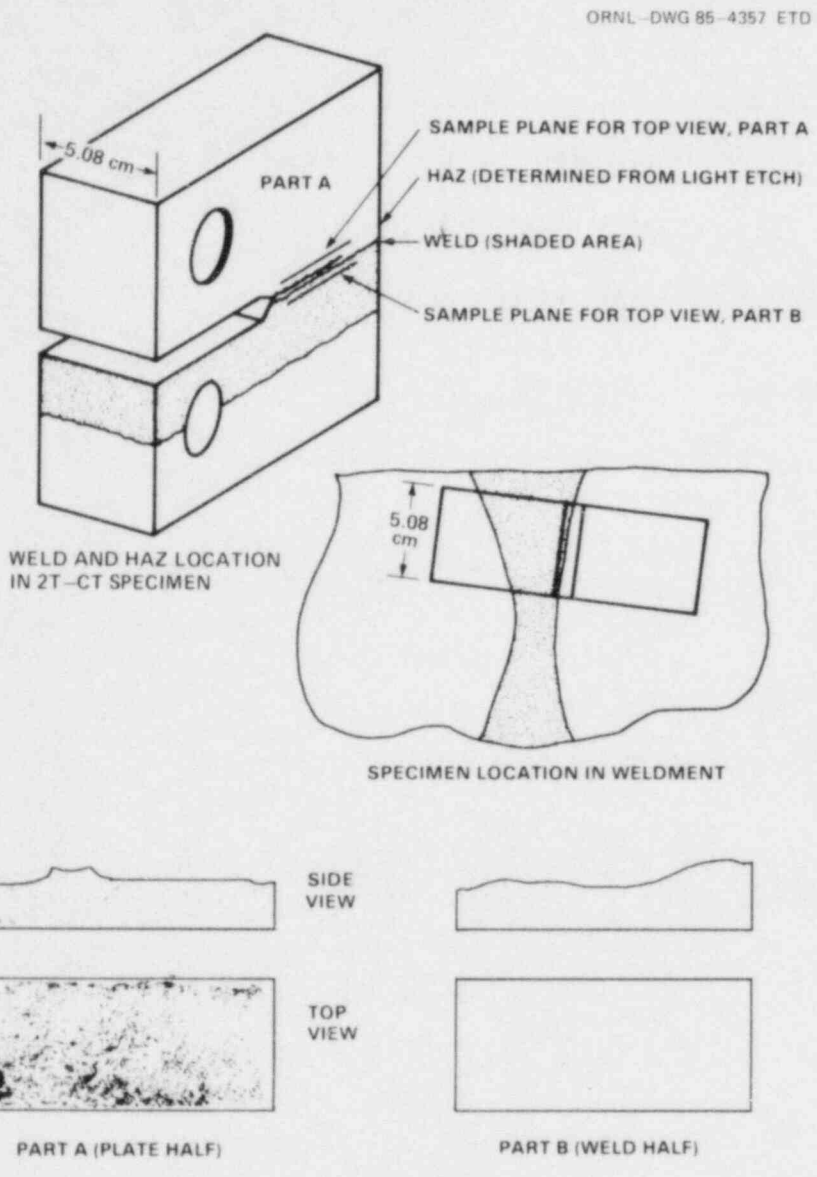

Fig. 4.8. Configuration of HAZ specimens and example sulfur prints for heat DD.

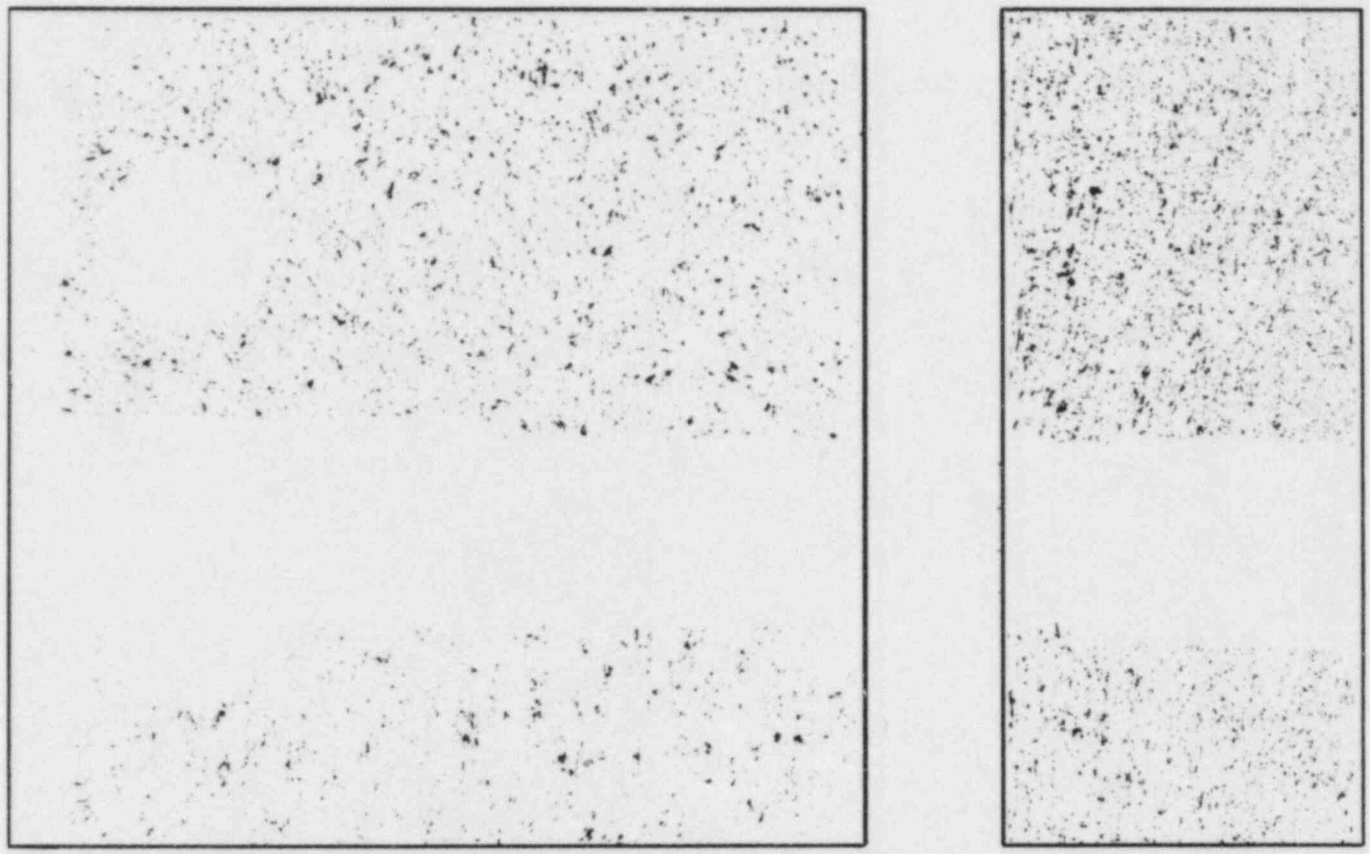

Fig. 4.9. Full-specimen sulfur prints for heat KH. (Note that the light area is the weld.)

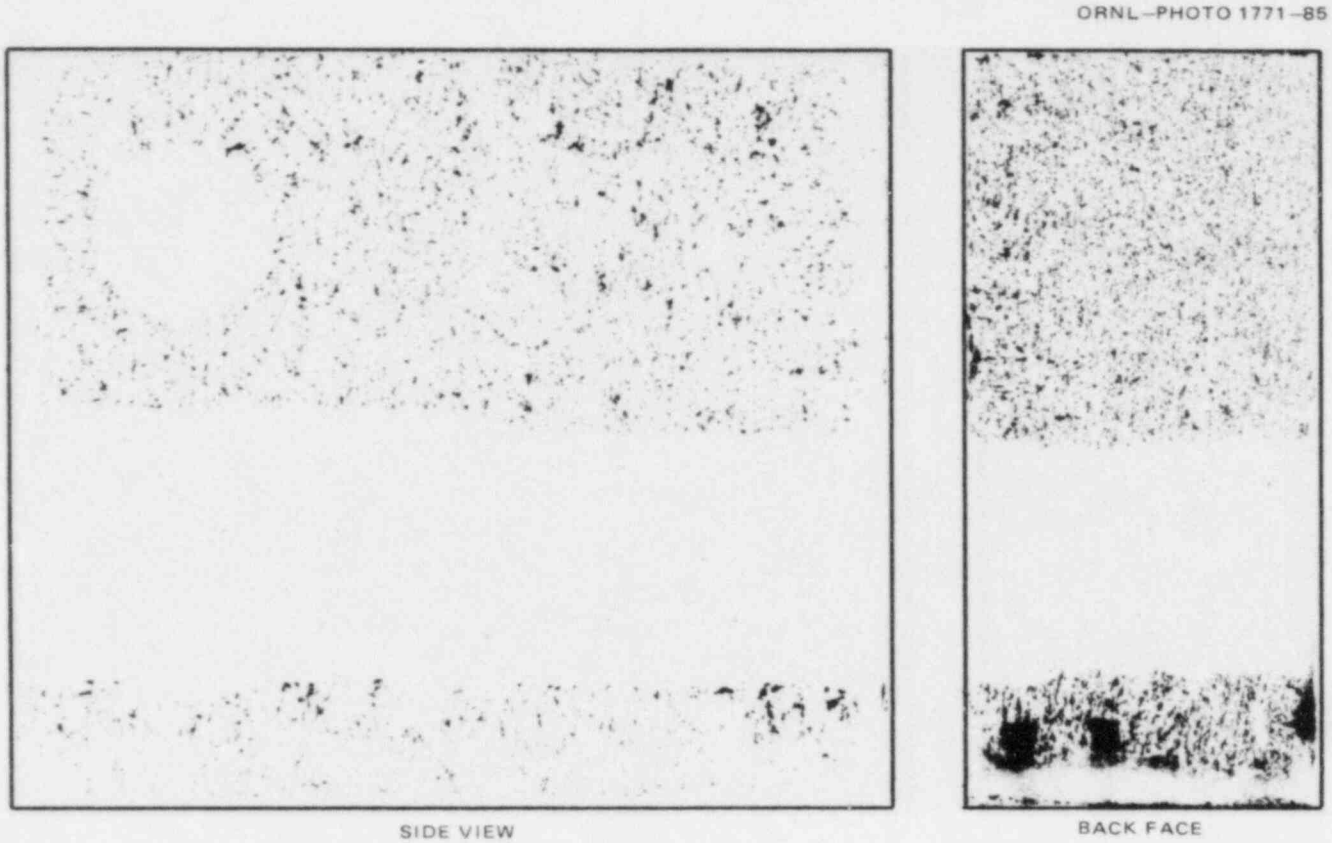

Fig. 4.10. Full-specimen sulfur prints for heat DD. (Note that the light area is the weld.)

The group is now composed of 46 member organizations from 11 countries, and 49 people attended the most recent meeting in Akron, Ohio, in October 1984. The group is organized into three subgroups, and the latest progress of the subgroups is reviewed individually in Sects. 4.5.1, 4.5.2, and 4.5.3.

4.5.1 Test methods and results subgroup

This subgroup develops standard test methods and promotes more reliable and consistent testing by members. Meetings also provide a forum for the exchange of recent test results.

The most recent meeting provided further confirmation of the two most important factors influencing corrosion fatigue crack growth: the sulfur content of the material and the flow rate and chemistry of the test environment. The trend of crack-growth-rate results with sulfur content is clear now, but the trend as a function of flow rate is not yet clear because different laboratories presently are obtaining what appear to be conflicting results.

Reliable electrochemical-potential monitoring methods have now been developed, a fact confirmed by a third and final survey of methods. The most reliable method, widely adopted by the members of the group, was found to be an externally installed (cold) silver-silver chloride electrode. A technical report is in preparation on the development and experience with this electrode. The state-of-the-art in this area was very quickly advanced as a result of the cooperative efforts of this group.

Another area receiving considerable attention was the measurement of static-load crack rates. Most laboratories, however, do not yet have long-time test results and have not yet observed cracking.

The long-time cracking results experienced in this program led to the discussion of the testing methods used by different laboratories, but no definitive conclusions were reached. A cooperative test program will be initiated to further study this question next year.

4.5.2. Mechanisms subgroup

This subgroup has set out to provide a mechanistic basis for the observed trends in fatigue crack-growth rates in water environments. It was concluded at the last meeting that a quantitative model that incorporates both anodic dissolution and hydrogen effects now exists. The model predicts strain-rate effects and is consistent with the *ASME Code* reference crack-growth-rate curves. The major issues that must be accounted for in the model are the cleavage-like appearance of high-sulfur steel crack-growth specimens, the relationship between sulfur content and plateau growth rates, the effect of oxygen, and a quantitative treatment of crack-tip blunting and initiation. These items do not appear to pose insurmountable challenges to the model, however.

4.5.3 Data collection and analysis subgroup

This subgroup is responsible for establishing a data base of existing corrosion fatigue data and for developing reference laws for use in

predictions for components. The computerized data base EDEAC was reported to be operational, but the authors of some data have not yet returned their verifications of the data base. Within six months a reevaluation of the data for carbon and low-alloy steels in air environments is expected to be completed, and a revised reference law proposed.

A tutorial on the statistical evaluation of crack-growth-rate data was presented, putting into perspective the advantages and pitfalls resulting from such a treatment. A separate presentation was made on the data analysis and manipulation capabilities for use with the EDEAC data base; these capabilities will make the development of new reference laws much more efficient.

Finally, a series of presentations was made on the status of efforts to develop reference crack-growth-rate laws for other pressure boundary materials. The reference law for stainless steels in air is essentially complete, and work is well along on treating the data on water environment effects. The available data were shown to be very consistent from lab to lab. Work is now beginning on development of a reference curve for Inconel 600 material.

References

1. W. H. Bamford, R. Jacko, and L. J. Ceschini, "Environmentally Assisted Crack Growth Studies," pp. 97–114 in *Heavy-Section Steel Technology Steel Program Quart. Prog. Rep. July–September 1983*, NUREG/CR-3334, Vol. 3 (ORNL/TM-8787/V3), Union Carbide Corp. Nuclear Div., Oak Ridge Natl. Lab., February 1984.

2. W. H. Bamford, "Environmental Cracking of Pressure Boundary Materials, and the Importance of Metallurgical Considerations," pp. 209–28 in *Aspects of Fracture Mechanics in Pressure Vessels and Piping*, ASME Publication PVP-vol. 58, 1982.

3. G. Slama and P. Rabbe, "French Approach and Results in Cyclic Crack Growth," pp. 311–25 in *Proceedings of the Sixth SMiRT Post-Conference Seminar, Paris, France, August 1981*.

4. *Corrosion Fatigue Characterization of Reactor Pressure Vessel Steels*, Progress Report, October 1, 1982–April 30, 1983, Project 1325-1, A. Van Der Sluys, Principal Investigator, Babcock & Wilcox; available from R. L. Jones, Electric Power Research Institute, Palo Alto, Calif.

5. W. H. Cullen et al., *The Effects of Sulfur Chemistry and Flow Rate on Fatigue Crack Growth Rates in LWR Environments*, NUREG/CR-4121 (MEA-2053), Materials Engineering Associates, Lanham, Md., January 1985.

6. W. H. Bamford et al., "Environmentally Assisted Crack Growth Technology," pp. 53–81 in *Heavy-Section Steel Technology Semiannual Prog. Rep. April–September 1984*, NUREG/CR 2744 Vol. 2 (ORNL/TM-9154/V2), Martin Marietta Energy Systems, Inc., Oak Ridge Natl. Lab., December 1984.

7. *ASME Boiler and Pressure Vessel Code*, Sect. XI, American Society Mechanical Engineers, New York, all editions since Winter 1980 addendum.

8. W. H. Bamford, "Applications of Corrosion Fatigue Crack Growth Rate Data to Integrity Analyses of Nuclear Reactor Vessels," *Trans. ASME J. Eng. Mater. Technol.* 101, 182–90 (July 1979).

9. W. H. Bamford, D. M. Moon, and L. J. Ceschini, "Studies of Statically and Dynamically Loaded Cracks in Simulated Pressurized Water Environment," paper No. 12 presented at *Corrosion 83*, Anaheim, Calif., to be published in *Corrosion*.

10. W. H. Bamford, R. J. Jacko, and L. J. Ceschini, "Environmentally Assisted Crack Growth Technology," pp. 28–44 in *Heavy-Section Steel Technology Program Semiannual Prog. Rep. October 1983–March 1984*, NUREG/CR-3744, Vol. 1 (ORNL/TM-9154/V1), Martin Marietta Energy Systems, Inc., Oak Ridge Natl. Lab.

11. G. Slama and R. Jones, "International Cooperative Group on Cyclic Crack Growth Rate," *Proceedings of the Sixth SMiRT Conference Post-Conference Seminar, Session 8, Paris, France, 1981.*

5. CRACK-ARREST TECHNOLOGY

5.1 Background Information on HSST Studies

C. E. Pugh

In crack-arrest studies sponsored by the Heavy-Section Steel Technology (HSST) Program, a primary objective has been to obtain reliable fracture-toughness data and to develop procedures for the prediction of crack arrest in materials at temperatures approaching the Charpy upper-shelf regime. Early laboratory studies of crack arrest by numerous investigators have led to the use of test specimens that reduce the dynamic effects of a running crack. The appropriateness of current American Society for Testing and Materials (ASTM) recommendations on laboratory test procedures is being examined through a round-robin test program that is discussed in Sect. 5.7. A data bank has been established of available crack-arrest data, and the status of this effort is discussed in Sect. 5.8. However, small laboratory specimens provide limited constraint of deformation in the crack-plane region and a driving force that decreases with crack extension. These factors have limited the generation of valid data from these specimens to temperatures below those where arrest is most likely to occur in a pressurized-thermal-shock (PTS) scenario. The HSST Program is measuring crack-arrest data over an expanded temperature range through thermal-shock[1] and PTS[2] tests, which also provide validation data under multiaxial transient conditions. More recently, the HSST Program has undertaken the performance of a series of wide-plate tests[3] as an opportunity to obtain significant numbers of data points at affordable costs. The wide-plate specimens are designed for the measurement of fracture-toughness values at temperatures approaching the upper-shelf of the material. A rising toughness field for crack arrest is achieved by applying a temperature gradient across the span of the plate. The plates are heavily instrumented to record pertinent data during the test. In conjunction with the wide-plate testing, a parallel research effort is under way that combines dynamic-viscoplastic finite-element analyses with small-scale fracture experimentation (see Chap. 2).

The HSST wide-plate crack-arrest tests are being performed at the National Bureau of Standards (NBS), Gaithersburg, in their 27-MN capacity tensile machine. The first series of six planned tests use specimens from the HSST plate 13A of A 533 grade B class 1 steel. The overall specimen assembly was described in Ref. 3 and is illustrated in Fig. 5.1. Figure 5.2 shows a specimen assembly (specimen plus pull plates) being installed in the NBS machine for testing, while Fig. 5.3 shows a specimen under tests.

While these tests are aimed primarily at providing crack-arrest data at temperatures up to or above that corresponding to the onset of the Charpy upper shelf (>50°C for this material), they also provide information on the dynamic fracture process for use in evaluating improved fracture-analysis methods. The tests use single-edge-notched plate specimens that are heated on one edge and cooled on the other to give a linear temperature gradient along the crack propagation plane. Upon initiating the

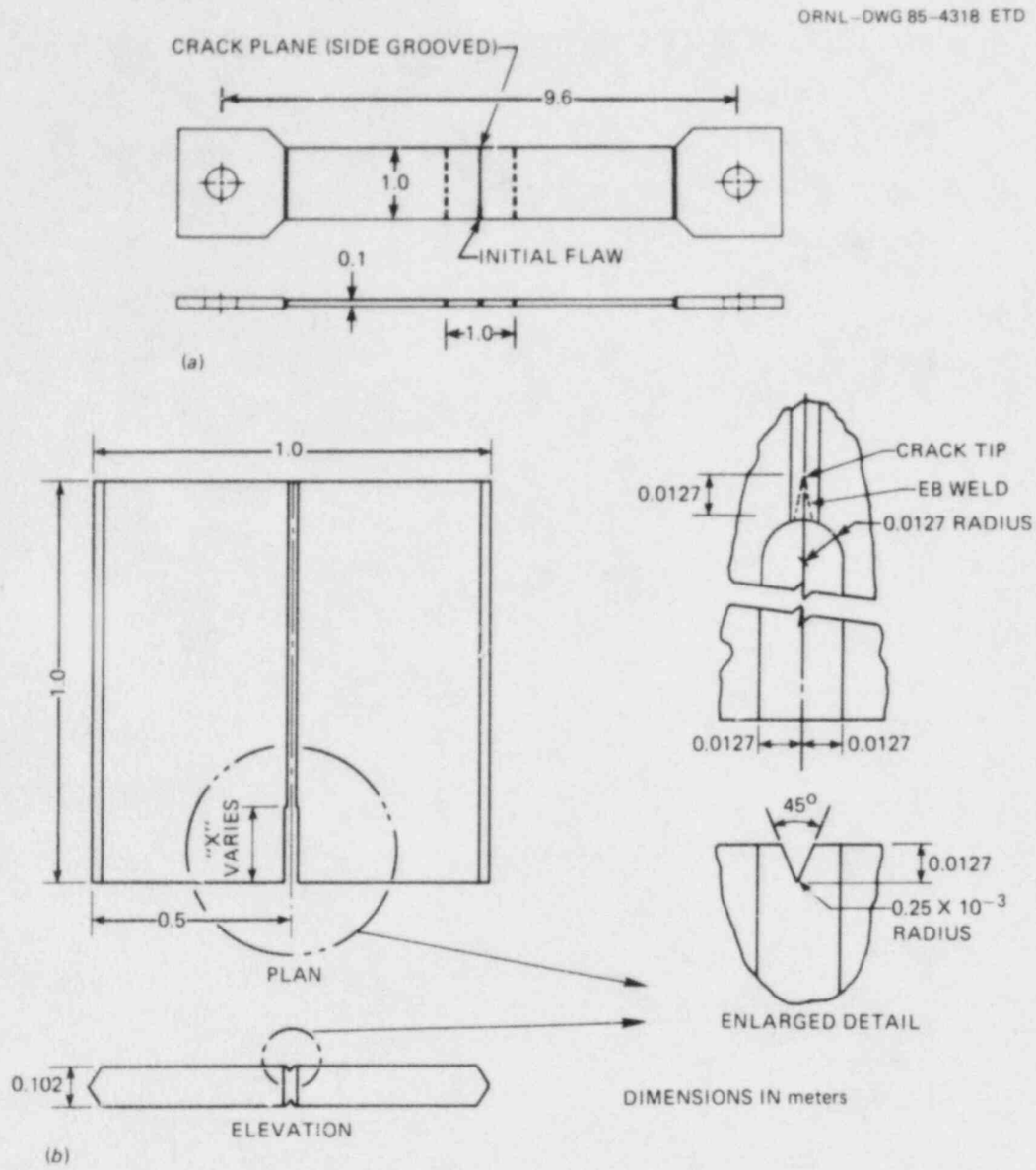

Fig. 5.1. Wide-plate crack-arrest specimen and pull-plate assembly. (*a*) Schematic of assembly, (*b*) detail of test specimen.

crack in cleavage, arrest is intended to occur in the higher-temperature ductile region of the specimen.

Two tests have been performed to date, WP-1.1 on September 27, 1984, and WP-1.2 on January 17, 1985. Oak Ridge National Laboratory (ORNL) provided the precracked specimens, and NBS instrumented them with thermocouples and strain gages. In addition, Battelle Columbus Laboratories (BCL) placed four conducting paint grids along the crack path to measure

ORNL-PHOTO 6716-85

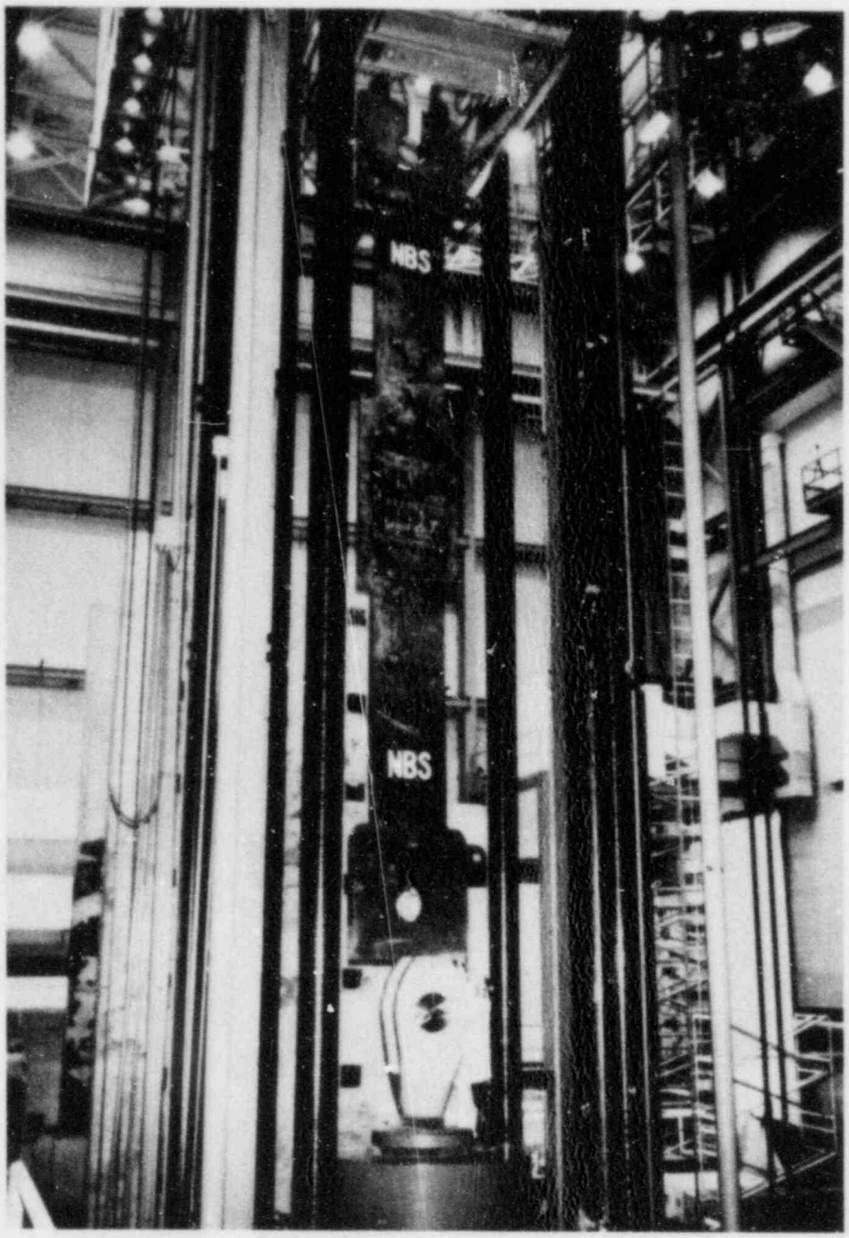

Fig. 5.2. Wide-plate crack-arrest specimen assembly being installed in the 27-MN capacity tensile machine at NBS Gaithersburg fracture laboratory.

the crack propagation velocity (Sect. 5.8.2). The pretest plans for instrumentation and loadings were described in Ref. 3. The actual tests are described in Sect. 5.2 that follows.

Mechanical and fracture properties data for this test material have been obtained and are discussed in Sect. 5.3. BCL obtained the crack-

ORNL-PHOTO 6718-85

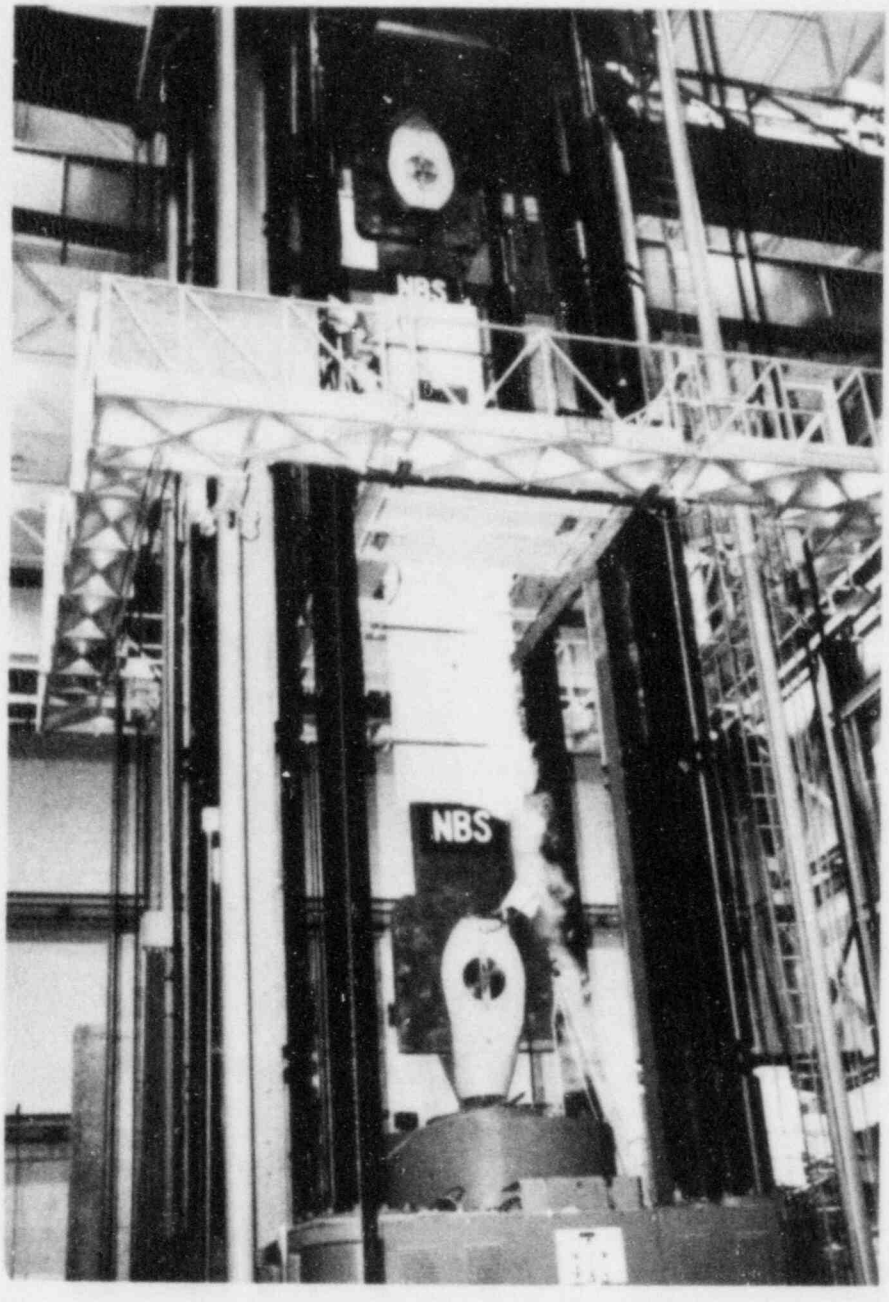

Fig. 5.3. Wide-plate crack-arrest test in progress using the 27-MN capacity tensile machine at NBS Gaithersburg fracture laboratory.

arrest data, while ORNL performed the other properties tests. Analyses have been performed of the wide-plate tests by ORNL, Southwest Research Institute (SwRI), and University of Maryland (UM), and these activities are reported in Sects. 5.4–5.6.

5.2 Wide-Plate Crack-Arrest Testing*

R. deWit[†]
S. R. Low III[†]
G. E. Hicho[†]
L. C. Smith[†]
D. Read[‡]
D. McColskey[‡]
D. E. Harne[†]
R. J. Fields[†]

5.2.1 Introduction

This report describes results from the first two wide-plate crack-arrest tests (WP-1.1 and WP-1.2) performed for the HSST Program. Testing procedure, preliminary results, and fractography are included. In addition, the results are included for two full-thickness, bend-bar tests that were performed to provide a basis for specifying the loading procedure and temperature gradient employed in WP-1.2. Three similar beam tests were performed earlier to support WP-1.1 (see Ref. 4).

Detailed specimen dimensions for WP-1.1 and WP-1.2 are shown in Figs. 5.4 and 5.5. The main differences in these two are the pull-tab shape and the length of the 100-mm-thick pull plates. The length of the pull plates changed from WP-1.1 to WP-1.2 because small amounts of the pull plates were removed in the process of cutting out the WP-1.1 specimen. Dimensions of specimens WP-1.1 and WP-1.2 are listed in Table 5.1.

Table 5.1. Detailed dimensions of wide-plate crack-arrest specimens

Dimensions (mm)	Specimen No.	
	WP-1.1	WP-1.2
Width, w	997	998
Thickness, B	101.0	101.8
Side-grooved thickness, B_N	76.3	77.5
Initial crack length, a_o	196.9	199.0

*Work sponsored by the HSST Program under Interagency Agreement No. DE-AI05-84OR21432 between the U.S. Department of Energy and the National Bureau of Standards.

[†]Fracture and Deformation Division, National Bureau of Standards, Gaithersburg, Maryland.

[‡]Fracture and Deformation Division, National Bureau of Standards, Boulder, Colorado.

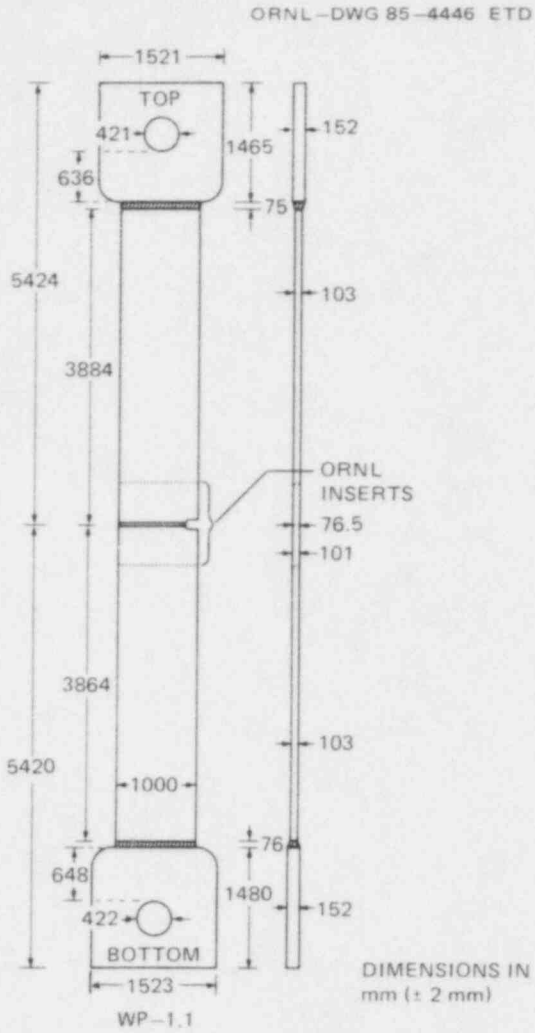

Fig. 5.4. Overall specimen dimensions for wide-plate crack-arrest test WP-1.1.

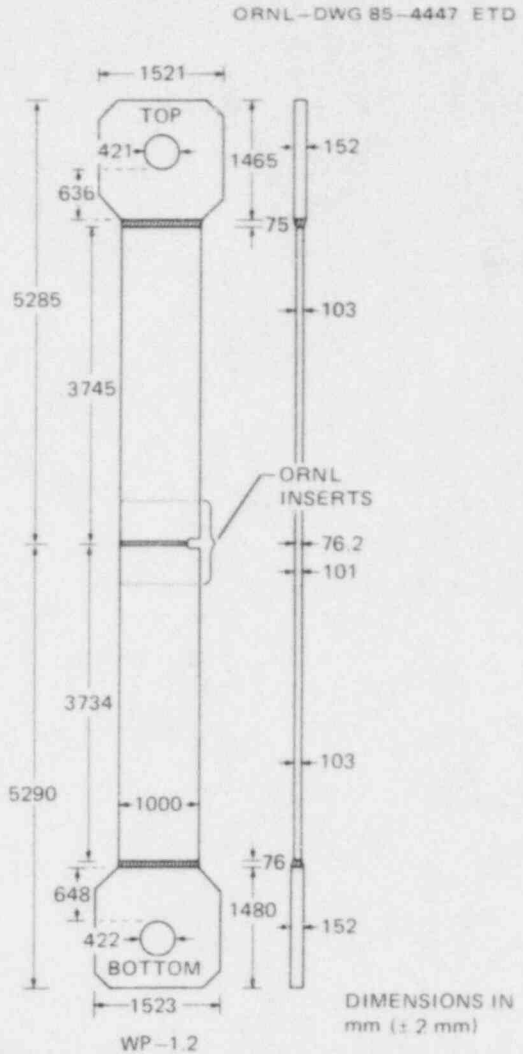

Fig. 5.5. Overall specimen dimensions for wide-plate crack-arrest test WP-1.2.

5.2.2 Applied loading histograms

5.2.2.1 Test WP-1.1. The first wide-plate test was intended to provide crack initiation in cleavage and arrest near the center of the plate at a temperature of about 55°C, which approximates onset of Charpy upper shelf (see Fig. 5.15 of Ref. 5 and also Sect. 5.3 of this report). Figure 5.6 shows the stress-intensity factor vs crack-tip temperature history that was planned for WP-1.1. To prevent initiation of crack propagation prior to the planned load (when $K_I \approx 130$ MPa$\cdot\sqrt{m}$), the crack tip was warm prestressed (WPS) by loading the specimen to $P_{WPS} = 10$ MN at 70°C. After the WPS, the load was reduced by 30% to 7 MN. The load was further decreased by 0.21 MN at four points between points 3 and 4 (in Fig. 5.6) to keep $K_I \sim K_{RED} = 82$ MPa$\cdot\sqrt{m}$, because thermal bowing takes place while the temperature gradient is being established. Thus, the stress-intensity factor when application of the fracture load began K_{oi} was approximately 82 MPa$\cdot\sqrt{m}$, which corresponded to a load of 6.12 MN when

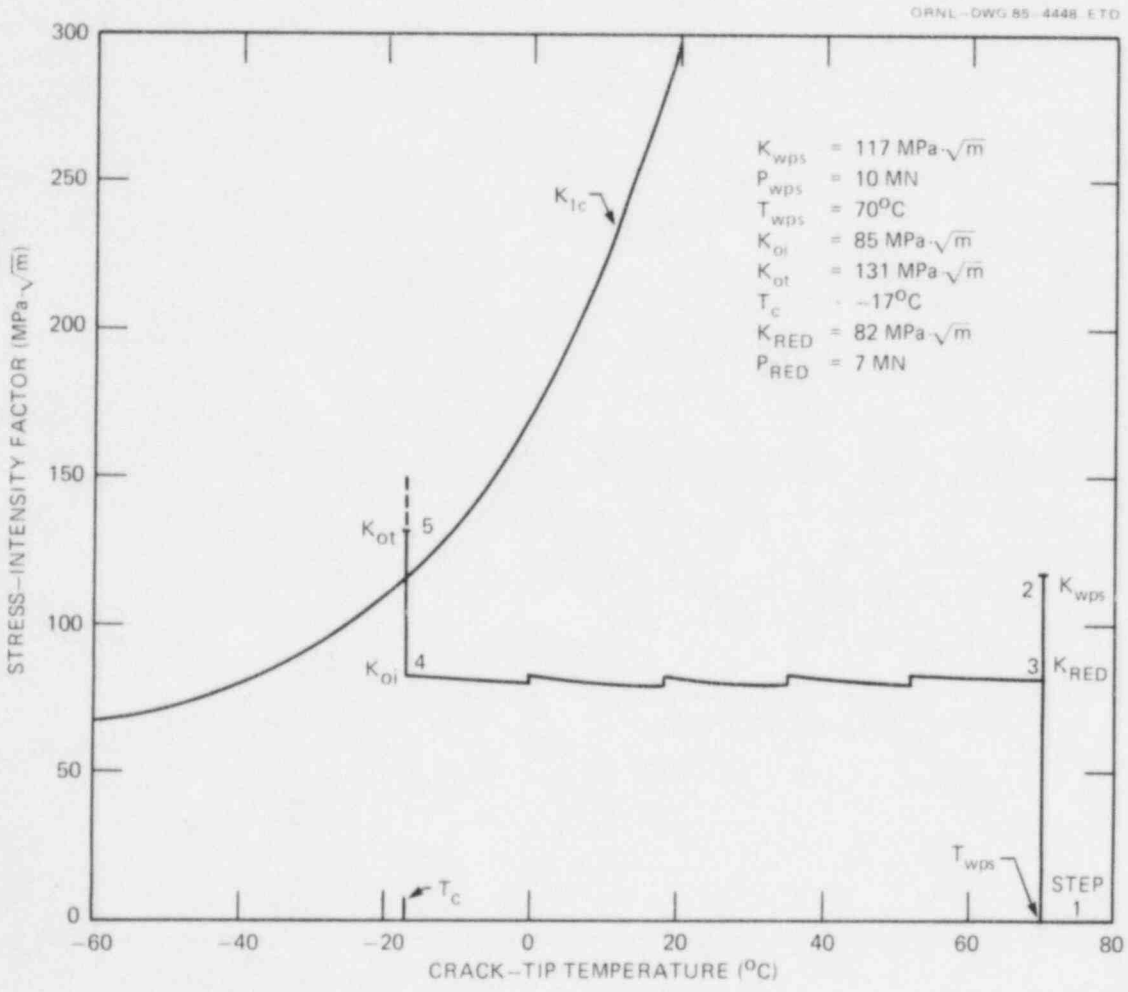

Fig. 5.6. Planned thermal and mechanical loading sequence for wide-plate crack-arrest test WP-1.1.

the temperature gradient was in place. The total actual histogram followed during the test is shown in Fig. 5.7. The temperature gradient was established by heating and cooling the edges of the plate and took about 28 h for completion after the WPS phase. An additional 3 h passed before the loading was increased.

The actual load-time curve for the WPS procedure (steps 1–3 in Fig. 5.7) are shown in Fig. 5.8. The hot edge of the plate was heated by electric heating bars covering 1220 mm above the crack plane and 1220 mm below the crack plane. The cooling box consisted of a wooden enclosure containing perforated copper tubing through which gaseous and liquid nitrogen could be pumped. Solid CO_2 was added in the enclosure after the start of the cooling process. The temperature distribution established is shown in Fig. 5.9.

Figures 5.6 and 5.7 show that crack initiation was expected to occur when K_I was between 131 and 150 MPa•$\sqrt{m}$, which corresponds to the load being between 9.5 and 10.9 MN. However, when the loading was applied from point 4, it was increased to 19.0 MN ($K_I \sim 252$ MPa•$\sqrt{m}$) and *initiation did not occur*. Concurrent with this load increase was an unplanned increase

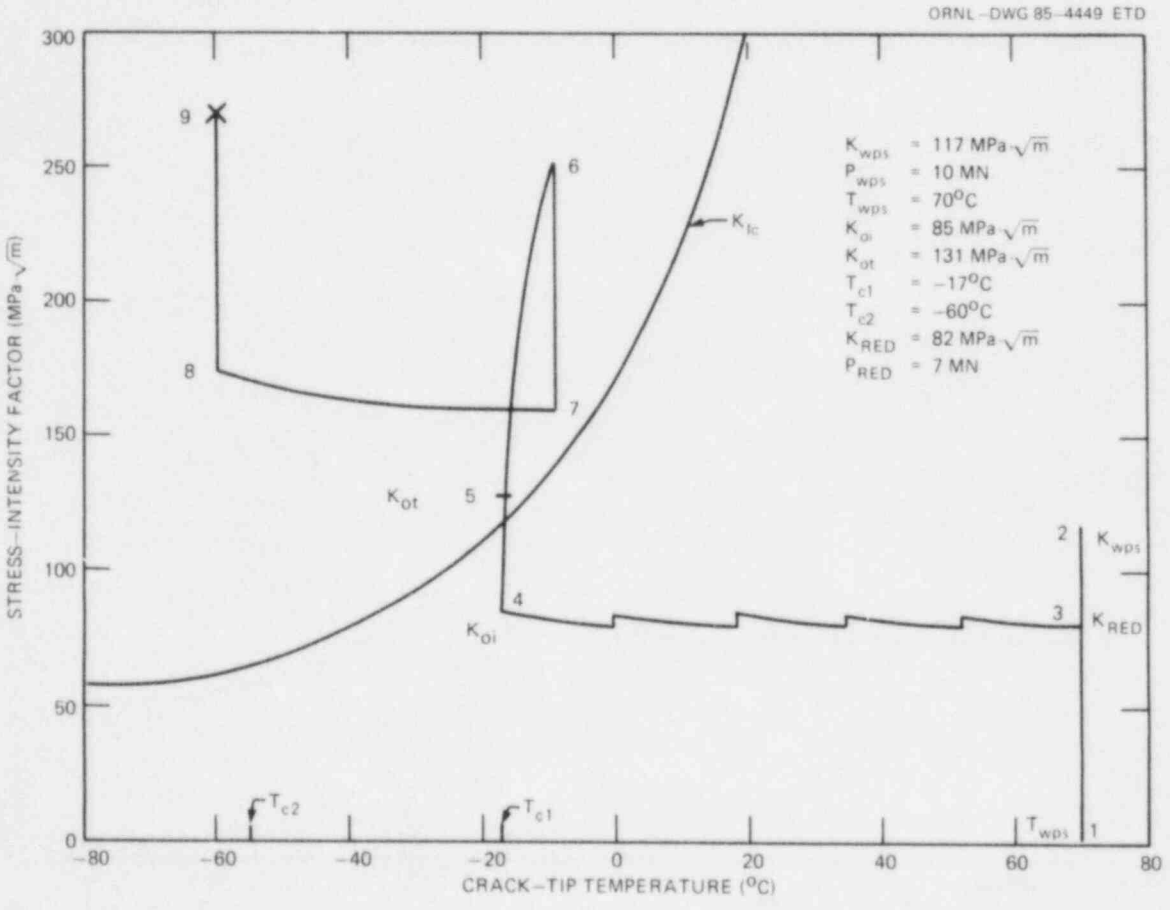

Fig. 5.7. Actual thermal and mechanical loading sequence for wide-plate crack-arrest test WP-1.1.

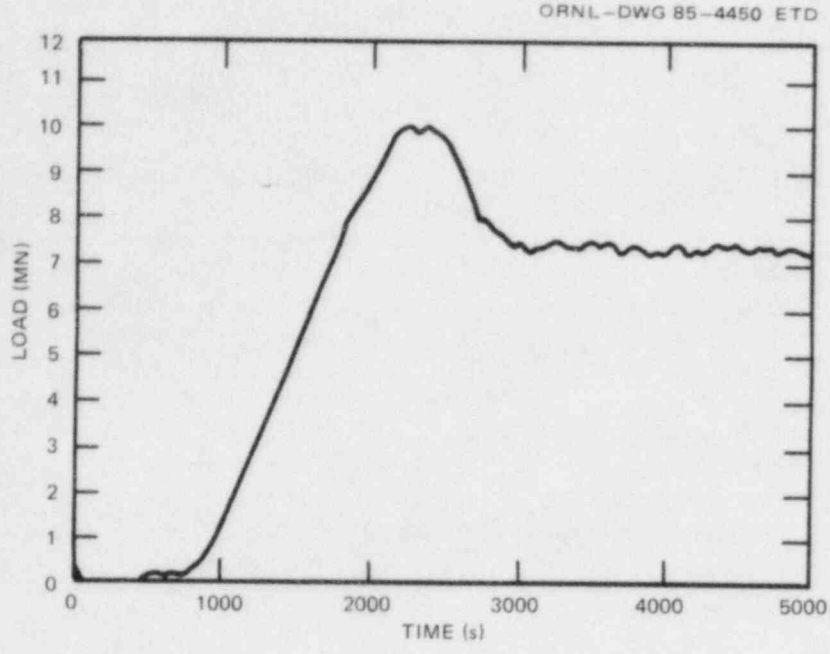

Fig. 5.8. Warm prestressing load-time history for WP-1.1 at 70°C.

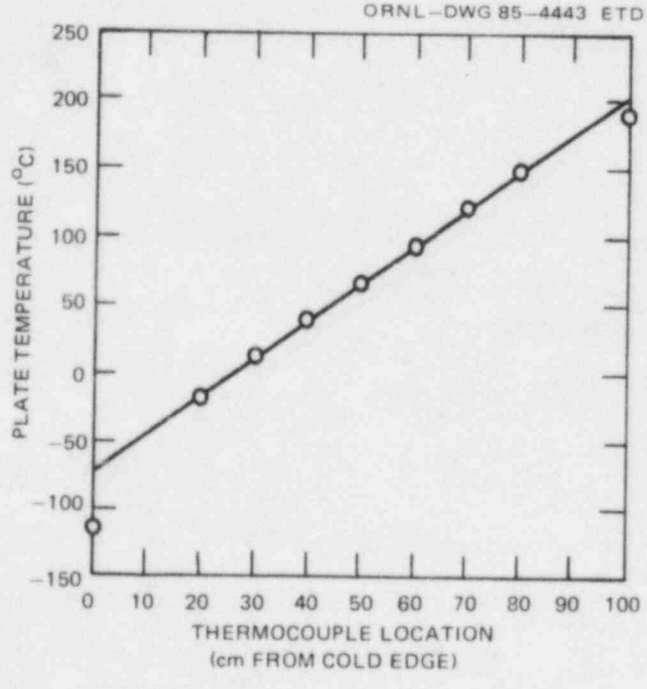

Fig. 5.9. Achievement of desired temperature gradient for WP-1.1 (crack tip is at the 20 cm location).

in the crack-tip temperature from −17 to −9°C. At this point, the loading was decreased to 12 MN; the load was held at that level for 3 h while the cold-side temperatures were decreased and the hot-side temperatures increased. The temperature gradient 15 s before fracture occurred upon load resumption is shown in Fig. 5.10. With the crack-tip temperature at about −60°C, loading was increased until fracture occurred at 20.1 MN (K_I = 268 MPa•$\sqrt{m}$).

The stress-intensity factor at fracture was about four times greater than the estimated K_{Ic} at −60°C (≈65 MPa•$\sqrt{m}$). However, this result is not surprising because loading phases 1–6 in Fig. 5.7 had clearly warm prestressed the specimen. On the other hand, it is surprising that the K_I = 252 MPa•$\sqrt{m}$ point 6 was about double the estimated K_{Ic} at −9°C (≈137 MPa•$\sqrt{m}$), and the crack did not initiate. Further data and fracture observations are given in Sect. 5.2.4.

5.2.2.2 Test WP-1.2. The second test WP-1.2 was performed without a WPS phase, and the temperature gradient was modified to drop the crack-tip temperature to −33°C. The cold and hot edges were at about −97 and 207°C, respectively, as shown in Fig. 5.11. Approximately 20 h was required to establish the temperature gradient across this specimen. The specimen was loaded monotonically at 11 KN/s until fracture occurred at 18.9 MN (K_I = 251 MPa•$\sqrt{m}$). This was substantially above the estimated K_{Ic} for this material at −33°C (see Sect. 5.3, K_{Ic} ≈ 88 MPa•$\sqrt{m}$). Data and fracture observations are discussed in Sect. 5.2.4.

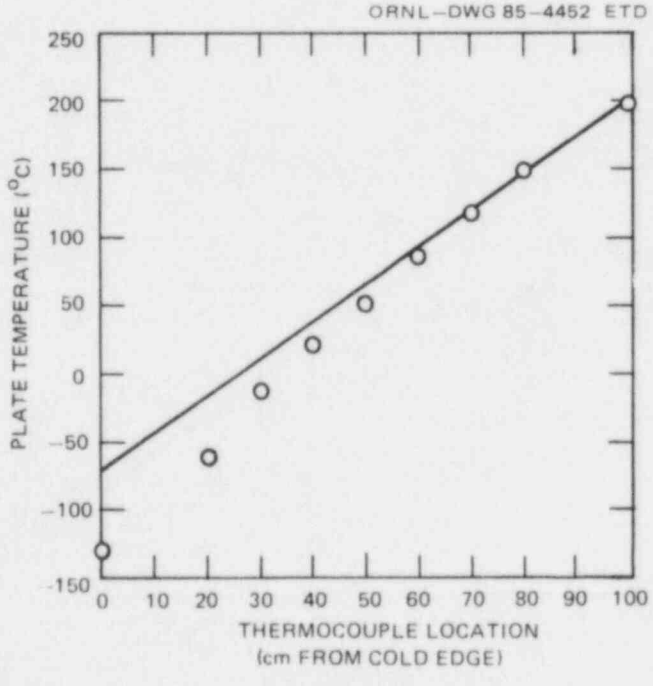

Fig. 5.10. Temperature gradient shortly before fracture of WP-1.1 (crack tip is at the 20 cm location).

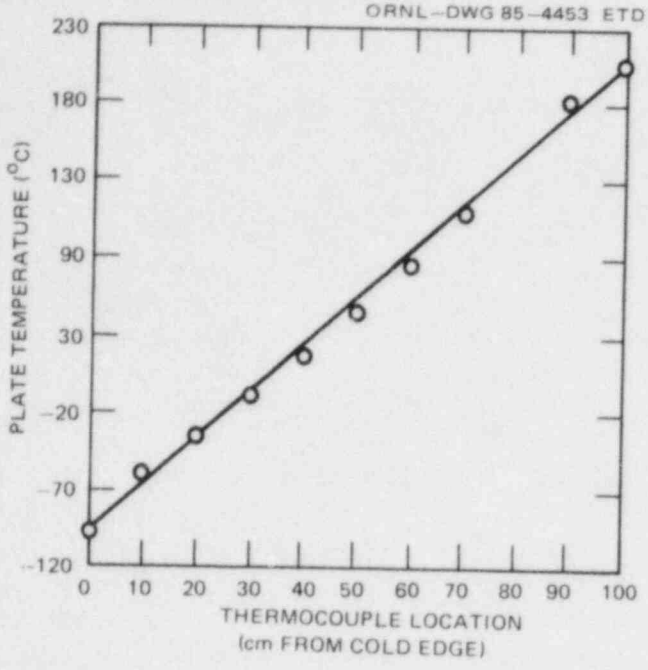

Fig. 5.11. Temperature gradient shortly before fracture of WP-1.2 (crack tip is at the 20 cm location).

5.2.3 Test instrumentation

Thermocouples were placed on WP-1.1 and WP-1.2 as shown in Figs. 5.12 and 5.13, respectively. While surface-mounted thermocouples were used in WP-1.1, small holes (1.5-mm diam and 3 mm deep) were drilled in WP-1.2, and thermocouples were inserted and potted in these. Additional thermocouples were used for control of heating and cooling, but these are not indicated. All thermocouple wires were connected to copper lead wires in an insulated junction box with the temperature monitored by a thermistor for room-temperature compensation. The thermocouple wires were sequentially monitored on a periodic basis and corrected for room temperature and the results recorded on magnetic tape. The results were also viewed on the computer screen that was collecting the data. This data collection system additionally monitored and recorded the load-cell output of the testing machine and the time.

Far-field strain gages were mounted on WP-1.1 and WP-1.2 as shown in Figs. 5.14 and 5.15, and near-field gage positions are shown in Figs. 5.16 and 5.17. In WP-1.1, all gages were 350-Ω constantan alloy gages on a polyimide backing and had a coefficient of expansion similar to that of steel. In WP-1.2, the line of gages near the crack path was changed to two-element 90° stacked rosettes of a nickel-chromium alloy grid whose gage factor temperature variation was less than that of constantan. The gages were connected to the bridges in a fashion to eliminate temperature effects. This approach meant that the crack-line gage outputs in WP-1.2 are proportional to the difference between the longitudinal and transverse strains.

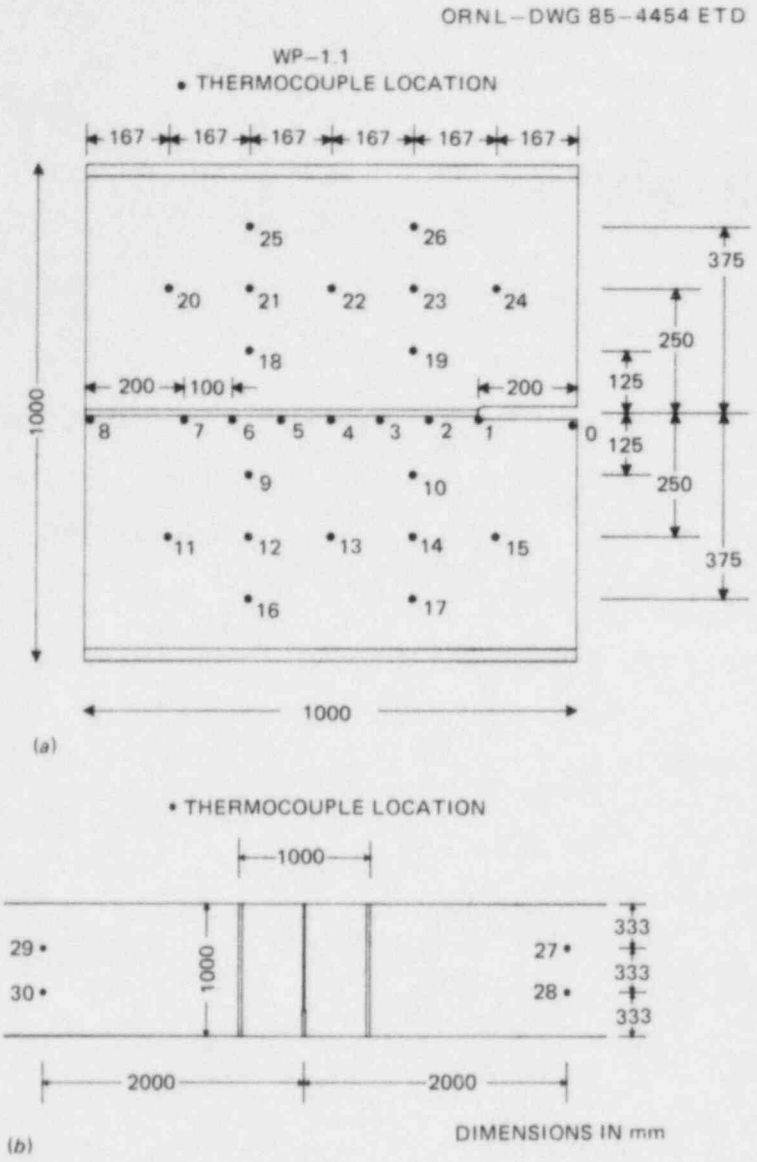

Fig. 3.12. Thermocouple locations on WP-1.1. (*a*) Thermocouple numbers and locations on test specimen, (*b*) far-field thermocouple numbers and locations on pull plates.

Strain gages were connected to low reactance bridges, the imbalances of which were amplified by wide-band differential amplifiers. Outputs from the amplifiers were then recorded on transient digital oscilloscopes for WP-1.1 and on a combination of oscilloscopes and a multichannel FM tape recorder for WP-1.2. Whenever transient oscilloscopes are used, a triggering signal is required. In the case of WP-1.1, this signal was provided by the crack breaking a conducting strip across the crack plane. In the case of WP-1.2, the trigger was provided by sending the output of the first crack-line strain gage to a conventional oscilloscope previously set to trigger off the expected pulse. The output of this oscilloscope was then used to trigger all the digital oscilloscopes. A device

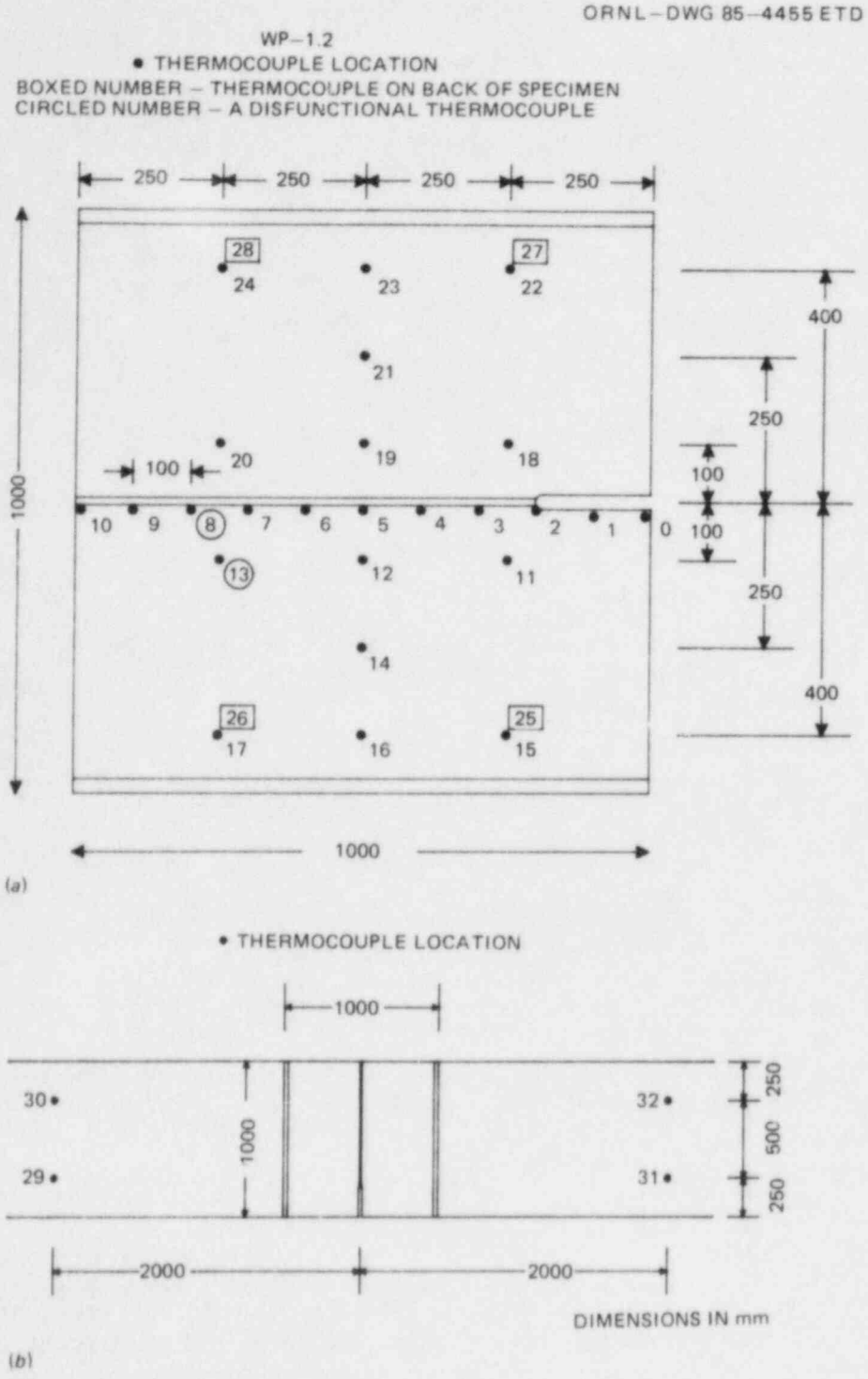

Fig. 5.13. Thermocouple locations on WP-1.2. (*a*) Thermocouple numbers and locations on test specimen, (*b*) far-field thermocouple numbers and locations on pull plates.

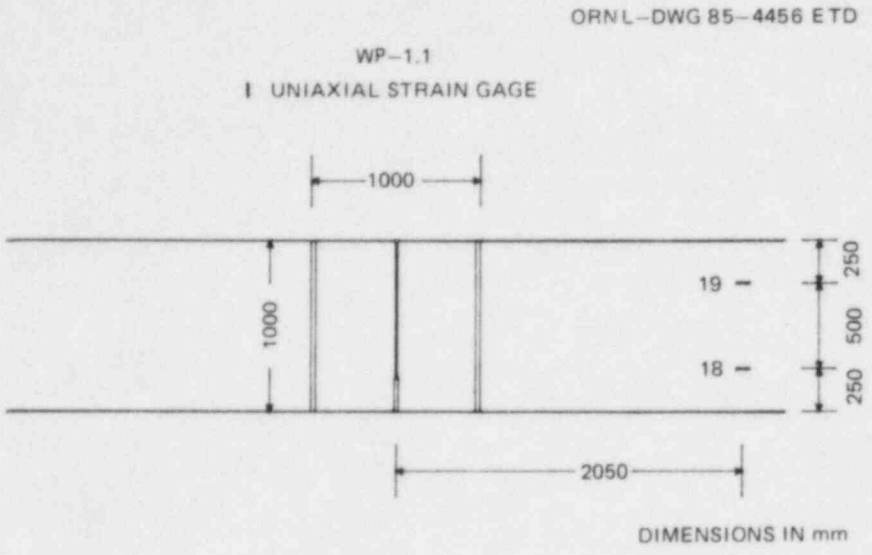

Fig. 5.14. Far-field strain-gage locations on WP-1.1.

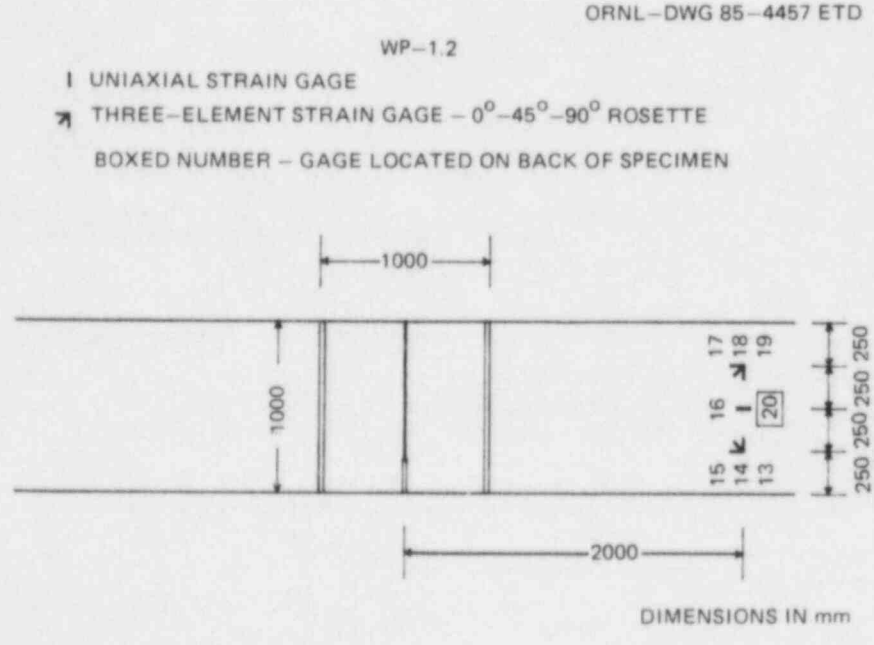

Fig. 5.15. Far-field strain-gage locations on WP-1.2.

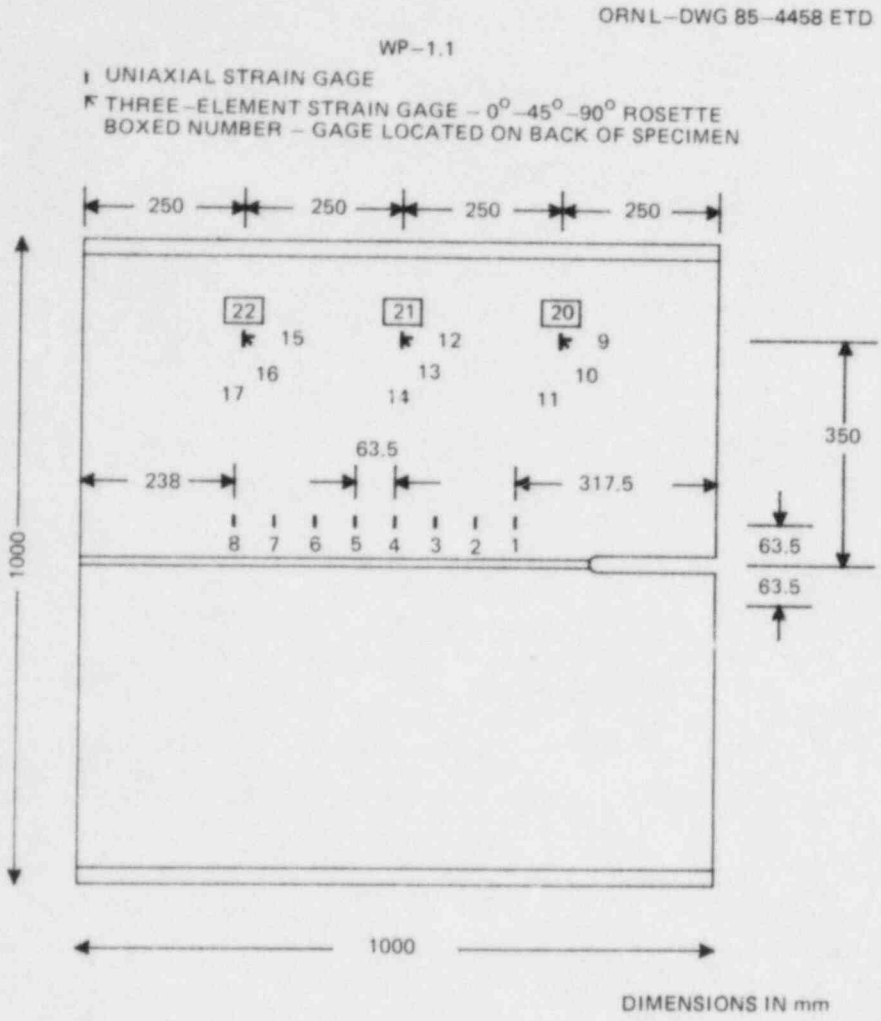

Fig. 5.16. Near-field strain-gage locations on WP-1.1.

was constructed to allow three back-up signals to also trigger the oscilloscopes, but this will not be covered here.

5.2.4 Data and fracture observations

Because of the large loads required to initiate crack propagation in these tests, both specimens were ruptured. Although the rupture appeared to the unaided eye and ear to be one event, the instruments and fracture surfaces revealed that arrest occurred and was quickly followed by reinitiation of the crack that led to complete rupture.

In the event of WP-1.1, all data recording devices were triggered by the conducting strip. However, it was discovered later that the strip broke many milliseconds after the arrest, due perhaps to the shear lip formation that occurs during reinitiation. As a result, the first 2 ms of the event were missed by the recorders. This, unfortunately, covers

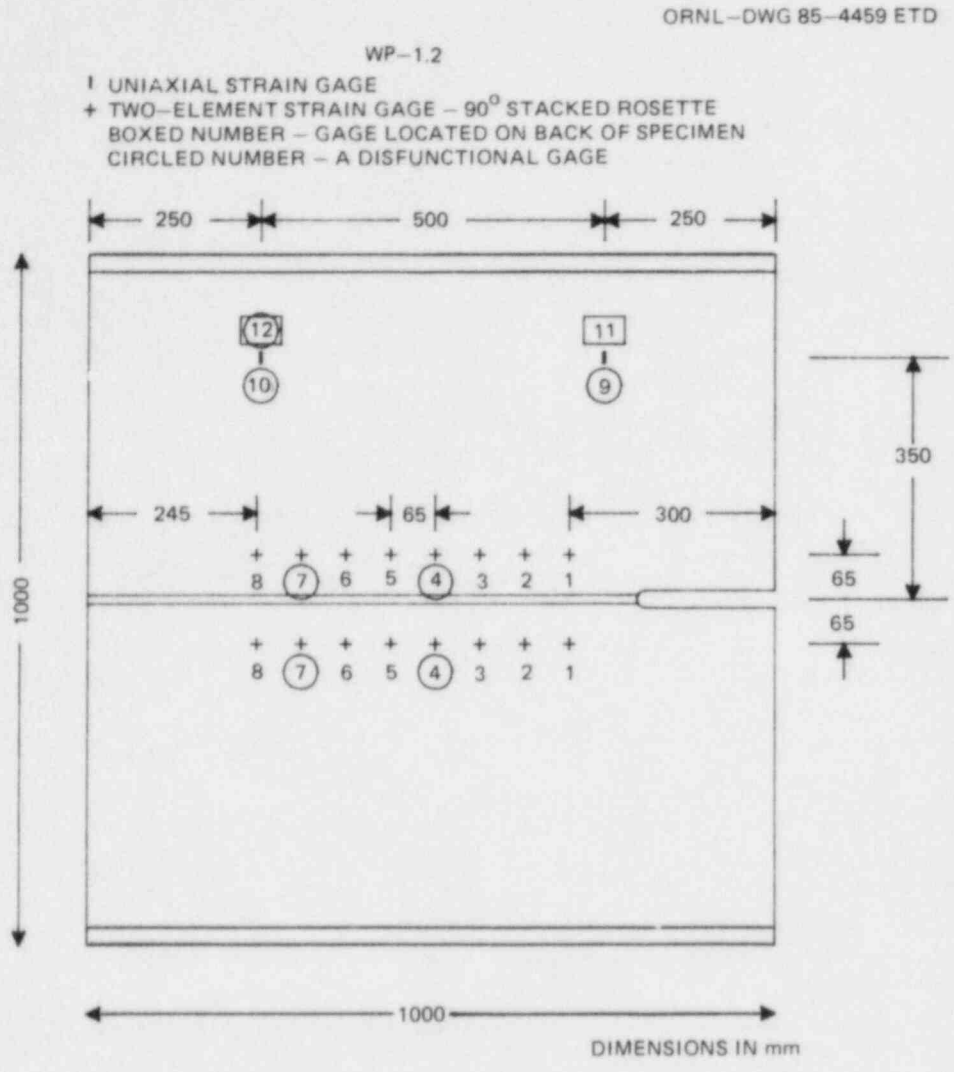

Fig. 5.17. Near-field strain-gage locations on WP-1.2.

the run-arrest event (as deduced from acoustic emission results). Nevertheless, records of the far-field gages during the reinitiation and tearing fracture of WP-1.1 are available. Furthermore, slow scans of all gages during WPS and temperature gradient development are also on hand. Analysis of these records is awaiting interpretation of the results of WP-1.2 and future wide-plate tests. In WP-1.1, an acoustic emission transducer located on a pull tab did record the entire event. Its output, shown in Fig. 5.18, indicates a burst of fracture (the run-arrest event) lasting about 2 ms followed by a quiescent period of 4 ms. This, in turn, is followed by additional acoustic activity that is indicative of tearing fracture. The time scale should be interpreted with caution because dispersion may have spread out the events in time. The actual events may have taken place in less time than is indicated. Based on the acoustic record and the fracture surface, the cleavage crack ran with an average speed of 138 m/s and the fibrous crack ran with an average velocity of 50 m/s.

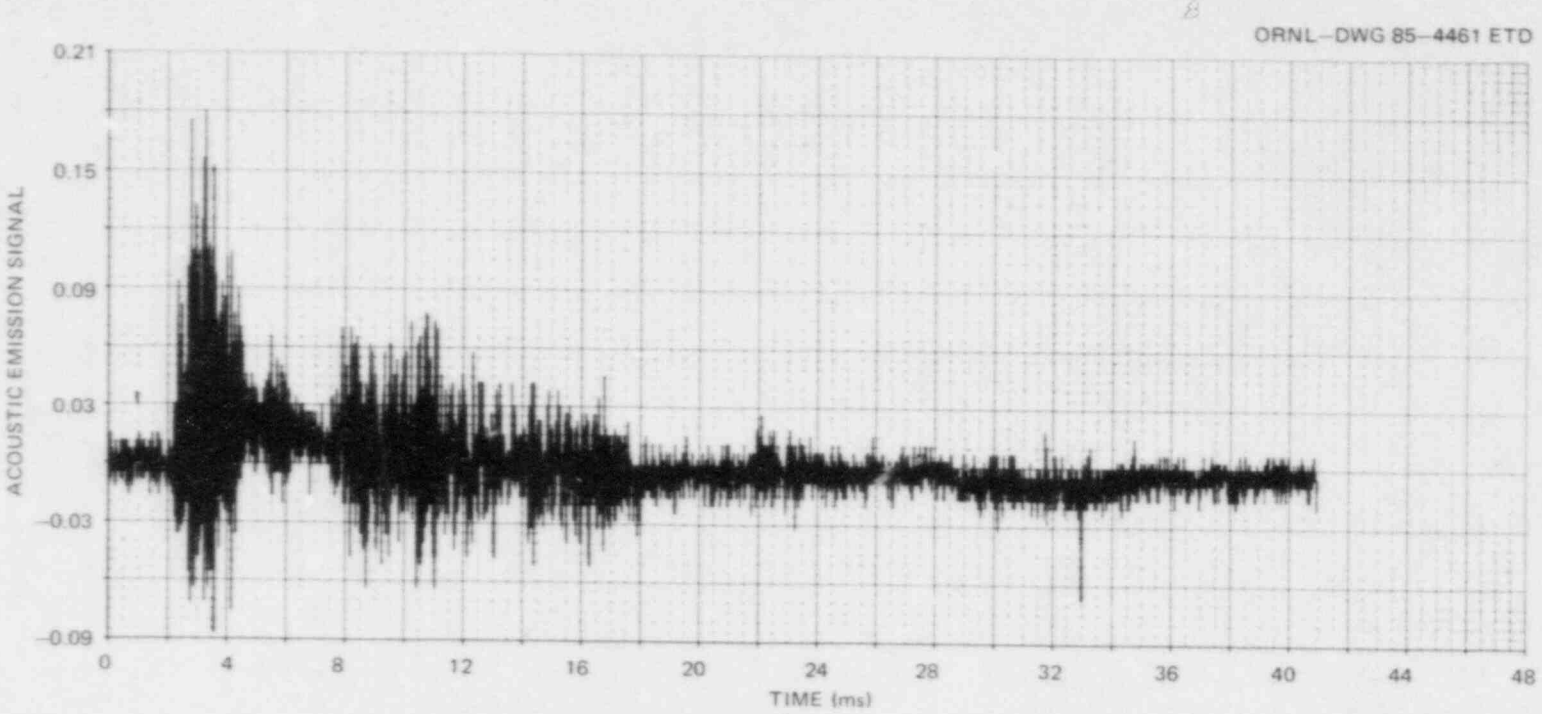

Fig. 5.18. Acoustic emission during fracture of WP-1.1.

In WP-1.2, triggering by the first crack-line strain gage was completely successful and, in addition, output of all instrumentation was continuously recorded on tape. The resolution of these recordings was extremely high and exceeded that obtained on the digital oscilloscopes. All the results reported below were taken from the magnetic tape record. Recordings of all the instrumentation outputs have been made during the temperature gradient development, the load up to fracture, and the fracture event itself. These include the outputs of the strain gages, load cell, timing strips, trigger, and a crack-mouth-opening-displacement (CMOD) gage located 175 mm from the cold edge. Again the timing strips were installed by Barns and Mincer of BCL, and the results were sent to them by NBS for analysis and interpretation (see Sect. 5.8.2). The data showed that the first timing strip broke at the same instant that the strain gages indicated that the crack had begun moving.

Figures 5.19 and 5.20 show the outputs of several crack-line and far-field strain gages during the fracture event. From these gages and from the fracture surface itself, the crack position as a function of time was estimated and is plotted in Fig. 5.21. Gage 8 (Fig. 5.20) suggests that there were two arrests or pauses in crack propagation. The interpretation of two arrests is supported by the CMOD measurements at a/w = 0.175 (Fig. 5.22). Two closely spaced plateaus appear in the CMOD, followed by continued opening until the amplifier saturates. Average measured crack velocities were determined from the crack-line gages and are shown in Table 5.2.

In addition to the results presented here, records of far-field gages were made. Of the 20 gages monitored, 5 did not function properly

Table 5.2. Average crack velocities determined (preliminary) from crack-line strain gages in test WP-1.2[a]

Average crack velocity (m/s)	Region of propagation	
	Gage span[b]	a/w span
786	Initial crack – gage 1	0.2–0.3
643	Gage 1 – gage 2	0.3–0.365
369	Gage 2 – gage 3	0.365–0.43
220	Gage 3 – 1st arrest	0.43–0.555
118	1st arrest – 2nd arrest	0.555–0.645
30	2nd arrest – rupture	0.645–1.0

[a]See Fig. 5.17 for illustration of gage locations.

[b]See Sect. 5.8.2 for preliminary velocity measurements made by BCL.

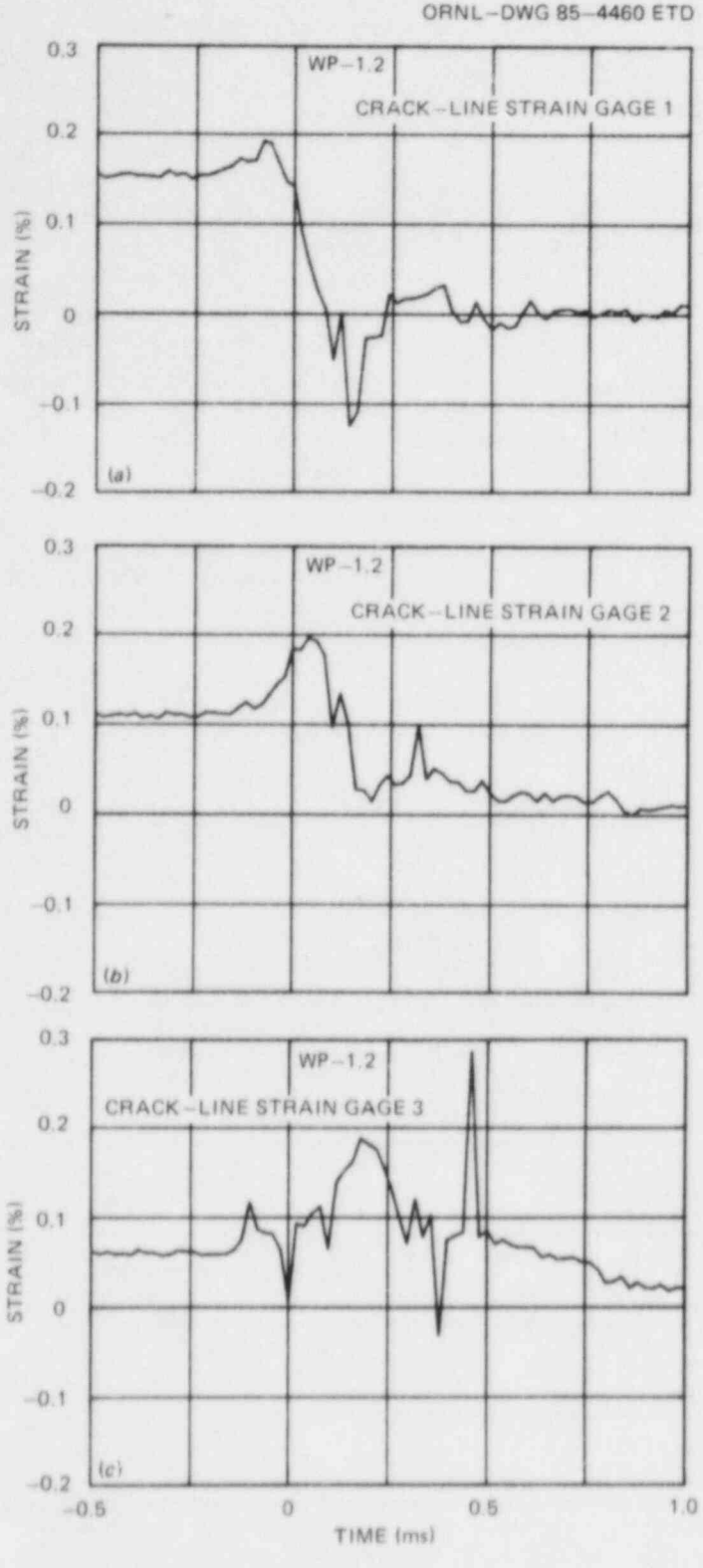

Fig. 5.19. Selected near-field strain-gage outputs during fracture of WP-1.2. (Zero time refers to trigger zero.)

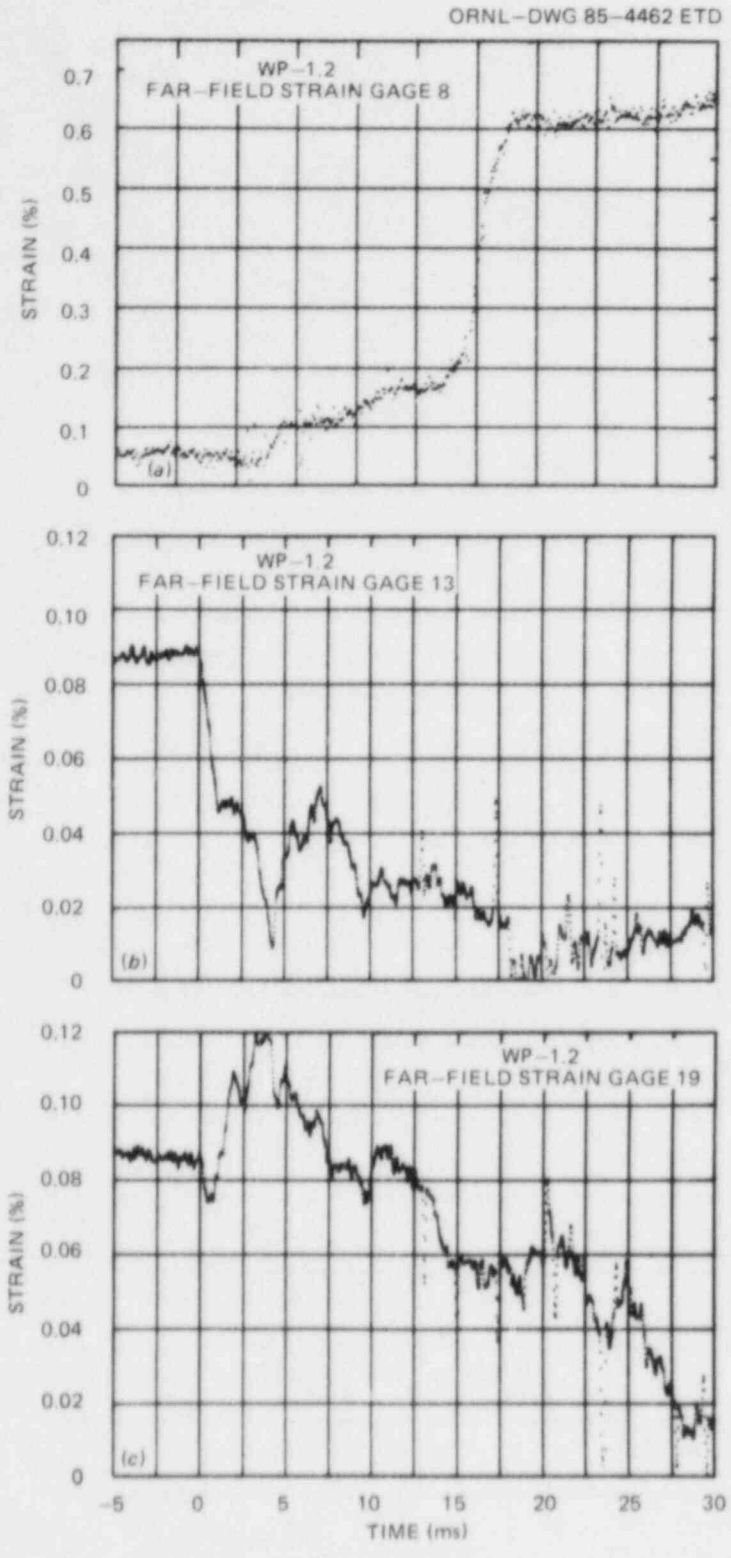

Fig. 5.20. Selected strain-gage outputs during fracture of WP-1.2. (Zero time refers to trigger zero.)

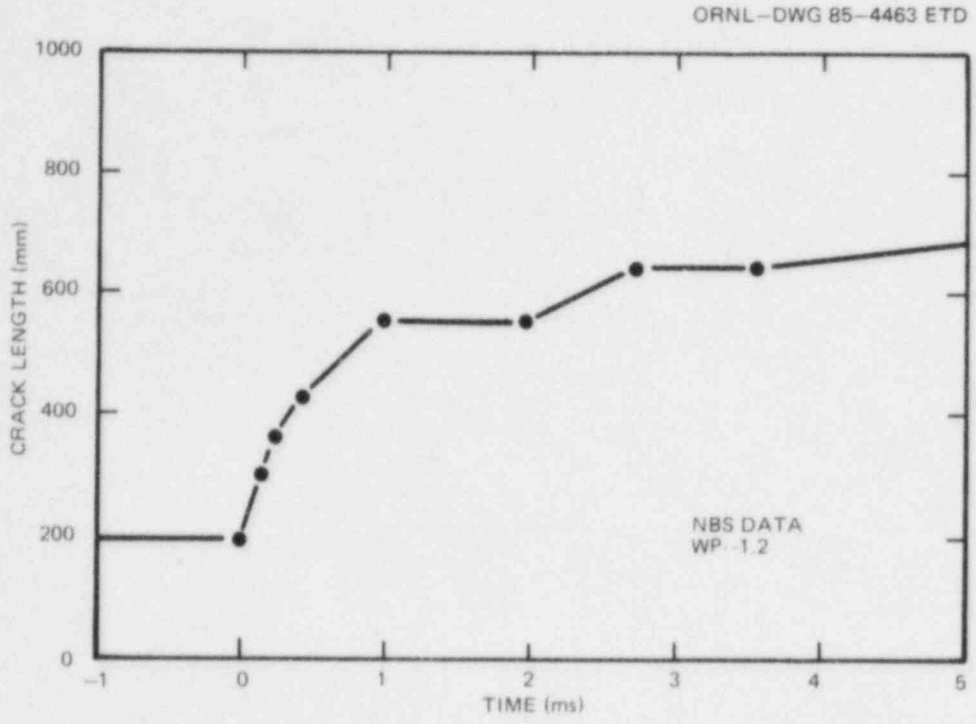

Fig. 5.21. Crack length vs time during fracture of WP-1.2.

during the test. This is believed to be due to shifting of insulation during the temperature gradient development and a consequent grounding of these gages to the plate. Efforts have been taken to ensure that this does not occur in future tests.

The fracture surfaces of WP-1.1 and WP-1.2 are shown in Fig. 5.23. The arrest positions determined from these surfaces are listed in Table 5.3 along with the temperatures determined for those locations. Microscopic examination, including scanning electron microscope replica fractography, indicates that the lighter regions of the fractures are predominantly cleavage. The darker portions are fibrous in character. We have assumed here that the end of a cleavage fracture region corresponds to an arrest point. While the preliminary data support this conclusion, no critical measurements or analyses unambiguously bear this out.

Finally, a great deal of plastic reduction in thickness was observed in the plates after fracture. This deformation has been measured as a function of transverse position on the plates and is shown in Figs. 5.24 and 5.25.

In summary, testing of the first two wide-plate tests has been completed, with initiation loads that correspond to higher than expected stress-intensity factors. The reason for this behavior is not yet known. Nevertheless, these high crack starting loads have led to significant run-arrest events that have been monitored with a wide variety of instrumentation. Crack velocities up to 750 m/s have been recorded as a function of crack length and applied load. Crack-arrest temperatures from 51 to 92°C have been observed. The most significant results are presented in this progress report without details. Because of the large quantity

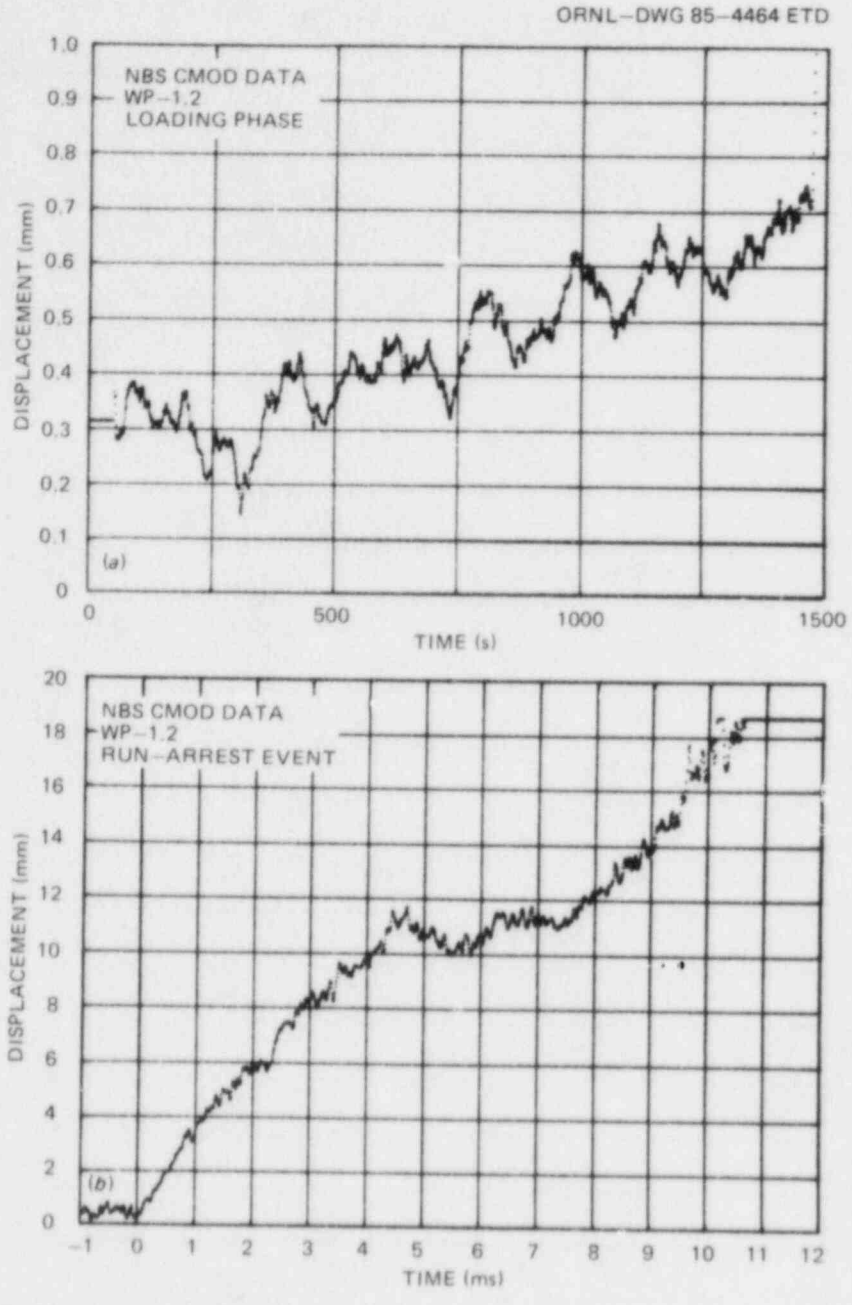

Fig. 5.22. Crack-mouth-opening displacement measured at a/w = 0.175 during (*a*) load up and (*b*) fracture of WP-1.2.

of data collected from these tests, most pertinent details will be published in a topical report by the Bureau of Standards.

5.2.5. Fracture tests of beams

Previous bend-bar tests[4] had suggested that the WPS procedure employed in WP-1.1 would initiate fracture at 1 to 1.25 times the WPS load

ORNL–PHOTO 1962–85

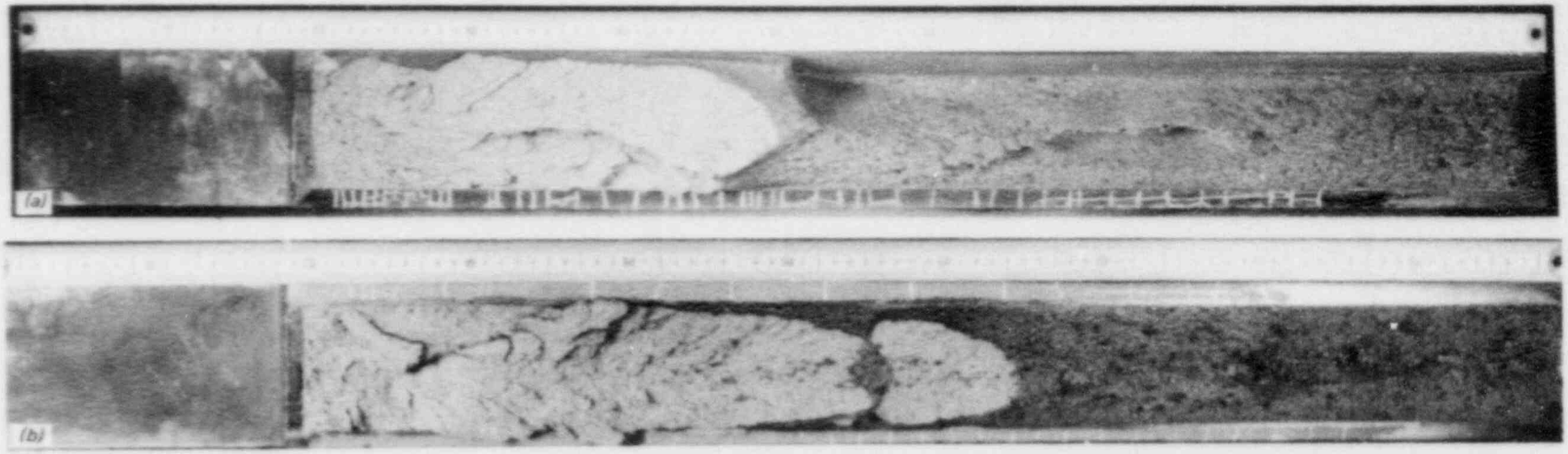

Fig. 5.23. Fracture surfaces of (*a*) WP-1.1 and (*b*) WP-1.2. Notch and precrack are on the left-hand side. Cleavage fracture appears light while fibrous fracture is dark. Arrest points occur at the end of the cleavage fractures.

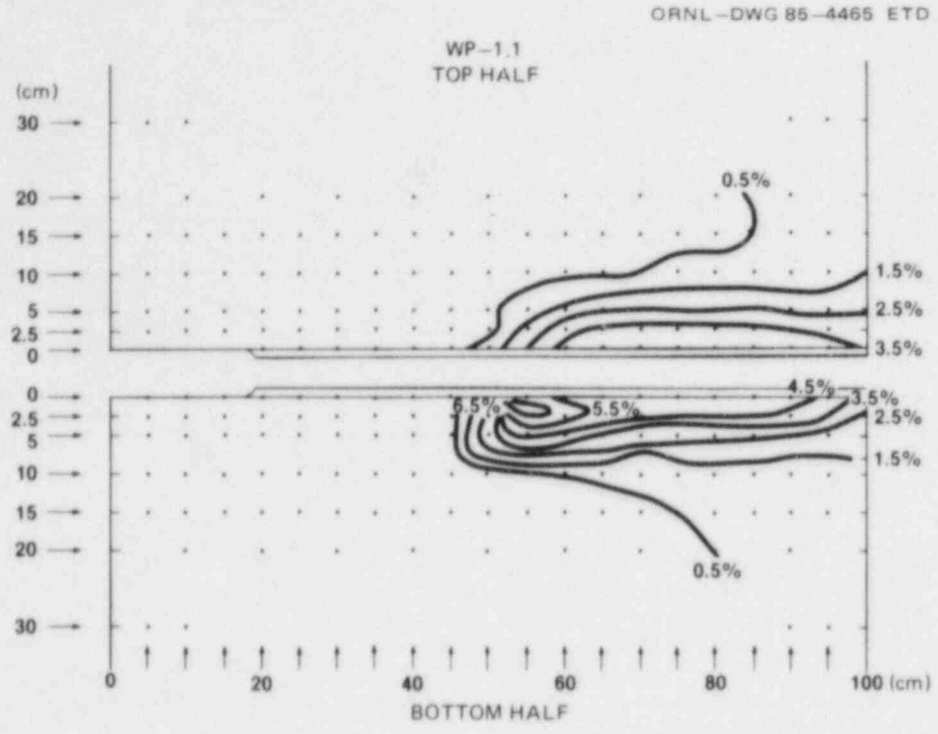

Fig. 5.24. Contour map of plastic reduction in thickness for WP-1.1.

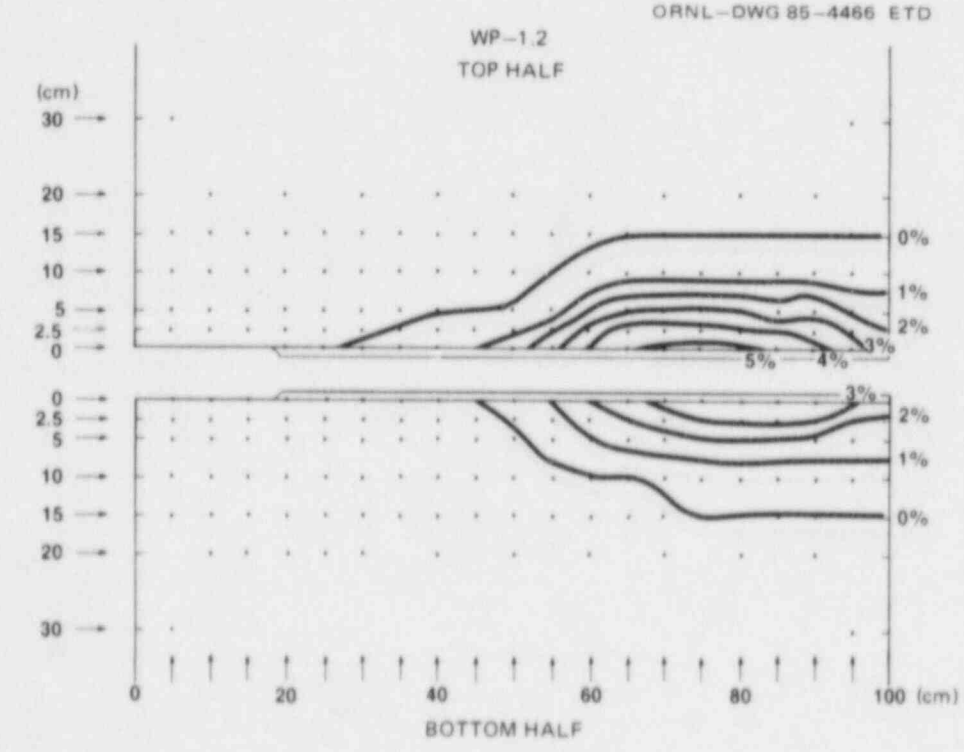

Fig. 5.25. Contour map of plastic reduction in thickness for WP-1.2.

Table 5.3. Arrest locations and temperatures for wide-plate crack-arrest tests

Specimen No.	Arrest position		Arrest temperature (°C)
	mm	a/w	
WP-1.1	500	0.502	51
WP-1.2	555	0.556	62
WP-1.2	645	0.646	92

(50 to 100% above K_{Ic}). As a consequence of the unexpectedly high initiating load for WP-1.1 (2 times the WPS load), a bend bar was tested under conditions that simulated the loading rate and hold times of WP-1.1. This bar fractured 25% above the WPS load. The results of this test (BB-1.4) were almost identical to those for test BB-1.2 reported earlier.[4] From these tests, it was concluded that loading rates and hold times were not the cause of the high load at initiation in WP-1.1. Another WPS procedure was agreed on at a meeting of the various researchers in the HSST Program. This procedure involved complete unloading of the bend bar to sharpen the crack after WPS at 70°C. The specimen was then cooled slowly to −50°C and loaded to fracture. This procedure was used with BB-1.5 and fracture occurred at 135% of the WPS load. In light of these and previous results, it was decided to test WP-1.2 without WPS.

5.3 Properties of Wide-Plate Crack-Arrest Test Material

5.3.1 Tensile properties (J. J. McGowan, R. W. Swindeman, C. E. Pugh, B. R. Bass)

The initial series of wide-plate crack-arrest specimens is taken from HSST plate 13A of A 533 grade B class 1 steel that is in a quenched and tempered condition. The specimens are taken from the central portion of the 18.73-cm-thick plate. Properties of the plate material include Young's modulus $E = 206.9$ GPa, Poisson's ratio $\nu = 0.3$, thermal expansion coefficient $\alpha = 11 \times 10^{-6}/°C$, and density $\rho = 7850$ kg/m^3. Multilinear representations of stress-strain curves for this material, with temperature as a parameter, are shown in Fig. 5.26. The temperature-dependent yield stress in these representations is given by the function

$$\sigma_y = 374.866 + 59.894\ e^{-0.0079328T}\ , \qquad (5.1)$$

where σ_y and T have units in megapascals and degrees Celsius, respectively. The stress-plastic-strain modulus $H'(T)$ as a function of temperature is given in Table 5.4.

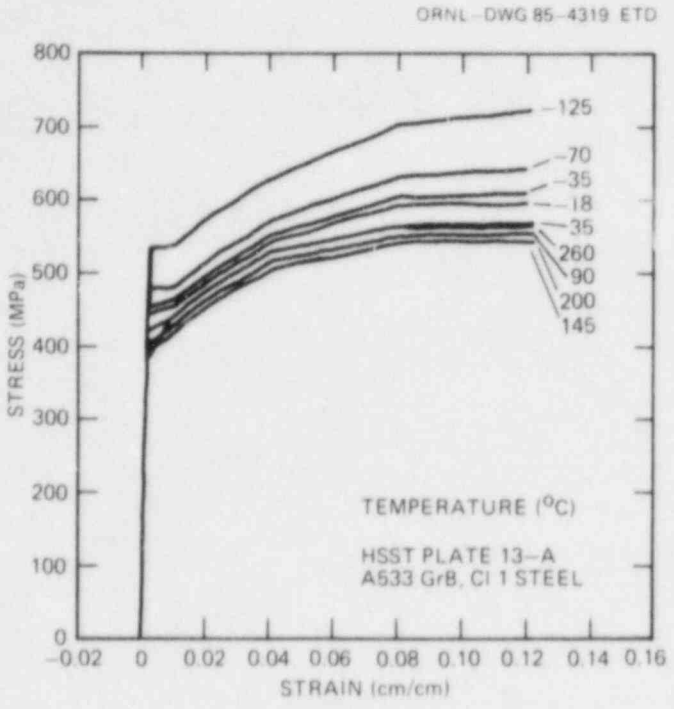

Fig. 5.26. Multilinear representations of uniaxial stress-strain behavior of HSST plate 13A of A 533 grade B class 1 steel.

Table 5.4. Stress-plastic-strain modulus H′ for HSST wide-plate material (HSST plate 13A of A 533 grade B class 1 steel)

Plastic strain interval (%)	Temperature interval (°C)	$H' = \Delta\sigma/\Delta E^P$ (MPa/%)
≤1	$-125.00 < T < -72.78$	0.345
	$-72.78 \leq T < 37.78$	16.044 + 0.214 T
	$37.78 \leq T < 148.89$	21.787 + 0.062 T
	$148.89 \leq T < 260.00$	−24.407 + 0.372 T
1–2	$-125.00 < T < 260.00$	37.23
2–4	$-125.00 < T < 260.00$	26.579 − 0.00776 T
4–8	$-125.00 < T < 37.78$	11.228 − 0.0599 T
	$37.78 \leq T < 260.00$	8.96
8–12	$-125.00 < T < -17.78$	−0.0276 − 0.0403 T
	$-17.78 \leq T < 260.00$	0.689

5.3.2 Fracture properties (J. J. McGowan and C. E. Pugh)

Fracture-toughness relations for crack initiation and arrest have been developed on the basis of small-specimen data and are given as follows:

$$K_{Ic} = 51.276 + 51.897\, e^{0.036\,(T-RT_{NDT})}\,, \tag{5.2}$$

$$K_{Ia} = 49.957 + 16.878\, e^{0.028738\,(T-RT_{NDT})}\,. \tag{5.3}$$

Units for K and T are megapascals times root meter and degrees Celsius, respectively. For the wide-plate material, $RT_{NDT} = -23°C$. Figure 5.27 compares the K_{Ia} function given in Eq. (5.3) with small-specimen data obtained for this material by BCL.[5] Charpy V-notch results are given in Fig. 5.28 for specimens taken from the middle (1/2 T) of HSST plate 13A (Ref. 6).

A dynamic fracture-toughness relation for the plate material is written as

$$K_{ID} = K_{Ia} + A\,(T)\,\dot{a}^2\,, \tag{5.4}$$

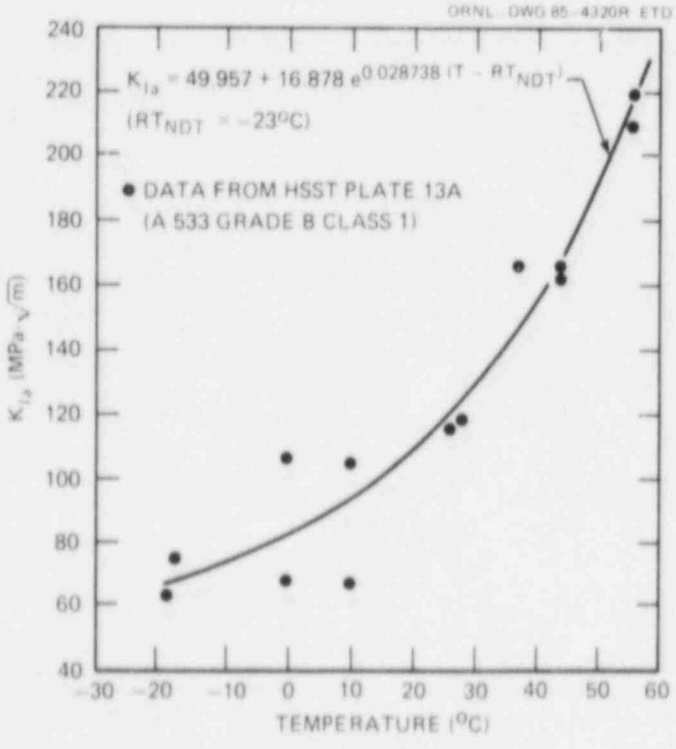

Fig. 5.27. Least-squares fit for laboratory specimens of K_{Ia} vs temperature data for HSST plate 13A of A 533 grade B class 1 steel. (Data obtained by Battelle Columbus Laboratories.[6])

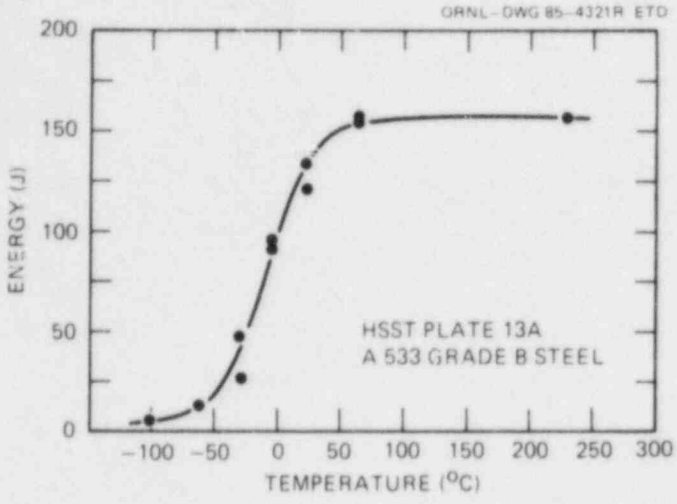

Fig. 5.28. Charpy V-notch data for HSST plate 13A of A 533 grade B class 1 steel. (Specimens taken from middle thickness of original plate.)

where K_{Ia} is given by Eq. (5.3). For

$$T - RT_{NDT} > -13.9°C \ , \tag{5.5}$$

$$A(T) = [329.7 + 16.25\ (T - RT_{NDT})] \times 10^{-6}, \ (MPa \cdot s^2 \cdot m^{-3/2})$$

and for

$$T - RT_{NDT} \leq -13.9°C \ , \tag{5.6}$$

$$A(T) = [121.71 + 1.2962\ (T - RT_{NDT})] \times 10^{-6}, \ (MPa \cdot s^2 \cdot m^{-3/2}) \ .$$

Units for K_{ID}, $\dot{a}$, and T are $MPa \cdot \sqrt{m}$, m/s, and degrees Celsius, respectively. The form of the K_{ID} expression in Eq. (5.4) and relations for A(T) [Eqs. (5.5) and (5.6)] are derived from Ref. 7 by estimating that $RT_{NDT} = -6.1°C$ for the material used in that study. Much of the data used in Ref. 7 are presented in Ref. 8.

The fracture-toughness properties of HSST Plate 13A were determined at ORNL using 25.4- and 50.8-mm compact specimens (1T-CS and 2T-CS, respectively) modified for load-line displacement measurement. The single-specimen unloading compliance technique was used to measure crack growth during testing. A Hewlett-Packard 9836 desk-top computer was used to control the test and acquire data. The specimens were loaded under load-line displacement control at a rate of 0.2 mm/min. When applicable, K_{Ic} was determined according to ASTM E399 (Ref. 9). Otherwise, the modified

Ernst J-integral[10] was used to infer K_{Ic} values from the following relation.

$$KJ_c = \sqrt{EJ_c} , \tag{5.7}$$

where

$$E(GPa) = 207.2 - 0.057T\ (°C). \tag{5.8}$$

A plasticity correction ("beta-correction") was determined from the K_J value at cleavage using the Merkle method.[11] A summary of the fracture-mechanics tests is provided in Table 5.5. To judge the inherent material variability, upper and lower bounds (two standard deviations from the mean) are shown with the measured data in Figs. 5.29 and 5.30 for the fracture toughness, beta-corrected fracture toughness, and the average tearing modulus. The variation in fracture toughness in the transition region is quite substantial, with one standard deviation near 35 MPa$\cdot\sqrt{m}$. The variation in the beta-corrected toughness values is somewhat less, with one standard deviation near 20 MPa$\cdot\sqrt{m}$. The tearing modulus values also show a moderate variation, with the standard deviation near 30. The upper-shelf fracture toughness shows a characteristically small amount of variation.

5.4 Wide-Plate Analyses at ORNL

B. R. Bass H. K. Stamm*
C. E. Pugh J. G. Merkle

5.4.1 Posttest analyses of WP-1.1

Following completion of wide-plate test WP-1.1, a posttest elastodynamic finite-element analysis was performed with the ORNL version of the SWIDAC code. Results from this analysis give a time history of crack depth, crack velocity, and stress-intensity factor as determined from loading conditions and material properties. These calculations also include a time history of the strain tensor components at selected points that are near strain-gage positions on the plate assembly.

From symmetry conditions, one-half of the complete pull-plate assembly was modeled using 620 nodes and 180 eight-noded isoparametric elements (Fig. 5.31) in the finite-element representation. A total of 23 spring elements were included in the plane of the crack to be released during crack-tip propagation. Prior to performance of the dynamic analysis, a static two-dimensional (2-D) plane-stress thermoelastic analysis

*On assignment through January 1985 to the ORNL HSST Program from the Institute für Reaktorbauelemente Kernforschungszentrum Karlsruhe, FRG.

Table 5.5. Fracture-tou

Specimen	Test temperature (°C)	Thickness (mm)	Side grooves (%)	(a/w_i)	Ductile Δa (mm)	J_{max} (kJ/m^2)
K33A	−150	50.8	0	0.554	<0.02	9.2
K33B	−150	50.8	0	0.555	<0.2	15.8
K34A	−75	50.8	0	0.556	0.071	97.5
K34B	−18	50.8	0	0.562	0.366	242.7
K35A	−150	50.8	0	0.555	<0.02	10.2
K35B	−150	50.8	0	0.543	<0.02	7.5
K41B	−18	50.8	0	0.563	0.221	195.9
K42B	−75	50.8	0	0.563	<0.02	49.1
K51A	−18	25.4	0	0.573	1.049	501.1
K51C	−75	25.4	0	0.554	<0.02	14.4
K51D	−18	25.4	0	0.570	0.157	136.4
K52B	−75	25.4	0	0.576	<0.02	26.3
K52D	24	25.4	20	0.569	0.875	298.2
K52F	24	25.4	0	0.567	2.66	506.7
K53B	−50	25.4	0	0.574	0.053	73.1
K53E	−18	25.4	0	0.562	0.196	177.6
K53F	−18	25.4	0	0.572	0.064	64.5
K54A	−75	25.4	0	0.573	<0.02	74.1
K54C	−50	25.4	0	0.566	0.051	75.9
K54D	24	25.4	0	0.567	3.180	473.1
K54E	−18	25.4	0	0.567	0.069	83.1
K54F	−18	25.4	0	0.568	1.122	124.4
K51E	121	25.4	20	0.568	2.139	NA
K51F	50	25.4	20	0.592	2.720	NA
K52C	24	25.4	20	0.564	2.037	NA
K52E	50	25.4	20	0.577	2.827	NA
K53A	24	25.4	20	0.569	2.101	NA
K53C	121	25.4	20	0.563	2.852	NA
K53D	50	25.4	20	0.564	3.033	NA
K54B	121	25.4	20	0.575	2.461	NA

[a] NA = not applicable.

[b] J_{Ic} used to calculate K_{Jc}; otherwise J_{max} load used.

[c] NM = not measured.

ghness results for wide-plate specimens

J_{Ic} (kJ/m^2)	J_{cleave} (kJ/m^2)	K_{Jc} (MPa$\cdot\sqrt{m}$)	$K_{J_{cleave}}$ (MPa$\cdot\sqrt{m}$)	Beta-corrected $K_{J_{cleave}}$ (MPa$\cdot\sqrt{m}$)	T_{av}	Cleave	Comments
NA[a]	9.2	44.6	44.6	44.2	NA	Yes	K_{Ic} = 47.1 MPa$\cdot\sqrt{m}$
NA	15.8	58.4	58.4	57.0	NA	Yes	K_{Ic} = 57.1 MPa$\cdot\sqrt{m}$
NA	97.5	143.6[b]	143.6	102.7	NA	Yes	
199.6	242.7	203.8[b]	224.8	119.9	NA	Yes	
NA	10.1	46.7	46.7	46.2	NA	Yes	K_{Ic} = 44.8 MPa$\cdot\sqrt{m}$
NA	7.5	40.2	40.2	40.0	NA	Yes	K_{Ic} = 40.8 MPa$\cdot\sqrt{m}$
NA	195.9	202.0	202.0	114.7	NA	Yes	
NA	49.1	101.9	101.9	84.8	NA	Yes	
NM[c]	501.1	NM	321.9	110.4	NA	Yes	
NA	14.4	55.2	55.2	50.7	NA	Yes	
NA	136.4	168.0	168.0	86.2	NA	Yes	
NA	26.3	74.6[b]	74.6	62.5	NA	Yes	
266.2	298.2	234.1[b]	247.7	96.5	NA	Yes	
NM	929.9	NM	437.5	119.9	NA	Yes	
NA	73.1	122.9	122.9	78.0	NA	Yes	
NA	177.6	192.3	192.3	91.5	NA	Yes	
NA	64.5	115.9	115.9	74.0	NA	Yes	
NA	74.1	125.2	125.2	82.6	NA	Yes	
NA	75.9	125.3	125.3	78.7	NA	Yes	
NM	906.4	NM	431.9	119.4	NA	Yes	
NA	83.1	131.1	131.1	77.7	NA	Yes	
NA	124.4	160.9	160.9	85.2	NA	Yes	
219.0	NA	209.5[b]	NA	NA	133.1	No	
276.4	NA	237.6[b]	NA	NA	166.1	No	
191.4	NA	198.5[a]	NA	NA	138.3	No	
263.2	NA	231.9[b]	NA	NA	187.6	No	
266.2	NA	234.1[b]	NA	NA	151.5	No	
203.2	NA	201.7[b]	NA	NA	92.2	No	
249.6	NA	225.9[b]	NA	NA	120.2	No	
225.5	NA	212.5[b]	NA	NA	136.4	No	

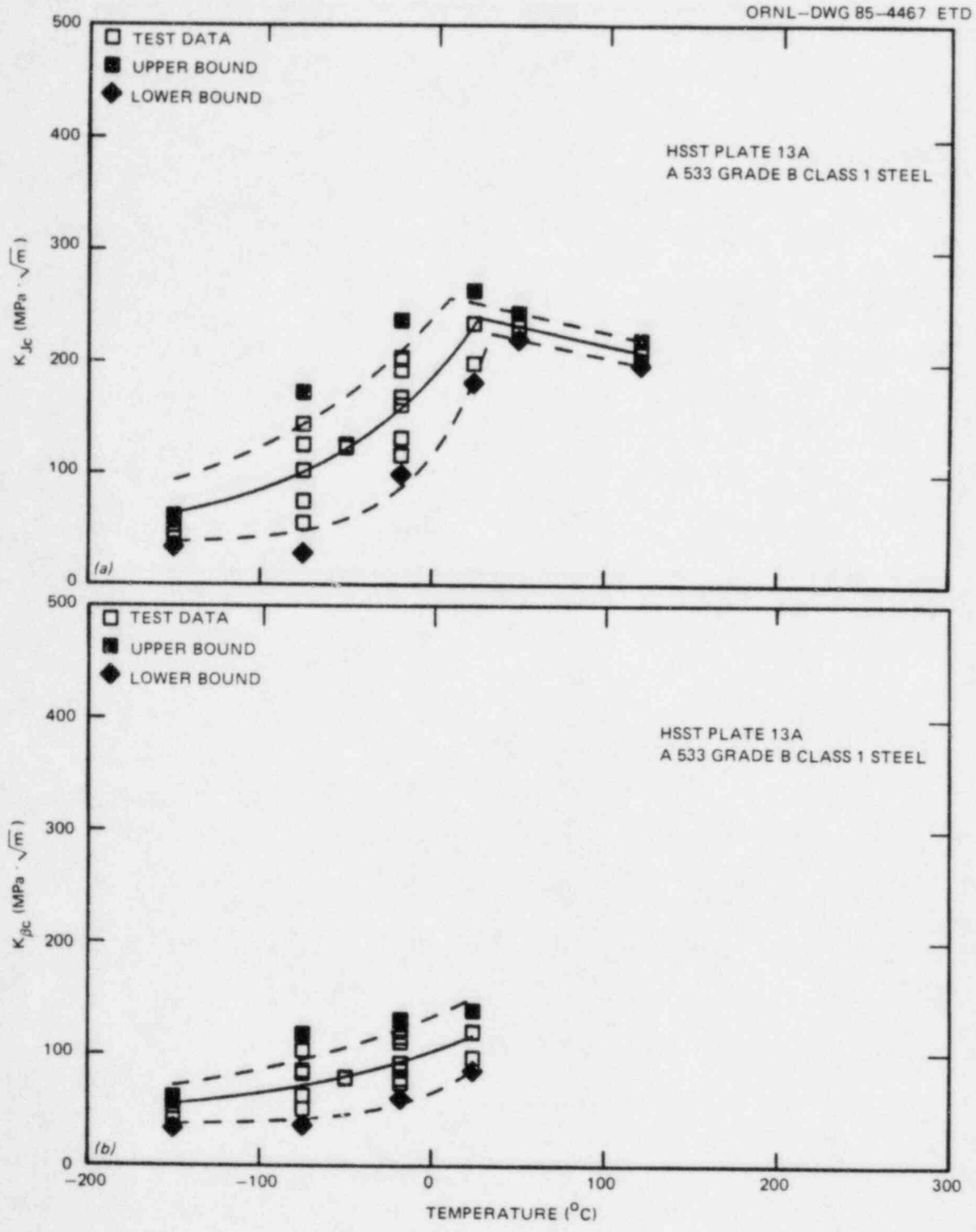

Fig. 5.29 (*a*) Fracture toughness for HSST plate 13A showing upper and lower bounds and (*b*) beta-corrected fracture toughness for HSST plate 13A showing upper and lower bounds (two standard deviations from the mean).

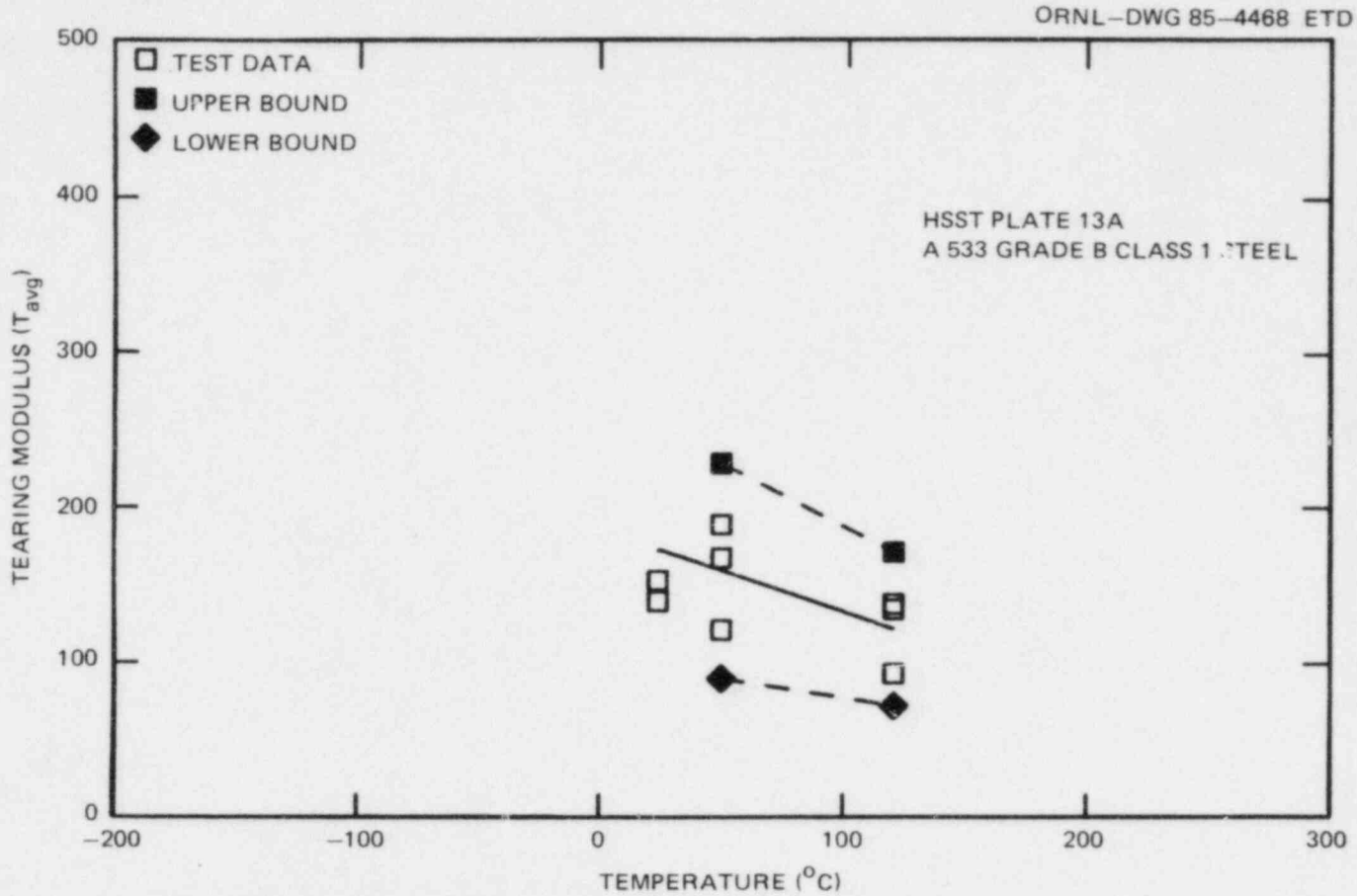

Fig. 5.30. Tearing modulus for HSST plate 13A showing upper and lower bounds (two standard deviations from the mean).

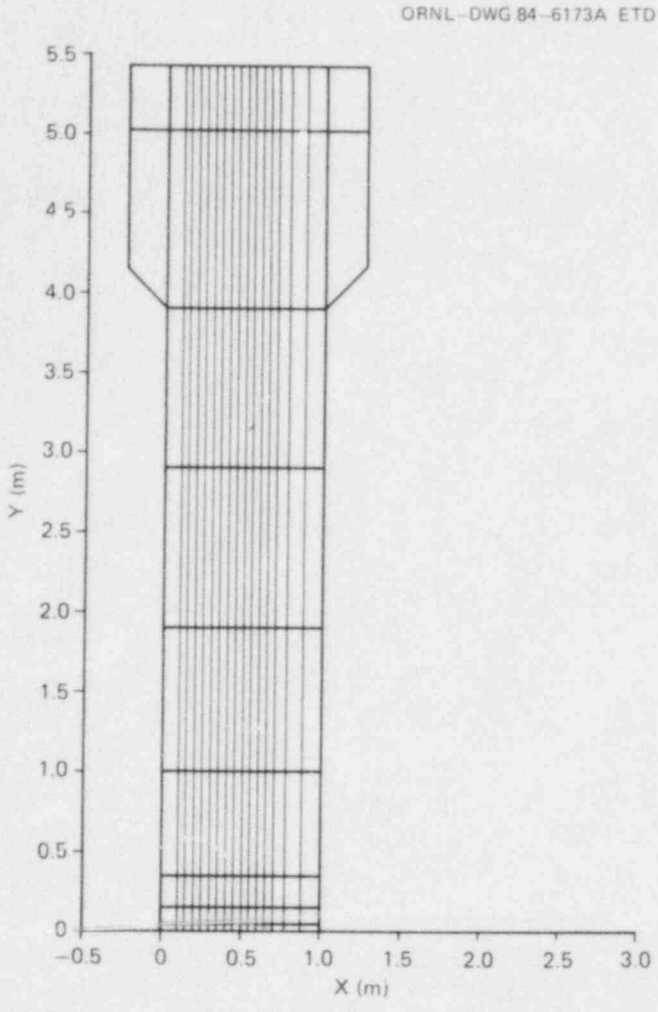

Fig. 5.31. Finite-element model for dynamic analyses for wide-plate crack-arrest tests WP-1.1 and WP-1.2.

was performed with the ADINAT/ADINA (Ref. 12) finite-element codes to determine the deformation of the plate assembly due to the imposed thermal gradient. Material properties used in both the static and dynamic analyses were given in Sect. 5.3. The boundary conditions of the analysis assumed that the heated and cooled edges of the plate were fixed at T_H = 200°C and T_C = −118.75°C, respectively, along a 2.4-m length (centered relative to the crack plane) and that the pull-tab edges were prescribed to be T = 20°C. The edge boundary condition T_C = −118.75°C was selected to yield a linear approximation to the measured temperatures (shown in Fig. 5.10) such that the linear distribution agrees with measured data at the crack tip and at the heated edge. The remaining surfaces of the assembly were assumed to be insulated. The thermal deformations computed from this analysis were superimposed on the SWIDAC finite-element model to account for the thermal bending effects in the dynamic analysis. Calculations of stress-intensity factors indicated that the load line eccentricity introduced by thermal bending of the pull-plate assembly caused an elevation of ~10%.

The thermally deformed pull-plate assembly was analyzed dynamically with SWIDAC (Ref. 13) neglecting thermal stresses (i.e., the thermal expansion coefficient was set to zero). Furthermore, the effects of 25% side grooving were accounted for by adjusting the stress-intensity factor $\overline{K}_I$ (computed from the J-integral) according to the relation $K_I = \sqrt{4/3}\,\overline{K}_I$. In the first step of the SWIDAC analysis, the measured fracture load of P = 20.1 MN was applied as a point load (at the top of the pin hole) in a static analysis to determine the corresponding load-point displacement $U_{LL} = 0.546 \times 10^{-2}$ m and the initiation $K_o = 268$ MPa$\cdot\sqrt{m}$. In the second step, the elastodynamic analysis was carried out with the load point fixed at the displacement obtained from the static analysis. The dynamic analysis utilized the unconditionally stable Newmark-Beta time integration scheme,[14] with the time step fixed at $\Delta t = 6$ μs. Propagation of the crack was modeled according to the relation $K = K_{ID}(T,\dot{a})$, where K is the adjusted dynamically computed stress-intensity factor and K_{ID} is the postulated dynamic fracture-toughness relation given by Eqs. (5.4)–(5.6). For purposes of evaluating K_{ID} at the crack tip, the dynamic analysis utilized the temperature profile of Fig. 5.10, which was measured in the test just before the crack run-arrest event.

Figures 5.32–5.34 show the results from the SWIDAC dynamic posttest analysis in comparison with similar pretest analyses that assumed a fracture load of 10.65 MN. The plot of crack-depth ratio vs time (Fig. 5.32)

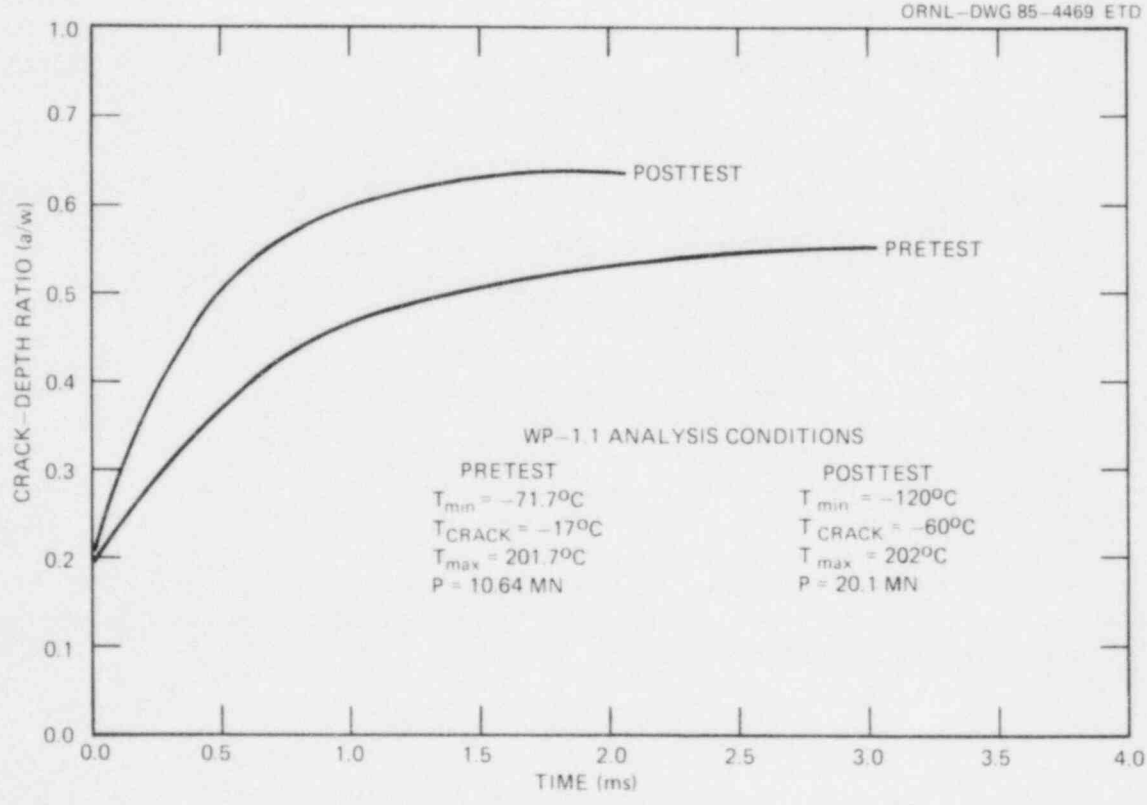

Fig. 5.32. Crack depth vs time for wide-plate crack-arrest test WP-1.1.

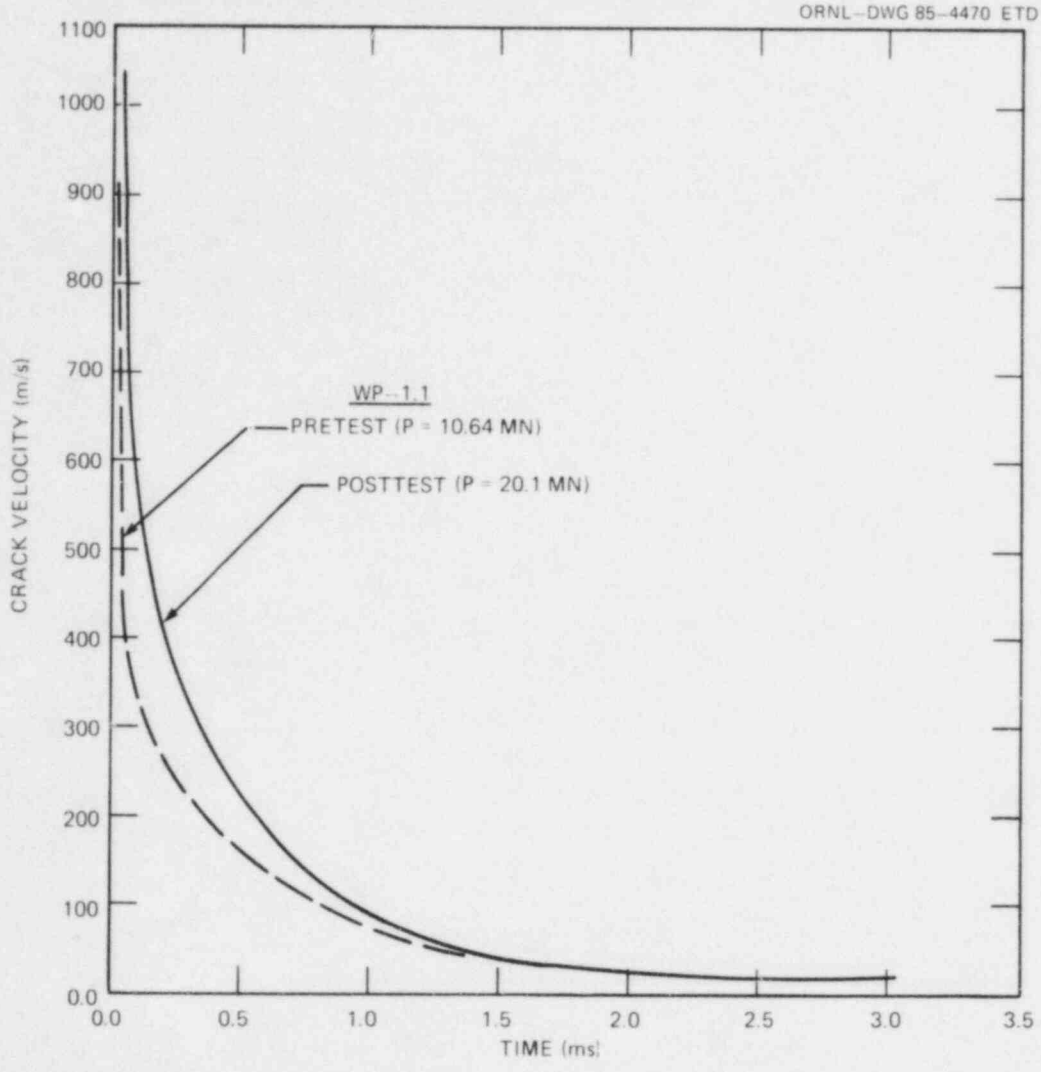

Fig. 5.33. Predicted crack velocity vs time for WP-1.1.

indicates crack arrest at (a/w) = 0.64 at time t = 1.3 ms. Figures 5.33 and 5.34 show calculated crack velocity and stress-intensity factor variations with crack propagation.

Table 5.2 shows that arrest was observed to occur at a/w = 0.5 in comparison with the predicted a/w = 0.64. Some factors that may contribute to this difference are (1) the crack ran out of the side-grooved plane as can be seen in Fig. 5.25, (2) the crack experienced considerable branching prior to arrest, and (3) a dynamic-toughness correlation has not been developed specifically for this material.

5.4.2 Analyses of WP-1.2

5.4.2.1 Analysis techniques. Analyses of WP-1.2 have also been carried out using both quasi-static and elastodynamic techniques. A 2-D

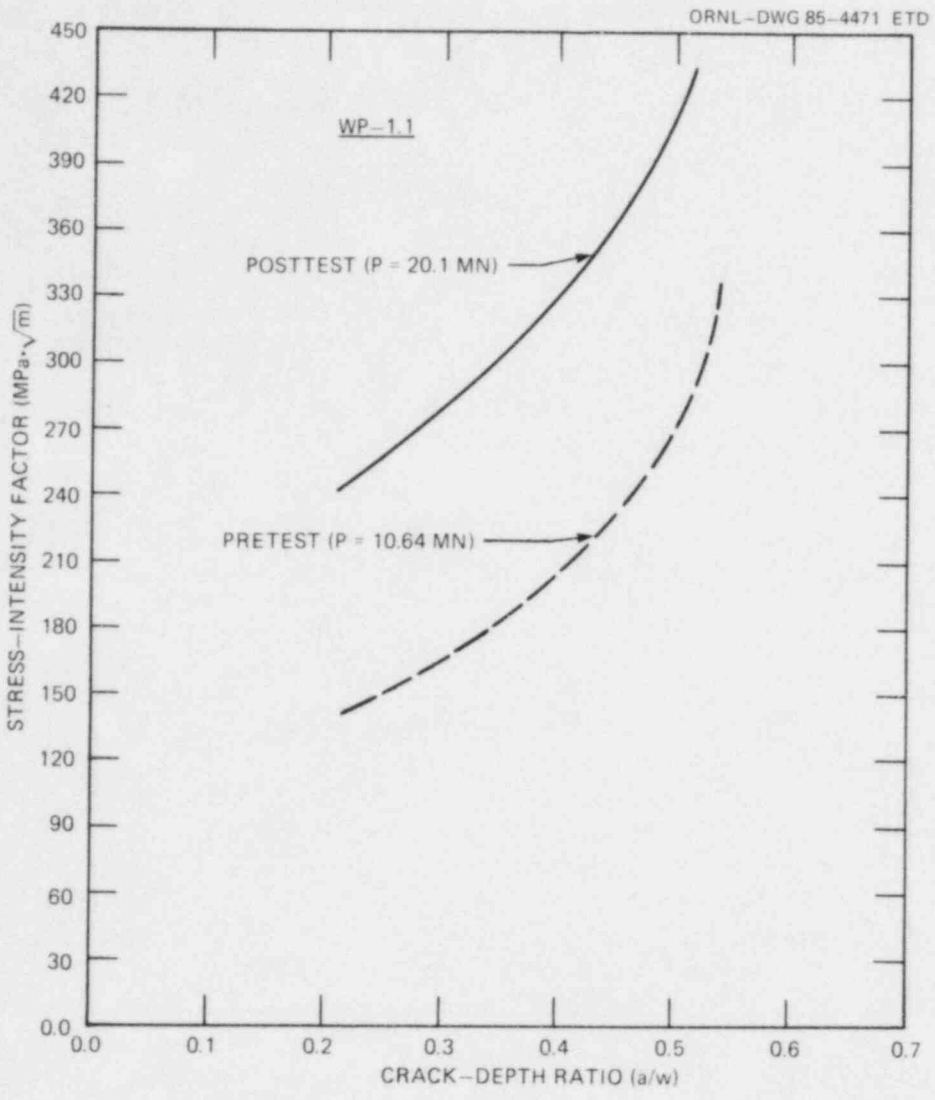

Fig. 5.34. Predicted stress-intensity factor vs crack depth for WP-1.1.

plane-stress model of the wide-plate configuration is used in the analyses, with the side grooves taken into account by adjustment of the resulting stress-intensity factor. While the steady state temperature distribution imposed on the plate assembly does not include thermal stresses, the global deformation of the assembly due to thermal strains is incorporated into the analyses. For applications of quasi-static analytical techniques (WPSTAT described below), this is accomplished by replacing the thermally deformed wide-plate assembly with an undeformed infinite plate of width w on which a combined load of pure tension and pure bending is imposed. As described in Ref. 15, the total solution for the assembly is obtained by superposing the contributions from tension and bending. For finite-element applications, static thermoelastic analyses were performed with the ADINA/ADINAT (Ref. 13) finite-element codes to

determine the thermal deformation of the plate assembly. These thermal displacements were added to the nodal point data defining the finite-element model. Generally, the load-line eccentricity caused by the thermal gradients used in the tests elevates the stress-intensity factors for the initial crack (a/w = 0.2) by ~10%.

After arrest, depending on the combination of applied load, temperature gradient, and point of arrest, the crack may be predicted to experience reinitiation in cleavage, or stable or unstable ductile tearing combined with tensile instability. Interactions of these factors were investigated using a number of different computational techniques. For the quasi-static analysis, the computer code WPSTAT (Ref. 15) was developed at ORNL to perform both crack-arrest and crack stability analyses. The WPSTAT code evaluates static stress-intensity factors as a function of crack length a and temperature differential $\Delta T = T_{max} - T_{min}$ across the plate. These factors are computed for fixed-force conditions $K_I^F(a,\Delta T)$ and for fixed load-pin displacement conditions $K_I^{DSP}(a,\Delta T)$ by superposing contributions from tension and bending handbook solutions. In addition, WPSTAT categorizes arrested crack lengths in terms of three types of instability limits. First, the instability crack length $a_{rein}(F)$, expressed as a function of the applied load F, defines the limiting value for the arrested crack length below which reinitiation in cleavage may occur. (This may be the case if the initial crack jump is very short, and the temperature of the arrested crack is in the lower-shelf range.) The $a_{rein}(F)$ curve is constructed by comparing the $K_I^F(a,\Delta T)$ curve obtained under fixed-force conditions with the $K_{Ic}(T)$ curve of Eq. (5.2), which is dependent on the location of the crack tip due to the applied temperature gradient. Reinitiation of the arrested crack is possible when the relation $K_I^F > K_{Ic}$ is satisfied.

The limit of the arrested crack length $a_{I1}(F)$ beyond which tensile instability occurs is taken to be the crack depth for which the average stress on the remaining ligament is equal to the ultimate stress σ_u. The value of σ_u = 550 MPa has been used in this study and represents the lowest value for the temperature range of interest (see Ref. 5).

If the crack arrests below the limit for tensile instability and beyond the limit of reinitiation, the possibility exists for the arrest to be stable or for failure to occur by ductile tearing. The region of arrested crack lengths for which tearing instability can occur is defined by the curve $a_{I2}(F)$. The material tearing resistance is assumed given in the form of a J-resistance curve $J_R(\Delta a)$, where Δa is the crack extension due to ductile tearing. A corresponding material-dependent quantity $K_y = \sqrt{EJ_R}$ can then be calculated. The point of impending tearing instability $a_{I2}(F)$ is required to satisfy the equations

$$K_I^F(a_{I2} + \Delta a) = K_y(\Delta a) , \qquad (5.9)$$

and

$$\left.\frac{dK_I^F}{da}\right|_{a_{I2}+\Delta a} = \left.\frac{dKy}{d(\Delta a)}\right|_{\Delta a} . \tag{5.10}$$

In this study, the J_R curve is represented by the power law $J_R = C(\Delta a)^m$, where $C = 0.3539$, $m = 0.4708$, and the units of J_R and Δa are megajoules per square meter and millimeters, respectively. Additional details of the solution techniques employed in the WPSTAT code are given in Ref. 15.

Elastodynamic analyses of the WP-1.2 were also carried out with the SWIDAC (Ref. 13) dynamic crack analysis code. The calculations were performed using the finite-element model shown in Fig. 5.31.

5.4.2.2 Pretest analyses. The temperature profile was defined by specifying a crack-tip temperature of $T_{CT} = -35°C$ and the onset of upper shelf material behavior ($T_{US} = 55°C$) at $X_{US} = 0.5$ m, implying $T_{min} = -95°C$ and $T_{max} = 205°C$. In the test, the temperature gradient was established first, followed by monotonic loading until initiation occurred. Because the apparent toughness of the material was uncertain, a range of possible initiation loads was considered in the analysis. For the specified temperature profile, the dependence of arrested crack length and crack stability on the applied initiation load F_{in} was investigated with the WPSTAT code,[15] and the results are presented in Fig. 5.35. In Fig. 5.35, the final length a_f of the arrested crack varies only between $0.5 \leq a_f \leq 0.7$ for loads that range from 6.5 to 21 MN (Note: 1 MN = 225 kips). [The F_{in} vs $a_f(F_{in})$ curve begins at 6.5 MN, which corresponds to a stress-intensity factor $K_I = K_{Ic}$ for the initial crack.] This observation indicates that the length of the crack jump is governed primarily by the temperature profile and the arrest toughness $K_{Ia}(T)$. Figure 5.35 includes the instability-limit crack lengths for reinitiation $a_{rein}(F_{in})$,

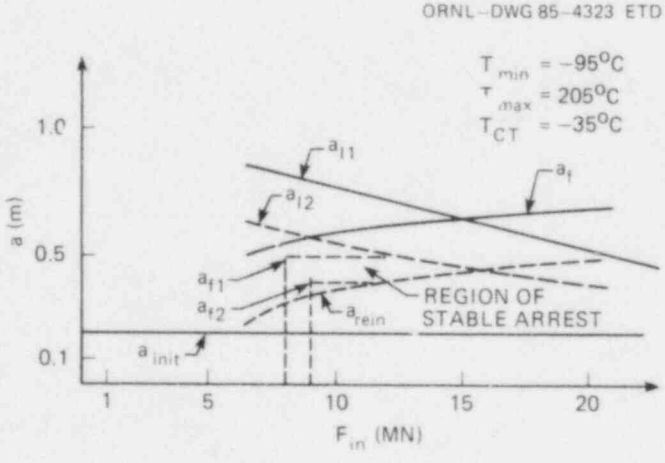

Fig. 5.35. Results of pretest crack-stability analysis of the wide-plate assembly showing limits of reinitiation, tearing, and tensile instability.

for tensile instability $a_{I1}(F_{in})$, and for tearing instability $a_{I2}(F_{in})$. The intersection of the $a_{I2}(F_{in})$ curve and the $a_f(F_{in})$ curve implies that for this situation tearing instability is expected if $F_{in} > 9$ MN. The gap between the reinitiation limit $a_{rein}(F_{in})$ and the tearing instability limit $a_{I2}(F_{in})$ shows the load-dependent range of stable arrested cracks. In addition, intersection of the $a_{rein}(F_{in})$ and $a_{I2}(F_{in})$ curves indicates that beyond a certain load ($F_{in} > 16$ MN), stable arrest becomes impossible. Figure 5.35 can also be used to assess whether reinitiation in cleavage or failure due to ductile tearing is to be expected with an increase in the applied load after stable crack arrest. This is shown in the figure for two crack lengths: a_{f1} at $F_{in} = 8$ MN (tearing) and a_{f2} at $F_{in} = 9$ MN (cleavage).

In Fig. 5.36, the K_{Ia} function of Eq. (5.3) is evaluated on the arrested crack length curve $a_f(F)$, on the incipient tearing instability curve $a_{I2}(F)$, and on the cleavage reinitiation curve $a_{rein}(F)$. The intersection of the $K_{Ia}(a_f)$ curve with the $K_{Ia}(a_{I2})$ curve provides the limiting value of K_{Ia} that presumably could be measured under the conditions of stable crack arrest. Assuming $K_{Ia}(T)$ to give a correct description of material behavior, this value is ~350 MPa$\cdot\sqrt{m}$.

Figures 5.37–5.39 show the results of both static and dynamic analyses in more detail for two load cases that define the interval of anticipated initiation load for the WP-1.2 test. In Fig. 5.37, the complete static and stability analyses are depicted for $F_{in} = 6.5$ MN ($K_I = K_{Ic}$) and $F_{in} = 10$ MN. Figures 5.38 and 5.39 show a comparison between static and dynamic calculations for the two load cases. The results indicate a significant difference between the displacement-controlled K^{DSP} values and the dynamic K^{DYN} values calculated with SWIDAC. However, the predicted crack-jump lengths are essentially identical, due primarily to the fact that in this large wide-plate configuration the elastic waves reflected from the free surface do not influence the stress field of the propagating crack tip. The figures also show the crack-tip velocity $\dot{a}$

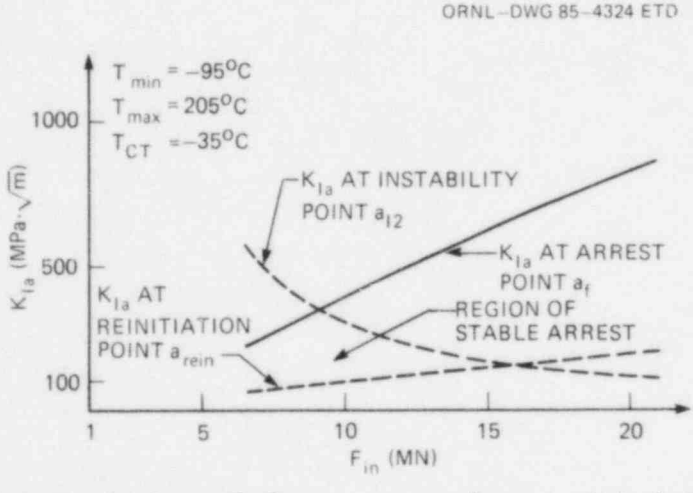

Fig. 5.36. Variation of fracture toughness with initiation load on the curves $a_f(F)$, $a_{rein}(F)$, and $a_{I2}(F)$.

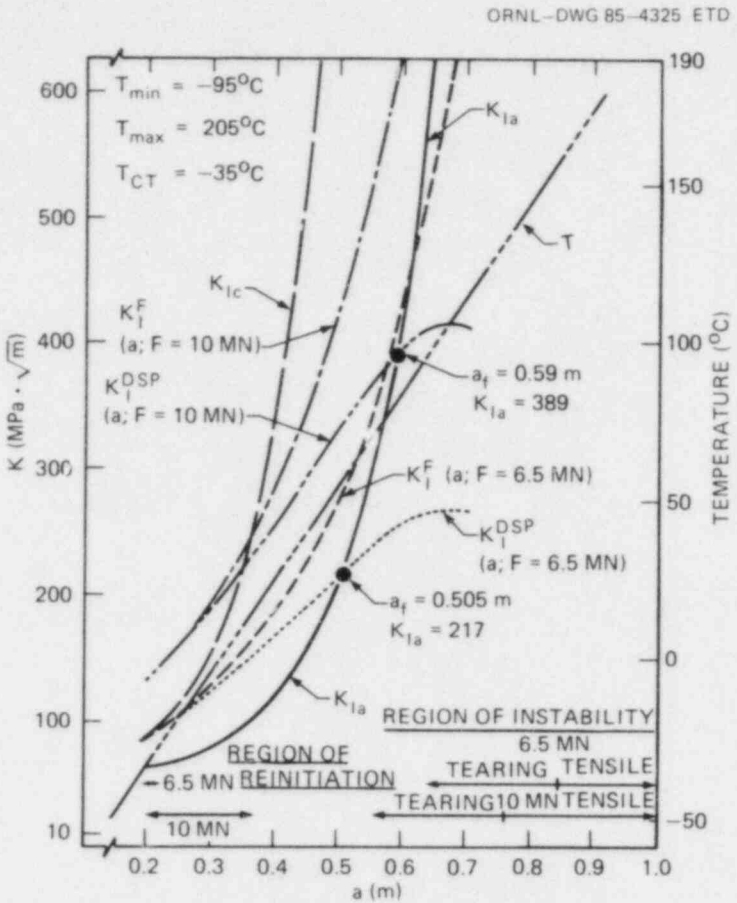

Fig. 5.37. Results of static and stabilit analyses of wide-plate assembly for postulated initiation loads F_{in} = 6.5 MN and F_{in} = 10 MN.

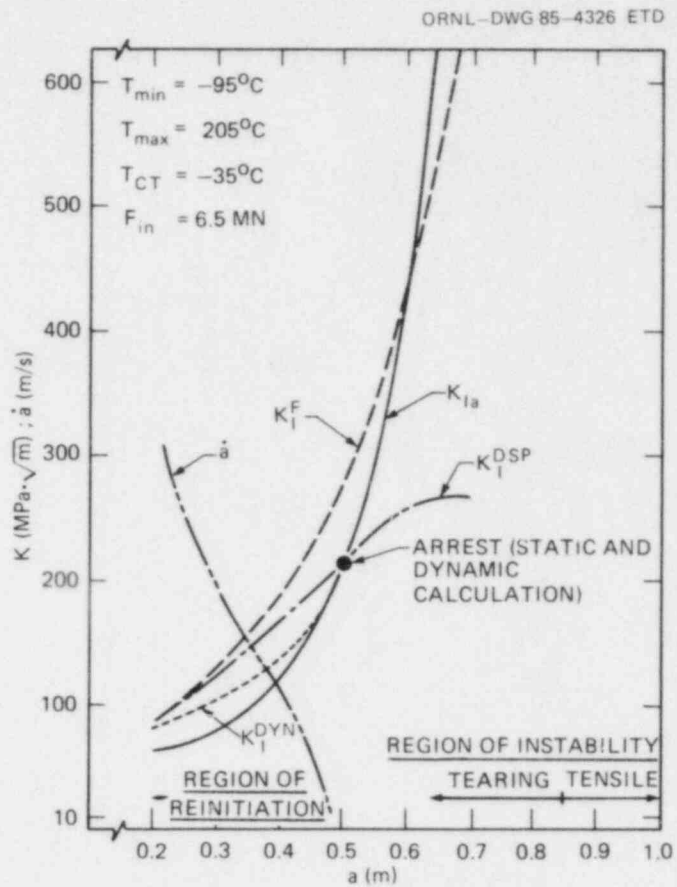

Fig. 5.38. Results of pretest static and dynamic analyses of the wide-plate assembly for a postulated initiation load of F_{in} = 6.5 MN.

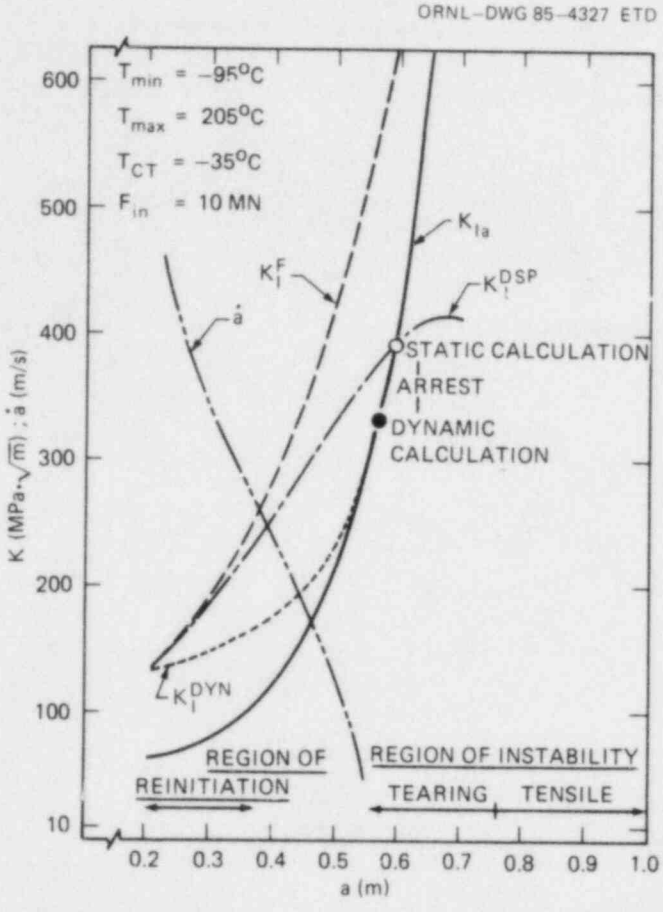

Fig. 5.39. Results of pretest static and dynamic analyses of the wide-plate assembly for a postulated initiation load of F_{in} = 10 MN.

as a function of instantaneous crack length, indicating that the crack tip slows down to relatively low velocities as it approaches regions where the temperature is near the Charpy upper-shelf regime.

5.4.2.3 Posttest analyses. Posttest elastodynamic analysis of WP-1.2 was also performed using the SWIDAC code with the model of Fig. 5.31, and the material properties given in Sect. 5.3. The measured fracture load of F_{in} = 18.9 MN (see Sect. 5.2.2.2) was applied to determine the load point displacement $U_{LL} = 0.51564 \times 10^{-2}$ m and the initiation stress-intensity factor K_I = 251.5 MPa·√m. For the dynamic analysis, the load point was fixed at the displacement value of the initiation load and the time step was set at Δt = 6 μs. The results of this analysis are given in Fig. 5.40, which depicts the variation of the static factor K_I^{DSP}, the dynamic factor K_I^{DYN}, the static toughness K_{Ia} [from Eq. (5.3) and the local temperature], and the crack velocity $\dot{a}$ as a function of instantaneous crack length. The crack propagates into a rising K_I field, with a computed arrest at a_f = 0.683 m where the crack-tip temperature would have been T = 104.4°C. The arrest toughness at the arrest-point temperature is given by Eq. (5.3) to be K_{Ia} = 706.7 MPa·√m. This K_{Ia} value can be compared with the dynamic factor of K_I^{DYN} = 621.7 MPa·√m computed by

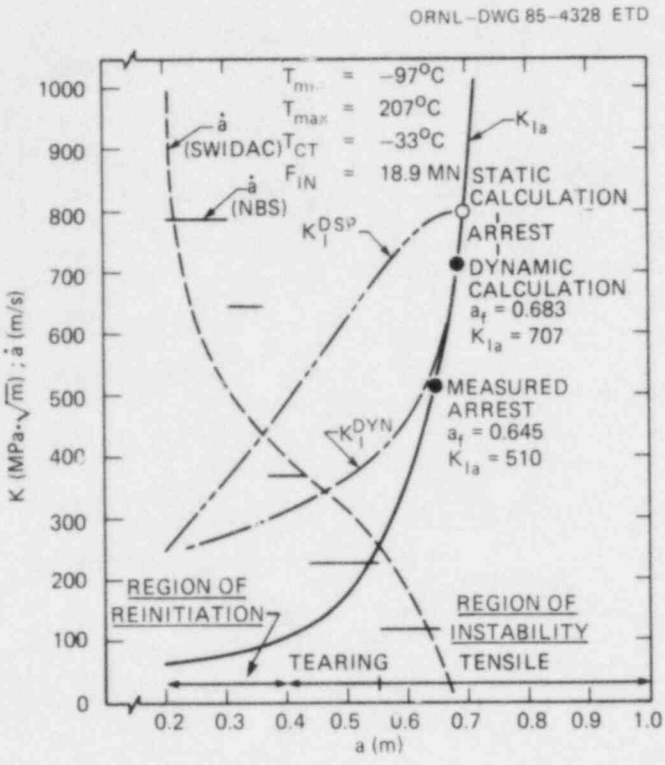

Fig. 5.40. Results of posttest static and dynamic analyses of the wide-plate assembly for the actual WP-1.2 initiation load of F_{in} = 18.9 MN.

SWIDAC in the time step immediately preceding crack arrest. As indicated in the figure, the computed arrest length exceeds the measured length of the second arrest event at a_f = 0.645 m, with crack-tip temperature T = 92°C and corresponding arrest toughness K_{Ia} = 509.8 MPa·$\sqrt{m}$ from Eq. (5.3). Preliminary crack-velocity data $\dot{a}_{NBS}$ were obtained from strain gages located near the crack plane (see Table 5.3) and are noted on Fig. 5.40 for comparison with computed values. The measured values are expressed as average velocities over the distance between adjacent strain gages.

The strain-time histories recorded by the crack-line gages 1, 2, and 3 (see Fig. 5.19) are depicted in Fig. 5.41 along with computed strain histories from points close to these gages. The computed curves are similar in trend and amplitude to the measured values. From the output of these crack-line gages and from an inspection of the fracture surface, an estimate of the crack position as a function of time was constructed and is given in Fig. 5.42. Figure 5.42 also shows that the dynamically calculated crack depth-time history from SWIDAC indicates that a higher velocity is predicted for crack depths greater than 0.4 m when compared with the estimates from measured data. This difference in velocity manifests itself by a shift in the time at which peak strains occur in the predicted and measured histograms shown in Fig. 5.41(*c*). The test results (solid curve) in Fig. 5.42 depict the previously described (Sect. 5.2) intermediate arrest at a = 0.55 m, with a frangible reinitiation occurring after a time delay of ~1 ms. The arrest-reinitiation scenario at this location is not predicted by the dynamic calculations.

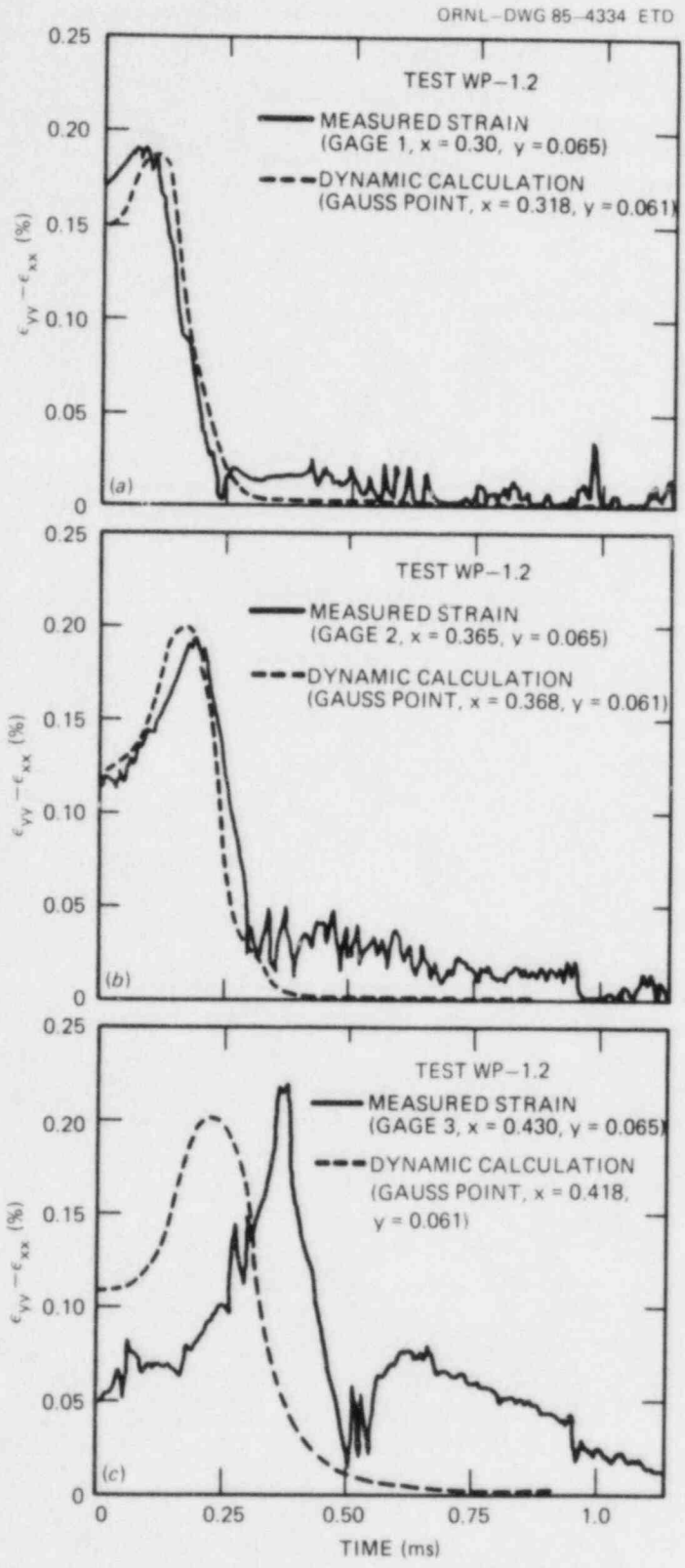

Fig. 5.41. Comparison between strain-time histories from measured data and dynamic calculations at strain gages 1, 2, and 3 (see Fig. 5.17) for test WP-1.2.

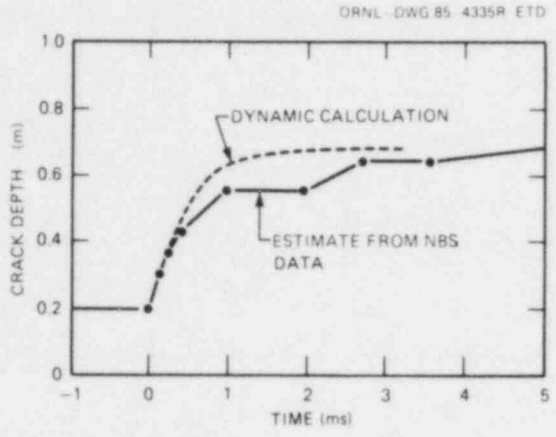

Fig. 5.42. Comparison between crack-depth histories from measured NBS data and dynamic calculations for test WP-1.2.

However, other elastodynamic analyses of the WP-1.2 test, described in Sect. 5.5 that follows, indicate that the intermediate arrest and reinitiation can be simulated computationally by inserting into the model a region of locally high fracture toughness at the point of arrest.

CMOD measurements were made at 175 mm from the cold edge of the plate. These measurements were made over a 10.2-cm-gage length that was centered over the crack plane. Figure 5.43 shows the dynamically calculated CMOD and the measurements taken from the eddy-current device. The

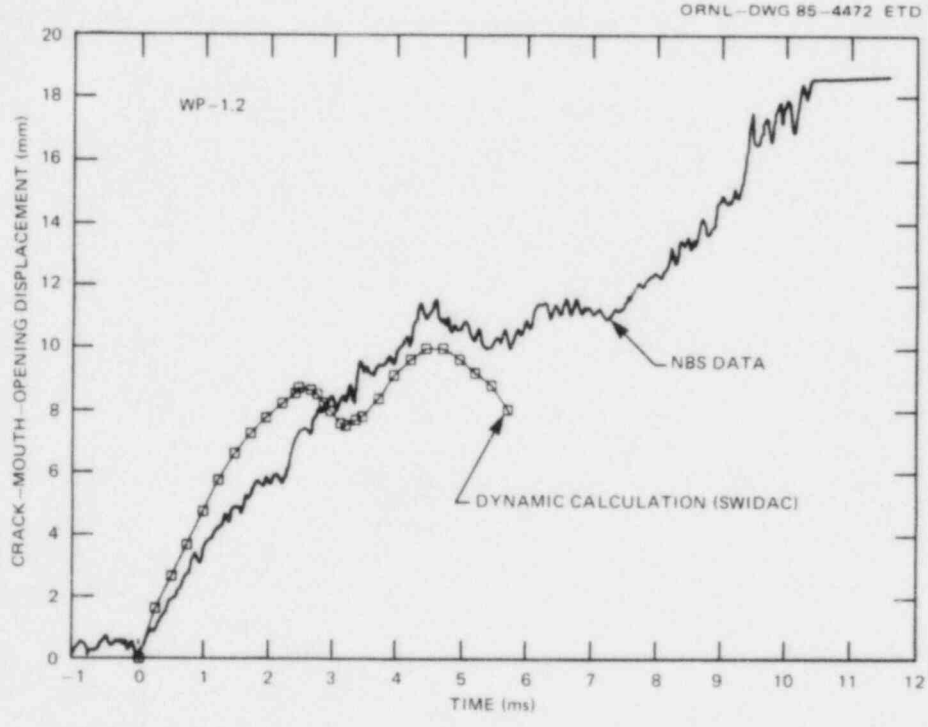

Fig. 5.43. Measured and dynamically calculated crack-mouth-opening displacements vs time for WP-1.2. (Gage located 17.5 cm from cold edge with a 10.2-cm gage length.)

comparisons are in keeping with other results in that the predicted CMOD exceeds measured values for early portions of the crack run when higher crack rates and no interim arrest period are predicted. Later, the measured and calculated CMOD shows good agreement when arrest occurred at a/w = 0.655.

5.5. SwRI Analysis of Wide-Plate Tests*

M. F. Kanninen† R. J. Dexter†
S. J. Hudak, Jr.† J. H. Fitzgerald†
K. W. Reed† K. S. Chan†
J. D. Achenback‡

A posttest elastodynamic analysis was made of the first NBS wide-plate test (WP-1.1). A crack-length to specimen-length ratio, a/w = 0.62, was predicted at arrest. Examination of the fracture surface by NBS indicated that arrest occurred at a/w = 0.50. Note that, while the elastic analysis considers the initial arrest to be permanent, for the given applied load, the average stress on the remaining ligament was 524 MPa. This value was well in excess of the ultimate stress for the material, and properly infers that complete fracture of the specimen would occur.

Figures 5.44 and 5.45, respectively, show the computed crack-length history and the computed values of the stress-intensity factor as a function of the crack length for WP-1.1. These computations compare very well with the ORNL results given in Sect. 5.4.2. This is significant in that, while the basic code formulation is the same, the ORNL computational model was considerably more refined. Specifically, the ORNL model employed 180 elements as opposed to 96 elements in the SwRI model.

In an effort to understand the difference between the prediction and the experimentally observed length of the arrested crack, an examination was made of the postulated dynamic fracture-toughness property used in this analysis. In particular, the expression given by Eqs. (5.4) and (5.5) was used for K_{ID} throughout this analysis. A plot of this relation is shown in Fig. 5.46. Note that this relation is plausible for the temperature range used in the pretest computations; that is, $T > -17°C$. However, the actual temperatures in WP-1.1 ranged upwards from $-55°C$, which is outside the range of Eq. (5.5). At low temperatures, the postulated relation gives rise to negative K_{ID} values at moderately high crack speeds. Correcting this physically unacceptable behavior would diminish the crack speed in the early portion of the crack propagation event, but

---

*Work sponsored by the HSST Program under subcontract 37X-97306C between Martin Marietta Energy Systems, Inc., and the Southwest Research Institute.

†Engineering and Materials Sciences Division, Southwest Research Institute, San Antonio, Texas.

‡Department of Civil Engineering, Northwestern University, Evanston, Illinois.

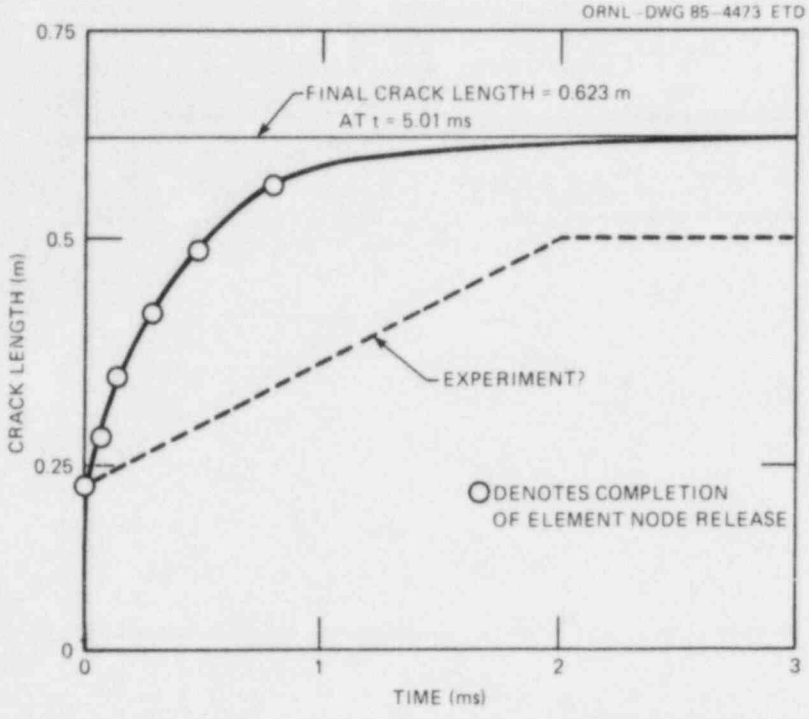

Fig. 5.44. Calculated crack history for NBS wide-plate experiment WP-1.1.

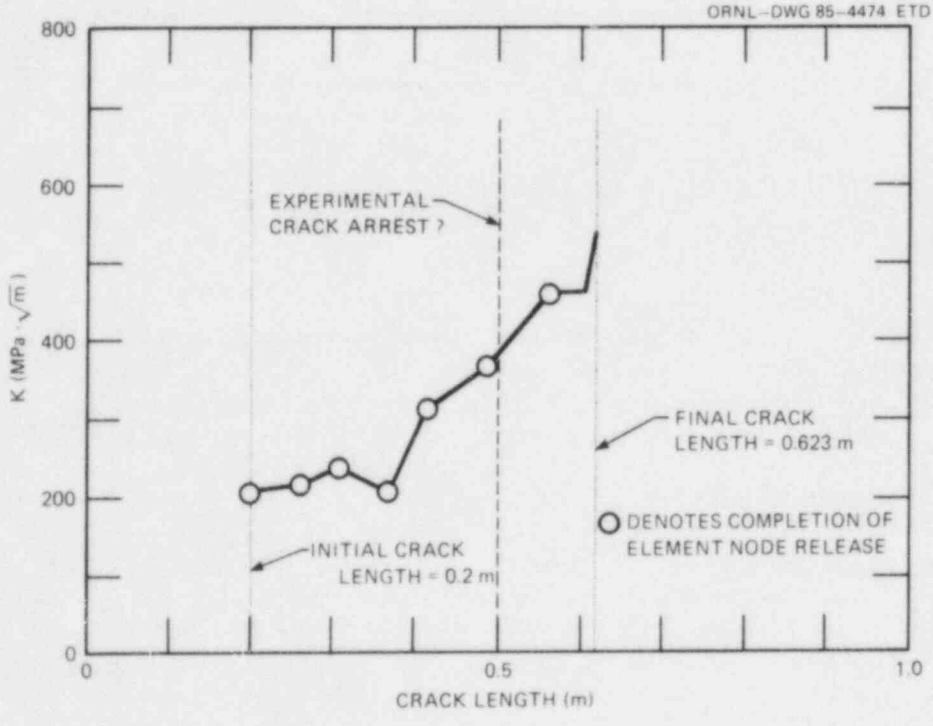

Fig. 5.45. Calculated stress-intensity factors for wide-plate experiment WP-1.1.

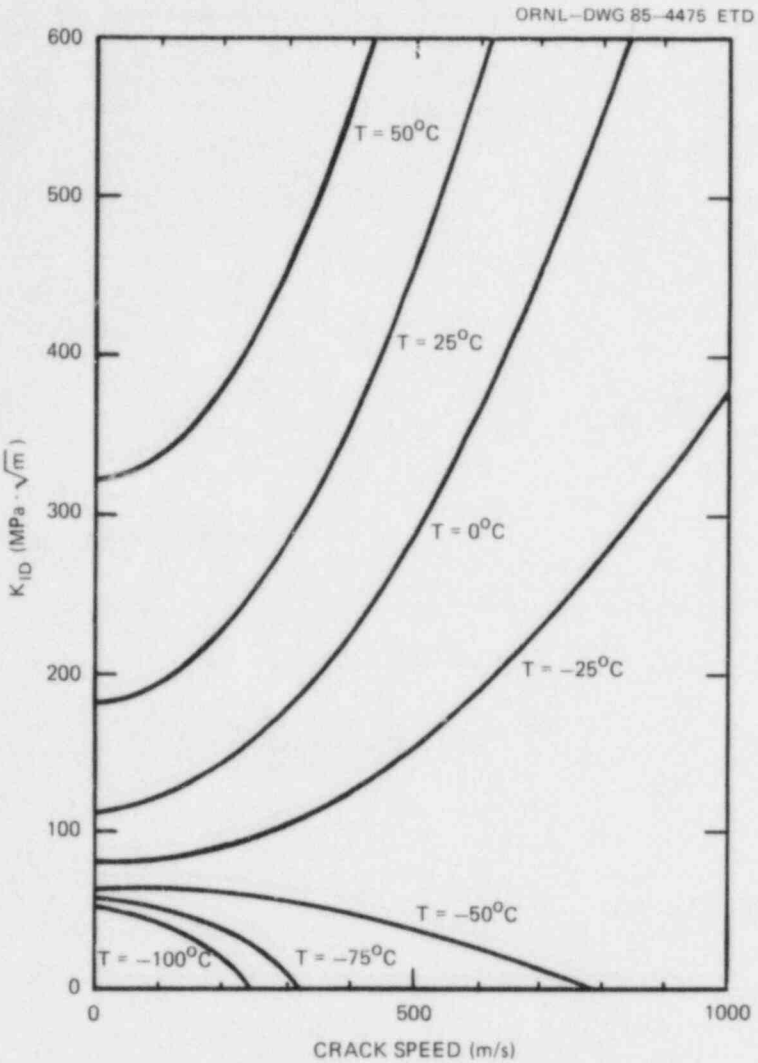

Fig. 5.46. Postulated dynamic-fracture toughness property for wide-plate test analyses.

it would have little effect on the crack length at arrest. Therefore, this does not offer an explanation for the lack of agreement with the observed arrest length. [Nevertheless, future use of Eqs. (5.5) and (5.6) will correct the inconsistency in the $K_{ID}(T)$ expression.]

Elastodynamic analyses were subsequently performed for the second wide-plate test, WP-1.2. These analyses also used the dynamic toughness relation illustrated in Fig. 5.46 together with the experimental initiation load and the imposed temperature gradient. The crack-length vs time predictions of the three analyses that were performed are shown in Fig 5.47. In the first analysis (curve A in Fig. 5.47), an initial crack speed of about 625 m/s was predicted with a subsequent gradual, but steady, decrease to arrest at a total crack length of 66.1 cm. These results are in excellent agreement with the preliminary NBS results (see Table 5.2). However, the possible intermediate arrest at a crack length of 55.5 cm was not predicted.

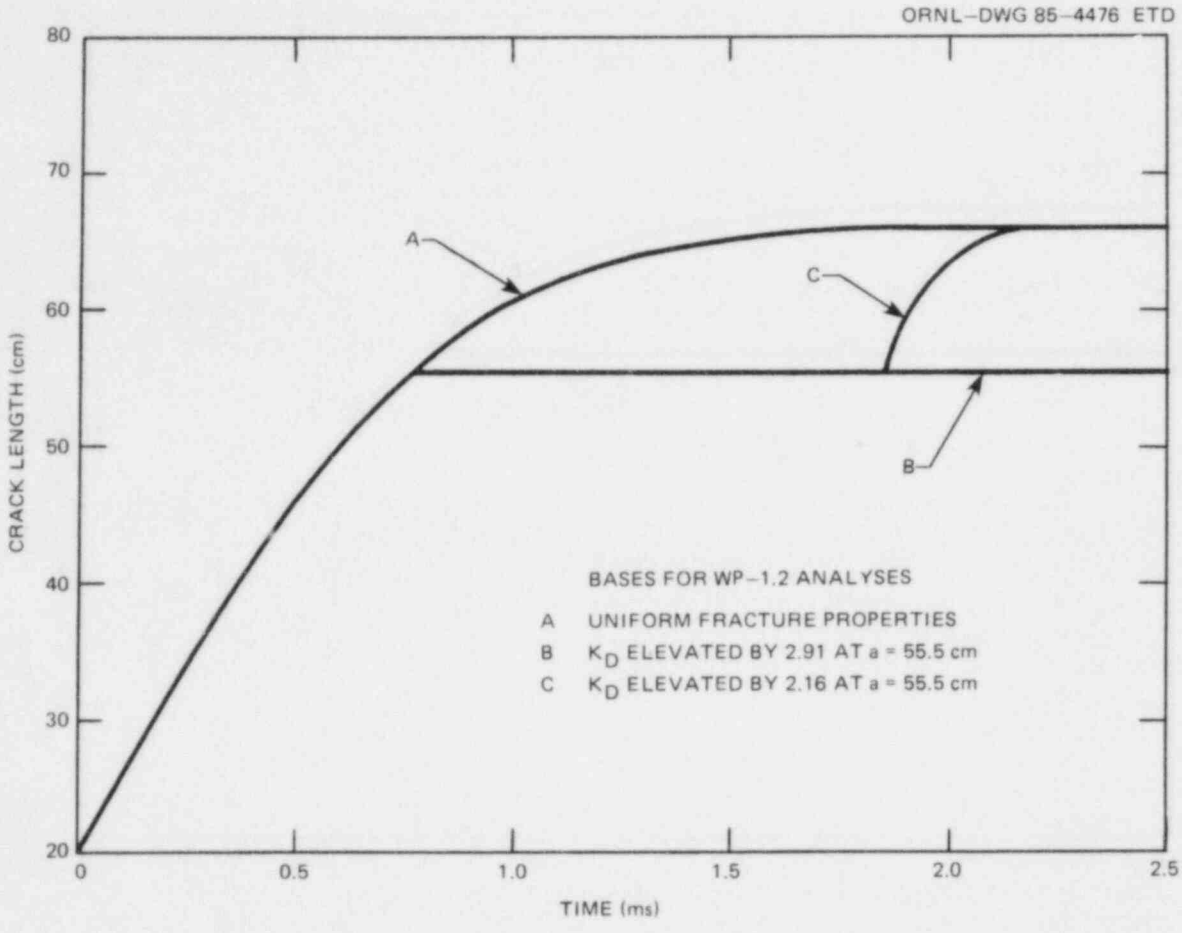

Fig. 5.47. Computational results for wide-plate experiment WP-1.2.

To determine if a discrete ductile region was responsible for the intermediate arrest observed in the WP-1.2, a local high-toughness strip was inserted into the calculation at a point representative of the observed intermediate arrest. The toughness initially assigned to this region was made to be commensurate with the observed disparity in the predicted and observed initiation toughnesses; that is, the K_{ID} values were multiplied by a factor of 2.91 at a = 55.5 cm. The result of this computation (curve B in Fig. 5.47) was that the crack was unable to penetrate the higher toughness region.

Examination of the detailed behavior of the dynamic stress-intensity factor while the crack dwelled at a = 55.5 cm showed that K achieved a maximum at a time roughly 1.8 ms following initiation. By selecting the "arrester region" toughness to be slightly less than this maximum (i.e., a multiplying factor of 2.16), it was therefore possible to achieve reinitiation at about this time. Figure 5.47 shows that reinitiation occurs after a pause of ~1 ms (curve C), in rough accord with the preliminary NBS observations. While not conclusive, this indicates that the intermediate arrest may indeed be a result of a local inhomogeneity.

5.6 Analyses and Experiments at University of Maryland in Support of Wide-Plate Testing*

W. L. Fourney† X-J. Zhang†
D. B. Barker† G. R. Irwin†
R. J. Sanford† R. Chona†
C. W. Schwartz‡

The University of Maryland is providing support to the wide-plate crack-arrest program through analytical modeling with the dynamic fracture-analysis computer code SAMCR and through model studies designed to improve the instrumentation and data acquisition systems being used in the tests at NBS. During the current report period, pretest analyses of the full-specimen geometry for WP-1.1 were completed, modified strain-gage layouts and a more reliable instrumentation triggering system were designed for WP-1.2, and on-site consultation was provided to NBS for both WP-1.1 and WP-1.2.

The finite-element mesh used for the full-specimen analysis of WP-1.1 is shown in Fig. 5.48. (The need for this was established and generally agreed upon by all participants in the benchmark analysis and pretest planning phases.) SAMCR predicted the crack length and crack-tip stress-intensity factor as functions of time as shown in Figs. 5.49 and 5.50, respectively. The run-arrest event was seen to be free of influences of reflected stress waves from the upper boundary, and crack arrest was predicted to occur 2750 μs after initiation, at an a_f/W of 0.60, with a crack arrest K value of 322 MPa$\cdot\sqrt{m}$, at a crack-tip temperature of 73°C. This agrees well with the predictions obtained from a full specimen analysis at ORNL.[16]

Difficulties experienced in triggering the digital oscilloscopes during WP-1.1 were felt to be due partially to the large thermal-strain component in the gage output and partially to the difficulty in setting precise trigger threshold levels without exact prior knowledge of failure load levels. In addition, the problems associated with determining crack velocities from ladder gage outputs placed an increased emphasis on obtaining the needed data from the crack-line strain gages.

The problem of the thermal-strain component was eliminated by using 90° rosettes for WP-1.2 in place of the uniaxial gages used in WP-1.1. By connecting the gages in adjacent arms of the bridge circuit, the apparent strain caused by the thermal mismatch was canceled out, and as an additional benefit, the gage output (which then became proportional to $\varepsilon_y - \varepsilon_x$) was increased. As as extension of this approach, experiments are currently under way to demonstrate that a variation of this scheme will result in a gage output that is directly proportional to K. This result is based on the observation that, for certain orientations of the

*Work sponsored by HSST Program under Subcontract No. 7778 between Martin Marietta Energy Systems, Inc., and the University of Maryland.

†Department of Mechanical Engineering, University of Maryland, College Park, Maryland.

‡Department of Civil Engineering, University of Maryland, College Park, Maryland.

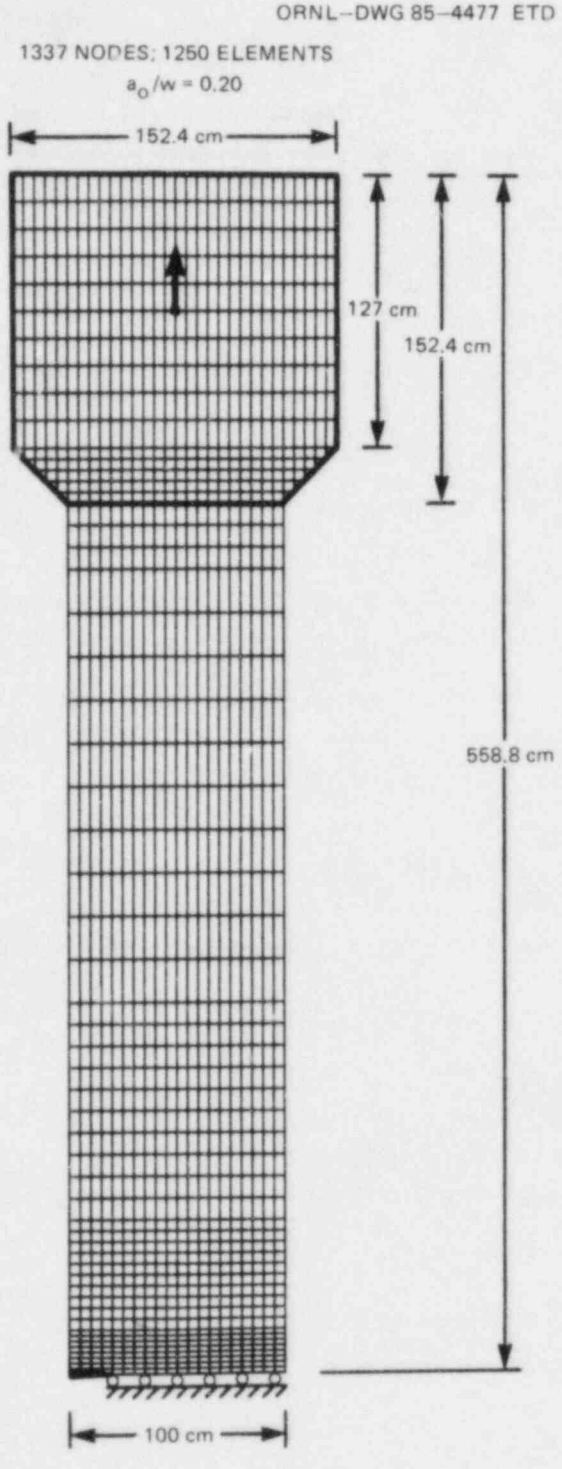

Fig. 5.48. Finite-element mesh used to analyze the full-specimen geometry for WP-1.1 using SAMCR.

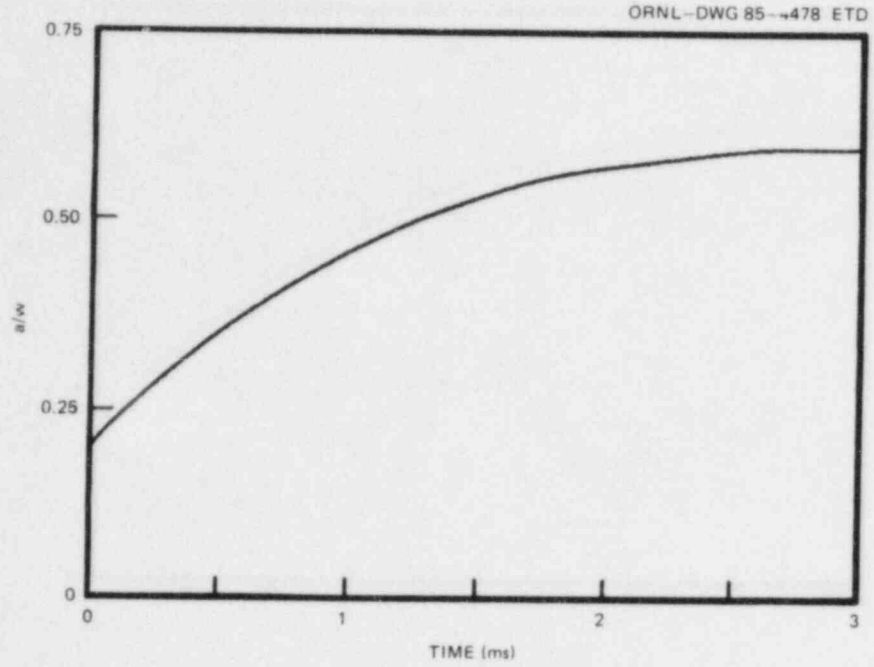

Fig. 5.49. SAMCR predictions of crack position as a function of time for the full-geometry analysis of WP-1.1 for the same temperature and load conditions as the benchmark problem.

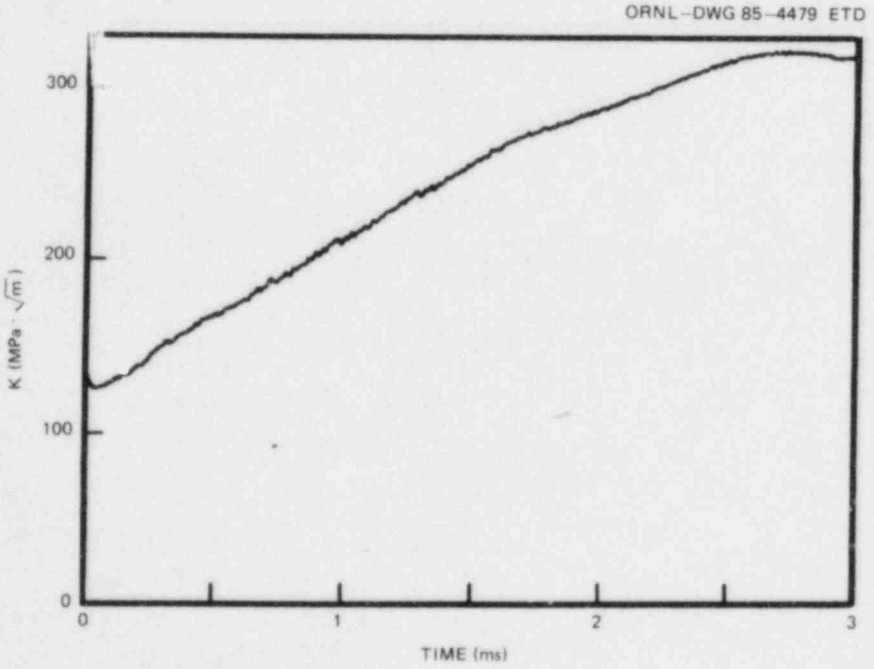

Fig. 5.50. SAMCR predictions of crack-tip stress-intensity factor as a function of time for the full-geometry analysis of WP-1.1 for the same temperature and load conditions as the benchmark problem.

gage(s), the effects of nonsingular stresses on the strain records can be made self-canceling.

The second problem, that of establishing trigger threshold levels, was solved in part by the elimination of thermal effects on the gage outputs as described above and by developing a scheme in which trigger calibration is performed using a function generator to simulate the dynamic signal. A laboratory experiment to demonstrate the effectiveness of this approach was conducted on an aluminum compact tension specimen, and the strains recorded from four gages located just above the crack line are shown in Fig. 5.51. Note that the crack arrested, reinitiated, and then arrested again between gage locations 3 and 4, giving rise to a strain record on gage 4 that is quite different from those recorded from gages 1, 2, and 3.

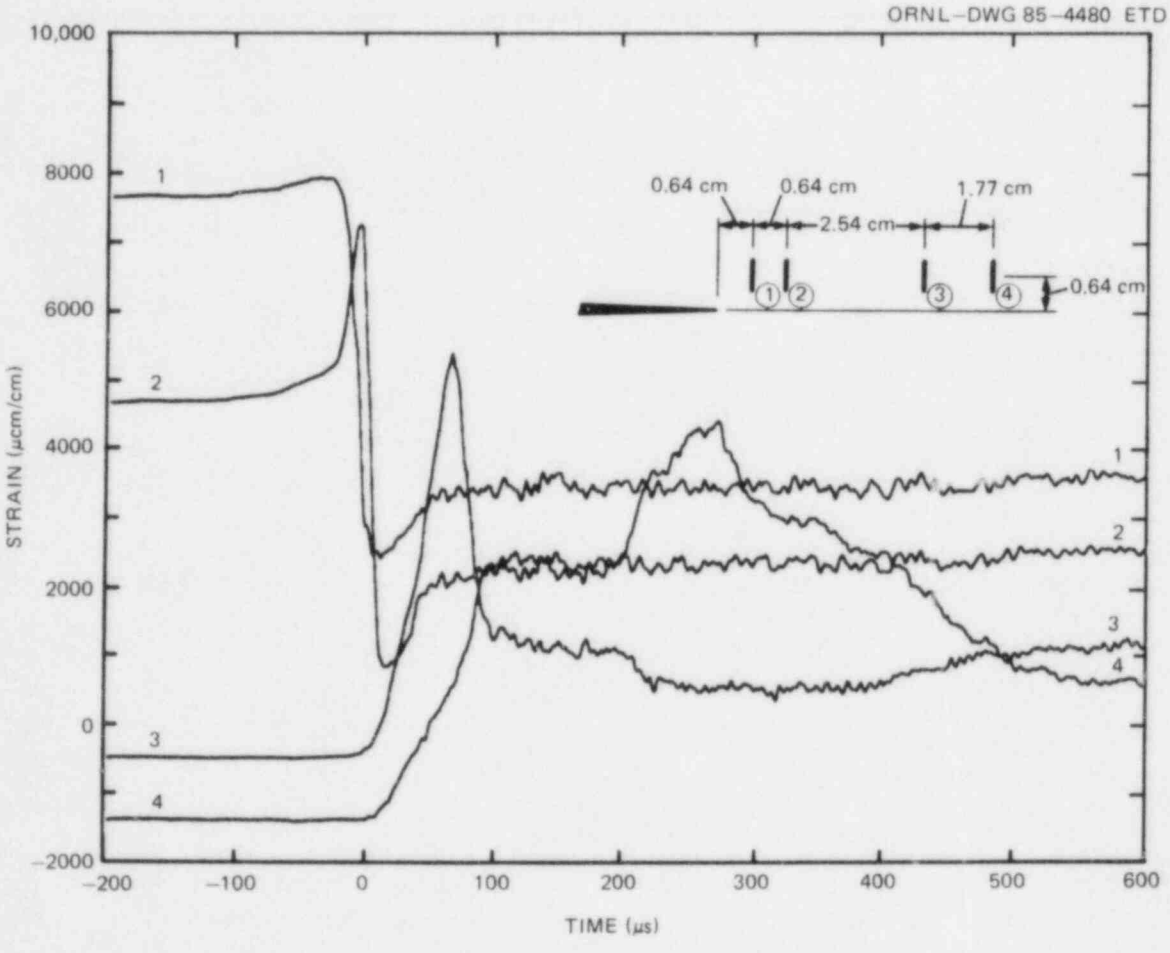

Fig. 5.51. Strain-gage outputs from four gages recorded using the same instrumentation triggering scheme as suggested for use in WP-1.2.

5.7 ASTM Round Robin on K_{Ia} Testing*

W. L. Fourney† R. Chona†

5.7.1 Participation by University of Maryland

Participation by UM as a test laboratory in the ASTM crack-arrest round robin was completed during the current reporting period. In addition to the standard participation that involved testing six specimens each of the bridge and reactor pressure vessel steels, six additional specimens of the A 533 grade B class 1 steel were tested with the inverted (no-flange) split-pin arrangement. Dynamic measurements of crack-opening displacements were made for all specimens tested using Kaman eddy current displacement transducers. These were placed at 0.25w above the load line and at 0.303w below the load line, as specified for double displacement compliance measurements of K-R curves.

5.7.2 Program administration

The University of Maryland is serving as coordinator of the ASTM round robin on crack-arrest test procedures. Test reports have been received to date from 12 of the 27 participants. The data have been compiled and were presented at the March meeting of ASTM E24.01.06 in Charleston, South Carolina. The results are similar to those obtained from the earlier Cooperative Test program. The remaining participants have been strongly urged to complete their testing and forward results by June, so that a report on the round robin and recommendations on the proposed test procedure can be presented at the October Meeting of ASTM Committee E-24. Unfortunately, few results have been received to date from the optional inverted-pin and subsize specimen testing.

The following program participants have completed their testing and reported results.

Technical Research Centre, Finland
MPA, Stuttgart, Federal Republic of Germany
BAM, West Berlin, Federal Republic of Germany
KWU, Federal Republic of Germany (partial results)
Nippon Kokan, Japan (partial results)
Mitsubishi, Japan (also results from subsize specimens)
SINTEF, Norway
Royal Institute of Technology, Sweden
UM, United States
ORNL, United States
BCL, United States
Westinghouse Research & Development Center, United States

---

*Work sponsored by HSST Program under Subcontract No. 7778 between Martin Marietta Energy Systems, Inc., and the University of Maryland.

†Department of Mechanical Engineering, University of Maryland, College Park, Maryland.

5.8 Battelle-Columbus HSST Support Program*

A. R. Rosenfield† C. R. Barnes†
P. N. Mincer†

5.8.1 Crack-arrest data bank

Over the past several years, researchers at BCL have been gathering the available crack-arrest-toughness (K_{Ia}) data. A draft report summarizing and characterizing this information has been submitted[17] to ORNL, and the highlights are discussed below. Data are presented in a form that can help provide predictions of material behavior under normal and faulted conditions. The data also provide information on the effects of specimen design and loading conditions on measured crack-arrest behavior.

The data bank includes both base plate and weldments and irradiated as well as unirradiated materials. Table 5.6 is a census showing that the bulk of data (88%) is for unirradiated base plate. Only 5% is for unirradiated welds, and less than 7% is for irradiated specimens. Although not indicated in Table 5.6, about 60% of all data were obtained at BCL, including all of the irradiated specimen data and almost all of the weldment data. Four other U.S. laboratories are represented, as well as laboratories from Japan, France, and Italy.

Table 5.6 Contents of BCL crack-arrest data bank

Condition	Base plate	Weld	Total
Unirradiated	485	28	513
Irradiated	19	17	36
Total	504	45	549

The draft report contains statistical descriptions of data obtained using varying test procedures. An earlier analysis[18] of part of the contents of the data bank using Bishop's method[19] revealed several useful tendencies of K_{Ia} behavior.

1. The K_{Ia} values can be described using a temperature-dependent Weibull distribution. However, the ratio K_{Ia}/K_{IR} is not strongly temperature dependent, indicating that the temperature dependence of K_{Ia} is effectively accounted for by the temperature dependence of K_{IR}.

*Work sponsored by HSST Program under Subcontract 85X-17264C between Martin Marietta Energy Systems, Inc., and Battelle-Columbus Laboratories.

†Battelle Columbus Laboratories, 505 King Avenue, Columbus, Ohio.

2. The Weibull modulus, which accounts for scatter, is approximately four at all temperatures. It follows from the Weibull formulation that the coefficient of variation (standard deviation/mean) is almost temperature independent. This result contrasts with the conventional statistical analysis of steel fracture,[20] which assumes a temperature-independent standard deviation.

Because the Weibull and Gaussian distributions are quite similar when the Weibull modulus is in the vicinity of four, these observations combine to suggest that the K_{Ia}/K_{IR} ratio can be conveniently described by a temperature-independent Gaussian distribution within the transition region. The result of the statistical analysis is also consistent with theory — when failure occurs by cleavage, microstructurally based models predict that the scatter in toughness is described by a Weibull distribution with a modulus of four.[21,22]

As an example of the statistical results, Table 5.7 compares the ORNL thermal shock data for large cylinders with several extensive collections of compact-specimen data. This table shows that the mean values

Table 5.7. Statistical parameters describing crack-arrest toughness

Test steel	RT_{NDT} (°C)	Test temperature (°C)	K_{Ia} (MPa·$\sqrt{m}$)		$T - RT_{NDT}$ (°C)	K_{Ia}/K_{IR}	
			Mean	Standard deviation		Mean	Standard deviation
		Compact specimens, ASTM Cooperative Test Program (Ref. 23)					
ASTM A 533 B	−20	0	85.1	12.5	20	1.61	0.24
ASTM A 533 B	−20	23	107.5	13.6	43	1.50	0.19
		Compact specimens ASTM round robin[a]					
ASTM A 533 B	−2	10	76.9	9.1	12	1.59	0.19
ASTM A 533 B	−2	25	83.9	10.1	27	1.46	0.18
		Additional compact specimens[b]					
ASTM A 508 and A 533 B	[c]	[c]	[c]	[c]	[c]	1.76	0.43
		Thermal shock of cylinders					
ASTM A 508 and A 533 B	[c]	[c]	[c]	[c]	[c]	1.63	0.47

[a] Incomplete results from 11 of 27 anticipated participants provided by R. Chona, University of Maryland.

[b] 179 specimens tested in accord with procedures currently being recommended by the ASTM Task Group.

[c] Various values.

of K_{Ia}/K_{IR} for the two geometries tend to be similar, but that the standard deviations of the multi-laboratory programs are much less than for the combined thermal-shock data. In contrast, the additional compact-specimen data (Table 5.7) have a standard deviation comparable to that of cylinders. The implications of these observations relating to the relative material and test-variable contributions to scatter were not firmly established. However, the data do seem to indicate a more significant contribution arising from material variability.

As indicated in Table 5.6, there are considerably fewer data for weldments and for irradiated materials than for unirradiated base plate. For this reason, detailed statistical analysis of these data is not possible. However, the available information suggests that the mean K_{Ia}/K_{IR} ratios for these materials are similar to those for unirradiated base plate. On the other hand, the standard deviations for both unirradiated and irradiated welds are much larger than those for base plate. This result is not surprising given the great variability in weldments.

This data bank is intended to be continually updated. Additional data are solicited from readers of this report. Copies of the individual data sheets are available to qualified requesters.

5.8.2 Wide-plate crack-arrest test support

The technique[24] used to monitor dynamic crack propagation in the first HSST wide-plate crack-arrest test (WP-1.1) was modified for use during the second test (WP-1.2). This was necessary for two reasons, both of which relate to the material used to insulate the conducting grid lines from the specimen surface. First, the transformer shellac that was used in WP-1.1 was not sufficiently viscous to cover the machining marks on the specimen surface, which were produced when the specimen blank was prepared. Even after several coatings of shellac, there were areas where the "peaks" of the grind marks protruded above the insulating surface. These uninsulated peaks often were not apparent until a conducting line was applied, at which time an electrical short was indicated. The second problem with the shellac surfaced when attempts to repair these shorted lines were made while the specimen was in place for testing. At that time, the shellac did not dry properly. Presumably, this was due to high humidity near the top of the test laboratory at NBS Gaithersburg.

Accordingly, it was decided to use a more viscous epoxy insulator, which cured by a molecular cross-linking process rather than the solvent-evaporative process. The reasoning was that high viscosity would cure the shorting problem. It was also thought that any problems associated with humidity would be avoided by using the chemically curing epoxy. The material selected (EA904) has not been shown to be stable from −196 to 260°C; moreover, it exhibits relatively low ductility up to about 150°C. This property helps to ensure that small crack openings would rupture the epoxy and, hence, a conducting line, to indicate the crack-tip position reliably. The application of this epoxy to Specimen WP-1.2 was relatively straightforward. No electrical shorts were encountered with the conducting grid lines.

Table 5.8 contains the crack-speed monitoring-grid data for WP-1.2. Note that specimen WP-1.2 had a grid installed on both the front and back

Table 5.8. BCL crack-speed grid data from wide-plate crack-arrest test WP-1.2

Grid array No.	Average velocity (m/s)	Line No.	Distance[a] from crack tip (mm)	Grid array No.	Average velocity (m/s)	Line No.	Distance[a] from crack tip (mm)
1	~877	1	7.62	3	~528	1[b]	267.97
		2[b]	13.97			2	287.02
		3	20.32			3	307.34
		4[b]	26.67			4	325.12
		5	33.02			5	344.17
		6[b]	39.37			6	363.22
		7	45.72			7[b]	383.54
		8[b]	52.07			8	401.32
		9	58.42			9	420.37
		10	65.53			10[b]	439.93
2	~733	1[b]	78.74	4	~115	1	452.12
		2	97.79			2[b]	474.98
		3	116.84			3	496.57
		4[b]	135.89			4[b]	519.43
		5	154.94			5	541.02
		6	173.99			6[b]	566.42
		7[b]	193.04			7	585.47
		8	212.09			8[b]	609.6
		9	229.87			9	629.92
		10	248.92			10	652.27

[a]Initial crack-tip location at 199 mm from cold edge of specimen.

[b]Line coincidence between front and back surface grids.

surfaces. The front surface grid was a 40-line array. The back surface grid array contained 16 lines, and its purpose was to serve as a check for the front surface grid. Table 5.8 also contains preliminary estimates of crack velocity within each grid. These velocity data are currently being refined through use of more definitive information than was available when Table 5.8 was prepared.

References

1. R. D. Cheverton et al., "Fracture Mechanics Data Deduced from Thermal-Shock and Related Experiments with LWR Pressure Vessel Material," *Journal of Pressure Vessel Technology* 105, 102–10 (May 1983).

2. R. H. Bryan et al., "The Heavy-Section Steel Technology Pressurized-Thermal-Shock Experiment, PTSE-1," submitted to *Engineering Fracture Mechanics* for publication in a special issue of the journal.

3. C. E. Pugh, "Crack Arrest Technology," pp. 83–137 in *Heavy-Section Steel Technology Program Semiannual Prog. Rep. April–September 1984*, NUREG/CR-3744, Vol. 2 (ORNL/TM-9154/V2), Martin Marietta Energy Systems, Inc., Oak Ridge Natl. Lab.

4. R. deWit et al., "Validation of Warm Prestressing Procedure," pp. 132–40 in *Heavy-Section Steel Technology Program Semiannual Prog. Rep. April–September 1984*, NUREG/CR-3744, Vol. 2 (ORNL/TM-9154/V2), Martin Marietta Energy Systems, Inc., Oak Ridge Natl. Lab.

5. D. P. Edmonds and J. J. McGowan, "Preliminary Characterization of Wide-Plate Test Material," pp. 96–102 in *Heavy-Section Steel Technology Program Semiannual Prog. Rep. April–September 1984*, NUREG/CR-3744, Vol. 2 (ORNL/TM-9154/V2), Martin Marietta Energy Systems, Inc., Oak Ridge Natl. Lab.

6. A. R. Rosenfield et al., "Crack-Arrest Studies at Battelle Columbus," pp. 102–9 in *Heavy-Section Steel Technology Program Semiannual Prog. Rep. April–September 1984*, NUREG/CR-3744, Vol. 2 (ORNL/TM-9154/V2), Martin Marietta Energy Systems, Inc., Oak Ridge Natl. Lab.

7. M. F. Kanninen et al., *Preliminary Analysis of Japanese Wide Plate Dynamic Crack Propagation Arrest Experiments*, Subcontract report from Battelle Columbus Laboratories to Oak Ridge National Laboratory, December 1983.

8. T. Kanazawa et al., "Study on Fast Fracture and Crack Arrest," *Exp. Mech.* 21(2), 78–88 (February 1981).

9. American Society for Testing and Materials, *Standard Test Method for Plane-Strain Fracture Toughness of Metallic Materials*, E399-83, Philadelphia, 1981.

10. H. A. Ernst, "Material Resistance and Instability Beyond J-Controlled Crack Growth," pp. I-191–213 in *Elastic-Plastic Fracture: Second Symposium*, STP-803, American Society for Testing and Materials, Philadelphia, 1983.

11. J. G. Merkle, *An Examination of the Size Effects and Data Scatter Observed in Small-Specimen Cleavage Fracture Toughness Testing*, NUREG/CR-3672 (ORNL/TM-9088), Martin Marietta Energy Systems, Inc., Oak Ridge Natl. Lab., April 1984.

12. K. J. Bathe, *ADINA — A Finite Element Program for Automatic Dynamic Incremental Nonlinear Analysis*, Report 82448-1, Massachusetts Institute of Technology, Cambridge, Mass, September 1975 (revised December 1978).

13. J. Jung et al., *Finite-Element Analysis of Dynamic Crack Propagation*, presented at the 1981 ASME Failure Prevention and Reliability Conference, September 23–26, 1981, Hartford, Conn.

14. K. J. Bathe and E. L. Wilson, *Numerical Methods in Finite Element Analysis*, Prentice-Hall, Inc., Englewood Cliffs, N.J., 1976, pp. 322–26.

15. H. K. Stamm, B. R. Bass, and C. E. Pugh, *Fracture Analysis of Plate Crack Arrest Specimens*, Martin Marietta Energy Systems, Inc., Oak Ridge Natl. Lab., in preparation.

16. B. R. Bass, "Wide-Plate Benchmark Problem Solutions," pp. 110–16 in *Heavy-Section Steel Technology Program Semiannual Prog. Rep. April–September 1984*, NUREG/CR-3744, Vol. 2 (ORNL/TM-9154/V2), Martin Marietta Energy Systems, Inc., Oak Ridge Natl. Lab.

17. A. R. Rosenfield, *Reactor-Pressure-Vessel-Steel Crack-Arrest Data Bank*, draft Battelle-Columbus Report to Oak Ridge National Laboratory, Jan. 28, 1985.

18. A. R. Rosenfield, P. N. Mincer, and C. W. Marschall, "BCL HSST Support Program," pp. 3–20 in *Heavy-Section Steel Technology Quarterly Prog. Rep. July–September 1983*, NUREG/CR-3334, Vol. 3 (ORNL/TM-8787/V3), Union Carbide Corp. Nuclear Div., Oak Ridge Natl. Lab.

19. T. A. Bishop, A. J. Markworth, and A. R. Rosenfield, "Analyzing Statistical Variability of Fracture Properties," *Metall. Trans. A* 14A, 687–93 (1983).

20. W. Oldfield and W. L. Server, pp. 9–26 in "Fracture Toughness Prediction for Pressure Vessel Steels: The Development of a Statistically Based Method," in *Reference Fracture Toughness Procedures Applied to Pressure Vessel Materials*, T. R. Mager, ed., ASME Publication MPC-24, 1984.

21. K. Wallin, "The Scatter in K_{Ic} Results," *Eng. Fract. Mech.* 19, 1085–93 (1984).

22. F. M. Beremin, "A Local Criterion for Cleavage Fracture of a Nuclear Pressure Vessel Steel," *Metall. Trans. A* 14A, 2277–87 (1983).

23. P. B. Crosley et al., *Cooperative Test Program on Crack Arrest Toughness Measurements*, NUREG/CR-3261, University of Maryland, College Park, April 1983.

24. P. N. Mincer and C. R. Barnes, *Crack Speed Determinations in Wide Plate Tests*, Preliminary Report to Martin Marietta Energy Systems, Inc., Dec. 21, 1984.

6. IRRADIATION EFFECTS STUDIES

R. K. Nanstad

6.1 Fourth HSST Irradiation Series

R. K. Nanstad

The cooperative testing program with Materials Engineering Associates (MEA) on specimens from the first three capsules of the Fourth HSST Irradiation Series is continuing. Testing of all unirradiated 1T-CS specimens has been completed. Testing of the irradiated 1T-CS specimens by MEA is completed, and the results are being analyzed.

The Oak Ridge National Laboratory (ORNL) testing of phase 1 irradiated 1T-CS specimens has been completed, and the phase 2 testing is continuing. The final results for the Fourth Irradiation Series will be reported in the next progress report.

6.2 Fifth HSST Irradiation Series

R. G. Berggren J. J. McGowan
R. K. Nanstad K. R. Thoms
F. B. Kam

The primary objective of the Fifth HSST Irradiation Series is to obtain valid fracture-toughness (K_{Ic}) curves for two pressure vessel materials irradiated at 288°C and to as high a toughness level as practical. The program philosophy, materials, test methods, specimen complements, and target fast neutron fluences have been described previously.[1-4]

Irradiation of 6 of the 12 planned capsules has been completed in the poolside facility (PSF) of the Oak Ridge Research Reactor (ORR), and preliminary testing of unirradiated (control) specimens is nearing completion. Capsules 1, 2, and 3 have been disassembled, and capsule 4 is awaiting disassembly. Each of these capsules contained two 4T compact specimens. Irradiation of capsules 5 and 6 was completed February 18, 1985. These capsules contained Charpy V-notch (CVN) impact specimens and tensile, drop-weight, and 1T compact specimens. Irradiation of capsules 7 and 8, containing 2T compact specimens, started on March 6, 1985, and completion of all irradiations (12 capsules) is scheduled for the end of November 1985.

6.2.1 Neutron dosimetry

Neutron dosimeter results from the first two capsules (4T-CS) indicate higher fluences of neutrons (>1 MeV) than had been predicted from the dosimetry experiments. The predicted fluences at the one-quarter- and three-quarter-thickness positions at the crack front of the 4T compact specimens were 1.5×10^{23} neutrons/m^2 while the dosimeter results

gave ~1.75 × 10^{23} neutrons/m^2. This difference was primarily due to changes in the ORR core loading between the dosimeter experiments and the exposure of capsules 1 and 2. The core loading pattern is to be maintained as constant as possible for the remainder of the Fifth HSST Irradiation Series. A primary criterion of this study is that all sizes and types of specimens receive, as nearly as possible, the same neutron exposure. Therefore, all capsules in the series will be irradiated for the originally scheduled periods, all specimens will receive ~17% greater fluence than originally predicted (previous target fluence was 1.5 × 10^{23} neutrons/m^2; the revised target fluence is 1.75 × 10^{23} neutrons/m^2), and the planned schedule will be maintained.

6.2.2 Irradiation capsule operation

The initial operation of capsules 5 and 6, containing CVN, tensile, drop-weight, and 1T compact specimens, indicated that desired temperatures (288°C) throughout both capsules were going to be impossible to achieve. The variety of specimens in the capsules has resulted in temperatures in the 1T compact specimens nearest the drop-weight specimens (top and bottom regions of the capsules) being ~10 to 14°C higher than desired. Lowering the temperatures of these 1T compact specimens would also lower the temperatures of the drop-weight specimens. It was decided to maintain the desired temperatures of the drop-weight specimens and the majority of the 1T compact specimen, CVN, and tensile specimens and to allow some of the 1T compact specimens to operate at the higher temperatures. This should not compromise the objectives of the study.

6.2.3 Scoping tests

The tensile specimen used in this study is shown in Fig. 6.1. The tensile properties for the two welds in the unirradiated condition are listed in Table 6.1. The tensile strengths of welds 72W and 73W are shown in Figs. 6.2 and 6.3, respectively. Note that there is no significant difference between the unirradiated tensile properties of the two welds.

The results of the scoping CVN tests are listed in Table 6.2 for welds 72W and 73W in the unirradiated condition. The absorbed energy, lateral expansion, and fracture appearance variations with temperature for the two welds are shown in Figs. 6.4, 6.5, and 6.6, respectively. A comparison of the results for both welds of the CVN tests and the drop-weight tests is in Table 6.3. Note that the transition temperature for weld 73W is nearly 20°C lower than weld 72W while the upper-shelf energies are nearly equal. These results compare favorably with test coupon results.[3]

A 1T-CS [American Society for Testing and Materials (ASTM) E399 (Ref. 5)] was used to perform scoping fracture-toughness tests on welds 72W and 73W in the unirradiated condition. These specimens had razor blades on the front face of the specimen for mounting an extensometer and were tested at a front face displacement rate of 0.01 mm/s. With an

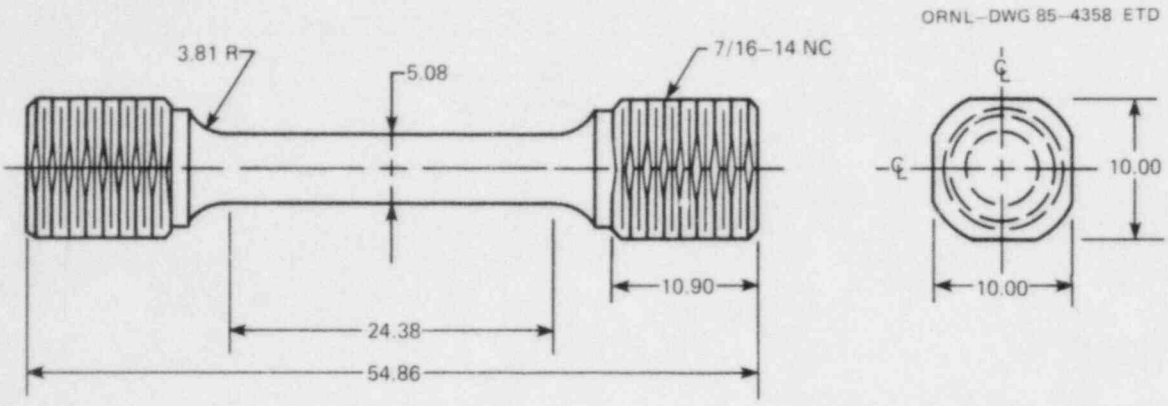

Fig. 6.1. Tensile specimen configuration.

Table 6.1. Tensile properties of unirradiated welds for Fifth HSST Irradiation Program

Specimen	Test temperature (°C)	Strength (MPa)		Uniform strain (%)	Reduction in area (%)	Total elongation (%)
		Yield	Ultimate			
72W251	−101	606.3	727.9	12.2	64.9	25.3
72W253	−101	597.6	738.8	12.9	65.8	24.9
72W255	−101	601.9	742.6	11.8	63.9	24.5
72W257	−59	552.0	689.1	11.7	63.4	20.7
72W259	−59	559.5	695.3	10.9	66.1	22.4
72W260	−59	576.8	712.6	11.3	65.3	23.4
72W263	−26	523.7	648.6	9.6	64.4	22.3
72W265	−26	530.2	657.3	10.0	66.1	23.4
72W267	−26	525.9	648.6	9.3	65.5	19.7
72W269	28	499.3	605.7	7.9	67.5	19.5
72W271	28	498.8	609.6	7.9	65.4	19.6
72W274	28	494.8	602.4	8.3	69.3	21.4
73W250	−101	608.4	745.3	11.6	64.9	24.6
73W252	−101	604.1	735.4	13.8	63.8	23.0
73W256	−101	591.7	722.9	13.7	64.1	23.0
73W258	−59	548.7	684.8	10.5	65.2	22.1
73W260	−59	543.2	680.1	13.9	65.2	22.9
73W262	−59	548.7	681.2	11.8	66.7	25.0
73W264	−26	531.4	656.2	9.9	68.2	23.2
73W266	−26	525.9	651.9	10.3	66.7	23.2
73W268	−26	530.2	654.1	10.2	69.0	23.2
73W270	28	488.9	597.6	8.3	67.3	21.7
73W272	28	497.6	608.4	9.2	70.1	24.1
73W274	28	481.9	591.7	8.2	66.5	20.3

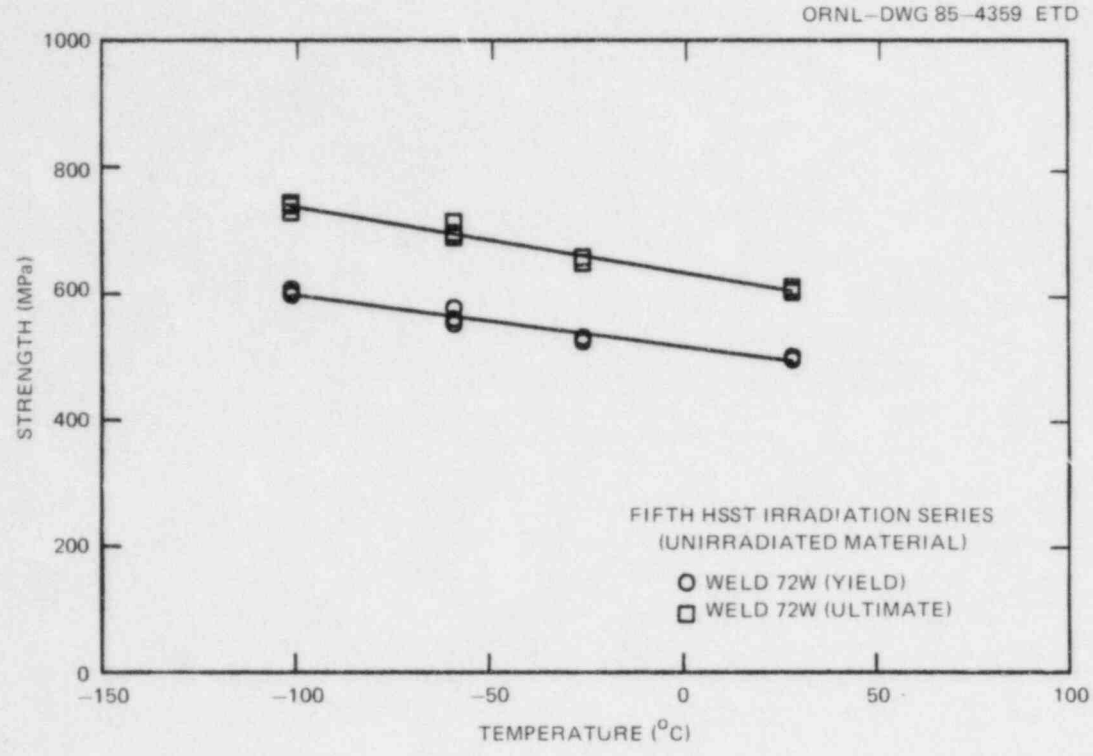

Fig. 6.2. Tensile strength for unirradiated weld 72W.

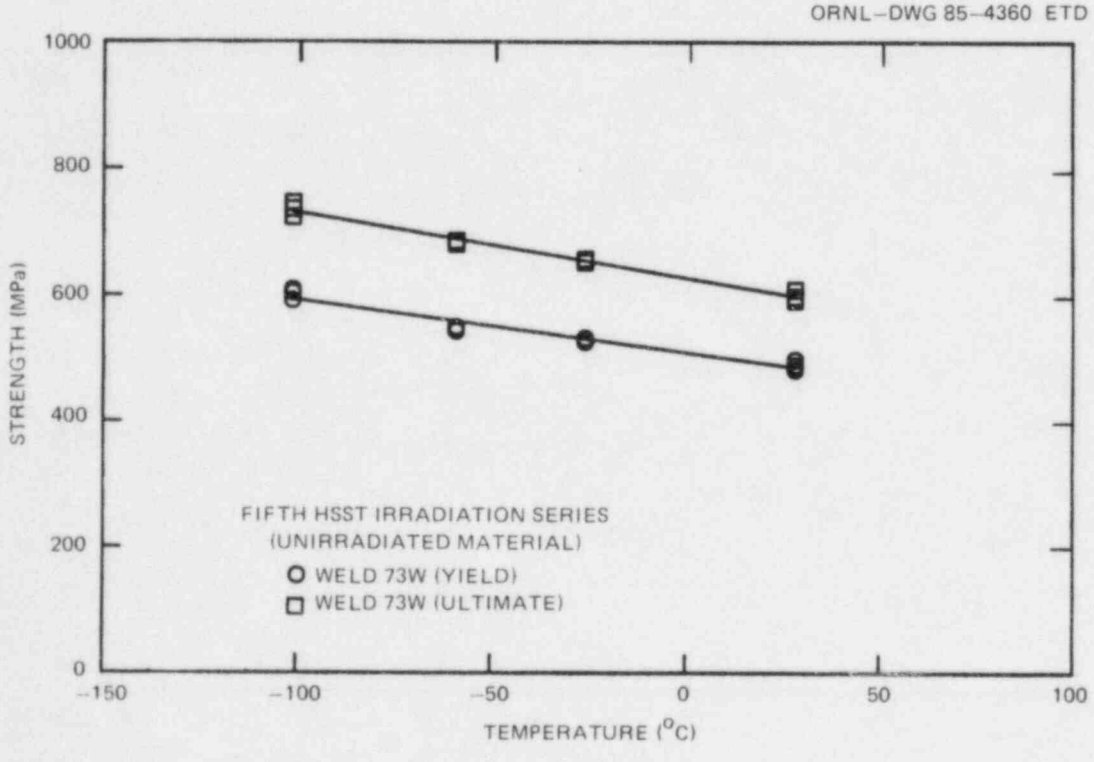

Fig. 6.3. Tensile strength for unirradiated weld 73W.

Table 6.2. CVN properties of unirradiated welds for Fifth HSST Irradiation Program

Specimen	Temperature (°C)	Energy (J)	Lateral expansion (mm)	Fracture appearance (% shear)
72W301	22	109.8	1.524	75
72W303	28	134.2	1.834	95
72W305	66	135.6	1.791	95
72W307	93	136.9	1.885	100
72W309	149	134.9	2.050	100
72W321	288	142.4	2.235	100
72W323	10	107.1	1.473	70
72W325	−18	71.9	0.828	52
72W327	−46	16.3	0.272	18
72W329	−73	9.5	0.081	10
72W331	−101	4.7	0.046	5
72W332	−32	35.3	0.541	20
72W333	−4	46.1	0.744	40
72W336	−4	77.3	1.181	48
72W338	−32	27.8	0.368	14
72W341	−32	19.7	0.338	12
72W343	−101	7.5	0.069	3
73W384	38	132.9	1.905	93
73W385	−18	69.8	1.092	54
73W386	66	139.6	2.108	100
73W387	149	132.2	1.981	100
73W388	288	133.8	2.235	100
73W389	10	104	1.575	78
73W390	−46	32.5	0.483	13
73W391	−32	64.1	1.016	36
73W392	−59	13.6	0.279	14
73W393	−4	108.5	1.651	85
73W394	−46	44.7	0.660	23
73W395	−73	7.5	0.102	0
73W397	−101	7.5	0.076	0

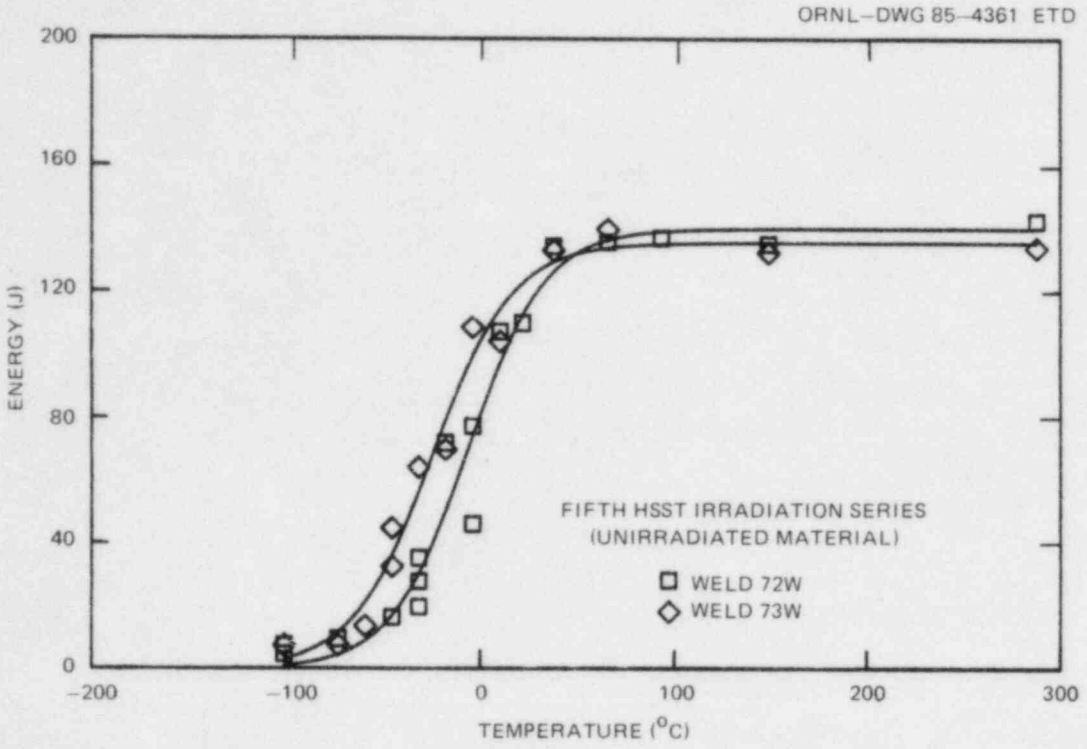

Fig. 6.4. CVN energy for unirradiated welds 72W and 73W.

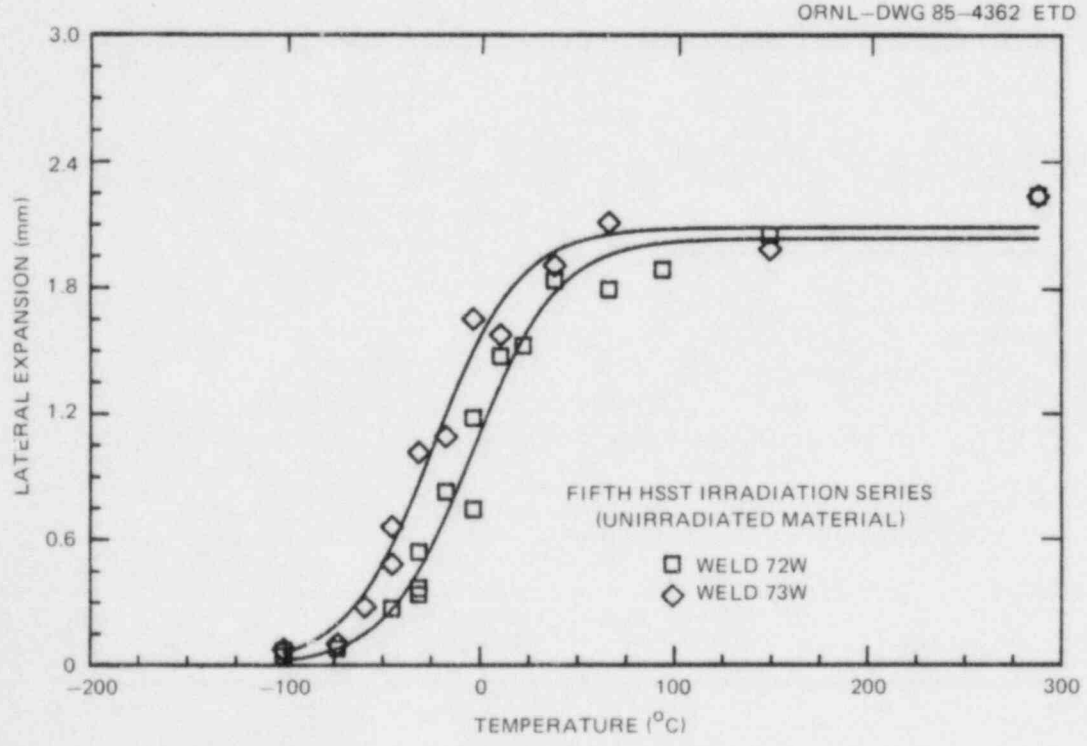

Fig. 6.5. CVN lateral expansion for unirradiated welds 72W and 73W.

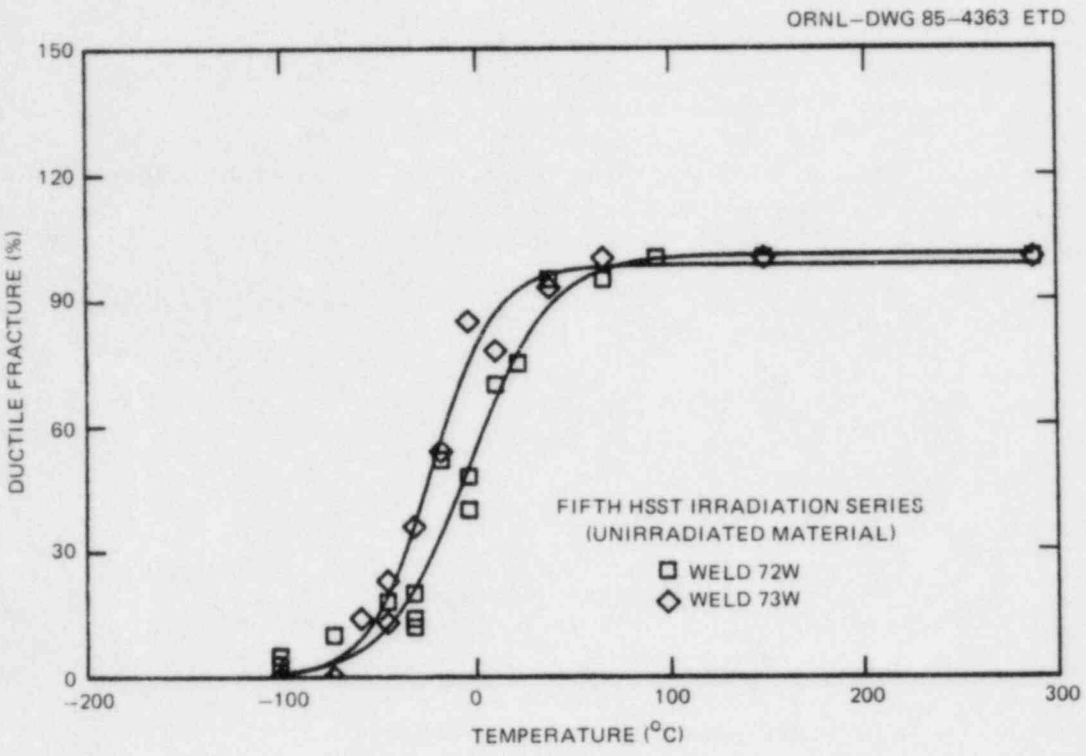

Fig. 6.6. CVN ductile fracture for unirradiated welds 72W and 73W.

Table 6.3. Comparison of CVN and drop-weight test results for Fifth HSST Irradiation Program

Material property	Weld	
	72W	73W
Upper-shelf energy, J	140	135
Upper-shelf lateral expansion, mm	2.04	2.09
41-J transition temperature, °C	−24	−42
0.9-mm lateral expansion transition temperature, °C	−10	−31
Fracture appearance transition temperature, °C	−4	−23
Drop-weight nil-ductility temperature, °C	−29	−46

HP-9836 desktop computer, the single specimen unloading compliance technique was used to determine the crack length throughout the test. A sufficient number of unloadings were performed so that an accurate R-curve could be determined. The parameters of each unloading were controlled by the desktop computer to ensure a crack-length measurement precision of 0.03 mm. When applicable, K_{Ic} according to ASTM E399 (Ref. 5) was determined; otherwise, the modified Ernst J-integral[6] was used to determine

$$K_{Jc} = \sqrt{EJ_c} \ , \tag{6.1}$$

where

$$E(GPa) = 207.2 - 0.057T \ (°C) \ . \tag{6.2}$$

A plasticity correction ("beta correction") was determined from the K_J value at cleavage using the Merkle method.[7] A summary of the scoping fracture-toughness results for the two welds is in Table 6.4. A comparison of the fracture toughness and beta-corrected fracture toughness is shown in Figs. 6.7 and 6.8, respectively. From the scarce data available, the differences in fracture toughness between the two welds do not appear significant.

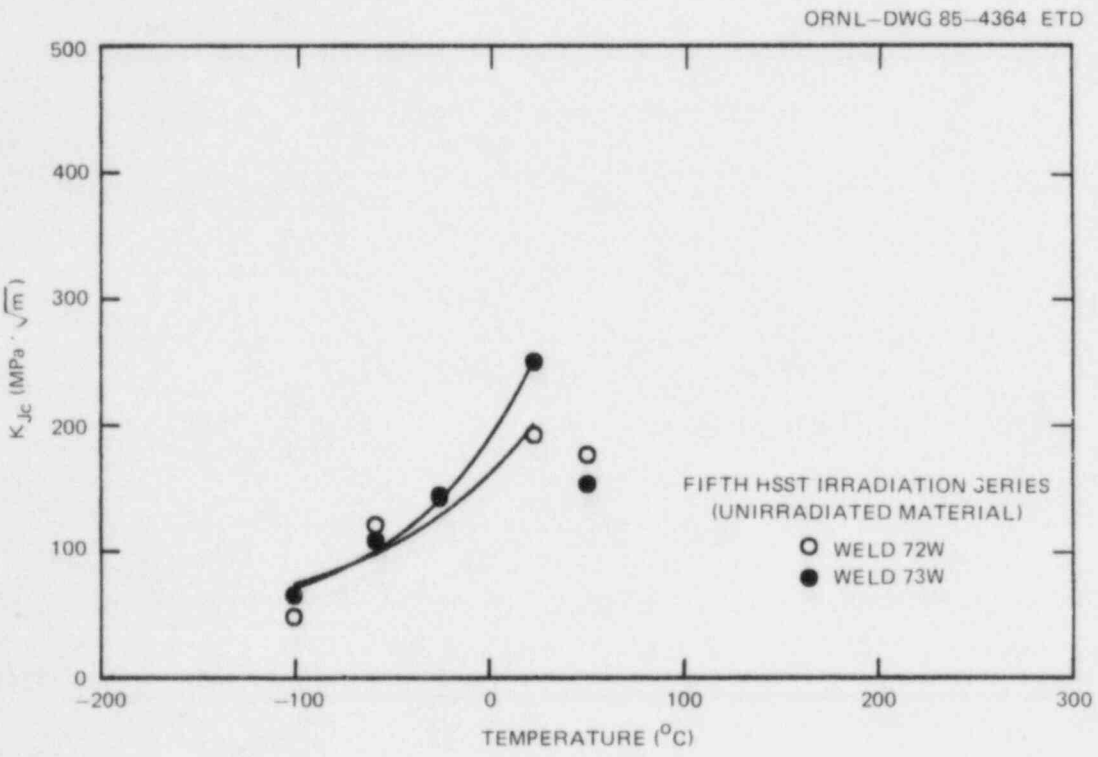

Fig. 6.7. Fracture toughness for unirradiated welds 72W and 73W.

Table 6.4. Fracture-toughness results of unirradiated specimens from Fifth HSST Irradiation Program

Specimen	Test temperature (°C)	Side grooves (%)	(a/w_1)	Ductile Δa (mm)	J_{max} (kJ/m^2)	J_{Ic} (kJ/m^2)	J_{cleave} (kJ/m^2)	K_{Jc} (MPa$\cdot\sqrt{m}$)	$K_{J_{cleave}}$ (MPa$\cdot\sqrt{m}$)	Beta-corrected $K_{J_{cleave}}$ (MPa$\cdot\sqrt{m}$)	T_{av}	Cleave	Comments
72W103	−101	0	0.525	<0.02	10.3		10.3	46.8	46.8	45.3		Yes	K_{Ic} = 48.3 MPa$\cdot\sqrt{m}$
72W105	−59	0	0.528	0.06	69.0		69.0	120.6	120.6	83.9		Yes	
72W109	−26	0	0.526	0.11	96.6		96.6	142.0	142.0	87.3		Yes	
72W111	23	0	0.520	0.92	270.4	180.0	387.8	192.0[a]	282.6	111.3	242	Yes	Cleaved after max load
72W101	50	20	0.609	5.52	240.9	152.0		176.0[a]			158	No	
73W127	−101	0	0.552	<0.02	19.8		19.8	64.9	64.9	59.2		Yes	
73W129	−59	0	0.557	0.06	55.5		55.5	108.1	108.1	78.3		Yes	
73W133	−26	0	0.553	0.12	99.2		99.2	143.9	143.9	88.2		Yes	
73W135	23	0	0.553	1.75	357.7	303.0		250.0[a]			276	No	
73W125	50	20	0.621	7.40	229.8	115.0		153.0[a]			138	No	

[a] J_{Ic} used to calculate K_{Jc}; otherwise, J_{max} load used.

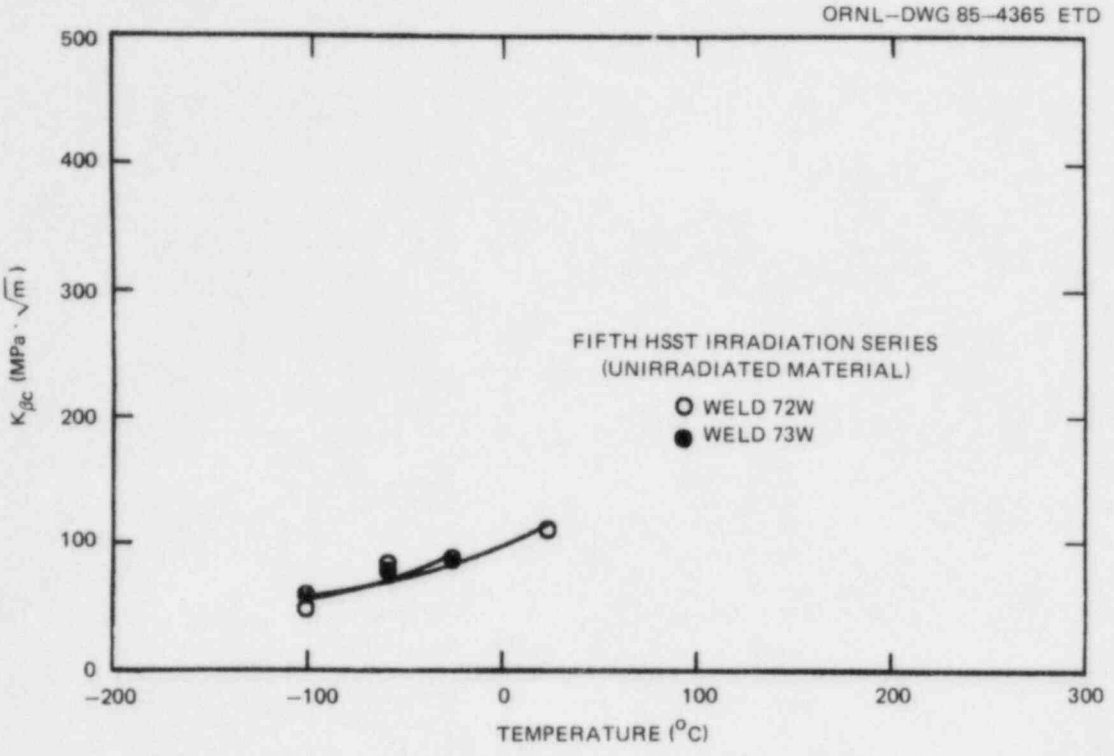

Fig. 6.8. Beta-corrected fracture toughness for unirradiated welds 72W and 73W.

6.3 Sixth HSST Irradiation Series: Crack Arrest

W. R. Corwin

This series will examine the amount and shape of the neutron irradiation-induced shift in the crack-arrest toughness of two weldments. This is a companion irradiation program to the Fifth HSST Irradiation Series, from which the same two high-copper weldments, irradiation facilities, and irradiation conditions will be utilized. The material is currently on hand, having been fabricated concurrently with that for the Fifth Irradiation Series. During this report period the preliminary specimen complement and capsule design were completed, for which temperature and fluence calculations are now in progress. It is currently anticipated that, rather than the three similarly sized capsules originally envisioned, two somewhat larger capsules than those in use in the Fifth Irradiation will be irradiated simultaneously. Each capsule will contain material from only one weldment. The tentative specimen complement per capsule is contained in Table 6.5. The majority of the largest specimens are now planned to be duplex specimens. Based on recent work at Battelle-Columbus Laboratories (BCL),[8] values of crack-arrest toughness exceeding 150 MPa·$\sqrt{m}$ can be obtained with these specimens. Work has been initiated at ORNL to develop the capability for the fabrication and testing of duplex specimens.

Table 6.5. Tentative specimen complement for each material for the Sixth HSST Irradiation Program

Specimen dimensions[a] (mm)	Specimen quantity
25.4 × 76.2 × 76.2	8
25.4 × 152.4 × 152.4	7
33.0 × 152.4 × 152.4	15

[a]All specimens will be transverse-loaded, compact crack-arrest.

6.4 Seventh HSST Irradiation Series: Stainless Steel Cladding

W. R. Corwin

6.4.1 Phase 1

This first phase of the Seventh Irradiation program evaluated stainless steel cladding applied in three layers by the single-wire submerged-arc method. Regardless of the cladding's microstructure, which varied from layer to layer, the cladding exhibited a ductile-to-brittle transition as a function of temperature in Charpy impact testing. These data, as well as a description of the progress to date, are contained in a summary report published during this report period.[9] To ascertain why a nominally austenitic material would exhibit transition behavior typical of a ferritic steel, an examination of the fracture path was undertaken. Results previously reported[10] showed that below the midtransition the fracture preferentially followed the small volume fraction of δ-ferrite present in the cladding. The results presented here show that this is not the case for fracture on the Charpy upper shelf.

A section showing the profile of the fracture surface (Fig. 6.9) was taken through the center of a Charpy specimen, which had been tested on the upper shelf. The notch of the specimen and, therefore, the initiation of the fracture are in the first applied layer of cladding, type 309 stainless steel. Due to the relative thickness of the first layer, the back of the specimen away from the notch was located in the second weld layer, type 308 stainless steel. Examining the fracture path in the type 309 stainless (Fig. 6.10, taken at location 1 in Fig. 6.9) shows that preferential fracture of the ferrite does not occur. As has been noted previously,[9] the microstructure of the type 309 weld metal is atypical of good quality cladding because of excessive base metal dilution during fabrication. It is composed of austenite, tempered martensite, and ferrite. The morphology of the ferrite (relatively large plates) is also

M&C PHOTO Y198600

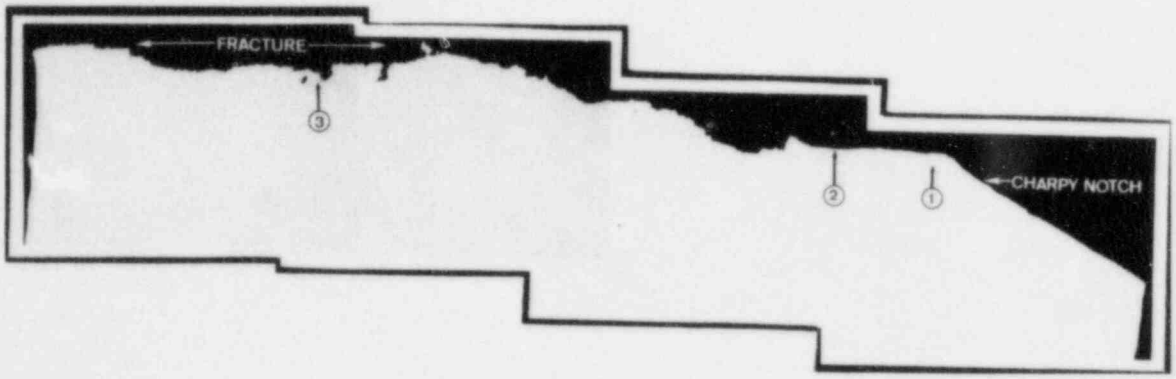

Fig. 6.9. Macroscopic section through the center of a Charpy specimen tested on the upper shelf. The notch is located in a weld pass of type 309 stainless steel; the back side of the specimen is type 308 stainless steel. (Original reduced 7%)

M&C PHOTO Y198387

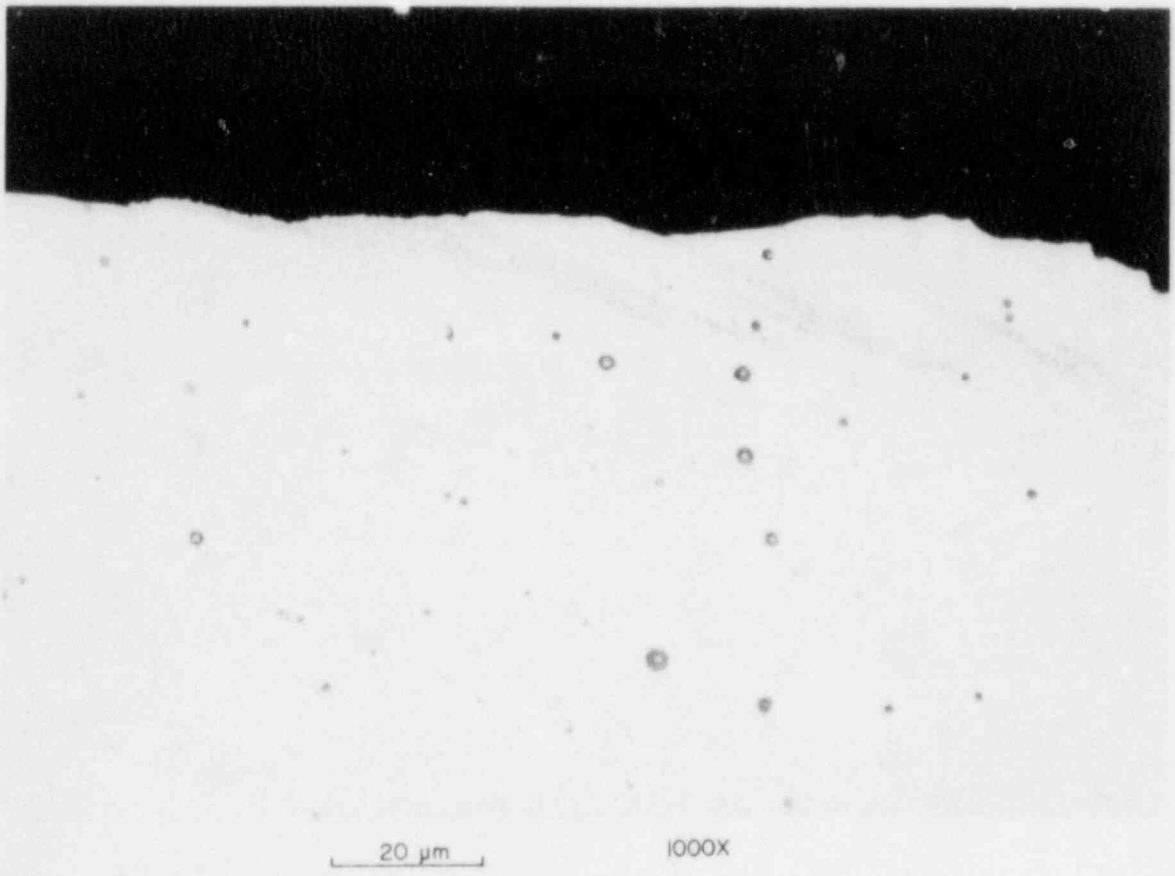

Fig. 6.10. Detail of the profile of the fracture path in the type 309 stainless steel in area 1 of Fig. 6.9, showing that the fracture does not preferentially follow the ferrite (gray patches), as opposed to the matrix of the austenite. (Original reduced 5%)

notably different than that in good quality cladding, as in the type 308 stainless steel layer. In the type 308 stainless steel layer, which does have a microstructure representative of good practice cladding — δ-ferrite in an austenite matrix — the same behavior is observed. Examining the fracture profile within the type 308 stainless steel (Fig. 6.11, taken at location 3 in Fig. 6.9) shows clear indications of a dimple rupture failure with no preferential δ-ferrite failure.

Based on the fractographic evidence, it is assumed that for both the types 308 and 309 stainless steel cladding at upper-shelf temperatures, the ferrite is at least as tough as the austenite; thus, the fracture proceeds primarily through the matrix, and the ferrite then fails only coincidentally.

6.4.2 Phase 2

In the second phase of the cladding irradiations, material that is commercially produced and representative of cladding actually used in the

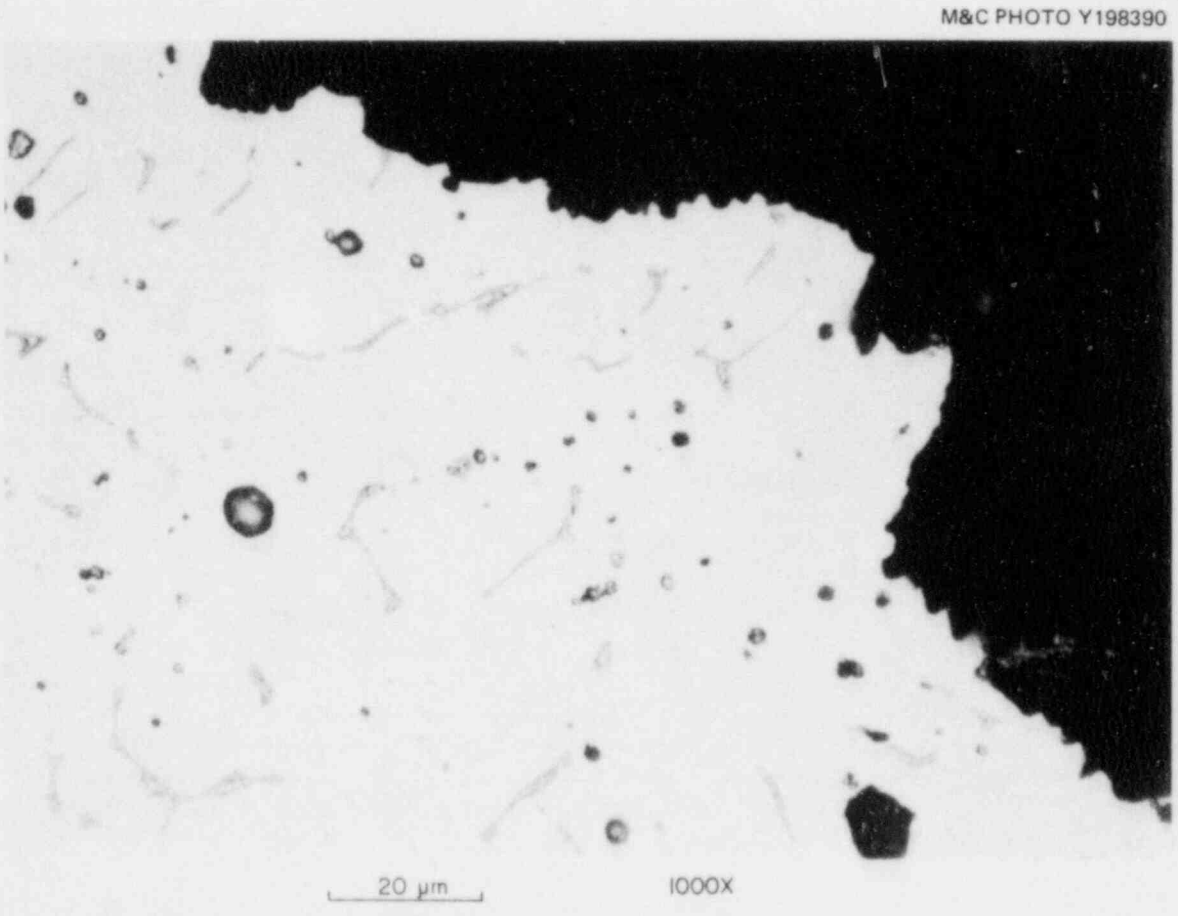

Fig. 6.11. Detail of the profile of the fracture path of the type 308 stainless steel in area 3 of Fig. 6.9, showing that the fracture does not preferentially follow the δ-ferrite (gray patches).

fabrication of early reactor vessels will be examined. To that end, a weldment, which had been ordered from Combustion Engineering (CE) and produced using their three-wire series-arc process, was received during this report period. In this submerged-arc welding process, an arc is drawn between two wire electrodes rather than between an electrode and the base plate. The third wire is fed cold into the weld puddle. By varying the weld wires (typically types 308, 309, and/or 312) and feed rates, a range of weld-puddle compositions can be achieved. For our purposes this wide potential range of composition control was very advantageous. Three layers of cladding are required to provide adequate thickness from which to obtain the specimens for the irradiation experiment. The first layer was applied using the parameters from a typical procedure originally utilized to clad vessels. Adjustments were then made in the second and third layers as needed to obtain similar material chemistries and properties. Table 6.6 provides the chemical compositions for each layer of the clad characterization block.

Table 6.6. Chemical composition of the three-layer stainless steel weld clad overlay to be used in phase 2 of the Seventh HSST Irradiation Program

Layer	Content (wt %)										
	C	Cr	Ni	Mo	Mn	Si	Co	Cu	V	P	S
1	0.052	19.75	9.75	0.18	1.59	0.63	0.03	0.07	0.03	0.016	0.014
2	0.049	19.38	9.18	0.23	1.28	0.78	0.07	0.36	0.06	0.023	0.017
3	0.049	19.34	9.04	0.23	1.34	0.82	0.08	0.39	0.06	0.023	0.017

The need for uniformity among the layers of cladding became obvious in phase 1 of this program,[9] and the specification for the production of the weldments incorporated several requirements to ensure adequate uniformity. Testing performed by CE under the terms of their subcontract showed that the degree of uniformity among layers was very good, and the chemical compositions of all layers were very similar. Subsize Charpy impact specimens (5 mm thick) were taken from each layer of the weldment and tested at 16°C*; the maximum variation in impact energy for any one layer was within ~15% of the average energy for all specimens.

Subsequent metallographic examination at ORNL confirmed that the microstructures (Fig. 6.12) of all three layers were similar both to one another and to the microstructure of good quality cladding that exists in the field.[11] The macroscopically measured ferrite number (FN) was also similar among layers and ranged from 4.7 to 6.4.

*This is the approximate expected test temperature of the phase 2 clad-beam experiments (see Sect. 3.2). Using identical cladding procedures, the clad-beam specimens were fabricated concurrently with the cladding for phase 2 of the Seventh Irradiation.

ORNL PHOTO 1772-85 (Part A)

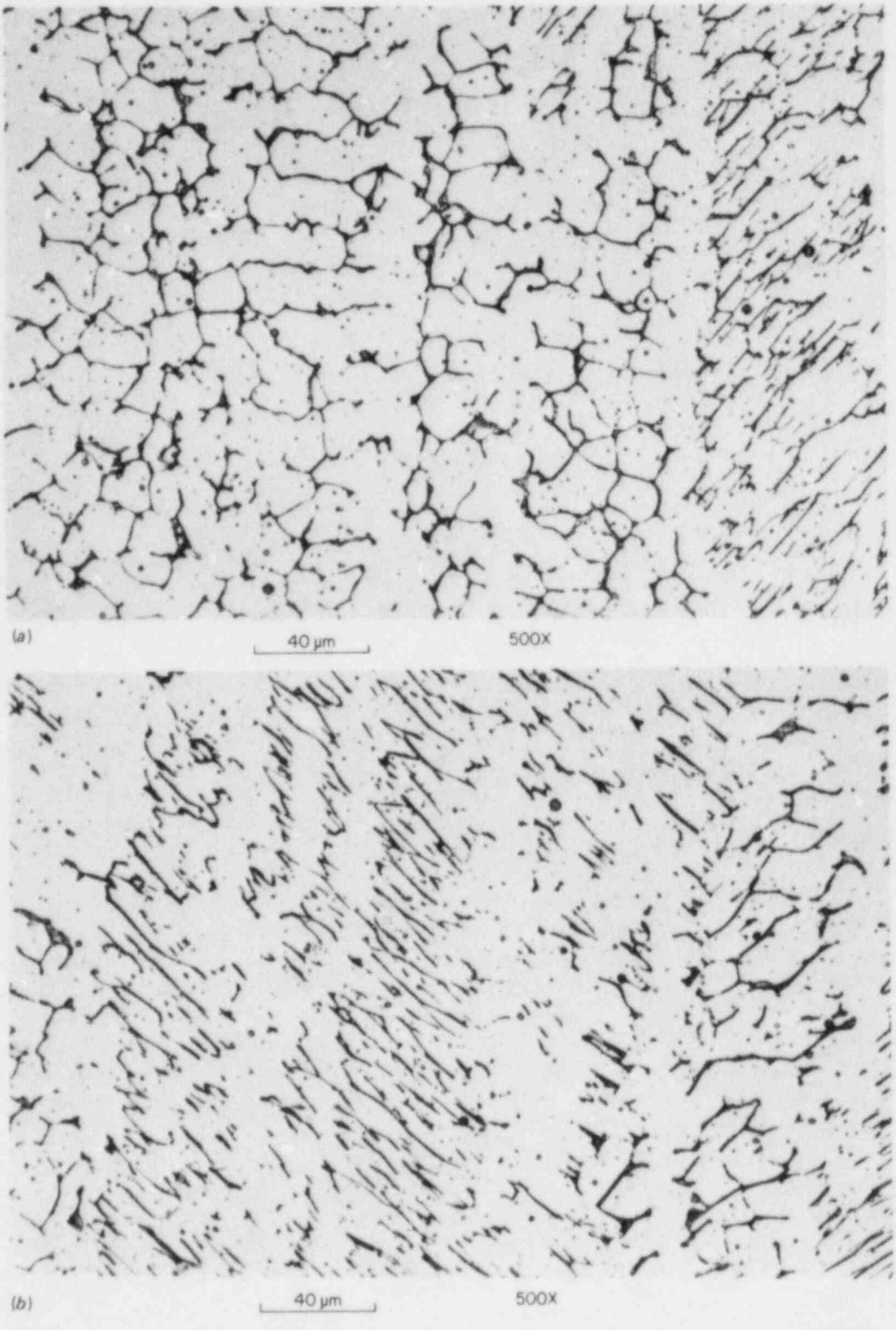

Fig. 6.12. Microstructures of the (*a*) top, (*b*) middle, and (*c*) bottom layers of the three-wire series-arc cladding for phase 2 of the Seventh Irradiation. All consist of δ-ferrite in an austenitic matrix and represent good-quality commercial cladding. (Original reduced 16%)

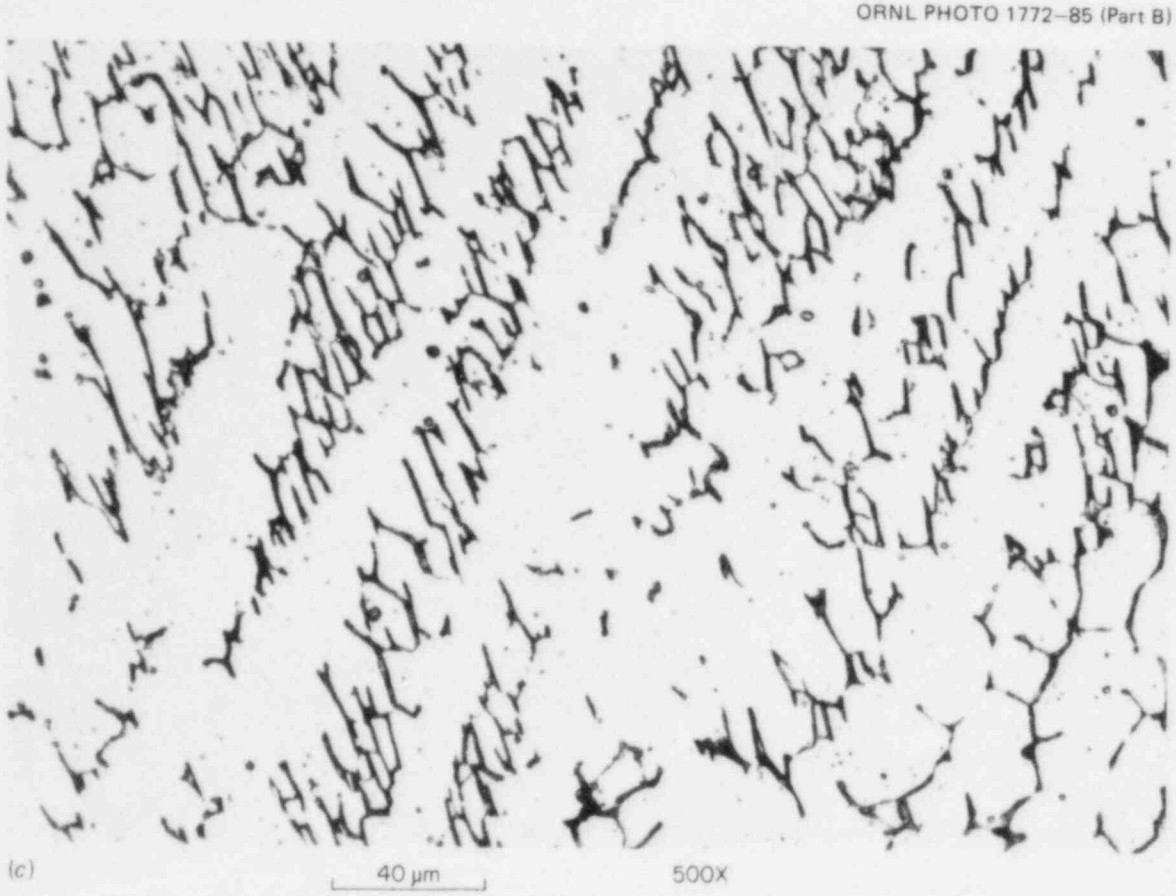

Fig. 6.12 (continued) (Original reduced 4%)

The cladding was given a postweld heat treatment (PWHT) at CE of 593°C for 10 h, notably less than the PWHT of 621°C for 40 h typically given to the cladding of a pressurized-water reactor (PWR) during fabrication. The cladding received this milder PWHT at CE due to requirements of the clad-beam program (see Sect. 3.2) with which the irradiation program cladding was concurrently fabricated. To bring the heat treatment of the cladding into the range more typically given PWRs, additional PWHT was performed. Calculations were made using the following tempering parameter (TP) (Ref. 12):

$$TP = T(20 + \log t) \times 10^{-3} \quad , \tag{6.3}$$

where

T ≡ temperature K and

t ≡ time h.

According to this method, the PWHT given the cladding at CE was calculated to be equivalent to a time of 2.2 h at 621°C. Therefore, an additional 37.8 h of PWHT at 621°C was given the cladding at ORNL to approximate the typical 40-h period.

Specimen fabrication for the irradiation experiment and contractural negotiations with MEA, who will perform the specimen irradiation, have been initiated. The irradiation is expected to be completed in the next report period.

References

1. R. G. Berggren and R. K. Nanstad, "Irradiation-Induced K_{Ic} Curve Shift," pp. 74–78 in *Heavy-Section Steel Technology Program Quart. Prog. Rep. April–June 1982*, NUREG/CR-2751, Vol. 2 (ORNL/TM-8369/V2), Union Carbide Corp. Nuclear Div., Oak Ridge Natl. Lab.

2. R. G. Berggren and R. K. Nanstad, "Irradiation-Induced K_{Ic} Curve Shift," pp. 61–62 in *Heavy-Section Steel Technology Program Quart. Prog. Rep. October–December 1982*, NUREG/CR-2751, Vol. 4 (ORNL/TM-8369/V4), Union Carbide Corp. Nuclear Div., Oak Ridge Natl. Lab.

3. R. G. Berggren et al., "Irradiation-Induced K_{Ic} Curve Shift," pp. 98–99 in *Heavy-Section Steel Technology Program Semiannual Prog. Rep. October 1983–March 1984*, NUREG/CR-3744, Vol. 1 (ORNL/TM-9154/V1), Martin Marietta Energy Systems, Inc., Oak Ridge Natl. Lab.

4. R. G. Berggren et al., "Fifth HSST Irradiation Series," pp. 144–65 in *Heavy-Section Steel Technology Quart. Prog. Rep. April–September 1984*, NUREG/CR-3744, Vol. 2 (ORNL/TM-9154/V2), Martin Marietta Energy Systems, Inc., Oak Ridge Natl. Lab.

5. *Standard Test Method for Plane-Strain Fracture Toughness of Metallic Materials*, E399-83, American Society for Testing and Materials, Philadelphia, 1983.

6. H. A. Ernst, "Material Resistance and Instability Beyond J-Controlled Crack Growth," pp. I-191–213 in *Elastic-Plastic Fracture: Second Symposium*, ASTM STP 803, American Society for Testing and Materials, Philadelphia, 1983.

7. J. G. Merkle, *An Examination of the Size Effects and Data Scatter Observed in Small-Specimen Cleavage Fracture Toughness Testing*, NUREG/CR-3672 (ORNL/TM-9088), Martin Marietta Energy Systems, Inc., Oak Ridge Natl. Lab., April 1984.

8. A. R. Rosenfield et al., "Crack-Arrest Studies at Battelle-Columbus Laboratories," pp. 102–9 in *Heavy-Section Steel Technology Program Semiannual Prog. Rep. April–September 1984*, NUREG/CR-3744, Vol. 2 (ORNL/TM-9154/V2), Martin Marietta Energy Systems, Inc., Oak Ridge Natl. Lab.

9. W. R. Corwin, R. G. Berggren, and R. K. Nanstad, *Charpy Toughness and Tensile Properties of a Neutron-Irradiated Stainless Steel Submerged-Arc Weld Cladding Overlay*, NUREG/CR-3927 (ORNL/TM-9309), Martin Marietta Energy Systems, Inc., Oak Ridge Natl. Lab., September 1984.

10. W. R. Corwin and R. J. Gray, "Seventh HSST Irradiation Series: Stainless Steel Cladding," pp. 154–65 in *Heavy-Section Steel Technology Program Semiannual Prog. Rep. April–September 1984*, NUREG/CR-3744, Vol. 2 (ORNL/TM-9154/V2), Martin Marietta Energy Systems, Inc., Oak Ridge Natl. Lab.

11. W. R. Corwin et al., *Effect of Stainless Steel Weld Overlay Cladding on the Structural Integrity of Flawed Steel Plates in Bending*, NUREG/CR-4015 (ORNL/TM-9390), April 1985.

12. R. W. Swindeman et al., *Effect of Tempering on the Strength and Toughness of 2 1/4 Cr-1 Mo Steel Weldments*, ORNL/TM-9307, Martin Marietta Energy Systems, Inc., Oak Ridge Natl. Lab, October 1984.

7. CLADDING EVALUATIONS

7.1 Crack-Arrest Behavior in Clad Beams

G. C. Robinson W. R. Corwin

As reported in Sect. 3.2, Combustion Engineering, Inc., (CE) delivered material for the second series of clad-beam experiments as well as the Seventh HSST Irradiation Series. Working to an Oak Ridge National Laboratory specification, CE developed a method for producing clad-beam specimen blanks that are composed of three-wire series-arc cladding, typical of that used in reactor pressure vessels, deposited on a base plate of pressure vessel steel that has a high ductile-to-brittle transition temperature. This combination of materials will allow testing of the clad beams in a temperature regime in which the cladding is appreciably tougher than the base plate (see Sect. 3.2). This situation will more closely simulate the materials properties expected to exist in good quality cladding in an operating vessel, as well as reduce the ambiguity that resulted from the first series of clad-beam experiments regarding the ability of cladding to mitigate crack propagation. The schedule for testing the first of these specimens is uncertain until more is known about future program budgets. A topical report[1] covering the first series of clad-beam tests was completed and reviewed this period and will be published early next report period.

7.2 Procurement of Clad BWR Vessel Material

G. C. Robinson

Two segments of a boiling-water reactor (BWR) pressure vessel from the Hope Creek Nuclear Power Station, Salem, New Jersey, were obtained for flaw and properties characterization. One piece from the beltline region includes segments of longitudinal and circumferential welds. The second includes a recirculation nozzle. The base material is A 533 grade B steel, and both have stainless steel cladding. Nondestructive and destructive examinations will be performed in FY 1985 to determine flaw distributions in the base metal, cladding, and weld metal. Properties values and variations will be obtained for each material. The efforts for this period have centered on nondestructive examinations of the material.

7.3 Flaw Characterization Studies of Clad BWR Vessel Material

K. V. Cook J. H. Smith
R. W. McClung

Plans were formulated in December 1984 for nondestructive examination of a pressure vessel section to determine flaw density. The vessel section contained both longitudinal and transverse (girth) seam welds and was originally purchased as one piece (~0.7 by 3 m). After locating the seam welds, the vessel section was cut into four samples so that both nondestructive and destructive testing could be performed. The three largest samples were delivered to the Nondestructive Testing Laboratory in early January 1985. The one piece that contains a transverse seam weld is the largest section that remains (identified as sample 1); it is approximately 0.67 × 1.2 × 0.17 m.

Manual ultrasonic examinations with several techniques are to be applied on both the weld seams (from both the clad and underclad surfaces). The clad and immediate underclad regions are also to be examined for flaws. Penetrant testing will be used for the clad evaluation, and special manual ultrasonic methods being applied by pressure vessel inspectors in the field will be used for underclad testing.

An outline of the activities to evaluate the pressure vessel section to determine the as-fabricated status was developed for consideration in mid-December 1984.

A. Evaluate longitudinal and girth welds for flaws (manual ultrasonics)
   1. From external surface
      a. Preliminary examinations, establishment of calibration standards and reflectors
      b. Conduct *ASME Code* examinations and supplementary examinations at higher sensitivity
   2. From internal surface (same as 1a and b above)
   3. Examination from external surface with tandem transducers (techniques for detection of midplane flaws)

B. Examination for underclad cracking (manual ultrasonics)
   1. Acquire special search units, establish procedures, and examine for flaws
   2. Acquire separate search units and perform sizing studies on detected flaws

C. Evaluation of cladding (liquid penetrant)
   1. Etch surfaces to remove smeared metal
   2. Perform high-sensitivity fluorescent penetrant examination

Manual (normal-beam) ultrasonic flaw detection tests (2 MHz) were performed on all three samples of the pressure vessel section. These tests confirmed that no large delaminations exist that could preclude valid angle-beam examination. Calibration of the ultrasonic pulse-echo normal (straight) beam examination was performed on a flat calibration block, previously fabricated[2] and patterned after the *ASME Code* (Fig. 7.1). No indications equivalent in response to that of *Code* calibration were detected.

ORNL PHOTO 3249-7

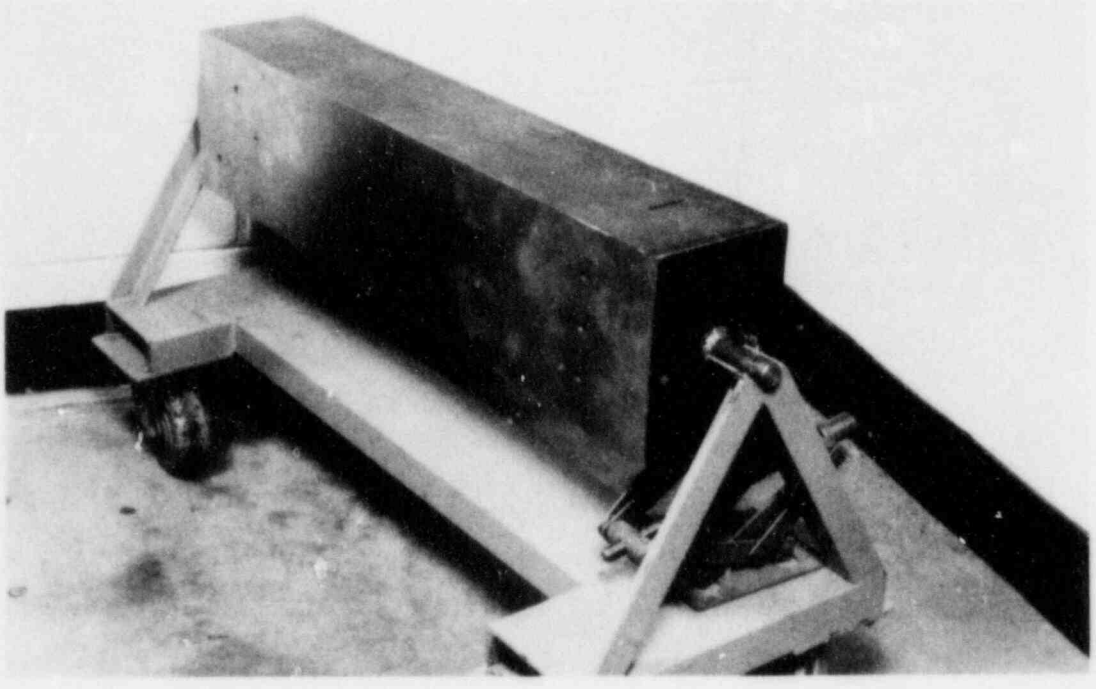

Fig. 7.1. Calibration block patterned after *ASME Code*.

The smallest of the three pieces of pressure vessel material (identified as sample 3) was selected (after both straight-beam and preliminary 45° angle-beam scans were completed) for the machining of reflectors required for calibration of angle-beam examination. As for the flat block, this curved calibration sample patterns the ASME block (i.e., both side-drilled holes and notches were made in accordance with *Code* requirements). In accordance with our sketch, the necessary reflectors have been machined in sample 3, and it has been returned. Thus, we have the necessary calibration reflectors to conduct task A (identified in the outline).

Concurrent with the activities on task A, the special search units required for task B1 were purchased. In addition, the surface grinding work was completed on a clad block of pressure vessel steel that has simulated flaws under the clad that represent those being used by pressure vessel inspectors. This block (previously identified as flawed block 2) had been fabricated for a previous Nuclear Regulatory Commission activity. Again, it is a flat block; however, we expect (for the underclad test) that it will suffice for the task B activities. A preliminary check of the two special flaw detection search units on this block (Fig. 7.2) successfully detected the underclad simulated flaws (e.g., S-1). Of course, the underclad test will not be performed until all examinations from the outer surface are completed and the samples are oriented for inner-surface access.

ORNL-DWG 81-22147

DESCRIPTION OF FLAWS IN BLOCK 2			
		DIMENSIONS, mm (in.)	
FLAW IDENTIFICATION	DESCRIPTION	LENGTH	DEPTH OR DIAMETER
1	MACHINED NOTCH	74.7 (2.94)	12.7 (0.5)
2	MACHINED NOTCH	69.9 (2.75)	6.4 (0.25)
3	EB WELD CRACK	76.2 (3.0)	9.5 (0.375)
5	MACHINED NOTCH	48.0 (1.9)	5.6 (0.22)
6	EB WELD CRACK	76.2 (3.0)	9.5 (0.375)
S-1	MACHINED SLOT BELOW REFERENCE CLAD SURFACE	12.7 (0.5)	5.6 (0.22)
S-2	MACHINED SLOT BELOW REFERENCE CLAD SURFACE	25.4 (1.0)	5.6 (0.22)
A	MACHINED HOLE	228.6 (9.0)	15.88 (5/8)
B	MACHINED HOLE	228.6 (9.0)	15.88 (5/8)
C	MACHINED HOLE	76.2 (3.0)	4.75 (3/16)
D	MACHINED HOLE	76.2 (3.0)	4.75 (3/16)
E	MACHINED HOLE	76.2 (3.0)	4.75 (3/16)
F	MACHINED HOLE	76.2 (3.0)	9.53 (3/8)
G	MACHINED HOLE	76.2 (3.0)	9.52 (3/8)
H	MACHINED HOLE	76.2 (3.0)	9.53 (3/8)

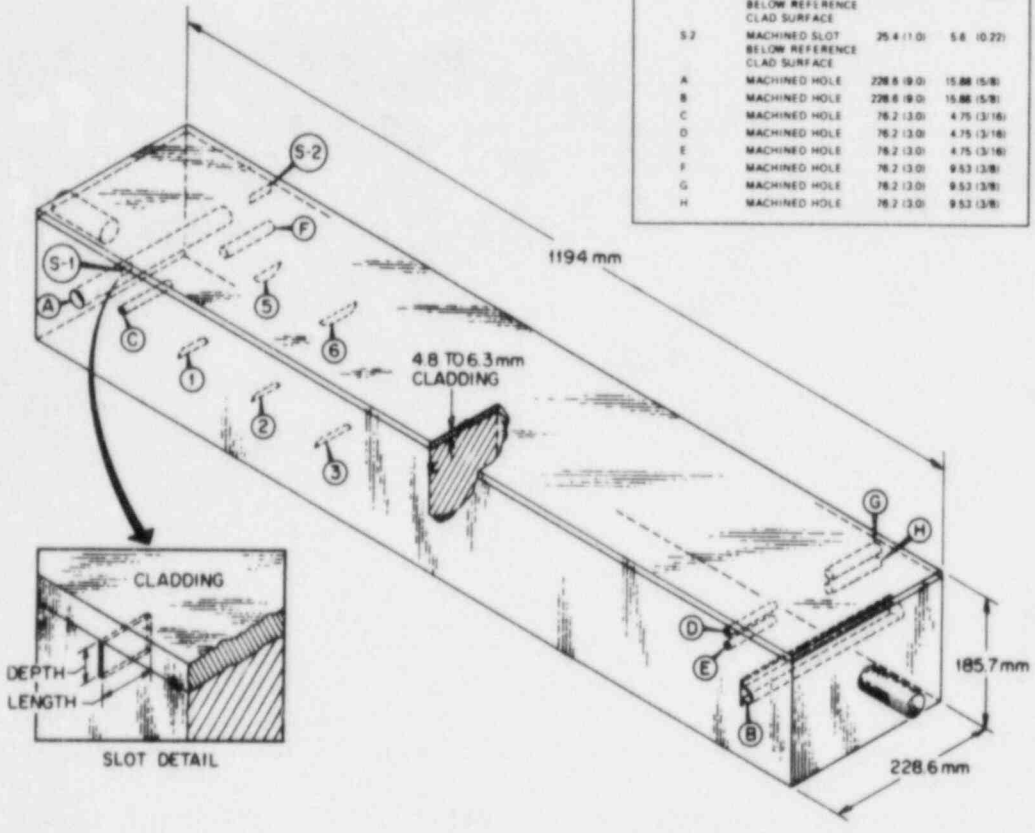

Fig. 7.2. Flawed block 2.

References

1. W. R. Corwin et al., *Effects of Stainless Steel Weld Overlay Cladding on Structural Integrity of Flawed Stainless Plates in Bending, Series No. 1*, NUREG/CR-4015 (ORNL/TM-9390), Martin Marietta Energy Systems, Inc., Oak Ridge Natl. Lab. (to be published).

2. K. V. Cook et al., *Flaw Measurements Using Ultrasonics in Thick Pressure Vessel Steel*, NUREG/CR-2661 (ORNL/TM-8295), Union Carbide Corp. Nuclear Div., Oak Ridge Natl. Lab., August 1982.

8. INTERMEDIATE VESSEL TESTS AND ANALYSIS

During this report period preparation of a topical report on the V-8A test was resumed. This test was an investigation of the tearing behavior of a weld with low toughness at upper-shelf temperatures.

9. THERMAL-SHOCK TECHNOLOGY

R. D. Cheverton

9.1 Summary

As a part of the Integrated Pressurized-Thermal-Shock (IPTS) Program, probabilistic fracture-mechanics (FM) calculations were made for the H.B. Robinson-2 (HBR-2) reactor pressure vessel to obtain a best estimate of the conditional probability of vessel failure [P(F|E)] associated with numerous postulated transients. Those studies indicated that P(F|E) for HBR-2 was very small because of low concentrations of nickel and low values of RT_{NDT_o}.

Studies pertaining to an evaluation of the behavior of subclad flaws under thermal-shock loading conditions were continued. Calculations were made for three test facilities to determine which one would be most suitable for thermal-shock experiments with clad cylinders having subclad flaws. The results indicate that the existing thermal-shock test facility (TSTF) would be appropriate for the first experiment.

9.2 Integrated Pressurized-Thermal-Shock Program Studies

R. D. Cheverton D. G. Ball

The general purpose of the IPTS program is to estimate the frequency of failure of specific pressurized-water reactor (PWR) pressure vessels during overcooling accidents (OCAs) that are postulated for the specific plants. The effort includes defining transients, estimating the frequency of these transients, calculating the corresponding primary-system pressure and downcomer coolant-temperature transients, and, finally, conducting a probabilistic FM analysis of the pressure vessel. In addition, sensitivity and uncertainty analyses are performed, and the effects of proposed remedial measures are investigated. Studies of this type were recently completed for the Oconee-1, Calvert Cliffs-1, and HBR-2 nuclear plants. Fracture-mechanics aspects of these studies have been reported previously[1-3] and are updated in the following paragraphs.

9.2.1 Inclusion of importance sampling in the probabilistic FM model

As discussed in Refs. 1-3, the OCA-P probabilistic model[4] is based on Monte Carlo techniques; that is, a large number of vessels is generated, and each vessel is then subjected to a deterministic FM analysis to determine whether the vessel will fail. Each vessel is defined by randomly selected values of several parameters that are judged to have significant uncertainties associated with them. The calculated conditional probability of vessel failure [P(F|E)] is simply the number of vessels that fail divided by the total number of vessels generated.

Thus,

$$P(F|E) = \sum_j \hat{P}_j V_j N_j \int_0^w f(a)B(a)da \ , \qquad (9.1)$$

where

$$\hat{P}_j = \frac{N'_{fj}}{N'_{vj}} \ ,$$

N'_{fj} = number of vessels with a flaw in the jth region that fail,

N'_{vj} = number of vessels simulated with a flaw in the jth region,

V_j = volume of jth region,

N_j = flaws of all depths per unit volume of the jth region,

a = flaw depth,

$f(a)$ = flaw-depth density function,

$B(a)$ = probability of nondetection,

w = wall thickness.

The parameters N and f(a) pertain to vessel conditions prior to preservice inspection and repair, and B(a) is derived on the basis of repairing or otherwise disposing of all detected flaws.

For very small values of $P(F|E)$, the values of N'_{vj} required to achieve reasonable accuracy become quite large. Under some circumstances, the value of N'_{vj} can be reduced by using importance sampling techniques. This was done in some cases by eliminating flaw depths that did not contribute significantly to initiation and by sampling only the tails of the RT_{NDT} and ΔRT_{NDT} distribution functions, where RT_{NDT} is the nil-ductility reference temperature and ΔRT_{NDT} is the increase due to radiation damage. In each of these cases, the portion of the distribution function not sampled is accounted for by multiplying the number of simulated vessels N'_{vj} by a correction factor. Equation (9.1) then becomes

$$P(F|E) = \sum_j \frac{\hat{P}_j}{F_{1j} F_{2j} F_{3j}} V_j N_j \int_0^w f(a)B(a)da \ , \qquad (9.2)$$

where

F_{1j} = correction factor for flaw-depth density function,

F_{2j} = correction factor for ΔRT_{NDT} distribution,

F_{3j} = correction factor for RT_{NDT} distribution.

For the IPTS studies, when importance sampling was used for the flaw-depth density function, only the first flaw-depth increment was omitted. Thus,

$$F_1 = \frac{1}{\int_{\Delta a_1}^{W} f(a)B(a)da} = 3.24 \ . \qquad (9.3)$$

When applying importance sampling to the ΔRT_{NDT} and RT_{NDT} distribution functions, only those portions of the distributions above 1σ were used. Table 9.1 gives the corresponding values of F_2 and F_3 as a function of the point on the distribution curve at which sampling is commenced. If the distribution is sampled above 1σ, F = 6; if it is sampled above 2σ, F = 46. If both ΔRT_{NDT} and RT_{NDT} are sampled only above 1.25σ and if the first crack-depth increment can be omitted, $F_1 \times F_2 \times F_3 \approx 300$, which represents a significant savings in computer costs for the same accuracy in $P(F|E)$. Of course, this type of importance sampling can only be used when the first crack-depth increment does not contribute much to $P(F|E)$ and when $P(F|E)$ is small enough that only the tails of the ΔRT_{NDT} and RT_{NDT} distribution functions contribute significantly to $P(F|E)$.

Table 9.1. Values of F_2 and F_3 associated with importance sampling of ΔRT_{NDT_s} and RT_{NDT} distributions

Identifying No. (NDLRS or NRTRS)	Start of sampling (number of standard deviations above mean)	Fraction of distribution not simulated[a]	F_2, F_3
1	1.0	0.8422	6.3
2	1.25	0.8954	9.6
3	1.50	0.9343	15.2
4	1.75	0.9611	25.7
5	2.00	0.9784	46.4
6	2.25	0.9891	91.7
7	2.60	0.9951	204.1
8	2.75	0.9983	588.2

[a]Assuming truncation at ±3σ.

The number of vessels that must be simulated depends on the accuracy required for the calculated value of $P(F|E)$, and as small a number as practical is used to minimize computer costs. The minimum number of simulated vessels required to satisfy a specified accuracy is estimated

by applying the central limit theorem.[4] Using this approach and specifying a 95% confidence level yields

$$P(F|E)_j = \hat{P}_j \; N_j V_j \int_0^W f(a)B(a)da \pm 1.96 \; \sigma_j \; , \tag{9.4}$$

where

$P(F|E)_j$ = true value of the conditional probability of vessel failure for those vessels having flaws in the jth region only,

σ_j = one standard deviation,

$$\hat{P}_j = \frac{N'_{fj}}{N'_{vj}} \; .$$

For the direct approach (not using importance sampling),

$$\sigma_j = \left[\frac{\hat{P}_j(1 - \hat{P}_j)}{N'_{vj}} \right]^{1/2} N_j V_j \int_0^W f(a)B(a)da \; . \tag{9.5}$$

When importance sampling is used,

$$\sigma_j = \left[\frac{\hat{P}_j(1 - \hat{P}_j)}{N'_{vj} \; F_{1j} \; F_{2j} \; F_{3j}} \right]^{1/2} N_j V_j \int_0^W f(a)B(a)da \; . \tag{9.6}$$

The value of σ corresponding to all of the vessels simulated is

$$\sigma_{P(F|E)} = \sqrt{\sum_j \sigma_j^2} \; , \tag{9.7}$$

and the error ε_j associated with the jth region is

$$\varepsilon_j = \frac{1.96 \; \sigma_j}{\hat{P}_j \; N_j V_j \int_0^W f(a)B(a)da} \; . \tag{9.8}$$

For $\hat{P}_j \ll 1$,

$$\varepsilon_j \approx 1.96 \left(\frac{1}{\hat{P}_j \, N'_{vj}} \right)^{1/2} = 1.96 \left(\frac{1}{N'_{fj}} \right)^{1/2} . \tag{9.9}$$

The total error ε considering all regions of interest is

$$\varepsilon = \frac{1.96 \, \sigma_{P(F|E)}}{\sum_j \hat{P}_j \, N_j V_j \int_0^W f(a)B(a)da} . \tag{9.10}$$

Note [Eq. (9.9)] that the error for a single region ε_j is only a function of N'_{fj}. For the estimate of ε_j to be reasonably accurate, N'_{fj} should be greater than 5 (Ref. 5) or 9 (Ref. 6). However, when calculating the total error [Eq. (9.10)], this rule needs to be adhered to strictly only for those regions that contribute significantly to $P(F|E)$.

9.2.2 The use of RT_{NDT} and ΔRT_{NDT} as independent variables

In some cases it is convenient to use RT_{NDT_s} as an independent variable in the probabilistic FM analysis,[3] where RT_{NDT_s} is the value of RT_{NDT} at the inner surface. This is because it allows one to apply the results to other reactor vessels, provided the transients analyzed are appropriate for the other vessels. However, since $RT_{NDT} = RT_{NDT_o} + \Delta RT_{NDT}$ and $\Delta RT_{NDT} = f(F_o, Cu, Ni)$ [where RT_{NDT_o} is the initial value of RT_{NDT}, F_o is the fast-neutron fluence at the inner surface, and Cu and Ni are the concentrations of copper and nickel in the vessel material (wt %)], RT_{NDT} is not actually an independent variable; that is, the actual independent variables are RT_{NDT_o}, F_o, Cu, and Ni and were used as such in two IPTS studies.[7,8] For the HBR-2 study, values of $\hat{P}_j$ were obtained as a function of $\overline{RT_{NDT_s}}$, and in doing so both RT_{NDT_o} and ΔRT_{NDT_s} were simulated, but only a single value of $\overline{RT_{NDT_o}}$ was considered (−18°C). Following is a discussion of the derivation of the distribution function for ΔRT_{NDT} and the error in using $\overline{RT_{NDT_s}}$ as the independent variable. This information supplements that given in Ref. 3.

The distribution function for $\overline{\Delta RT_{NDT_s}}$ was obtained by performing a Monte Carlo analysis with

$$\Delta RT_{NDT}\ (^{\circ}C) = 0.556[-10 + 470\ Cu + 350\ Cu\ Ni]\ (F \times 10^{-19})^{0.27}\ , \qquad (9.11)$$

in which case F_o and Cu were simulated, and different values of $\overline{F_o}$, $\overline{Cu}$, and Ni were included. As in the two previous studies,[7,8] it was assumed that F_o and Cu had normal distributions with $1\sigma = 0.3\ \overline{F_o}$ and 0.025 wt %, respectively. Based on this analysis, a normal distribution with $1\sigma = 0.14\ \overline{\Delta RT_{NDT}}$ was selected for ΔRT_{NDT_s}.

The specific Monte Carlo cases calculated to obtain the typical distribution for ΔRT_{NDT} are shown in Table 9.2, and a typical histogram is presented in Fig. 9.1. It is apparent that (1) the distributions are essentially normal, although the tails are not well defined; (2) the sensitivity of σ to $\overline{F_o}$ and Ni is very small; and (3) the sensitivity to Cu is perhaps significant, although the extent to which it is significant depends on the sensitivity of $P(F|E)$ to the distribution function for ΔRT_{NDT}.

Rather than investigate this latter sensitivity directly, two sets of calculations were made to obtain $P(F|E)$ vs $\overline{Cu}$ for several HBR-2 postulated transients (8.6, 9.19B, 9.33, 9.41).[9] For one set, $\overline{\Delta RT_{NDT_s}}$ was used as an independent variable; for the other set, F_o, Cu, and Ni were used as independent variables. The results, shown in Fig. 9.2, indicate that the error in using $\overline{\Delta RT_{NDT_s}}$ as an independent variable is (1) dependent on the transient, (2) positive for $Cu > 0.25$ and negative for $Cu < 0.25$ (the value of σ used for ΔRT_{NDT} was based on $Cu \simeq 0.25$), (3) larger for the less severe transients, and (4) substantial (factors of ~25 and 7) for the least severe dominant transient and the two extreme values of Cu considered (0.15 and 0.35, respectively).

Note that the error associated with using ΔRT_{NDT_s} as an independent variable is not only the result of having to approximate the distribution function. This can be illustrated by calculating $P(F|E)$ for different combinations of F_o, Cu, and Ni that result in the same value of $\overline{\Delta RT_{NDT_s}}$. Table 9.3 shows the results of a comparison analysis in which F_o and Cu were simulated, two values of $\overline{Cu}$ were considered (0.2 and 0.35), and $\overline{F_o}$ and Ni were adjusted so that $\overline{\Delta RT_{NDT_s}}$ was the same for both values of $\overline{Cu}$. As indicated, the lower value of Cu resulted in a higher value of $P(F|E)$, and the less severe the transient the greater the ratio.

Table 9.2. Monte Carlo-derived distributions for ΔRT_{NDT}

Input parameters			σ (% of mean)	ΔRT_{NDT} (°C)			
				2.5 percentile		97.5 percentile	
$\overline{Cu}$ (wt %)	Ni (wt %)	$\overline{F_o}$ (10^{19} neutrons/cm^2)		Monte Carlo	Normal approximation	Monte Carlo	Normal approximation
0.2	1.0	2.0	16.1	71	69	135	135
0.3	1.0	2.0	12.5	100	100	194	196
0.2	0.2	2.0	16.4				
0.3	0.2	2.0	12.6				
0.15	1.0	2.0	20.2				
0.25	1.0	2.0	13.8				
0.35	1.0	2.0	11.6				
0.20	1.0	1.0	16.0				
0.20	1.0	4.0	16.1				

ORNL-DWG 85-4366 ETD

STATISTICS FOR OUTPUT VARIABLE DRTNDT

MINIMUM 44.47 MAXIMUM 231.87

MEAN 156.59 VARIANCE 383.0 STD. DEVIATION 19.57

PERCENTILES: 2.5% 118. 5.0% 124. 50.0% 157. 95.0% 188. 97.5% 194.

50000 POINT HISTOGRAM * = 77 POINTS

PROB	CUMP	DRTNDT(°C)		
0.0001	0.0	44.44	7	*
0.0001	0.0001	50.00	4	*
0.0002	0.0002	55.56	11	*
0.0002	0.0004	61.11	8	*
0.0002	0.0006	66.67	8	*
0.0002	0.0008	72.22	11	*
0.0004	0.0010	77.78	19	*
0.0005	0.0014	83.33	23	*
0.0011	0.0018	88.89	54	*
0.0015	0.0029	94.44	77	*
0.0027	0.0044	100.0	133	**
0.0052	0.0071	105.6	261	***
0.0096	0.0123	111.1	480	******
0.0182	0.0219	116.7	908	************
0.0288	0.0401	122.2	1440	********************
0.0448	0.0689	127.8	2241	******************************
0.0631	0.1137	133.3	3153	***
0.0827	0.1768	138.9	4134	**
0.1008	0.2594	144.4	5039	**
0.1130	0.3602	150.0	5651	**
0.1147	0.4732	155.6	5736	**
0.1079	0.5880	161.1	5397	**
0.0939	0.6959	166.7	4697	**
0.0743	0.7898	172.2	3713	**
0.0538	0.8641	177.8	2699	************************************
0.0364	0.9179	183.3	1821	************************
0.0224	0.9543	188.9	1122	***************
0.0122	0.9767	194.4	611	********
0.0058	0.9890	200.0	292	****
0.0030	0.9948	205.6	151	**
0.0015	0.9978	211.1	75	*
0.0003	0.9993	216.7	17	*
0.0003	0.9997	222.2	14	*
0.0001	0.9999	227.8	3	*
	1.0000	233.3		

Fig. 9.1. ΔRT_{NDT_s} distribution from a Monte Carlo run for $\mu(Cu)$ = 0.3, $\mu(F_o) = 2 \times 10^{19}$, and Ni = 1.0.

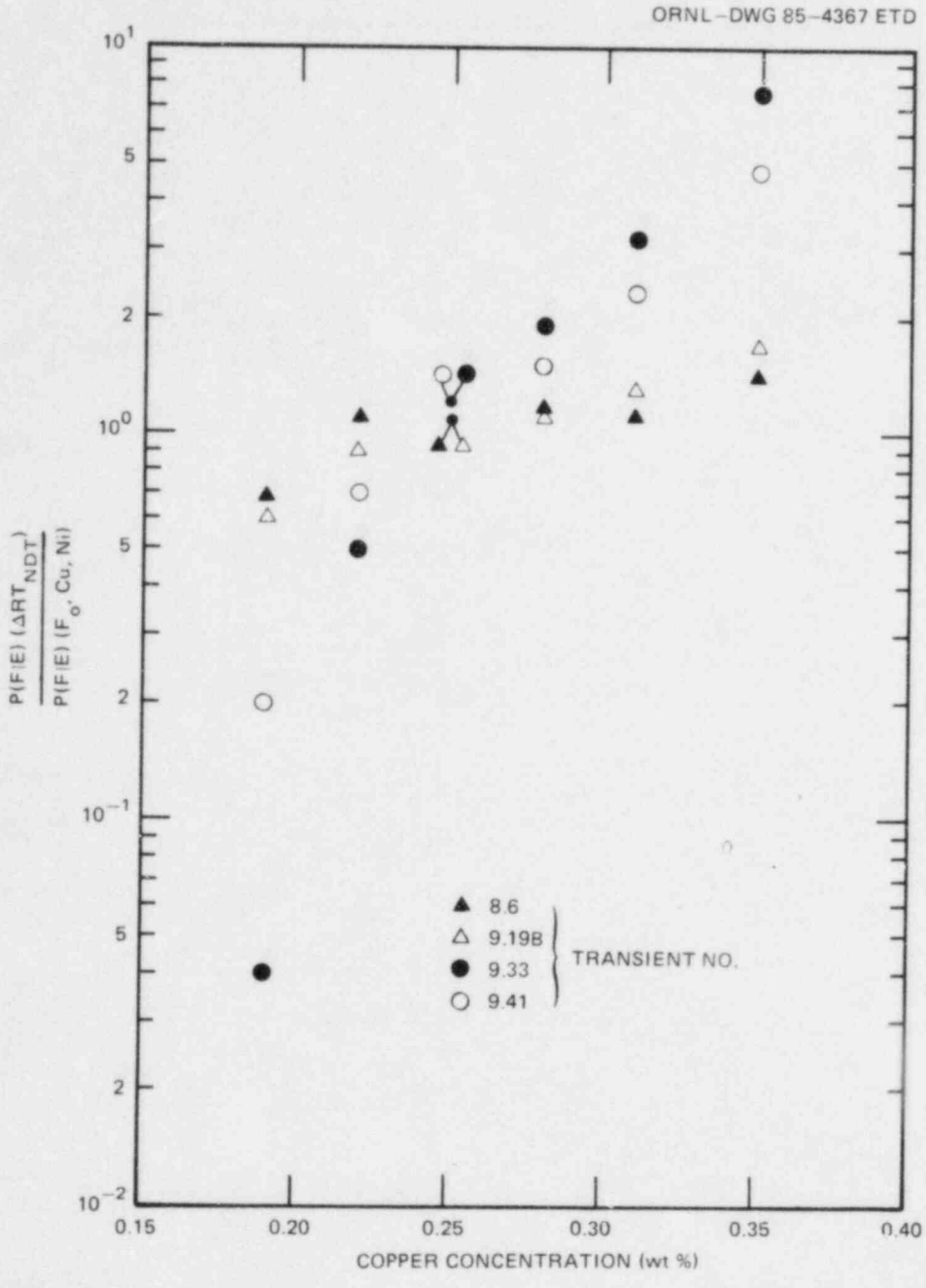

Fig. 9.2. Comparison of calculated values of $P(F|E)$ using ΔRT_{NDT_s} as the independent variable and F_o, Cu, and Ni as independent variables.

The additional error introduced by variations in $\overline{RT_{NDT_o}}$, when using RT_{NDT} as an independent variable, was examined in a similar manner, that is, by comparing values of $P(F|E)$ corresponding to different values of $\overline{RT_{NDT_o}}$. Three values of $\overline{RT_{NDT_o}}$ were considered (−49, −18, +13°C), and values of $P(F|E)$ corresponding to the two extremes were compared with

Table 9.3. Comparison of $P(F|E)$ values[a,b] calculated using F_o, Cu, and Ni as independent variables, considering two values of Cu but only one value of $\overline{\Delta RT_{NDT_s}}$

HBR-2 transient	Minimum coolant temperature (°C)	Pressure at time of failure (MPa)	$\frac{P(F\|E)_1}{P(F\|E)_2}$
8.6	94	12.8	1.5
9.19B	95	10.3	1.9
9.41	131	10.3	6.7
9.33	146	12.1	17

[a] $P(F|E)_1$: Cu = 0.20, Ni = 1.00, F_o = 3.49E19, $\overline{RT_{NDT_o}}$ = −18°C, $\overline{\Delta RT_{NDT_s}}$ = 102°C.

[b] $P(F|E)_2$: Cu = 0.35, Ni = 0.50, F_o = 1.00E19, $\overline{RT_{NDT_o}}$ = −18°C, ΔRT_{NDT_s} = 102°C.

that corresponding to −18°C, because $\overline{RT_{NDT_o}}$ = −18°C was used to obtain the $\hat{P}_j$ vs $\overline{RT_{NDT_s}}$ curves for the HBR-2 study. The results of the comparison, shown in Fig. 9.3, indicate that the error (1) is positive for $\overline{RT_{NDT_o}} < -18°C$, (2) increases with decreasing $\overline{RT_{NDT_s}}$, (3) is small for $\overline{RT_{NDT_s}} > 93°C$, and (4) is greater for the less severe transients.

Although it is convenient to use RT_{NDT_s} as an independent variable, it is apparent from the preceding discussion that the error in doing so can be substantial. Thus, one must use $\hat{P}_j$ vs $\overline{RT_{NDT_s}}$ curves with this understanding. For the most accurate results, RT_{NDT_o}, F_o, Cu, and Ni should be used as the independent variables in a detailed probabilistic FM analysis.

9.2.3 Summary of results for HBR-2

A complete summary of results for the HBR-2 studies is beyond the scope of this report. Furthermore, the full significance of the FM results cannot be appreciated without combining them with estimated frequencies of occurrence of the postulated transients, which is also beyond

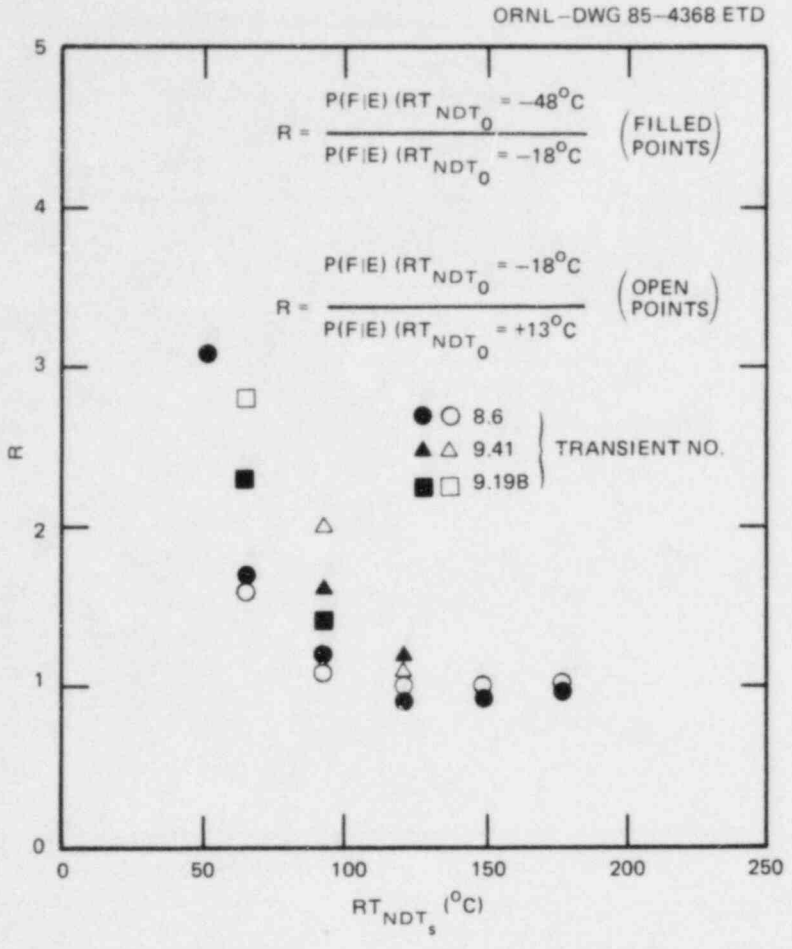

Fig. 9.3. Effect of RT_{NDT_0} on values of P(F|E) calculated using RT_{NDT_s} as an independent variable.

the scope of this report. However, a few points of particular interest will be discussed.

9.2.3.1 Selection of a hypothetical vessel. The IPTS FM studies have included the contributions to the probability of vessel failure of three separate basic regions of the vessel: the axial welds, the circumferential welds, and the plate. For HBR-2, the estimated value of RT_{NDT} at the inner surface is greatest for the plate region, and, of course, the surface area of the plate is substantially greater than that for the welds. Thus, assuming the same flaw surface density for each region, the plate region makes the greatest contribution to the probability of vessel failure.

At 32 effective full-power years (EFPY), the value of RT_{NDT} for the plate is quite low compared with the Nuclear Regulatory Commission screening criteria [132°C (270°F)], and thus the calculated frequency of vessel failure is quite low. This made it difficult to calculate the conditional probability of failure, and thus HBR-2 was not an appropriate

choice for illustrating the probabilistic FM methods of analysis. For this reason, a hypothetical HBR vessel (HBR-HYPO) was created that had a much greater probability of failure. This was done by making adjustments in Cu, Ni, and RT_{NDT_o} so that at 32 EFPY $RT_{NDT_s}(2\sigma)$ = 132°C (270°F) for the region of the wall that would be the dominant contributor to P(F|E), and this region was an axial weld.

9.2.3.2 Conditional probability of vessel failure. The specific transients considered for a detailed analysis are described in Ref. 9. For the FM analysis, these transients were divided into two categories: (1) final coolant temperature >150°C and (2) final coolant temperature ≤150°C. Bounding-type calculations were made for the first category because this approach was much less expensive and because it was expected that the contribution of this category to the frequency of failure [Φ(F)] would be negligible. Transients for the bounding calculations were characterized by a constant pressure of 17 MPa, a step change in coolant temperature and a fluid-film heat transfer coefficient of 2300 $W/m^2 \cdot °C$. The results of these bounding calculations are shown in Fig. 9.4.

Values of P(F|E) for category-2 transients having significantly high values of P(F|E) and/or Φ(F) at 32 EFPY are listed in Table 9.4 for HBR-2 and HBR-HYPO. The listed values of P(F|E) include the contributions from all of the vessel beltline regions. For HBR-HYPO, the contribution of the circumferential welds and of the plate segments was relatively small. However, because of the rather low values of Cu, Ni, and RT_{NDT_o} for the HBR-2 welds, the plate regions were the dominant contributor to P(F|E) for HBR-2, and the corresponding estimated values of P_j were quite low ($<10^{-6}$). As a consequence of these low values, the estimated value of Φ(F) for HBR-2 is quite low ($<10^{-11}$). Therefore, values of P(F|E) for HBR-2 were estimated for only a few of the transients in Table 9.4. The particular transients selected were the six that contributed the most to Φ(F) for HBR-HYPO.

9.2.3.3 Effect of including WPS. During many of the postulated PTS transients, the stress-intensity factor K_I for all crack depths first increases with time, reaches a maximum, and then decreases. For the shallow flaws that are generally responsible for the initial crack-initiation event, once K_I begins to decrease it does so throughout the remainder of the transient. This time-dependent behavior of K_I may prevent failure of a vessel because a flaw cannot initiate while K_I is decreasing, even though $K_I/K_{Ic} > 1$. This phenomenon is referred to as warm prestressing (WPS), and the time of incipient WPS (IWPS) is the time at which K_I becomes equal to zero.

For most of the HBR-2 postulated transients, WPS could be a factor because the calculations indicate that for these transients K_I does not become equal to K_{Ic} until after the time of IWPS. However, WPS is not included in most of the calculations because the K_I vs t curves for the shallow flaws are very flat, making it difficult to determine the maximum. Furthermore, unforeseen variations in pressure and coolant temperature might exist and defeat WPS. Even so, it is of interest to see what the effect is for the idealized transients, and the results of such a study are presented in Table 9.5.

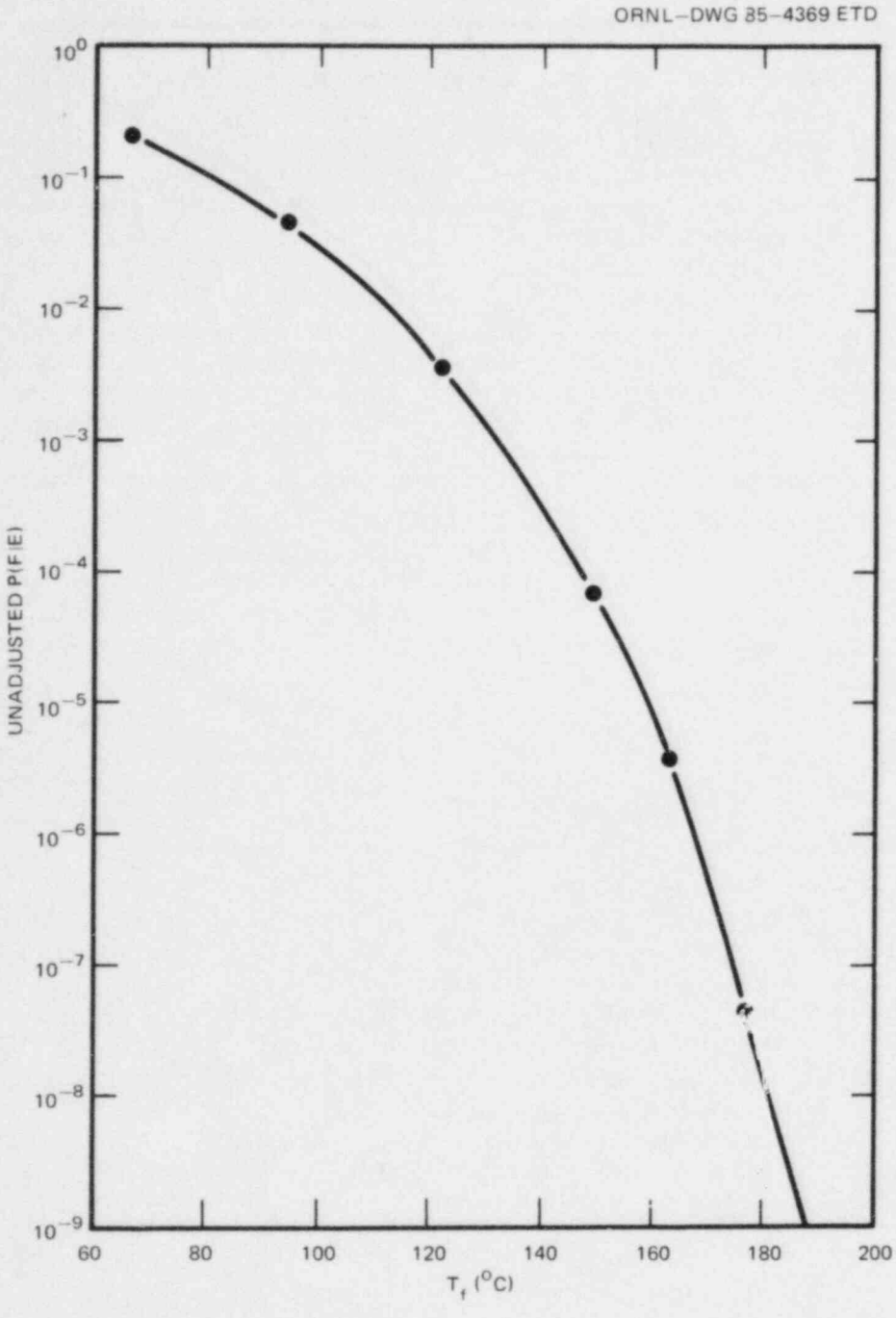

Fig. 9.4. $\hat{P}_j \int_0^W f(a)B(a)da$ vs T_f for HBR-HYPO bounding calculations.

Table 9.4. Summary of calculated values of P(F|E) for HBR-2 and HBR-HYPO at 32 EFPY

Transient	P(F|E) HBR-HYPO	Transient	P(F|E)	
			HBR-2	HBR-HYPO
1.8	~1E-8	9.11A		<1E-7
1.9	<1E-10	9.11B		2.8E-5
2.1	<1E-9	9.12A		2E-7
3.1	<1E-10	9.12B		3.6E-5
4.1	<1E-9	9.14		1.1E-5
5.15	5E-7	9.15		1.2E-5
5.17	6E-7	9.17		1.8E-4
5.19	2E-7	9.18		8.6E-6
5.20	4.8E-6	9.19A		1E-7
6.6	3.7E-4	9.19B(3)[a]	5E-7	9.5E-5
6.9	1.0E-4	9.20A		1E-7
7.5	4.2E-6	9.20B(5)	5E-7	1.0E-4
7.6	1E-7	9.22A		<1E-6
7.8	6E-8	9.22B(6)	4E-5	5.5E-4
7.9	3.0E-6	9.23A		<1E-6
7.10	9.3E-6	9.23B		1.3E-4
7.11	5.6E-5	9.26		2E-7
8.2	1.4E-6	9.28		3.9E-6
8.3	2E-7	9.32		1.8E-6
8.5	4E-7	9.33(2)	<1E-11	2E-7
8.6	6.6E-4	9.34		3E-7
9.4	8E-8	9.37		2E-7
9.5	1.5E-6	9.39		4E-7
9.6	<2E-9	9.40		1E-6
9.9A	<4E-9	9.41(1)	<1E-9	9E-7
9.9B	8E-7	9.42		1.2E-6
9.10A	<2E-8	9.43(4)	<1E-9	1.2E-5
9.10B	1.1E-6	9.45		5E-7

[a] Numbers in parentheses indicate order of dominance in terms of $\Phi(F)$ for HBR-HYPO.

Table 9.5. Effect of including WPS in calculation of $P(F|E)$ for HBR-HYPO at 32 EFPY

Transient	$P(F\|E)$ (w/o WPS)	Time of WPS (min)	$\frac{P(F\|E)_{w/WPS}}{P(F\|E)_{w/o\ WPS}}$
9.41	9E-7	26	$<2 \times 10^{-3}$
9.33	2E-7	48	0.01
9.19B	9.5E-5	26	$<3 \times 10^{-3}$
9.43	1.2E-5	54	0.2
9.20B	1.0E-4	26	$<3 \times 10^{-3}$
9.22B	5.5E-4	50	0.2

For some transients, there can be more than one time during the transient at which $\dot{K}_I = 0$. For these transients, the time selected for IWPS was that corresponding to the maximum value of K_I.

Table 9.5 shows, for each of the transients considered, the time of IWPS, the calculated values of $P(F|E)$ without WPS included in the analysis, and the ratio of $P(F|E)$ with and without WPS included. It is apparent that for these idealized transients the benefit of WPS can be large but is dependent on the transient.

9.3 Subclad-Crack Thermal-Shock Studies

R. D. Cheverton J. W. Bryson

A program[3] is under way at ORNL to evaluate the behavior of subclad cracks in PWR pressure vessels during thermal-shock loading conditions. The effort includes development of FM methods of analysis for subclad cracks; an experimental investigation of the validity of the method of analysis; and, if and when validated, the application of the method of analysis to determine the benefit of cladding in restricting the propagation of flaws.

A three-dimensional (3-D) elastic-plastic FM model for a subclad crack is presently under development, and details regarding the finite-element mesh and material properties that have been used thus far are discussed in Ref. 3. The flaws of particular interest[3] at this time are semielliptical in shape with an aspect ratio of 6/1 (see Fig. 9.5). For this particular flaw in a typical Heavy-Section Steel Technology (HSST) thermal-shock-experiment test cylinder and under severe thermal-shock loading conditions, it has been determined that for the deepest point on the crack front a two-dimensional (2-D) elastic analysis gives nearly the same value of K_I as the 3-D elastic-plastic analysis. Although the 3-D model does not yet provide K_I values at the clad-base interface, it can be argued that the 2-D elastic analysis yields reasonably accurate values

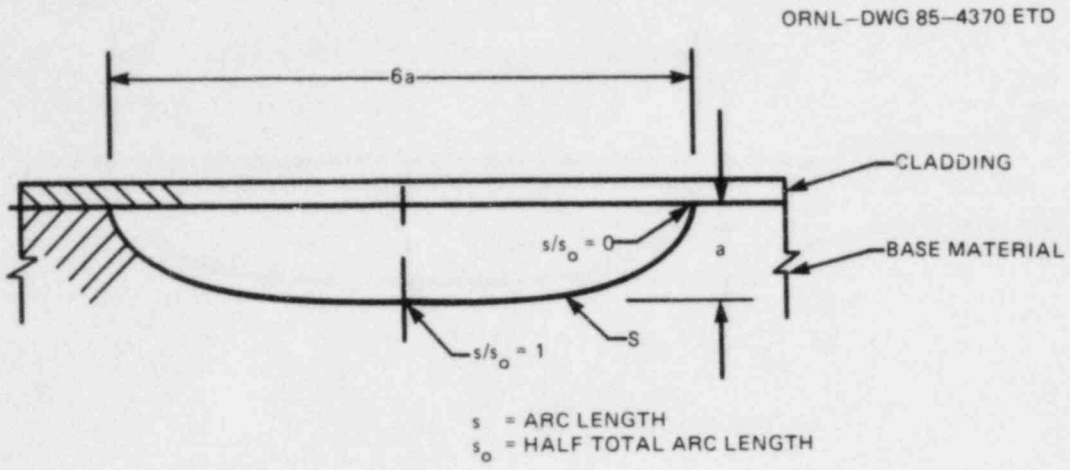

Fig. 9.5. 6/1 semielliptical subclad flaw.

at the interface also. Thus, the 2-D elastic model has been used extensively for a continuing feasibility study associated with the experimental aspect of the subclad-crack program. Results of the feasibility studies and various aspects of the model-development effort are discussed in the following paragraphs.

9.3.1 Model development

The strain energy release rate (G) is being calculated using ORVIRT,[10] which is a postprocessor for ADINA[11] that incorporates the virtual-crack-extension technique of deLorenzi.[12] This procedure evaluates G along the curved portion of the crack front but not at the clad-base interface because of the difference in material properties and also because an appropriate mesh is not yet available for the interface. An appropriate mesh is available at the interface for the 2-D flaw[3] (Fig. 9.6), but the change in material properties is a problem for the 2-D model as well.

For the elastic analysis, the difference in material properties at the interface is not large; thus, 2-D values of G can be estimated for both crack fronts. However, an attempt is being made to modify ORVIRT so that G can be calculated with the elastic-plastic model. One idea being considered involves a small change in the physical configuration so that the interface and crack tip do not coincide (Fig. 9.7). With reference to Fig. 9.6, it is apparent that the semicircular depression into the cladding or base material allows a ring element at the crack tip to reside in a single material and thus permits a calculation of G. In principle, if several calculations are made, each with a different size depression, the value of G corresponding to zero depression can be obtained by extrapolation.

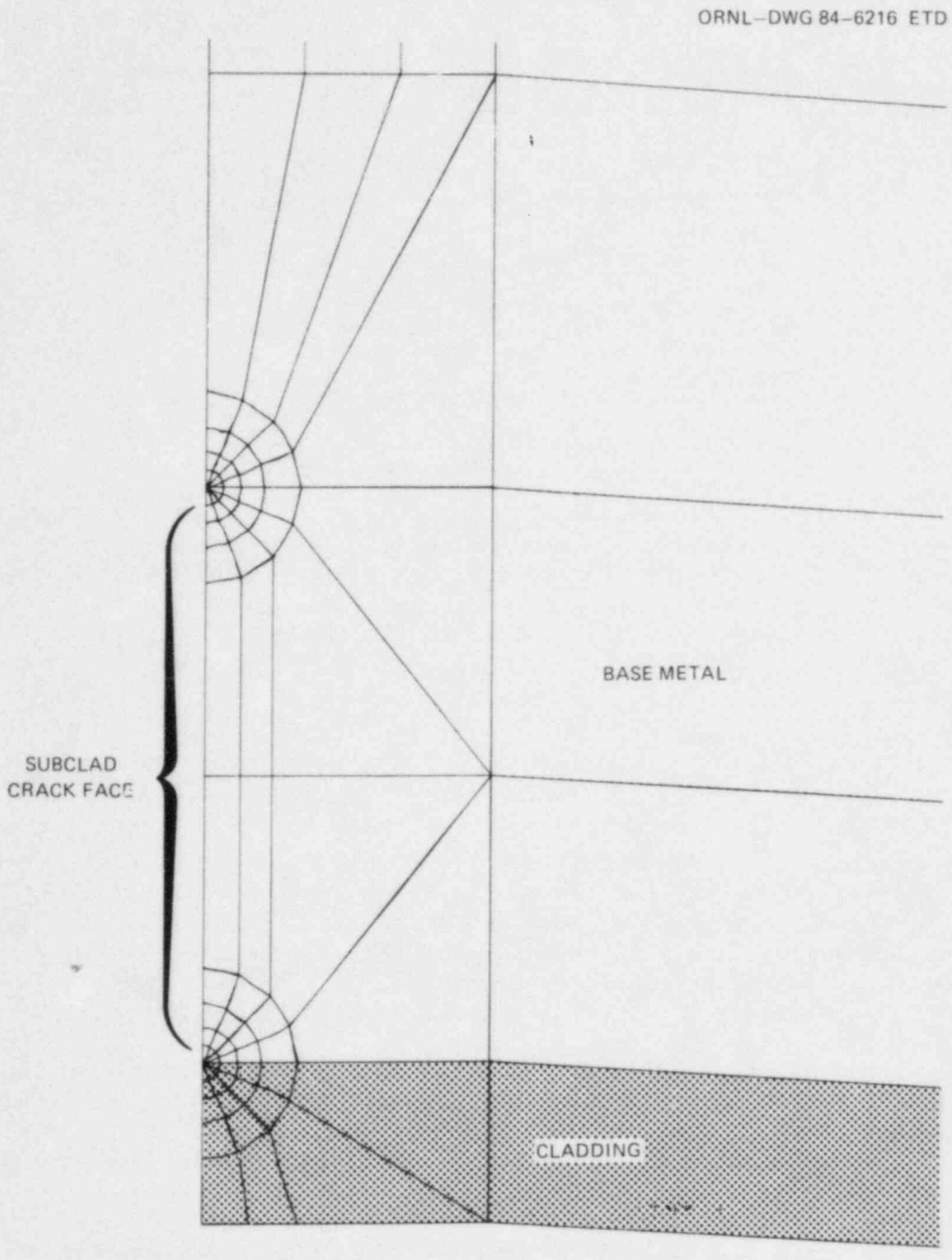

Fig. 9.6. Enlarged view of crack-tip region for 2-D finite-element analysis of subclad flaw in TSE test cylinder.

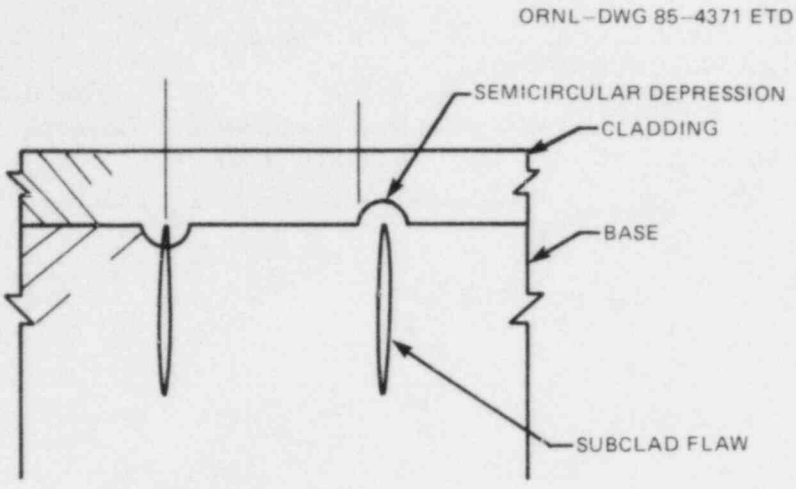

Fig. 9.7. Proposed configuration for avoiding coincidence of clad-base interface and tip of flaw.

9.3.2 Feasibility studies for thermal-shock experiments

9.3.2.1 Test facilities. Three test facilities have been considered for the confirmation-type thermal-shock experiments: TSTF (Ref. 13), which is the existing liquid-nitrogen test facility; STSTF, which is a proposed facility in which liquid nitrogen is sprayed on the surface; and PTSTF (Ref. 14), which is the existing pressurized thermal-shock test facility. The test-cylinder initial temperature for TSTF is limited to ~100°C, the sink temperature is −197°C, and the fluid-film heat transfer coefficient is a strong function of surface temperature, ranging from ~600 to 6000 $W/m^2 \cdot °C$ during a typical experiment.

The STSTF concept has not yet been developed, but it is believed that a fluid-film heat transfer coefficient of ~6000 $W/m^2 \cdot °C$ can be achieved throughout the transient, starting with a test-cylinder temperature of ~290°C. The advantage of STSTF over TSTF would be a higher temperature for the same value of G.

The advantage of PTSTF would be an even higher temperature to better cope with the transition temperature of the cladding. Although the facility in its present state has a minimum sink temperature of approximately −25°C, it was assumed for these studies that −73°C could be achieved by using pure alcohol as the quench medium instead of the present alcohol-water mixture. It was also assumed that a heat transfer coefficient of ~6000 $W/m^2 \cdot °C$ could be achieved throughout the transient, as it is with the present quench medium.

9.3.2.2 Calculational model. The results to be discussed here were obtained primarily with the 2-D elastic model for an axially oriented subclad crack in a typical HSST thermal-shock-experiment test cylinder (991-mm OD × 152-mm wall × 1.2-m length). The cladding thickness was 5.3 mm, and the material properties were those indicated in Ref. 3, assuming RT_{NDT} = 66°C (quench-only heat treatment) for the base material. Essentially no fracture-toughness data are available for the cladding, although results of clad-plate tests[15] indicate $K_c \simeq 100$ MPa·$\sqrt{m}$ at −40°C.

9.3.2.3 Results of analysis pertaining to TSTF. Table 9.6 summarizes the results of a 2-D elastic parametric study for the TSTF. For this study, four flaw depths (13, 19, 25, and 38 mm) and four times in the transient (1, 3, 5, and 7 min) were included. Longer times were not considered because, as indicated in Table 9.6, K_I reached a maximum at or before 7 min (time of IWPS), and this would preclude crack initiation thereafter.

Table 9.6. TSTF calculations for 2-D subclad flaw with RT_{NDT} = 66°C

Crack depth (mm)	Time (min)	Crack-tip temperature (°C)		2-D K_I values (MPa·$\sqrt{m}$)		Crack-tip K_{Ic}[a] (MPa·$\sqrt{m}$)	K_I/K_{Ic}
		Interface	Maximum depth	Interface	Maximum depth	Maximum depth	Maximum depth
13	1	−2	40	37	22	83	0.26
	3	−79	−36	64	44	67	0.66
	5	−108	−71	69	50	66	0.74
	7	−126	−93	69	48	66	0.74
19	1	−2	55	43	20	94	0.21
	3	−79	−17	77	47	68	0.70
	5	−108	−54	84	54	66	0.81
	7	−126	−77	84	54	66	0.82
25	1	−2	68	47	17	111	0.15
	3	−79	3	88	46	70	0.65
	5	−108	−35	97	55	67	0.82
	7	−126	−58	97	56	66	0.84
38	1	−2	81	53	9	138	0.06
	3	−79	28	105	39	76	0.50
	5	−108	−9	117	51	68	0.73
	7	−126	−34	118	53	67	0.79

[a]Values of K_{Ic} > 220 MPa·$\sqrt{m}$ are fictitious.

The results in Table 9.6 indicate that at the time of IWPS and for RT_{NDT} = 66°C, the maximum value of K_I/K_{Ic} (maximized relative to crack depth) is ~0.97, after correcting for the difference between the 2-D elastic and 3-D elastic-plastic models. The corresponding crack depth is in the range 19 to 38 mm, and the corresponding crack-tip temperatures are less than −34°C ($T - RT_{NDT} < -120$°C, which is realistic for some PWRs near the end of vessel design life). Although the probability of crack initiation is not large, the value of $(K_I/K_{Ic})_{max}$ is large enough so that useful information can be obtained even if crack initiation does not take place in the base material.

At the clad-base interface, K_I increases with crack depth. For a crack depth of 25 mm, the uncorrected value of K_I for $\dot{K}_I = 0$ is ~100 MPa·$\sqrt{m}$, and the crack-tip temperature (<−110°C) is well below the Oak Ridge National Laboratory (ORNL)-cladding Charpy-energy transition temperature.[15] Thus, unless a tougher cladding could be applied, there is

a reasonably good chance that the cladding would fail; this would trigger propagation in the base material.

Similar calculations were made for a surface flaw that extended through the cladding into the base material. As indicated by a comparison of Figs. 9.8 and 9.9, which are based on TSTF test conditions, the K_I values at the clad-base interface and the deepest point of the surface flaw are about 2.0 and 1.8, respectively, times the values for the deepest point of the subclad flaw. Thus, if the subclad flaw penetrates the cladding to become a surface flaw, this event is likely to trigger propagation in the base material, which will probably result in extensive surface extension of the flaw.

9.3.2.4 Results of analysis pertaining to STSTF. Table 9.7 summarizes the results of the 2-D parametric study for the "spray" facility. As indicated, substantially larger values of K_I and K_I/K_{Ic} can be achieved than with the TSTF facility, if the assumed test conditions can be achieved. At the deepest point of the subclad flaw, the calculated value of K_I/K_{Ic}, with RT_{NDT} = 66°C and at the time of IWPS, is ~1.4 without the plasticity correction, which is expected to increase this value. Thus, crack initiation in the base material would be expected even if the cladding were not penetrated. Also note that the crack-tip temperatures

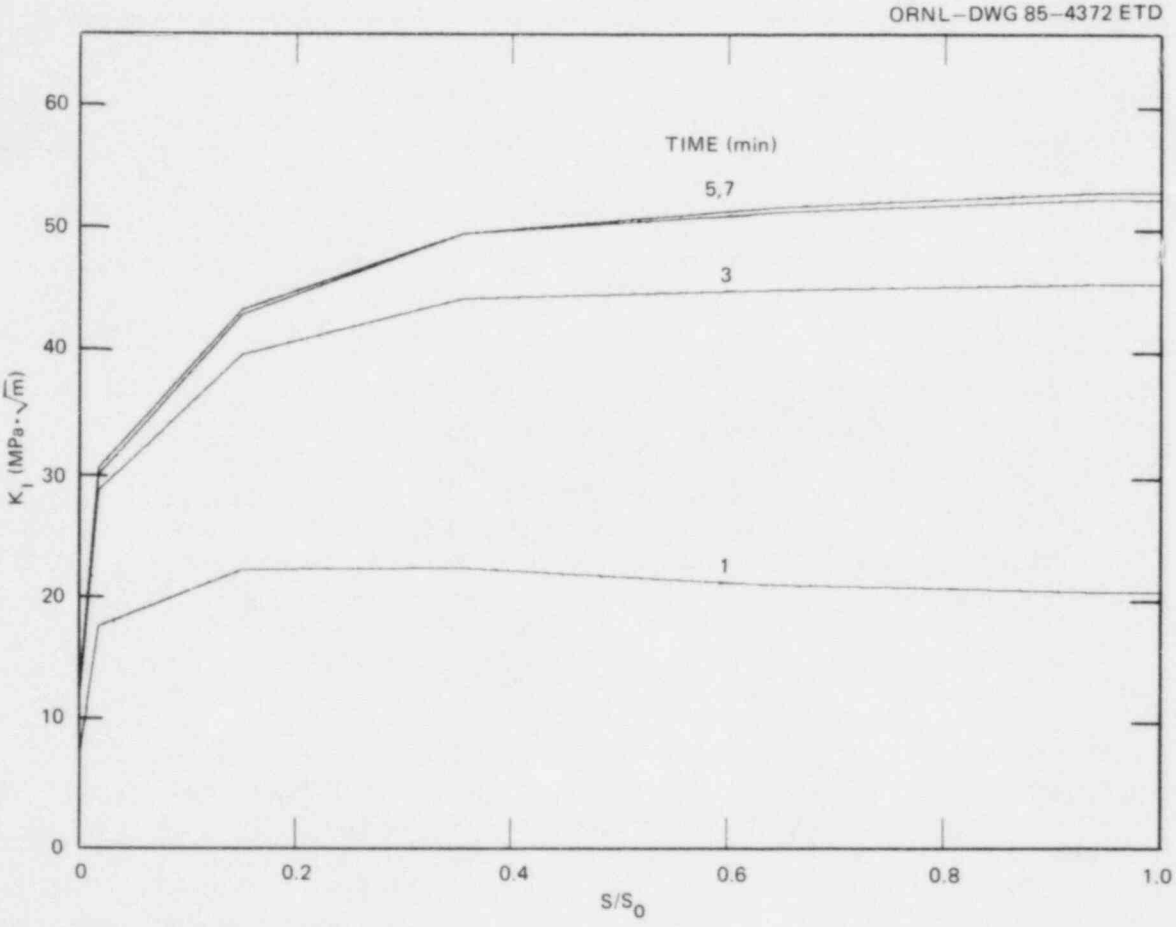

Fig. 9.8. K_I along crack front of a 6/1 semielliptical subclad flaw; TSTF test conditions, elastic analysis, a = 1.9 cm.

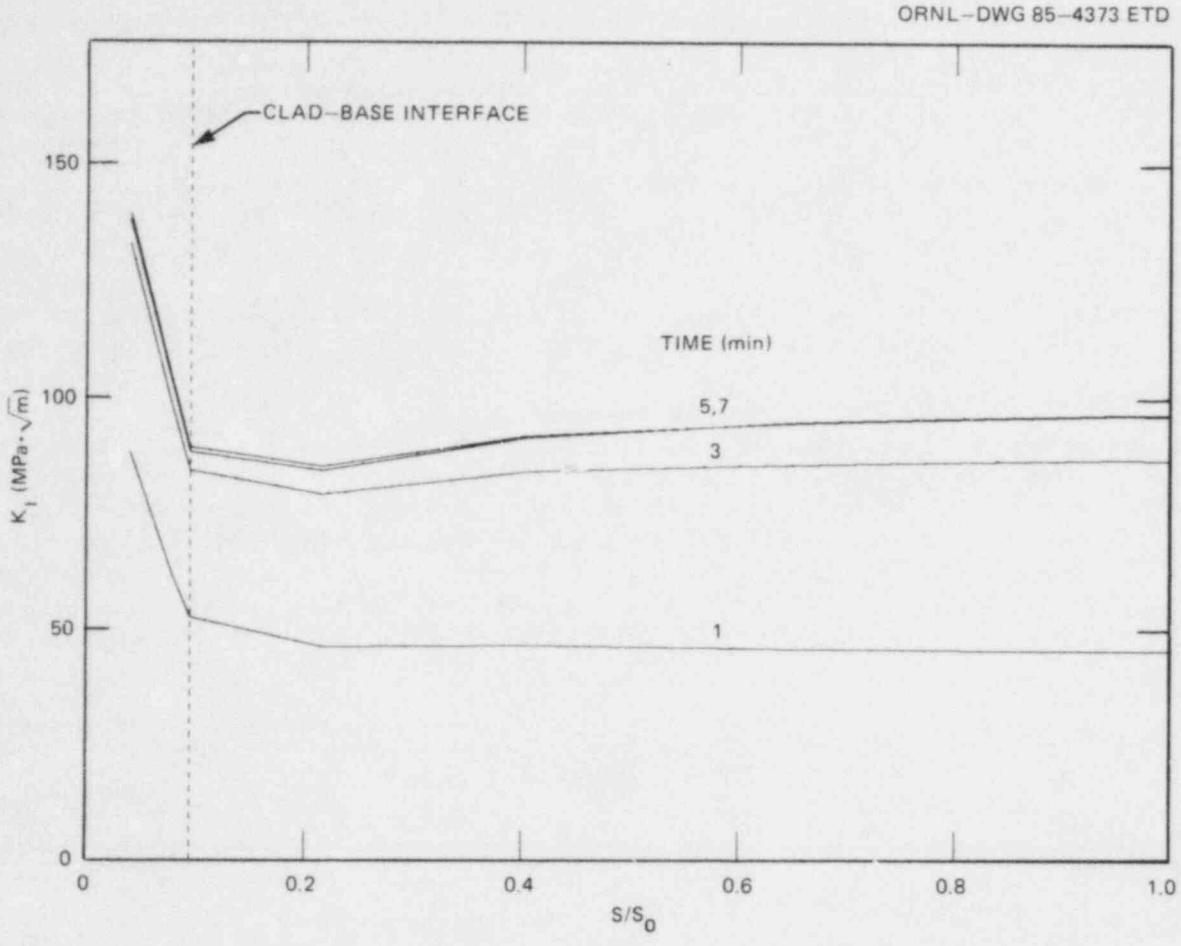

Fig. 9.9. K_I along crack front of a 6/1 semielliptical surface flaw; TSTF test conditions, elastic analysis, a = 1.9 cm.

at the most likely time for crack initiation are substantially higher than for TSTF. This, of course, is because of the higher initial temperature.

Values of K_I at the clad-base interface are also much higher, and the crack-tip temperatures are higher but still quite low compared with the transition-temperature range for the ORNL cladding. Thus, if this cladding were used, it is still likely that the cladding would be penetrated before propagation of the flaw into the base material.

9.3.2.5 Results of analysis pertaining to PTSF. Relatively few calculations have been made for the PTSF facility. The first set of calculations was performed assuming the present capability of the facility (pressure = 69 MPa, coolant temperature = −26°C). The results were not encouraging; thus, the remainder of the calculations were performed with a coolant temperature of −73°C, the assumption being made that pure alcohol could be used in the facility.

Results of the 2-D elastic analysis for the subclad flaw are shown in Table 9.8. For a flaw depth of 19 mm, a time in the transient corresponding to IWPS and for RT_{NDT} = 66°C, K_I/K_{Ic} at the deepest point is equal to 0.91 after being corrected for plasticity and 3-D effects. Thus,

Table 9.7. STSTF 2-D calculations for a subclad flaw; RT_{NDT} = 66°C, elastic analysis

Crack depth (mm)	Time (min)	Crack-tip temperature (°C)		2-D K_I values (MPa•√m)		Crack-tip K_{Ic} [a] (MPa•√m)	K_I/K_{Ic}
		Interface	Maximum depth	Interface	Maximum depth	Maximum depth	Maximum depth
13	1	11	121	110	67	366	0.18
	3	−60	19	129	90	74	1.23
	5	−86	−21	128	91	67	1.35
	7	−100	−43	122	87	66	1.31
19	1	11	163	129	65	1,454	0.04
	3	−60	54	156	97	94	1.04
	5	−86	9	155	100	72	1.41
	7	−100	−17	149	97	68	1.43
25	1	11	204	142	55	5,996	0.01
	3	−60	94	178	97	179	0.54
	5	−86	44	178	103	85	1.22
	7	−100	14	171	100	73	1.38
38	1	11	245	160	32	26,301	0.00
	3	−60	144	213	84	769	0.11
	5	−86	91	218	96	167	0.57
	7	−100	57	209	97	96	1.01

[a] Values of K_{Ic} > 220 MPa•√m are fictitious.

Table 9.8. PTSF 2-D calculations for a subclad flaw; RT_{NDT} = 66°C, elastic analysis

Crack depth (mm)	Time (min)	Crack-tip temperature (°C)		2-D K_I values (MPa•√m)		Crack-tip K_{Ic} [a] (MPa•√m)	K_I/K_{Ic}
		Interface	Maximum depth	Interface	Maximum depth	Maximum depth	Maximum depth
19	1	83	197	134	83	4,634	0.02
	3	29	116	155	107	314	0.34
	5	10	82	155	110	140	0.79
	7	−1	62	151	108	102	1.05
25	1	83	222	144	76	11,301	0.01
	3	29	140	173	107	662	0.16
	5	10	103	173	111	227	0.49
	7	−1	82	167	110	139	0.79

[a] Values of K_{Ic} > 220 MPa•√m are fictitious.

propagation of the flaw in the base material prior to failure of the cladding is not likely, at least if the pressure is maintained constant.

It may be that WPS can be delayed by gradually increasing the pressure, in which case temperatures at the time of IWPS would be lower. However, the temperature of the cladding could drop below the cladding transition temperature. For the constant-pressure case, the temperature at the clad-base interface at the time of IWPS is already down to ~10°C, which is within the transition regime of the ORNL cladding.

The clad-base interface temperatures for PTSF are substantially higher than for either TSTF or STSTF. Although the higher temperature may be more appropriate for the cladding, the higher temperatures in the base material tend to prevent crack propagation in the base material, as previously indicated.

9.3.3 Conclusions regarding suitability of test facilities

Based on preliminary studies, it is tentatively concluded that neither of the test facilities considered would necessarily provide the exact preferred test conditions. However, if sufficient cladding toughness can be achieved and if the assumed test conditions for STSTF can be developed, then the "spray" facility would provide the preferred conditions; that is, crack propagation would take place in the base material prior to failure of the cladding, and subsequent failure of the cladding would be of no consequence.

Substantial confirmatory information could also be obtained from TSTF, even though propagation of the flaw in the base material prior to failure of the cladding is not likely. The value of this experiment would be enhanced if the cladding did not fail, since the benefit of the cladding increases with increasing toughness of the cladding at least up to the point where propagation of the flaw into the base material takes place (prior to failure of the cladding).

The PTSF facility has the capability of subjecting the cladding to very high K_I values (>130 MPa$\cdot\sqrt{m}$) at temperatures well above the transition temperature of the ORNL cladding. However, since it is not likely that crack propagation in the base material would take place before failure of the cladding, PTSF appears to have no advantage over STSTF and perhaps none over TSTF, depending on the toughness of the cladding. However, even though PTSF would require some modifications for these tests, the facility does exist, while the STSTF does not (nor has the spray concept been demonstrated).

References

1. R. D. Cheverton and D. G. Ball, "Thermal-Shock Investigations," pp. 55–74 in *Heavy-Section Steel Technology Program Quart. Prog. Rep. July–September 1983*, NUREG/CR-3334, Vol. 3 (ORNL/TM-8787/V3), Union Carbide Corp. Nuclear Div., Oak Ridge Natl. Lab.

2. R. D. Cheverton et al., "Thermal-Shock Technology," pp. 134–37 in *Heavy-Section Steel Technology Program Semiannual Prog. Rep. October 1983–March 1984*, NUREG/CR-3744, Vol. 1 (ORNL/TM-9154/V1), Martin Marietta Energy Systems, Inc., Oak Ridge Natl. Lab.

3. R. D. Cheverton et al., "Thermal-Shock Technology," pp. 173–89 in *Heavy-Section Steel Technology Program Semiannual Prog. Rep. April–September 1984*, ORNL/TM-9154/V2, Martin Marietta Energy Systems, Inc., Oak Ridge Natl. Lab.

4. R. Y. Rubinstein, *Simulation and the Monte Carlo Method*, Israel Institute of Technology, John Wiley & Sons, New York, 1981, pp. 115–17.

5. P. G. Hoel, *Introduction to Mathematical Statistics*, 3rd ed., John Wiley & Sons, New York, 1962.

6. A. Hald, *Statistical Theory with Engineering Applications*, John Wiley & Sons, New York, 1952.

7. T. J. Burns et al., *Pressurized Thermal-Shock Evaluation of the Oconee-1 Nuclear Power Plant*, NUREG/CR-3770 (ORNL/TM-9176), Martin Marietta Energy Systems, Inc., Oak Ridge Natl. Lab., April 13, 1984 (Draft).

8. D. G. Selby et al., *Pressurized Thermal-Shock Evaluation of the Calvert Cliffs Unit 1 Nuclear Power Plant*, NUREG/CR-4022 (ORNL/TM-9408), Martin Marietta Energy Systems, Inc., Oak Ridge Natl. Lab., Oct. 9, 1984 (Draft).

9. D. G. Selby, ed., *Pressurized Thermal-Shock Evaluation of the H. B. Robinson-2 Nuclear Power Plant*, Oak Ridge National Laboratory report in preparation.

10. B. R. Bass and J. W. Bryson, *Applications of Energy Release Rate Techniques to Part-Through Cracks in Plates and Cylinders, Vol. 2. ORVIRT: A Finite Element Program for Energy Release Rate Calculations for 2-Dimensional and 3-Dimensional Crack Models*, NUREG/CR-2997, Vol. 2 (ORNL/TM-8527/V2), Union Carbide Corp. Nuclear Div., Oak Ridge Natl. Lab., February 1983.

11. K. J. Bathe, *ADINA — A Finite Element Program for Automatic Dynamic Incremental Nonlinear Analysis*, Report 82448-1, Mechanical Engineering Department, Massachusetts Institute of Technology, December 1978.

12. H. G. deLorenzi, "On the Energy Release Rate and the J-Integral for 3-D Crack Configuration," *Inter. J. Fract.* 19, 183 (1982).

13. R. D. Cheverton et al., "Thermal-Shock Investigations, pp. 57–77 in *Heavy-Section Steel Technology Program Quart. Prog. Rep. April–June 1983*, NUREG/CR-3334, Vol. 2 (ORNL/TM-8787/V2), Union Carbide Corp. Nucl. Div., Oak Ridge Natl. Lab.

14. G. C. Robinson, "Pressurized Thermal-Shock Test Studies," pp. 105–8 in *Heavy-Section Steel Technology Program Quart. Prog. Rep. July–September 1981*, NUREG/CR-2141, Vol. 3 (ORNL/TM-8145), Union Carbide Corp. Nuclear Div., Oak Ridge Natl. Lab.

15. W. R. Corwin et al., *Effect of Stainless Steel Weld Overlay Cladding on the Structural Integrity of Flawed Steel Plates in Bending*, ORNL/TM-9390, Martin Marietta Energy Systems, Inc., Oak Ridge Natl. Lab. (in publication).

10. PRESSURIZED-THERMAL-SHOCK TECHNOLOGY

R. H. Bryan

10.1 Posttest Fracture Analysis of Pressurized-Thermal-Shock Experiment

R. H. Bryan

In the first Heavy-Section Steel Technology pressurized-thermal-shock experiment (PTSE-1) three separate transient loadings were imposed on the thick-wall test vessel. As a consequence, two fast crack jumps were induced, and both were arrested. Earlier accounts of the experiment[1,2] described the test results and conclusions on the basis of preliminary observations and analyses. This report presents a summary of subsequent posttest flaw examination, test data evaluation, and fracture analysis. Details of this work have been assembled in a topical report on PTSE-1 (Ref. 3).

The final analysis of the experiment was based on direct measurements of flaw dimensions and recorded data that had been evaluated for validity and corrected as indicated by instrumentation calibrations. Furthermore, the final fracture-mechanics analyses performed with the OCA/USA computer program[4] used temperature-dependent values of Young's modulus E and the coefficient of thermal expansion α that were based on laboratory data.[3]

10.1.1 Flaw and vessel geometry

Times of crack jumps were determined in each transient from the recorded measurements of crack-mouth-opening displacement. Flaw shape and depth were measured directly on the fracture surfaces after the flaw was removed from the vessel. Data records of crack-mouth-opening displacement are shown in Fig. 10.1 for each of the three transients, which have been labeled PTSE-1A, -1B, and -1C. The actual crack-mouth-opening displacement is probably represented best by the change in the apparent crack-mouth-opening displacement minus the change in the output of the dummy crack-mouth-opening-displacement gage. The crack-mouth-opening-displacement data showed that there was no crack jump in the A transient, and there was one jump in each of the subsequent transients.

The coordinates of several points on the boundaries of the initial, intermediate, and final flaws were measured with the aid of a low-power microscope and a scale graduated in millimeters. The results are represented graphically in Fig. 10.2. The initial flaw was 12.2 mm deep on the average. The points on the intermediate flaw are well fit by a semiellipse with a semiminor axis of 24.4 mm, while the final flaw is fit best over most of its length by a semiellipse with a semiminor axis of 41 mm. The geometry of the vessel and the flaw and times of events are presented in Tables 10.1 and 10.2.

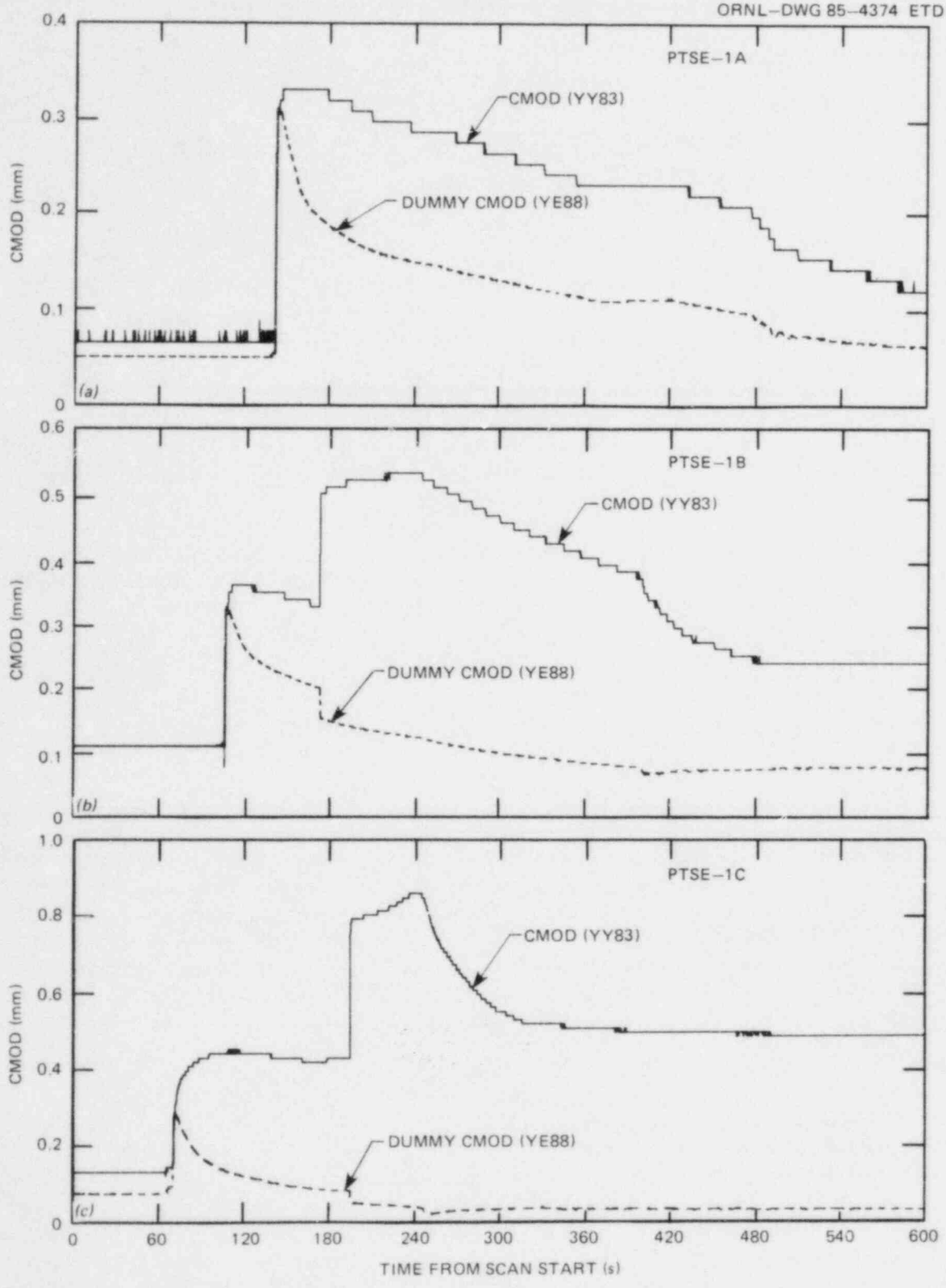

Fig. 10.1. Crack-mouth-opening-displacement data from an active gage at the middle of the flaw and a dummy gage nearby. (*a*) PTSE-1A, (*b*) PTSE-1B, and (*c*) PTSE-1C.

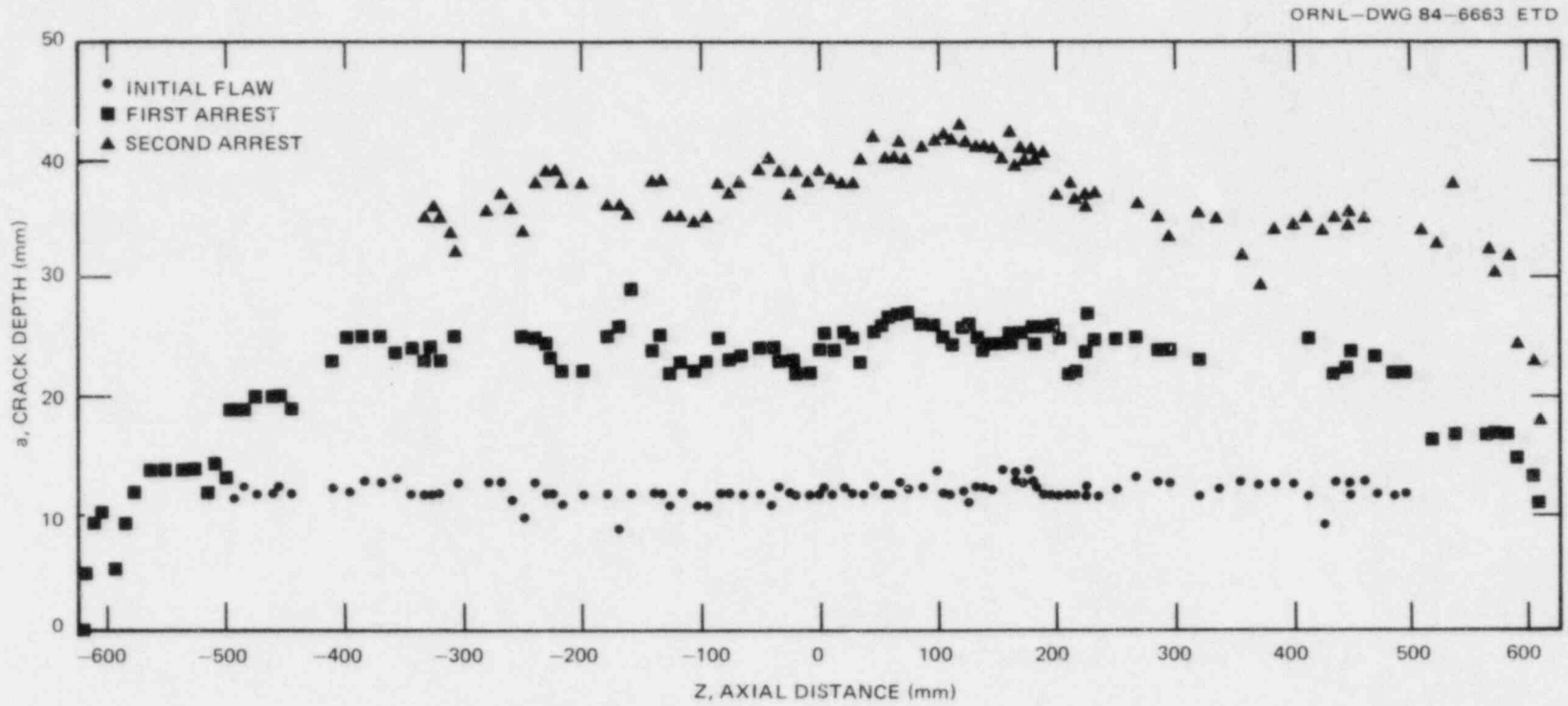

Fig. 10.2. Measured crack depths of the PTSE-1 flaw.

Table 10.1. Temperature-independent characteristics of the PTSE-1 vessel used in final post-test OCA/USA analyses

Parameter	Value
Geometry of vessel	
Inside radius r_i, mm	343.0
Wall thickness w, mm	147.6
Flaw length 2b, mm	1000
Elastic-plastic parameters	
Yield strength σ_Y, MPa	600
Toughness	
Upper-shelf threshold temperature T_D, °C	175
J_R parameters[a]	
c	2.60
n	0.359
Thermoelastic parameters	
Poisson's ratio ν	0.3

[a] $J_R = c(\Delta a)^n$, where J_R is in megajoules per square meter and Δa is in meters.

Table 10.2. Summary of experimental observations

Parameters	Transient		
	PTSE-1A	PTSE-1B	PTSE-1C
t_0, time of initiation of shock, s	141	105 70	
T_0, °C	277.6	290.7	287.4
Crack depth			
Initial			
a, mm	12.2	12.2	24.4
a/w	0.083	0.083	0.165
Final			
a, mm	12.2	24.4	41
a/w	0.083	0.165	0.278
Time of crack jump, s		172.1	195.3
Time of maximum K_I, s	202	240.9	242.0
	260.0		
	421.2		

10.1.2 Pressure and temperature transients

The pressure histories used in final OCA/USA analyses were taken from the most reliable of two available data records. The pressure data used in the analyses are represented by Fig. 10.3.

Temperatures for input to OCA/USA were a set of values T(r,t) defined for the domain of radial coordinates r within the cylindrical wall of the vessel for a conveniently spaced set of time points t. All recorded data were processed to produce, first, a set of time-averaged values for each sensor at 0.2-s intervals. The requisite temperature profiles T(r,t) were then derived from the time-averaged measurements made by thermocouples arrayed in thimbles that penetrated the cylindrical wall of the vessel and by supplementary thermocouples attached to the inside surface of the vessel. Thus, thimbles located at seven axial-circumferential coordinates provided the basis for a profile at each location.

Thermocouple signals were converted into temperature by the data acquisition system by means of standard conversions published by the National Bureau of Standards.[5] The thimble and inside-surface thermocouples were individually calibrated in the laboratory against a standard thermocouple. One function of posttest processing was to adjust the raw temperature data from each thermocouple by its individual calibration expression

$$T_x - T = a_0 + a_1 T + a_2 T^2 \ , \qquad (10.1)$$

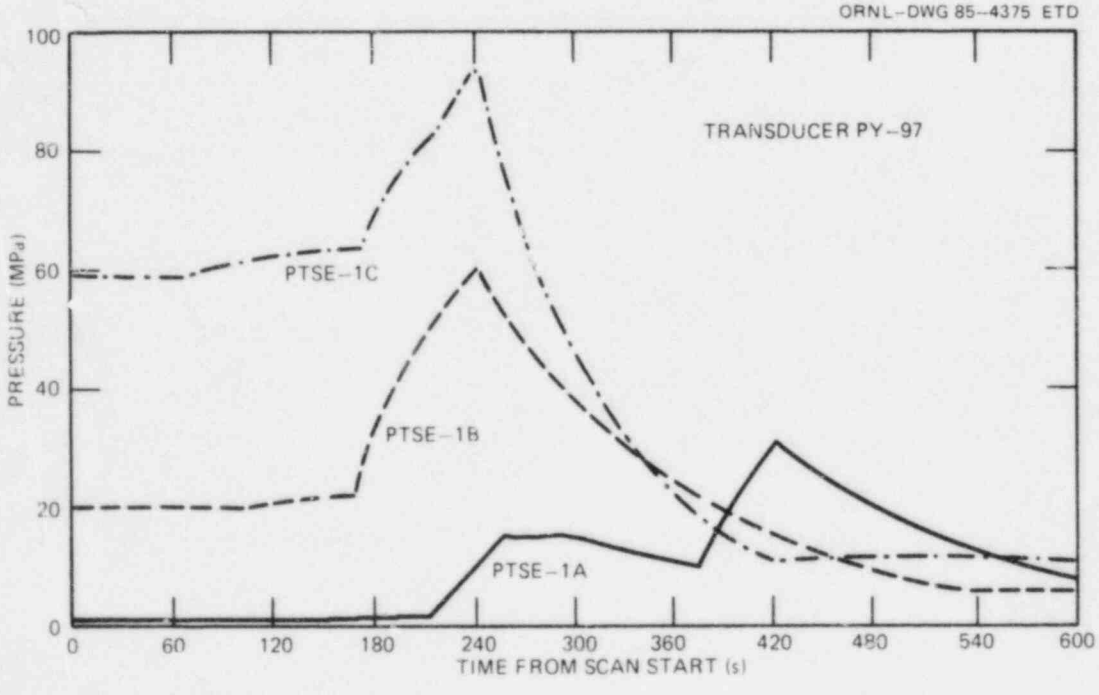

Fig. 10.3. Pressure vs time for the three transient phases of PTSE-1.

where T_x is the temperature inferred from the experimental thermocouple (or the raw temperature); T is the temperature inferred from the standard thermocouple (or the true temperature); and a_0, a_1, and a_2 are coefficients determined by least-squares fit of the calibration data. The adjusted (true) temperatures are usually 3 to 6 K lower than the raw data at ~290°C, while the adjustment is much smaller at low temperature (~0°C).

PTSE-1 and calibration laboratory data from each thermocouple were reviewed for inconsistencies with physical reality. In cases in which an error was evident, the thermocouple was omitted from the list of those to be processed by OCA/USA unless a rational correction could be justified. Of the 84 thermocouples in 7 thimbles, 5 were omitted, 3 location corrections were made, 4 pairs (8) of adjacent thermocouples had their positions transposed, and calibration expressions were altered for 4 thermocouples. Location transpositions, caused by errors in connecting thermocouple wires to terminal strips, were easily evident because they produced a reversed gradient. Other location errors were from obvious errors in recording or copying locations of junctions. The four calibration errors arose from calibration runs that were obviously erroneous. The thermocouples involved behaved normally during all transients and were, therefore, given adjustments accorded other thermocouples in the same thimble. All of the erroneous thermocouples could have been omitted without significantly affecting the conclusions of posttest analyses. The effects of typical adjustments are illustrated in Figs. 10.4–10.6. The solid curves in these figures represent temperatures in a thimble.

Temperatures for OCA/USA input must be defined over the domain of the entire thickness of the test vessel wall (147.6 mm), while thimble measurements extend only to a depth of ~100 mm from the outside surface. Furthermore, thimble and wall temperatures at the same depth are slightly different.[3] The type of temperature profile generated for OCA/USA input is illustrated by the dotted curve in Fig. 10.6. This profile was obtained by a nonlinear mapping of the temperature and depth coordinates of the thimble to the corresponding temperature and depth coordinates of the vessel wall as described in Ref. 3. Examples of temperature profiles used in the OCA/USA analysis of each transient are shown in Figs. 10.7–10.9.

10.1.3 Material properties

Characteristics of the vessel assumed to be independent of temperature are presented in Table 10.1. Pretest material toughness values, namely curve B of Fig. 10.10 for $K_{Ic}(T)$ and Fig. 10 11 for $K_{Ia}(T)$, were used for comparison with values implied by the experiment.[6,7] Temperature-dependent values of Young's modulus E(T) and the coefficient of thermal expansion $\alpha(T)$ were estimated from experimental measurements described in Ref. 3.

An average value of α is required for OCA/USA analysis. This is defined by

$$\alpha_m(T_0,T) = \frac{1}{T - T_0} \int_{T_0}^{T} \alpha(T') \, dT' \, , \qquad (10.2)$$

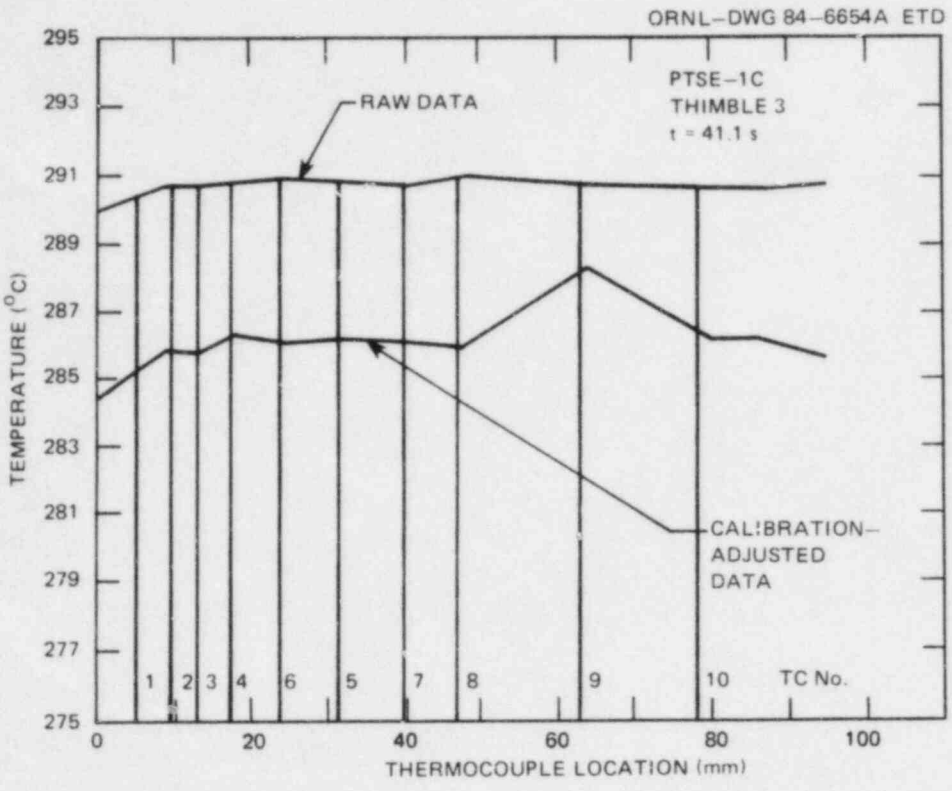

Fig. 10.4. Comparison of temperature profiles from raw and calibration-adjusted data for thermocouple thimble 3 when vessel was nearly isothermal before the PTSE-1C transient. The high adjusted temperature at thermocouple 9 confirmed that anomalous calibration coefficients were wrong.

where T_0 is the initial temperature at the time the cylindrical section of the test vessel is essentially isothermal and, therefore, free of thermal stresses. Values of α_m for T_0 = 300°C were used as input for analysis of all transients because the small differences in T_0 would change α_m by only 0.5%. Values of E and α_m as functions of T used in the OCA/USA posttest analyses are given in Table 10.3.

To evaluate the importance of using E and α values as explicit functions of T in the OCA/USA analysis, calculations of K_I for the PTSE-1C transient were made for a series of constant E and α values for comparison with the base case in which variable values were used. It was found that a constant value of $\alpha_m = 14.41\ 10^{-6}\ K^{-1}$ and of E = 202.3 GPa produced K_I values that deviated <1% from the base case values over a period of 140 s for cracks no deeper than 40% of the wall thickness.

10.1.4 Analysis of experiment

Transient data from the experiment were analyzed by the OCA/USA program. K_I values were calculated with the options invoked to use the three-dimensional influence coefficients (applicable only for crack-depth

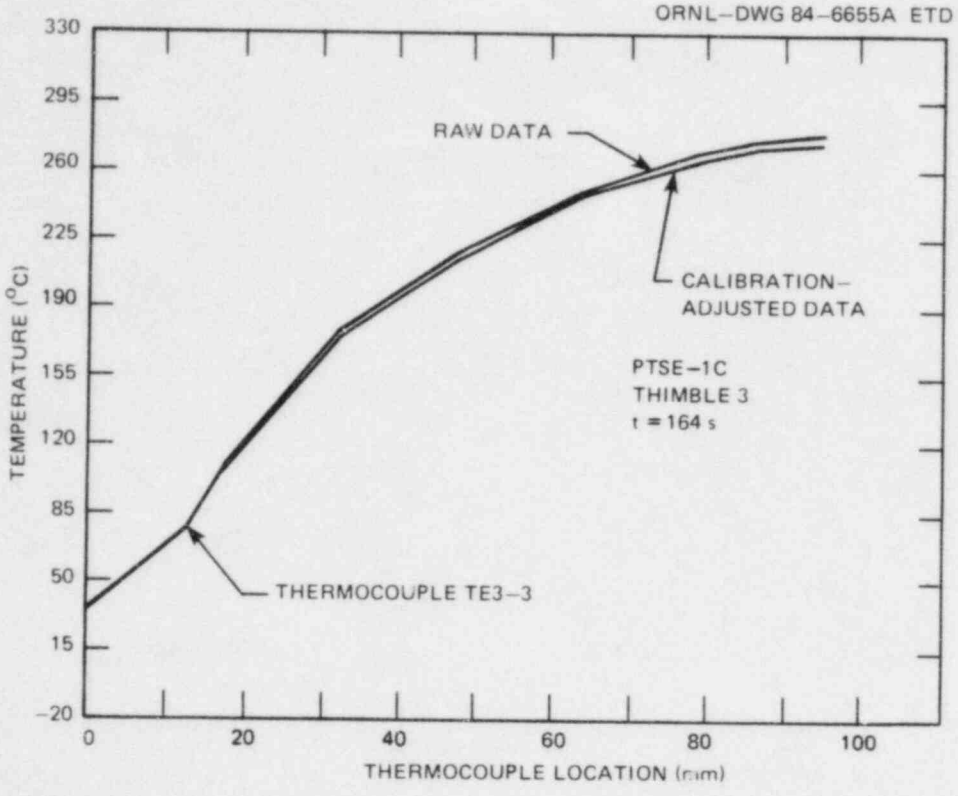

Fig. 10.5. Comparison of temperature profiles from raw and calibration-adjusted data for thermocouple thimble 3 at t = 164 s in PTSE-1C transient. The depressed point at depth = 12.62 mm is atypical of other thimble profiles. Such anomalies were excluded from data for final OCA/USA analysis.

ratio a/w ≥ 0.1) and to adjust K_I for the effect of the plastic zone. The analyses include the times of important events identified in Table 10.4.

Results presented here are based on temperature data from thermocouple thimble 5. This thimble was located at the beltline of the vessel about 250 mm from the flaw and is believed to give the best representation of temperature. Observed axial and circumferential variations in temperature are discussed in Ref. 3.

Crack-tip conditions and fracture events are presented in Fig. 10.12 for the three transients. The crack trajectory (curve A) for the A transient indicates that the crack first became simply warm prestressed (i.e., $K_I \leq 0$) just as K_I became equal to K_{Ic}. The crack was evidently inhibited from propagating for the remainder of the A transient, although during two subsequent periods the crack was simply antiwarm prestressed ($K_I > 0$). In the B transient the crack jumped and arrested when $K_I \simeq K_{Ic}$ and $K_I \simeq K_{Ia}$, respectively (see trajectory B in Fig. 10.12). The crack had a narrow opportunity to reinitiate but did not prior to another episode of simple warm prestressing. In the C transient, the crack propagated and

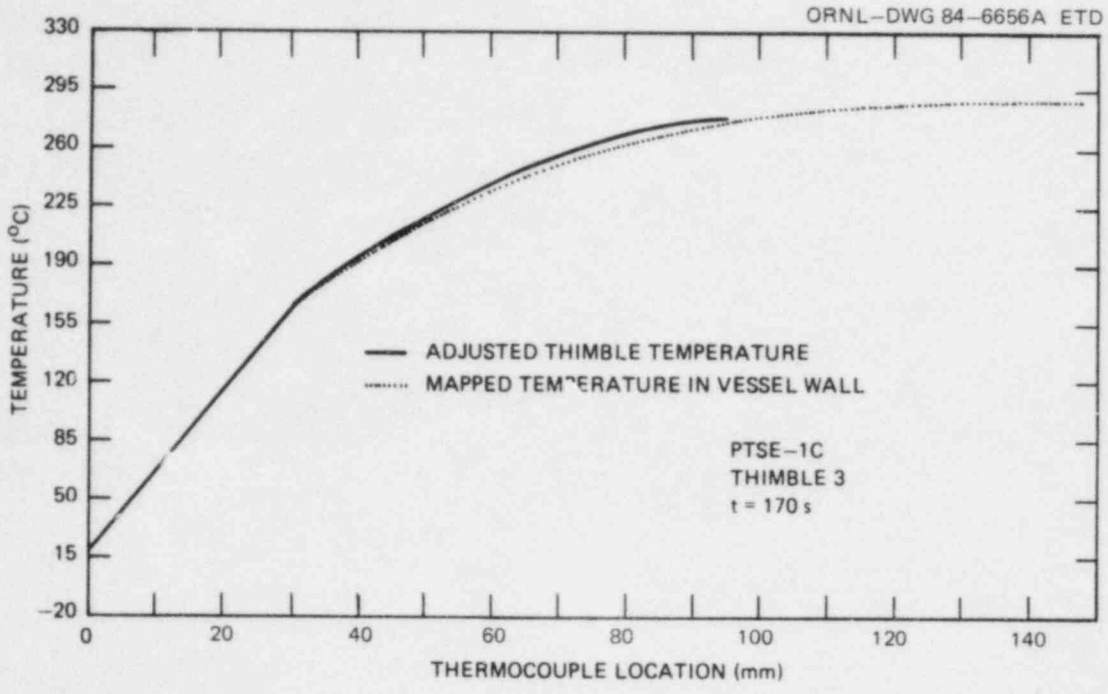

Fig. 10.6. Temperature profiles in thermocouple thimble 3 and vessel wall from PTSE-1C transient at t = 170 s. Data from thermocouples 1 and 3 were excluded, and calibration coefficients typical of the group were attributed to thermocouple 9.

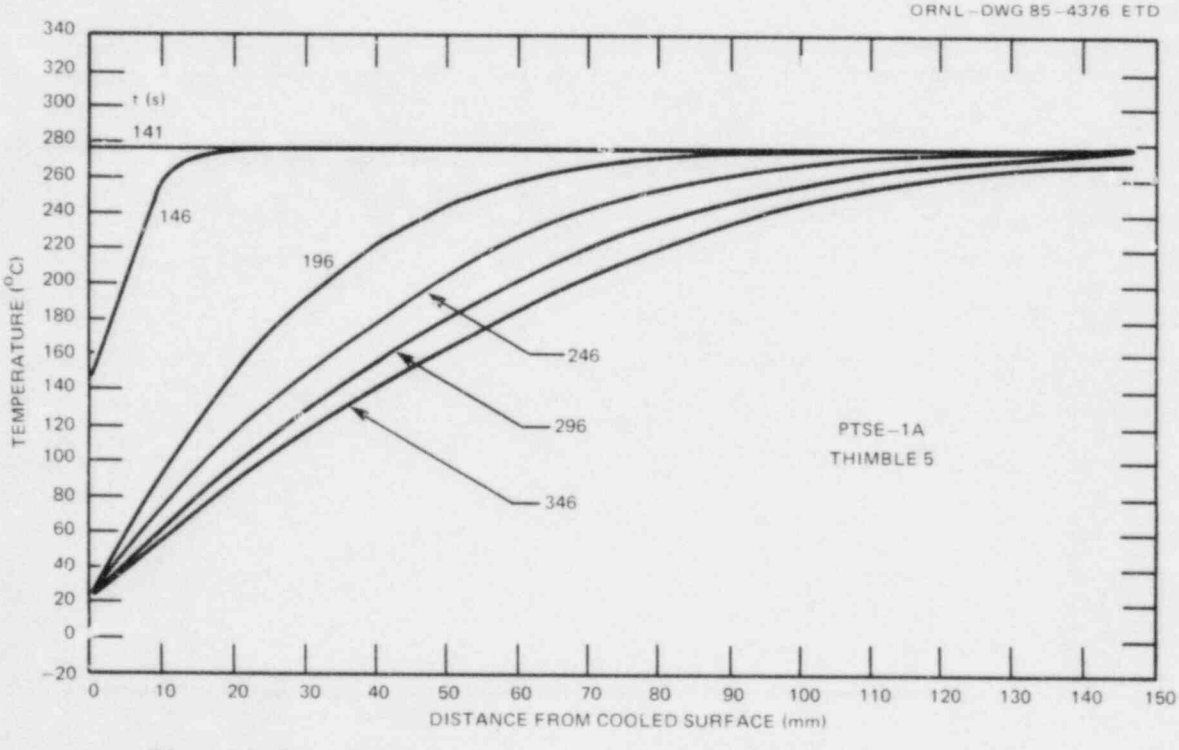

Fig. 10.7. Temperature profiles for PTSE-1A transient.

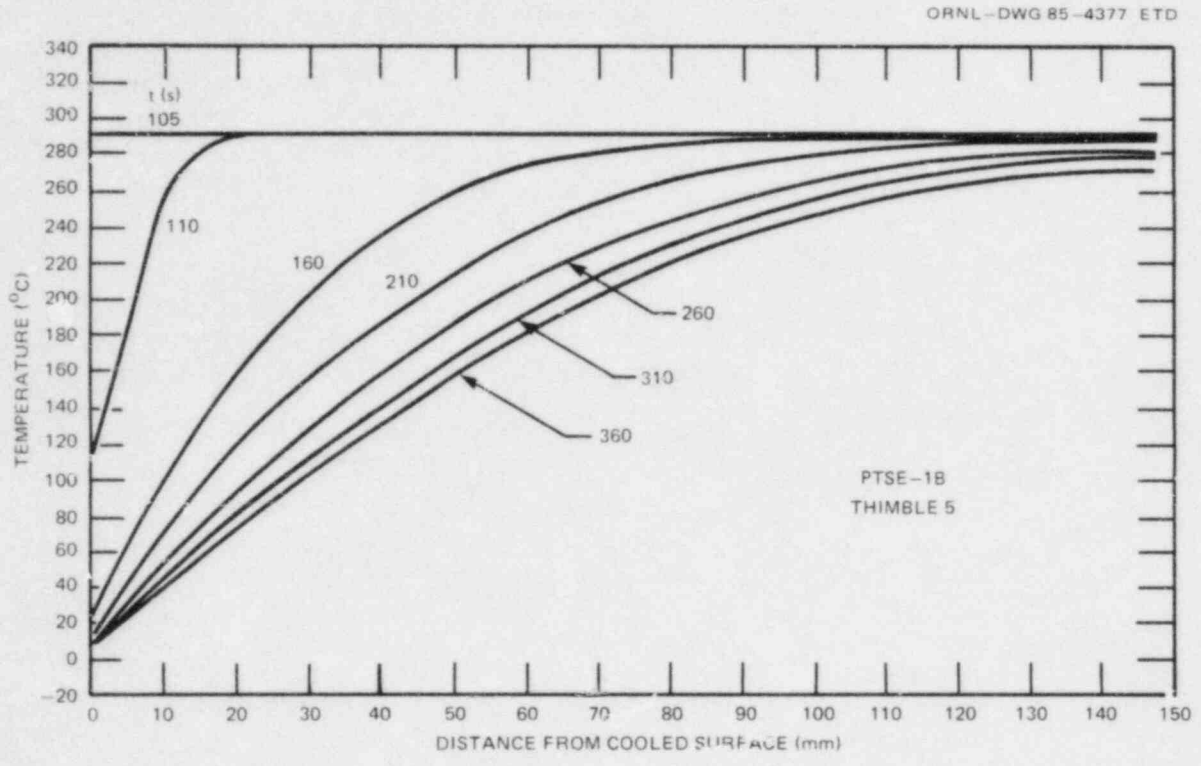

Fig. 10.8. Temperature profiles for PTSE-1B transient.

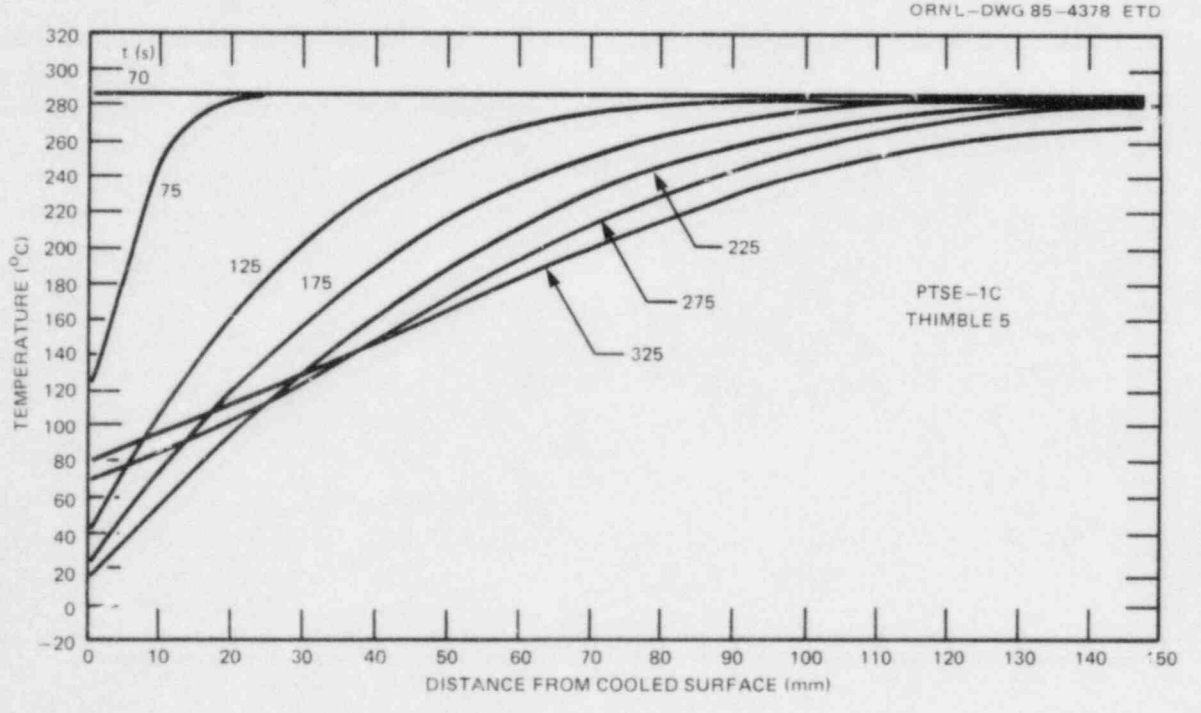

Fig. 10.9. Temperature profiles for PTSE-1C transient.

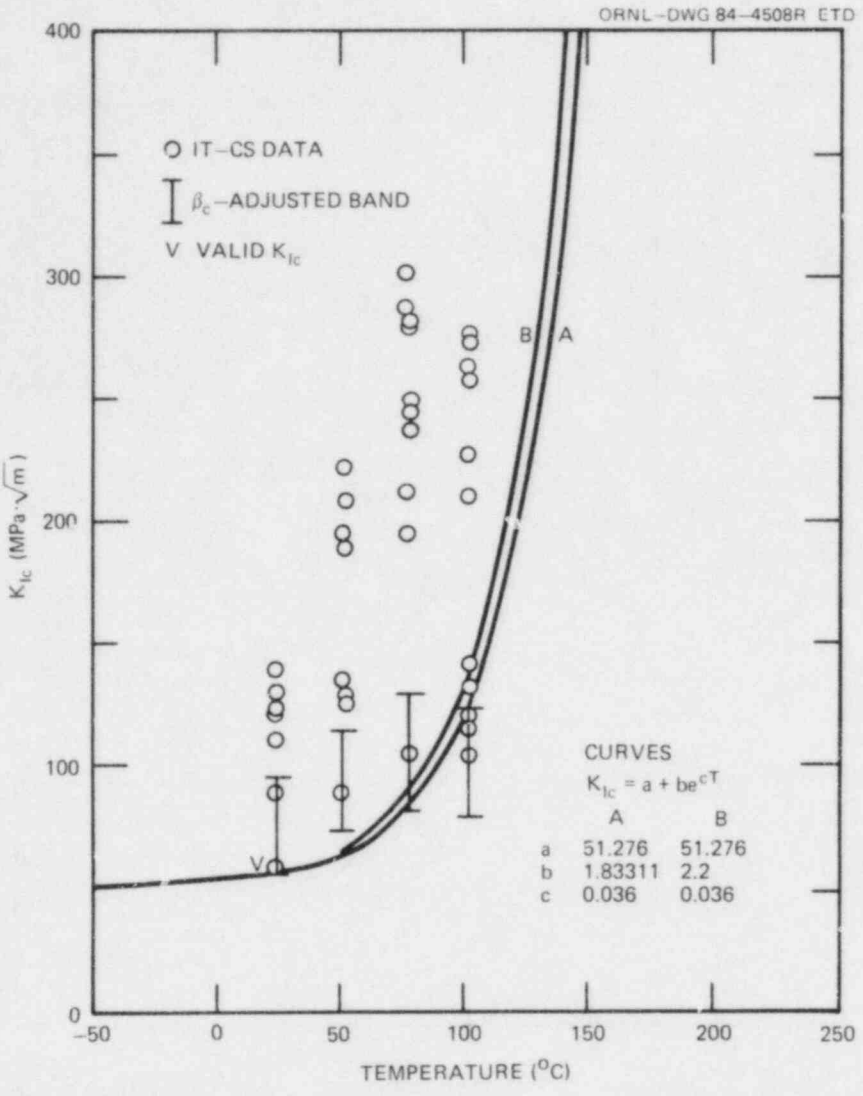

Fig. 10.10. K_{Ic} data for PTSE-1 vessel. Curves represent functions used in OCA/USA analyses. Data plotted were from preliminary reports of results of specimen tests. Three points are at variance with final property determinations reported in Ref. 6, but correction would not have affected the curves.

arrested under approximately the expected conditions (see trajectory C in Fig. 10.12).

The arrested cracks in the B and C transients were expected to tear about 2 and 11 mm, respectively. However, fractographic examination of the fracture surfaces disclosed no continuous areas of ductile tearing except at the tip of the initial flaw, where there was a narrow, nearly continuous band of tearing.[3] The areas of crack extension were 85 to 100% cleavage. The absence of ductile tearing is not consistent with tearing analysis based on pretest tearing resistance data[6] in terms of the J-integral vs crack extension.

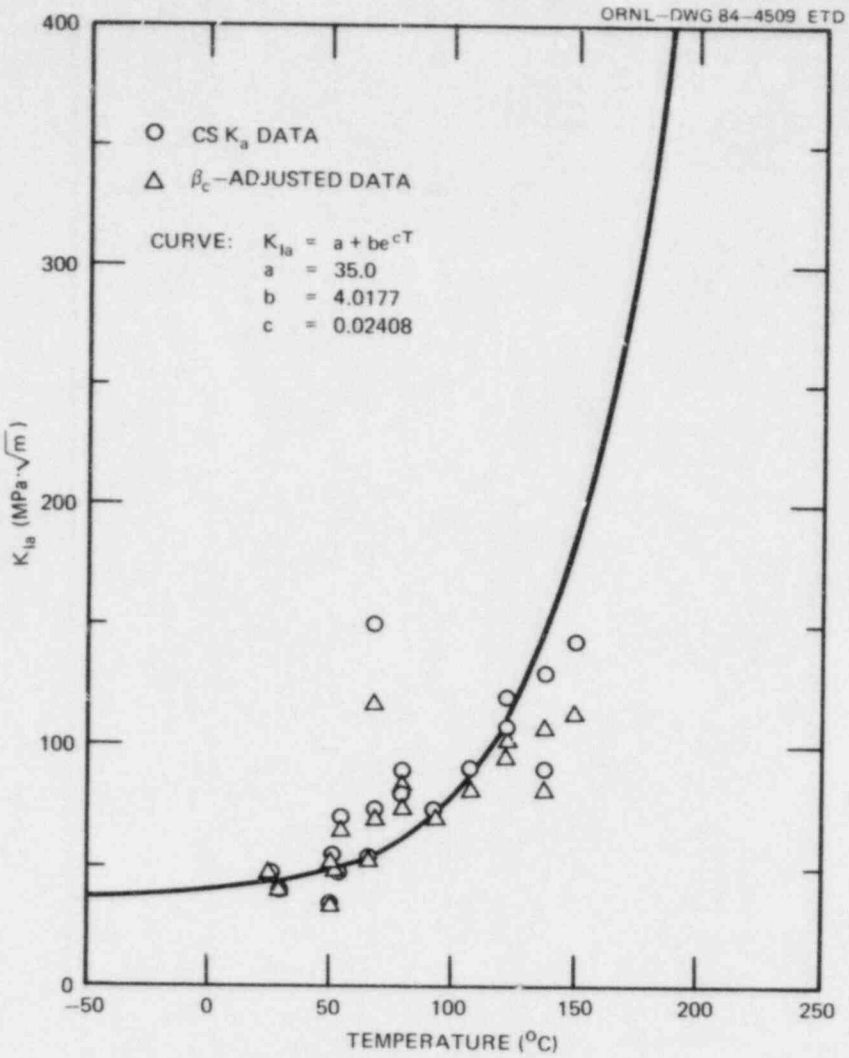

Fig. 10.11. K_{Ia} data for PTSE-1 vessel obtained by Battelle-Columbus Laboratories (Ref. 7). Curve represents function in OCA/USA analyses.

Table 10.3. Values of E(T) and $\alpha_m(T_0,T)$ used in final posttest OCA/USA analyses

T (°C)	E (GPa)	$10^6\alpha_m$ (K^{-1})
0	210.5	13.89
40	208.2	14.08
60	207.1	14.17
80	205.9	14.26
100	204.6	14.35
120	203.5	14.44
140	202.3	14.53
160	201.0	14.61
180	199.5	14.69
200	198.3	14.77
220	196.9	14.84
240	195.4	14.92
260	194.0	14.99
280	192.6	15.06
300	191.0	15.12

Table 10.4. Summary of PTSE-1 posttest evaluation based on calibrated and qualified data

Transient	Event	Time[a] (s)	Crack depth		Crack-tip temperature (°C)	K_I (MPa·$\sqrt{m}$)	K_I/K_{Ic}
			a (mm)	a/w			
PTSE-1A	First K_I maximum	202	12.2	0.083	104.7	151.95	1.04
	Second K_I maximum	260.0			77.8	154.27	1.76
	Third K_I maximum	421.2			56.9	138.85	2.03
PTSE-1B	Crack initiation	172.1	12.2	0.083	103.7	177.44	1.24
	Crack arrest	172.1	24.4	0.165	163.5	200.93	
	K_I maximum	240.9	24.4	0.165	117.9	246.52	1.20
PTSE-1C	Crack initiation	195.3	24.4	0.165	125.3	254.27	1.01
	Crack arrest	195.3	41	0.278	179.0	298.86	
	K_I maximum	242.0	41	0.278	156.0	339.60	0.52

[a]Time from start of data record. See Table 10.2 for the time of initiation of the thermal transient.

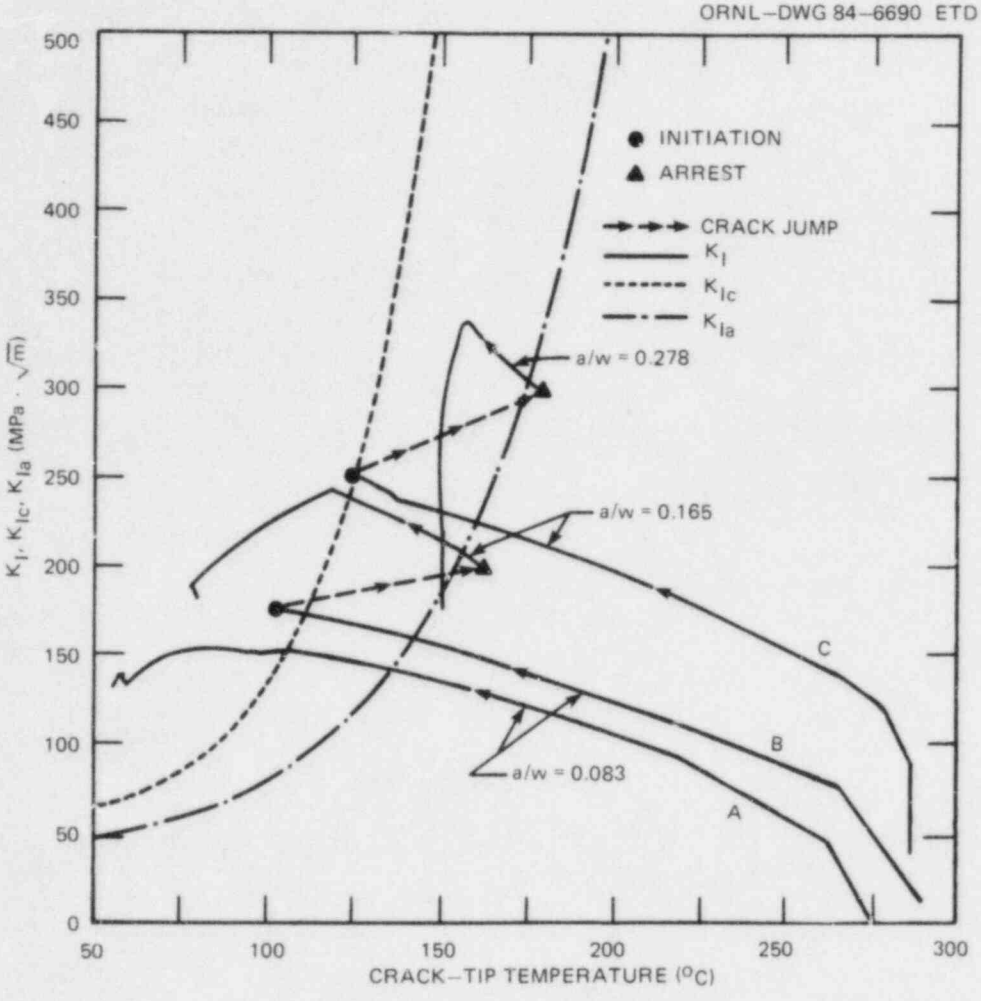

Fig. 10.12. Applied stress-intensity factor and toughness vs crack-tip temperature curves for the three phases of PTSE-1. K_{Ic} and K_{Ia} curves are based on pretest data (Figs. 10.10 and 10.11).

10.2 Elastodynamic Analysis of the PTSE-1 Experiment

B. R. Bass C. E. Pugh

For purposes of comparison with quasi-static posttest analyses described in a previous report,[8] elastodynamic analyses of the PTSE-1 experiment were carried out with the SWIDAC (Ref. 9) dynamic crack-analysis code. The salient features of the crack propagation technique used in SWIDAC are reviewed briefly in Sect. 5.1. In the dynamic analysis of PTSE-1, a two-dimensional plane-strain finite-element formulation was utilized to model the test vessel of Fig. 10.13 with initial crack-depth ratio a/w = 0.083. The finite-element model is depicted in Fig. 10.14 and consists of 696 nodes and 208 eight-noded isoparametric elements. A

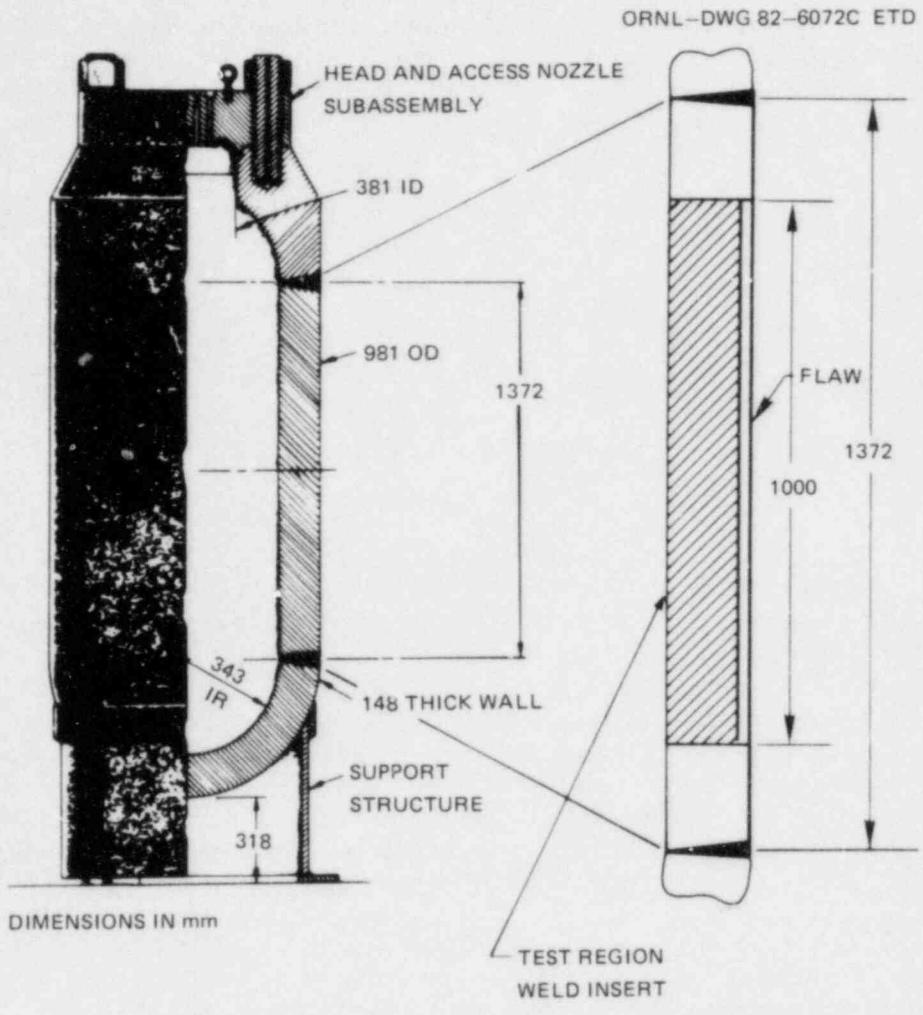

Fig. 10.13. Geometry of PTSE-1 test vessel.

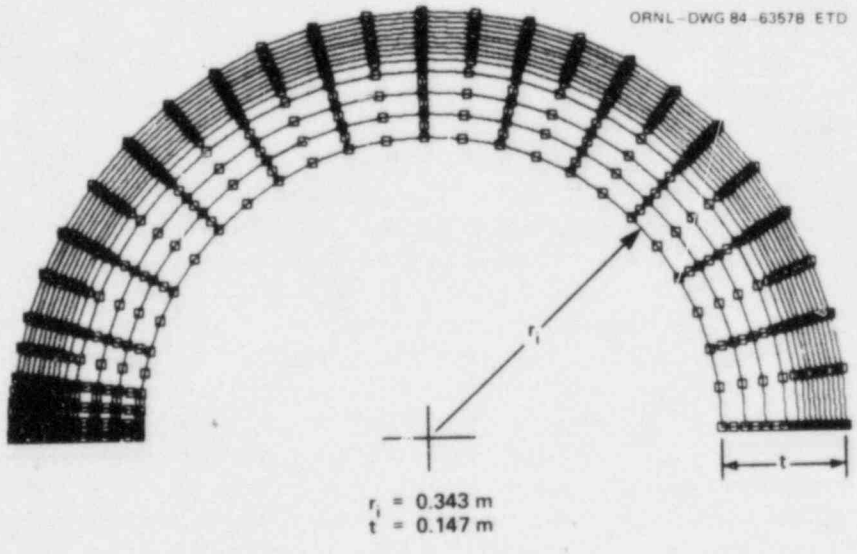

Fig. 10.14. Finite-element model for posttest elastodynamic fracture analysis of PTSE-1 (696 nodes and 208 elements).

total of 13 spring elements are used in the crack plane to model propagation of the crack tip. Constant material properties were employed in this analysis and are given by Young's Modulus E = 202.3 GPa, Poisson's Ratio $\nu = 0.3$, thermal-expansion coefficient $\alpha = 1.44 \times 10^{-5}/K$, and density $\rho = 7850\ kg/m^3$. The dynamic fracture-toughness relation that was used has the form (see Sect. 5.1)

$$K_{Id} = K_{Ia} + A\,(\dot{a})^2 \ , \tag{10.3}$$

where

$$K_{Ia} = 35.0 + 4.0177\ e^{0.02408T} \ , \tag{10.4}$$

and A(T) is given by Eqs. (5.5) and (5.6) of Sect. 5.1 with RT_{NDT} = 91.3°C. Units for K, $\dot{a}$, and T are megapascals times square root meters, meters per second, and degree Celsius, respectively. Measured conditions of radial temperature profile and internal pressure at the time of crack propagation in transients B and C of the PTSE-1 experiment are given in Table 10.5 and are assumed to be constant during the brief run-arrest events. Also included in the table are the pressure and initial (uniform) temperature conditions.

Initial displacement conditions for the dynamic analysis were obtained from a quasi-static thermoelastic analysis performed with ADINA (Ref. 10) and the thermal and mechanical loading of Table 10.5. The ADINA program was employed for this calculation because of the absence of a consistent pressure-element formulation in SWIDAC. For the dynamic analysis, the internal pressure boundary nodes of the model were fixed at the initial static displacement values from ADINA, and the nodal temperatures were interpolated from Table 10.5. The stress-intensity factor calculated for the initial condition was taken as the critical initiation factor K_{Ic}. The time step Δt for the dynamic analyses was fixed at Δt = 5 μs.

Results from the elastodynamic analyses of the B and C transients are depicted in Figs. 10.15 and 10.16 and in Table 10.6. The variation of crack-depth ratio a/w with time is given in Fig. 10.15 for the two transients, and good agreement is seen between measured data [$(a_f/w)_B$ = 0.165; $(a_f/w)_C$ = 0.278)] and computed values [$(a_f/w)_B$ = 0.16; $(a_f/w)_C$ = 0.26)] at arrest when the crack length is a_f. Figure 10.16 depicts the dynamic K_I vs a/w relations for the transients and indicates that the crack propagated into a rising K_I field for both run-arrest events. Table 10.6 compares selected results obtained from the quasi-static OCA/USA (Ref. 11) analyses and the dynamic ADINA/SWIDAC analyses. The differences in computed K_I initiation values from OCA/USA (B: K_{Ic} = 177.4 MPa•$\sqrt{m}$; C: K_{Ic} = 254.3 MPa•$\sqrt{m}$) and from ADINA/SWIDAC (B: K_{Ic} = 164.3 MPa•$\sqrt{m}$; C: K_{Ic} = 234.8 MPa•$\sqrt{m}$) are due in part to a relatively coarser radial refinement and the slightly shallower initial crack depth of the dynamic finite-element model. The K_I arrest values given in Table 10.6

Table 10.5. Pressure and temperature conditions[a] at time of crack initiation in tests PTSE-1B and -1C

Radius (m)	Temperature (°C)	
	Transient B	Transient C
0.49060	20.45	18.45
0.48714	44.65	34.75
0.48347	70.25	52.05
0.47953	96.4	70.35
0.47584	118.3	86.85
0.46846	154.1	117.05
0.46125	182.6	142.75
0.44741	229.0	185.15
0.43173	263.3	223.45
0.41680	278.85	248.7
0.40226	285.7	264.9
0.38745	288.95	275.65
0.37274	290.5	282.45
0.36514	290.9	284.8
0.35798	291.2	286.3
0.34300	291.4	287.3

[a]Pressure at time of crack jump and initial uniform temperature:

Transient B: P = 24.91 MPa and T = 290.7°C

Transient C: P = 75.12 MPa and T = 287.4°C

for the dynamic analyses are obtained from the K_{Ia} fracture-toughness relation of Eq. (10.4) evaluated at the temperature of the crack-tip location predicted by SWIDAC (interpolated from Table 10.5) at arrest. These K_{Ia} values [B: $K_{Ia}(T = 161.4) = 230.8$ MPa$\cdot\sqrt{m}$; C: $K_{Ia}(T = 172.6) = 291.4$ MPa$\cdot\sqrt{m}$] can be compared with the dynamic K_I values computed by SWIDAC in the time step immediately preceding crack arrest (B: $K_I = 207.1$ MPa$\cdot\sqrt{m}$; C: $K_I = 277.9$ MPa$\cdot\sqrt{m}$) and not given in Table 10.6 In summary, the comparisons presented in Table 10.6 support the perception that quasi-static and dynamic methods of fracture analysis should be in good agreement for the relatively short run-arrest events observed in PTSE-1.

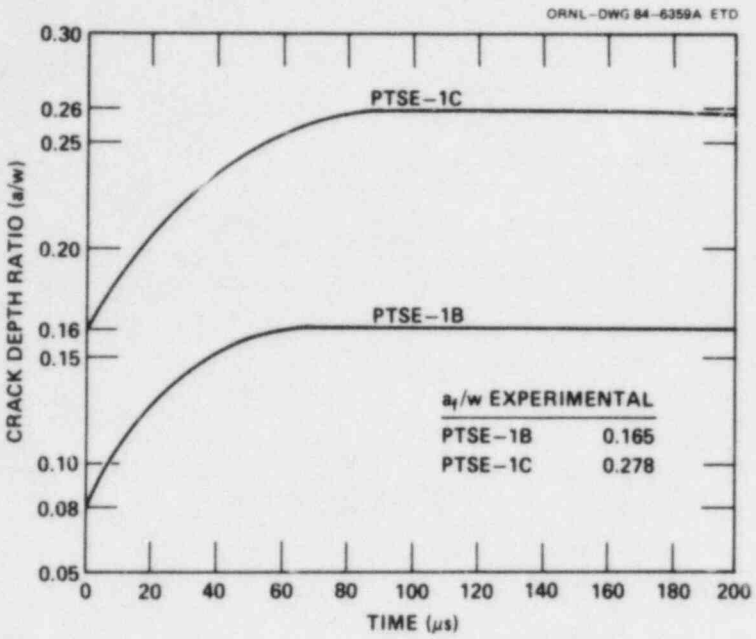

Fig. 10.15. Crack-depth ratio (a/w) vs time for posttest elastodynamic analysis of PTSE-1.

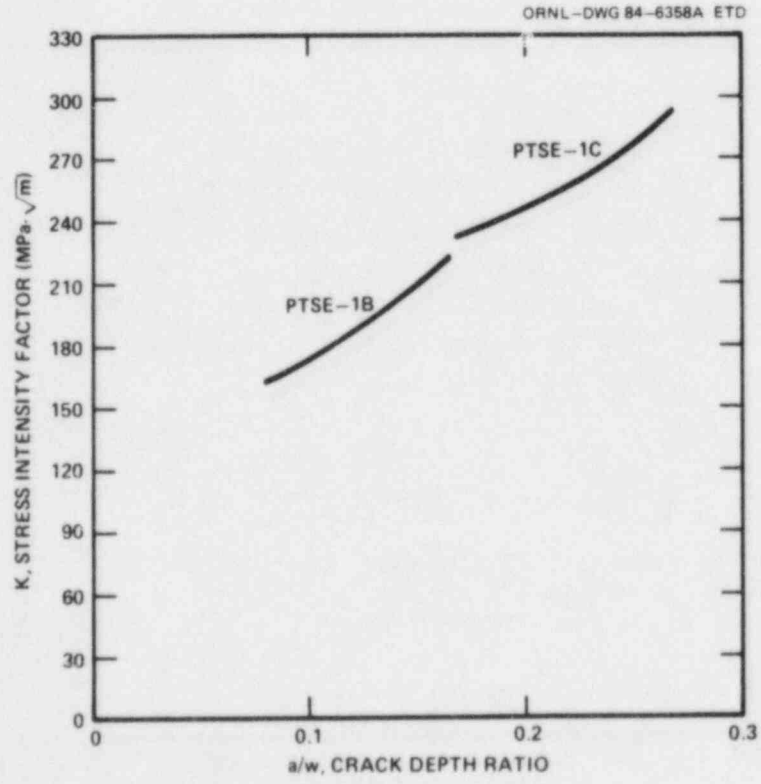

Fig. 10.16. Stress-intensity factor vs crack-depth ratio (a/w) for posttest elastodynamic analysis of PTSE-1.

Table 10.6. Comparison of initiation and arrest parameters from posttest quasi-static and dynamic analyses of PTSE-1

Experiment phase	a/w	a (mm)	Temperature (°C)	K_I (MPa·$\sqrt{m}$)	Event
PTSE-1A					
OCA/USA	0.083	12.2	78	154	Maximum K_I; no initiation
PTSE-1B					
OCA/USA	0.083	12.2	103.7	177.4	Initiation
ADINA	0.08	12.0	101.9	164.3	
OCA/USA	0.165	24.4	163.5	200.9	Arrest
SWIDAC	0.16	24.0	161.4	230.8	
OCA/USA	0.165	24.4	118.0	247.0	Subsequent maximum K_I
PTSE-1C					
OCA/USA	0.165	24.4	125.3	254.3	Initiation
ADINA	0.16	24.4	123.7	234.8	
OCA/USA	0.278	41.0	179.0	298.9	Arrest
SWIDAC	0.26	39.0	172.6	291.4	
OCA/USA	0.278	41.0	156.0	340.0	Subsequent maximum K_I

10.3 Pretest Analyses for PTSE-2 Experiment

G. D. Whitman R. Wanner*

Additional studies of pressurized-thermal-shock transients using the OCA/USA code were performed with the primary objective of determining the allowable variation in fracture toughness of the test material required to perform the second pressurized-thermal-shock experiment (PTSE-2). A low-upper-shelf material will be utilized with the primary objective of determining the fracture behavior of a material having a low tearing resistance, initially specified by low Charpy upper-shelf energy, to obtain data on the behavior of cleavage fracture propagating into the ductile region. In addition, the effect of warm-prestressing and antiwarm-prestressing scenarios on crack initiation will be determined.

The warm-prestressing phenomenon to be studied is one in which K_I proceeds from an initial peak to a second peak that is designed to be greater than the first, such as the transient ABCDE shown in Fig. 10.17. With a given cooldown transient, this variation in the stress-intensity factor at a crack tip is achieved by concurrently varying the internal

*On temporary assignment to Oak Ridge National Laboratory from the Swiss Federal Institute for Reactor Research.

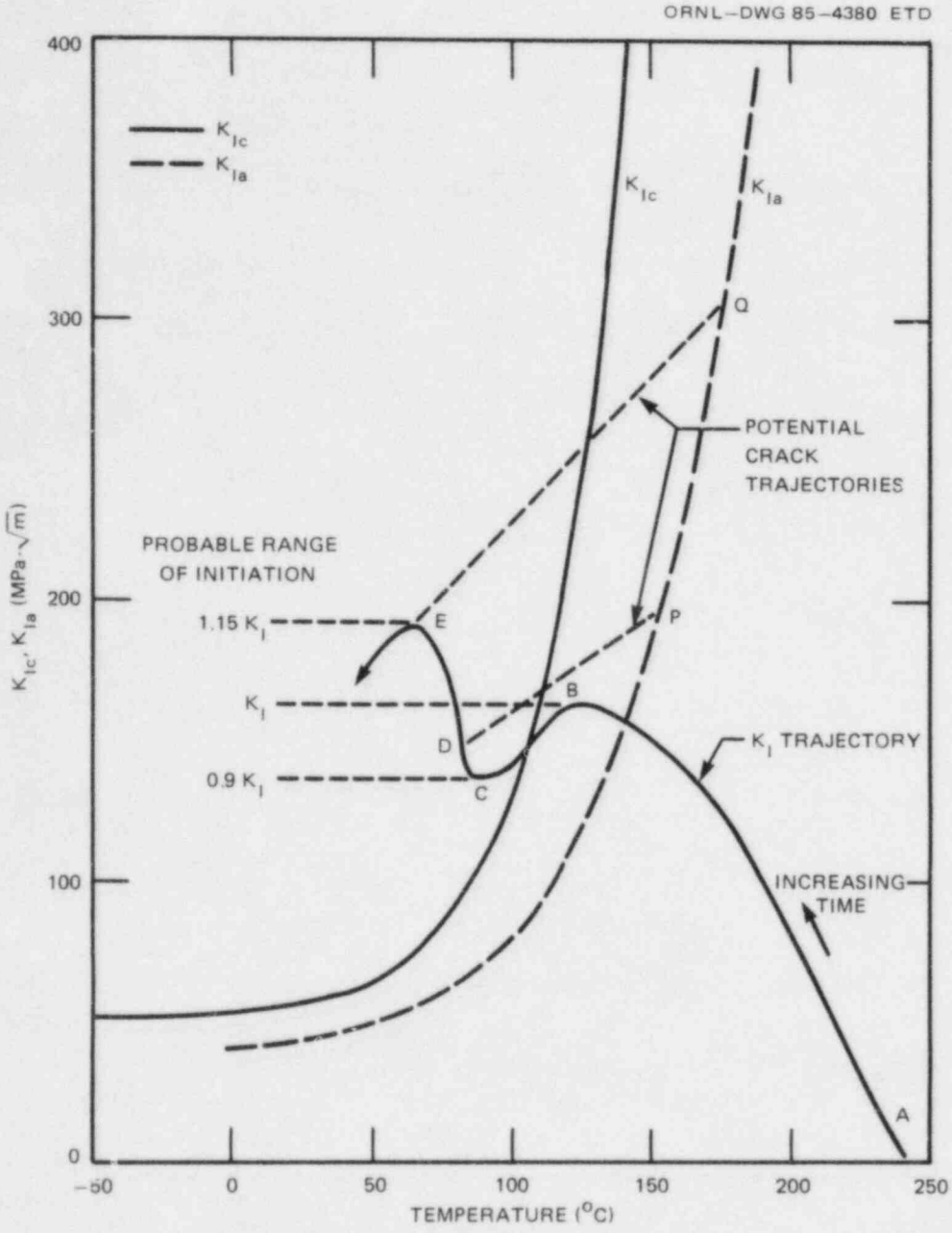

Fig. 10.17. Pressurized-thermal-shock scenario for PTSE-2 that combines warm prestressing and ductile regime crack arrest in a single transient.

pressure in the test vessel. Ideally, a K_I/K_{Ic} ratio equal to unity would be achieved in the negative slope region BC just beyond the first peak B so that the magnitude of K_I at initiation, relative to the first peak, could be ascertained. The ratio of stress intensities, as shown on Fig. 10.17, is designed to ensure a clear definition of the regimes and a high probability of initiation after a warm-prestressing event. The attainment of an arrest condition in the ductile regime at a level below tearing instability will have to be further evaluated when the ductile-

fracture properties and arrest toughness of a specific test material have been ascertained.

Utilizing initial crack depths attainable by electron-beam-flawing techniques, facility coolant temperature and flow rates, pressurization levels and rates of change, and initial vessel temperature, a range of fracture-toughness properties was evaluated that would be compatible with the desired warm-prestressing (BCD), crack-initiation (D or E), and crack-arrest (P or Q) scenario. These results are shown in Fig. 10.18 with an initial flaw having an a/w = 0.12. It can be seen that initiation toughness as specified by RT_{NDT} must be >50°C, and the variation in

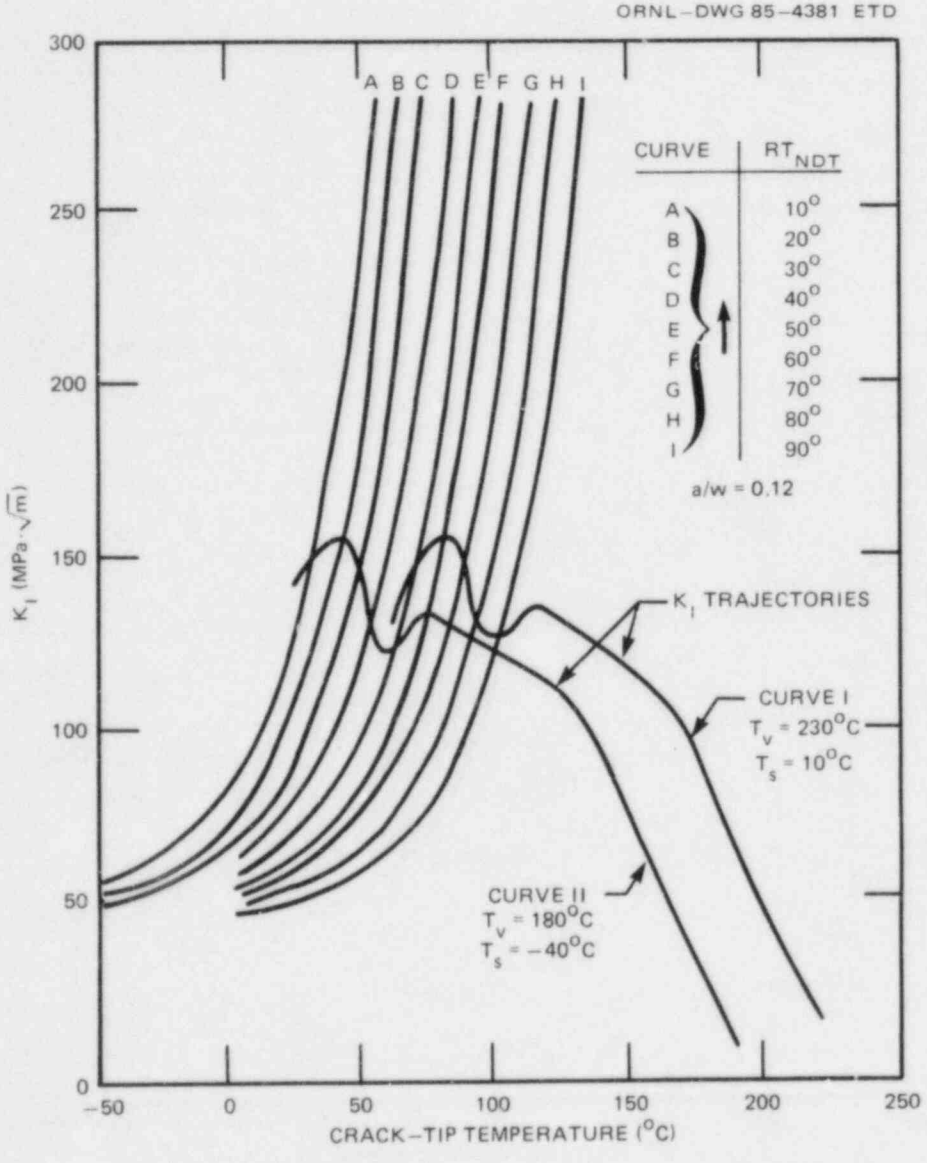

Fig. 10.18. Parametric examination of RT_{NDT} requirements to meet PTSE-2 objectives and capabilities of the ORNL pressurized-thermal-shock test.

this property should not be greater than approximately ±5°C to achieve an initiation in the region of the first negative slope in K_I. The results of these parametric analyses have been used to specify the materials to be procured for the test vessel and will be used to evaluate allowable variations in properties to meet the test objectives. In Fig. 10.18, T_v is the initial uniform vessel temperature, T_s is the coolant sink temperature, and the K_{Ic} curves are based on the correlation used in PTSE-1 analyses with RT_{NDT} treated as a parameter. In particular, K_{Ic} in Fig. 10.18 is given by

$$K_{Ic} = 51.276 + 51.897\, e^{0.036(T-RT_{NDT})}, \qquad (10.5)$$

where K_{Ic} is in megapascals times root meters and T and RT_{NDT} are in degrees Celsius. [Equations (10.5) and (5.2) are representations of K_{Ic} for the PTSE-1 material (curve B in Fig. 10.10) upon assuming RT_{NDT} = 87.8°C.] The two cases represented by Curves I and II in Fig. 10.18 correspond to the pressurized-thermal-shock scenario shown in Fig. 10.17 for the highest RT_{NDT} considered in the study (90°C) and the coldest practicable sink temperature (−40°C), respectively. Curve II illustrates the need for the PTSE-2 test material to have an RT_{NDT} ≥50°C (Curve E) to meet the objectives illustrated in Fig. 10.17.

10.4 Preparation of Vessel for the PTSE-2 Experiment

R. H. Bryan G. C. Robinson

As noted in our previous progress report,[2] an attempt was made to obtain, by means of a sole source contract, a material having both a low-upper-shelf Charpy energy and a relatively high transition temperature to apply to the PTSE-2 experiment. It was believed at the time that the technology developed for the V-8 vessel repair[12] and the PTSE-0 and PTSE-1 insert preparation and characterization[6] would be applicable in large degree to the PTSE-2 experiment with only minor adjustments to obtain the properties desired. During negotiation with the prospective supplier, it became evident that the successful development of the insert material was strongly keyed to a relatively large number of trial attempts with an unanticipated high cost. Consequently, a new approach was taken.

A specification was prepared for competitive bidding that permitted a wide latitude of insert materials in the PTSE-2 experiments with two principal provisions:

1. specified mechanical and toughness properties must be met, and
2. material must be demonstrated to be weldable to the PTSE-2 vessel and to the A 533 grade B class 1 plate material employed in wide-plate crack-arrest tests (for performance under Task H.5).

The stipulated properties for the insert material were (1) yield strength, 448 to 621 MPa; (2) Charpy-V upper-shelf energy, 54 to 68 J; (3) temperature at midpoint of Charpy-V energy transition, 52 to 91°C; (4) maximum temperature at which 100% shear first occurs, 121 to 177°C. In addition,

the insert material should exhibit a tearing resistance vs Charpy-V energy correlation that falls within the bounds given by Fig. 10.19.

Three responses were received from the solicitation for quotation and were reviewed for technical merit. Two were judged to be technically responsive, and a recommendation was made to the Martin Marietta Energy Systems, Inc., Purchasing Division to let a contract to the low bidder. At this time, the contract award is pending, awaiting resolution of terms and conditions and justification of pricing.

Specifications and drawings were prepared for competitive bidding of swaged thimble assemblies, each containing 12 miniature stainless sheathed bed, ceramic-insulated, Type K thermocouples similar to those used in the

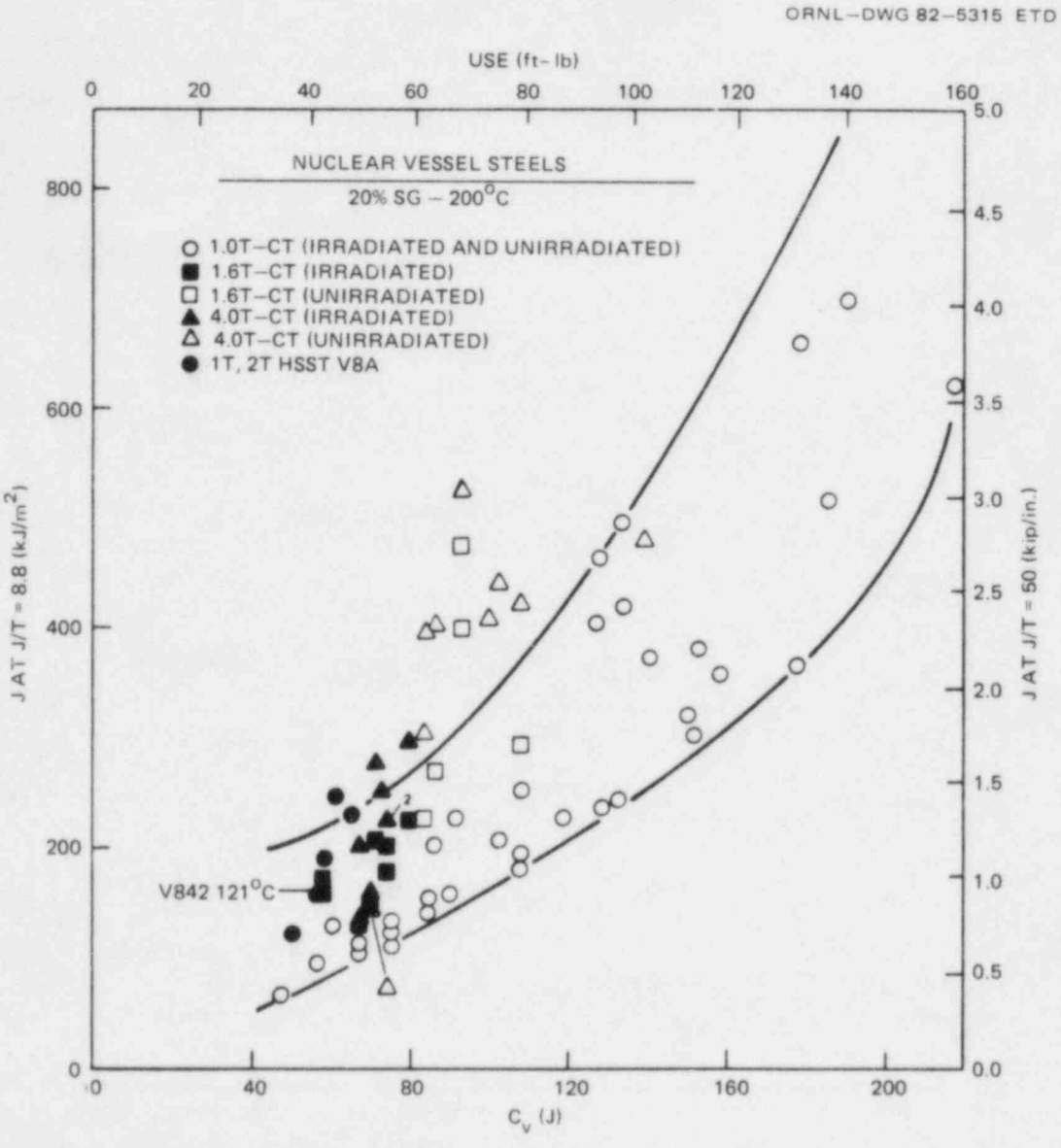

Fig. 10.19. Correlation of CVN, USE, and J at fixed value of J/T.

PTSE-0 and PTSE-1 experiments. A preliminary inquiry process was followed to establish that competitive bidding was feasible and to obtain responses to the technical requirements. The specifications and drawings were revised in response to the inputs received from the prospective suppliers. A solicitation for quotation was then advertised, and three responses were received. No significant technical exceptions were taken by any of the prospective suppliers. To ensure delivery of the assemblies commensurate with the PTSE-2 experiment schedule, we have recommended that the Martin Marietta Energy Systems, Inc., Purchasing Division award contracts to the two lowest bidders for ten assemblies each.

References

1. R. H. Bryan, "Pressurized-Thermal-Shock Technology," pp. 142–73 in *Heavy-Section Steel Technology Program Semiannual Prog. Rep. October 1983–March 1984*, NUREG/CR-3744, Vol. 1 (ORNL/TM-9154/V1), Martin Marietta Energy Systems, Inc., Oak Ridge Natl. Lab.

2. R. H. Bryan, "Pressurized-Thermal-Shock Technology," pp. 201–17 in *Heavy-Section Steel Technology Program Semiannual Prog. Rep. April–September 1984*, NUREG/CR-3744, Vol. 2 (ORNL/TM-9154/V2), Martin Marietta Energy Systems, Inc., Oak Ridge Natl. Lab.

3. R. H. Bryan et al., *Pressurized-Thermal-Shock Test of 6-in.-Thick Pressure Vessels. PTSE-1: Investigation of Warm Prestressing and Upper-Shelf Arrest*, NUREG/CR-4106 (ORNL-6135), Martin Marietta Energy Systems, Inc., Oak Ridge Natl. Lab., April 1985.

4. B. R. Bass, R. H. Bryan, and J. W. Bryson, "The OCA/USA Program for Analysis of PTS Experiments," pp. 78–88 in *Heavy-Section Steel Technology Program Quart. Prog. Rep. July–September 1983*, NUREG/CR-3334, Vol. 3 (ORNL/TM-8787/V3), Union Carbide Corp. Nuclear Div., Oak Ridge Natl. Lab.

5. R. L. Powell et al., *Thermocouple Reference Tables Based on the IPTS-68*, Monograph 125, U.S. National Bureau of Standards, Washington, 1975.

6. H. A. Domian, *Vessel V-7 and V-8 Repair and Characterization of Insert Material*, ORNL/Sub/82-52845/1, Martin Marietta Energy Systems, Inc., Oak Ridge Natl. Lab., May 1984.

7. A. R. Rosenfield et al., "Crack-Arrest Studies at BCL," pp. 57–60 in *Heavy-Section Steel Technology Program Semiannual Prog. Rep. October 1983–March 1984*, NUREG/CR-3744, Vol. 1 (ORNL/TM-9154/V1), Martin Marietta Energy Systems, Inc., Oak Ridge Natl. Lab.

8. R. H. Bryan et al., "Analysis of PTSE-1," pp. 150–58 in *Heavy-Section Steel Technology Program Semiannual Prog. Rep. October 1983–March 1984*, NUREG/CR-3744, Vol. 1 (ORNL/TM-9154/V1), Martin Marietta Energy Systems, Inc., Oak Ridge Natl. Lab.

9. J. Jung et al., *Finite-Element Analysis of Dynamic Crack Propagation*, presented at the 1981 ASME Failure Prevention and Reliability Conference, September 23–26, 1981, Hartford, Conn.

10. K. J. Bathe, *ADINA — A Finite Element Program for Automatic Dynamic Incremental Nonlinear Analysis*, Report 82448-1, Massachusetts Institute of Technology, Cambridge, Mass., September 1975 (revised December 1978).

11. R. H. Bryan and J. G. Merkle, Upper-Shelf Arrest Analysis Based on J_R-Controlled Tearing," pp. 111–24 in *Heavy-Section Steel Technology Program Quart. Prog. Rep. January–March 1983*, NUREG/CR-3334, Vol. 1 (ORNL/TM-8787/V1), Union Carbide Corp. Nuclear Div., Oak Ridge Natl. Lab.

12. H. A. Domian, *Vessel V-8 Repair and Preparation of Low Upper-Shelf Weldment*, NUREG/CR-2676 (ORNL/Sub/81-85813/1), Union Carbide Corp. Nuclear Div., Oak Ridge Natl. Lab., June 1982.

CONVERSION FACTORS[a]

SI unit	English unit	Factor
mm	in.	0.0393701
cm	in.	0.393701
m	ft	3.28084
m/s	ft/s	3.28084
kN	lb_f	224.809
kPa	psi	0.145038
MPa	ksi	0.145038
$MPa \cdot \sqrt{m}$	$ksi \cdot \sqrt{in.}$	0.910048
J	ft•lb	0.737562
K	°F or °R	1.8
kJ/m^2	$in.\text{-}lb/in.^2$	5.71015
$W \cdot m^{-2} \cdot K^{-1}$	$Btu/h\text{-}ft^2\text{-}°F$	0.176110
kg	lb	2.20462
kg/m^3	$lb/in.^3$	3.61273×10^{-5}
mm/N	$in./lb_f$	0.175127
$T(°F) = 1.8\ T(°C) + 32$		

[a]Multiply SI quantity by given factor to obtain English quantity.

NUREG/CR-4219
Volume 1
ORNL/TM-9593/V1
Dist. Category RF

Internal Distribution

1. B. R. Bass
2. R. G. Berggren
3. S. E. Bolt
4. R. H. Bryan
5. J. W. Bryson
6. R. D. Cheverton
7. J. M. Corum
8. W. R. Corwin
9. D. M. Eissenberg
10. J. A. Getsi
11. R. C. Gwaltney
12. S. K. Iskander
13. A. P. Malinauskas
14. S. S. Manson
15. R. W. McCulloch
16. J. J. McGowan
17. J. G. Merkle
18-19. R. K. Nanstad
20. D. J. Naus
21-25. C. E. Pugh
26. G. C. Robinson
27. G. M. Slaughter
28. J. E. Smith
29. R. W. Swindeman
30. K. R. Thoms
31. H. E. Trammell
32. C. D. West
33-36. G. D. Whitman
37. G. T. Yahr
38. ORNL Patent Office
39. Central Research Library
40. Document Reference Section
40-42. Laboratory Records Department
43. Laboratory Records (RC)

External Distribution

44. C. Z. Serpan, Division of Engineering Technology, Nuclear Regulatory Commission, Washington, DC 20555
45. M. Vagins, Division of Engineering Technology, Nuclear Regulatory Commission, Washington, DC 20555
46. W. H. Bamford, Plant Engineering Division, Westinghouse Electric Corporation, Pittsburgh, PA 15230
47. R. A. Fields, Fracture and Deformation Division, National Bureau of Standards, Gaithersburg, MD 20899
48. W. L. Fourney, Department of Mechanical Engineering, University of Maryland, College Park, MD 20742
49. M. F. Kanninen, Engineering and Material Science Division, Southwest Research Institute, San Antonio, TX 78284
50. Office of Assistant Manager for Energy Research and Development, DOE, ORO, Oak Ridge, TN 37831
51-52. Technical Information Center, DOE, Oak Ridge, TN 37831
53-327. Given distribution as shown in category RF (NTIS – 10)

NRC FORM 335 (2 84) NRCM 1102 3201 3202

U.S. NUCLEAR REGULATORY COMMISSION

BIBLIOGRAPHIC DATA SHEET

SEE INSTRUCTIONS ON THE REVERSE

1 REPORT NUMBER (Assigned by TIDC add Vol No. if any)

NUREG/CR-4219/V1
ORNL/TM-9593/V1

2 TITLE AND SUBTITLE

Heavy-Section Steel Technology Program Semiannual Progress Report for October 1984-March 1985

3 LEAVE BLANK

4 DATE REPORT COMPLETED

MONTH: May | YEAR: 1985

5 AUTHOR(S)

C. E. Pugh

6 DATE REPORT ISSUED

MONTH: June | YEAR: 1985

7 PERFORMING ORGANIZATION NAME AND MAILING ADDRESS (Include Zip Code)

Oak Ridge National Laboratory
P. O. Box X
Oak Ridge, TN 37831

8 PROJECT/TASK/WORK UNIT NUMBER

9 FIN OR GRANT NUMBER

B0119

10 SPONSORING ORGANIZATION NAME AND MAILING ADDRESS (Include Zip Code)

Division of Engineering Technology
Office of Nuclear Regulatory Research
U. S. Nuclear Regulatory Commission
Wshington, DC 20555

11a TYPE OF REPORT

Semiannual

b PERIOD COVERED (Inclusive dates)

Oct. 1984-March 1985

12 SUPPLEMENTARY NOTES

13 ABSTRACT (200 words or less)

The Heavy-Section Steel Technology (HSST) Program is an engineering research activity conducted by the Oak Ridge National Laboratory for the Nuclear Regulatory Commission. The program comprises studies related to all areas of the technology of materials fabricated into thick-section primary-coolant containment systems of light-water-cooled nuclear power reactors. The investigation focuses on the behavior and structural integrity of steel pressure vessels containing cracklike flaws. Current work is organized into ten tasks: (1) program management, (2) fracture-methodology and analysis, (3) material characterization and properties, (4) environmentally assisted crack growth studies, (5) crack arrest technology, (6) irradiation effects studies, (7) cladding evaluations, (8) intermediate vessel tests and analysis, (9) thermal-shock technology, and (10) pressurized thermal-shock technology.

14 DOCUMENT ANALYSIS - a KEYWORDS/DESCRIPTORS

Pressure vessels
Ferritic steels
Weldments
Irradiation
Cladding
Flaws
Thermal shock
Fracture mechanics
Crack arrest
Crack growth

b IDENTIFIERS/OPEN-ENDED TERMS

15 AVAILABILITY STATEMENT

Unlimited

16 SECURITY CLASSIFICATION

(This page) Unclassified

(This report) Unclassified

17 NUMBER OF PAGES

18 PRICE